Movement on Demand: Pharmacological and Protein-based Inhibition of Mitotic Kinesins

by

April L. Solon

A dissertation submitted in partial fulfillment
of the requirements for the degree of
Doctor of Philosophy
(Cancer Biology)
In the University of Michigan
2022

Doctoral Committee:

Professor Nouri Neamati, Chair
Professor Howard Crawford
Associate Professor Ryoma Ohi
Professor Kristen Verhey

April L. Solon

alsolon@umich.edu

ORCID iD: 0000-0001-9869-1548

Dedication

To my family

Acknowledgements

This work was made possible by the support of many. To my mentor Puck Ohi, I cannot thank you enough. Your mentorship has truly shaped the scientist I have become. Thank you for your constant encouragement and for always supporting my scientific and career aspirations, for giving me the freedom to pursue new areas and the mentorship to help chart my course, and for always making the lab a fun place to be. Thank you to the past and present Ohi lab members; Margo Gebbie, Takashi Hotta, Brittany Salazar, Erica Colicino, and Alex Plemmons, thank you for all the laughs and snacks and wasted time.

To my thesis committee members Kristen Verhey, Nouri Neamati, and Howard Crawford, thank you for your support and mentorship over the years, my work was made so much better with all of your input. Thank you as well to the Microtubule Supergroup, my second unofficial thesis committee, and to our KIFBP project collaborators. You have all made science more achievable, more interesting, and more fun.

I would like to thank the Cancer Biology program students past and present. I've been lucky to meet some of my dearest friends in this program, and I have seen time and time again how the CBP could not function without its students who care so much about the program and each other. And thank you of course to the CBP leadership and admins; Dawn Storball, Zarinah Aquil, Chanise Holmes, Beth Lawlor, and David Lombard, thank you for your tireless efforts on behalf of all CBP students. I would also like to thank the Cell and Developmental Biology department. To Pierre Coulombe and everyone on the CDB administrative team, thank you for always making me feel welcome and at home in the department and for all of your help during my time in Puck's lab.

Lastly, I would like to thank my friends and family, without whom I would not have made it to the end of my PhD or to grad school in the first place. To all of my friends, thank you for keeping me sane, and loving and supporting me endlessly. To my partner Elird Haxhiu, thank you for being my rock and for making me laugh every single day. And

to my parents, thank you for your inspiration, love, and support; I mean it when I say I wouldn't be here without you!

Financial Acknowledgements

I would like to thank the funding sources that supported this research. Thank you to the Cancer Biology Program for support *via* Rogel Cancer Center Funds, and to NIH grant R01 GM086610, pilot project funding from Michigan Drug Discovery, and start-up funds from the University of Michigan for funding this work.

Table of Contents

List of Figures

List of Tables

Abstract

Mitosis is the process by which the cell's duplicated genome is divided into two daughter cells. Accuracy of chromosome segregation is essential for maintaining healthy cells, and thus numerous cellular networks and signaling pathways are charged with ensuring mitotic fidelity. As deregulated cell division and chromosome instability are two hallmarks and drivers of cancer, a leading cause of death worldwide, it is imperative to continue improving our understanding of the molecular mechanisms underpinning mitosis.

Kinesins comprise a superfamily of molecular motor proteins whose functions include organizing the mitotic spindle, the microtubule-based machine that powers chromosome segregation. As they are essential for mitotic progression, mitotic kinesins have been recognized as promising therapeutic targets for the development of anticancer agents. Numerous chemical inhibitors of the Kinesin-5 Eg5, a motor critical for building bipolar spindles, have been designed and tested against a range of cancers; unfortunately, while Kinesin-5 inhibitors (K5Is) perform well in preclinical studies, they fail to induce tumor regression in patients. One potential mechanism behind this discrepancy is the existence of another motor protein that is capable of driving spindle assembly in an Eg5-independent manner. Indeed, several functional redundancies exist among the kinesin superfamily, and it has been shown that Eg5-independent mitosis relies on the Kinesin-12 KIF15.

KIF15 is non-essential for mammalian cells; however, under the selective pressure of K5I treatment, some cells acquire genetic alterations that make KIF15 essential for spindle assembly. We hypothesize that K5Is may not reach their clinical potential unless paired with an inhibitor of KIF15. Unfortunately, the field lacks a well-characterized, selective KIF15 inhibitor with which to test this theory. Additionally, much remains unknown about how KIF15 is able to drive Eg5-independent spindle assembly, including the mechanisms by which KIF15 is regulated in cells.

In this thesis, I present the discovery of two chemical inhibitors of KIF15 identified from a library of 24,000 small molecules (Chapter 3). These inhibitors potently and selectively inhibit KIF15 activity both *in vitro* and in cells, and have distinct mechanisms of inhibition. The findings of this screen represent a useful resource that can be harnessed to study the role of KIF15 in spindle organization. Additionally, I show how this work can be extended to the identification of other kinesin inhibitors through adaptation of our screening pipeline (Chapter 2).

I then focus in on KIF15's physiological role in cells and present work characterizing a novel mechanism of kinesin regulation *via* kinesin-binding protein (KIFBP) (Chapter 4). A combination of structural biology, biochemistry, and cell-based assays shows that KIFBP binds to the motor domain of KIF15 and remodels its conformation to enable complex formation and prevent interaction with microtubules. Our findings identify several regions of KIFBP that are essential for kinesin-binding, and suggest a conformational basis for how KIFBP selectively binds a subset of kinesins in cells. Collectively, this work advances our understanding of how cellular reorganization is regulated each cell cycle, and provides a valuable tool with which to continue advancing our knowledge of the role of KIF15 in cell division.

Chapter I: Introduction

1.1 Mitosis, motors, and the cytoskeleton

1.1.1 Microtubule structure

Microtubules are polymers composed of α- and β-tubulin heterodimers that stack to form hollow tubes roughly 25 nm in diameter. They are inherently dynamic, going through phases of polymerization and depolymerization sometime on the scale of seconds, a phenomenon called dynamic instability (Mitchison and Kirschner 1984). Both the α- and β-tubulin subunits bind GTP, but α-tubulin does not hydrolyze the nucleotide. On the other hand, the β-tubulin subunit hydrolyzes GTP to GDP upon polymerization, and nucleotide exchange occurs upon depolymerization (Spiegelman, Penningroth, and Kirschner 1977).

Microtubules assemble, or nucleate, from either pre-formed microtubule seeds *in vitro* or from nucleating structures like centrosomes or axonemes in cells (Fygenson et al. 1995). Once nucleated, microtubules can rapidly assemble into long polymers with the addition of tubulin heterodimers to each end. The heterodimers stack head-to-head, making microtubules polar structures with much faster polymerization dynamics at the plus end compared to the minus end (Allen and Borisy 1974).

Microtubule organization and dynamics vary greatly throughout the cell cycle. During interphase, they form the tracks that mediate intracellular transport and aid in motility. Upon mitotic entry, the microtubule network reorganizes into what is termed the mitotic spindle, the microtubule-based machine that facilitates chromosome alignment and segregation. In the spindle, a combination of plus end-polymerization, minus end depolymerization, and outward sliding forces creates a poleward translocation of microtubules, a phenomenon known as microtubule flux (Forer 1965; T. Mitchison et al. 1986). While the exact mechanism of and reason for flux remain unclear, it appears necessary for establishing and maintaining chromosome alignment and spindle length in

metaphase spindles and contributes to the polewards-movement of chromosomes during anaphase (Rogers et al. 2004).

1.1.2 The mitotic spindle & the spindle assembly checkpoint

The function of the mitotic spindle is to organize the duplicated genome and accurately segregate it into two genetically identical daughter cells during cell division. The multitude of events that comprise mitosis can be classified into five stages. In prophase, chromatin condenses into chromosomes and the centrosomes start to separate to opposite sides of the nucleus. Prometaphase begins with nuclear envelope breakdown (NEB) and chromosomes begin to attach to spindle microtubules emanating from each centrosome. Chromosomes form stable attachments to microtubules extending from opposite poles in metaphase, and align at the spindle equator. Proper chromosome attachments are necessary to satisfy the spindle assembly checkpoint (SAC) before the cell can proceed past metaphase. In anaphase, sister chromatids are separated towards each pole as the spindle elongates. In the final phase, telophase, a cleavage furrow forms between the two sets of chromosomes and constructs to complete division into two cells.

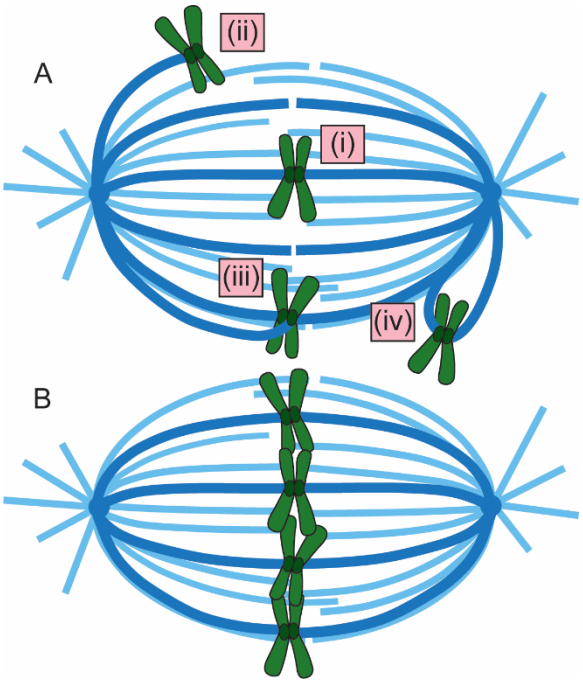

Fig. 1.1: Amphitelic attachments are necessary for accurate chromosome segregation. A) The four types of chromosome attachments that can form during chromosome congression. (i) Amphitelic: each kinetochore is attached to microtubules from opposite poles. (ii) Monotelic: only one kinetochore is attached to microtubules from one pole. (iii) Merotelic: at least one kinetochore is attached to microtubules from both poles. (iv) Syntelic: both kinetochores are attached to microtubules from the same pole. B) Only when all kinetochores are attached ampitelicly can the spindle assembly checkpoint be turned off.

The spindle assembly checkpoint (SAC) is one of signal transduction pathways in the cell cycle that impede cycle progression until the necessary parameters are met. The purpose of the SAC is to ensure chromosomes are attached stably and aligned at the metaphase plate before anaphase onset. After nuclear envelope breakdown at the start of pro-metaphase, condensed chromosomes attach *via* their kinetochores to microtubules

extending from each pole. Several types of attachments can form, and only one is stable enough to satisfy the SAC.

The desired type of attachment is amphitelic, where each kinetochore of sister chromatids attaches to k-fibers from opposite centrosomes. This is the most stable type of attachment and all chromosomes must be amphitelicly attached in order to satisfy the SAC and proceed to anaphase (*Fig. 1.1B*). Amphitelic attachments produce tension across the kinetochores, created by a force-balance between outward force on kinetochore microtubules generated by mitotic motors and the inward forces that hold sister chromatids together (Zhou, Yao, and Joshi 2002). It is still unclear where the signal for SAC satisfaction comes from, but it is thought to either arise from tension between sister kinetochores or from the attachment of microtubules to kinetochores (Richard McIntosh 1991; Pinsky and Biggins 2005). Several other non-amphitelic attachments can form during the process of chromosome congression: monotelic attachments, where only one kinetochore is attached; merotelic attachments, where one kinetochore is attached to microtubules from both poles; and syntelic attachments, where both kinetochores are attached to microtubules from the same pole (*Fig. 1.1A*). All three of these are erroneous attachments and must be corrected *via* various error-correction mechanisms before anaphase can proceed. Notably, merotelic attachments are not detected by the SAC, and are the source of most chromosome segregation errors in mammalian cells (Cimini et al. 2001). With all non-amphitelic attachments, the correction process results in an intermediate state comprised of a mono-oriented chromosome with one unattached kinetochore, which results in SAC activation until it becomes amphitelicly attached (Rieder and Maiato 2004).

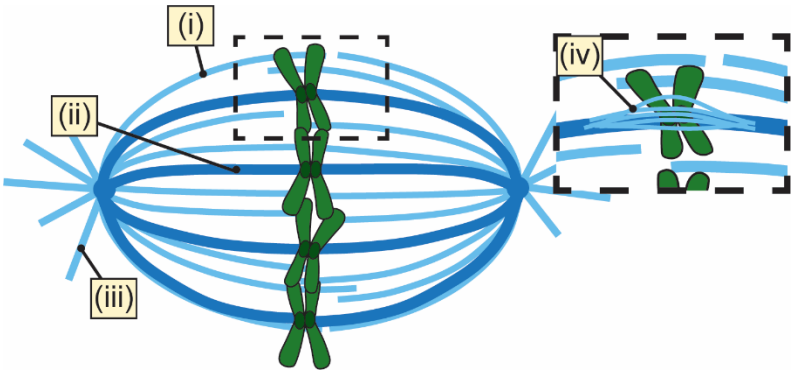

Fig. 1.2: Microtubule populations within the spindle. (i) Interpolar microtubules span the length of the spindle. (ii) Kinetochore microtubules form bundles that attach to chromosomes at their kinetochores. (iii) Astral microtubules extend outward from the spindle and anchor the spindle in the cell. (iv) Bridging fibers are bundles of interpolar microtubules that interact with kinetochore microtubules and bridge the spindle equator across sister kinetochores.

1.1.3 Organization of the mitotic spindle

The mitotic spindle contains at least three populations of microtubules: interpolar, kinetochore, and astral microtubules (*Fig 1.2*). The network of interpolar microtubules spans the length of the spindle, emanating from the microtubule organizing center (MTOC) at each pole and overlapping in the midzone. The antiparallel microtubules in the overlap provide a substrate for crosslinkers and molecular motors to act on, establishing the bipolarity of the spindle and keeping it from collapsing (Mastronarde et al. 1993). Kinetochore microtubules function to exert outwards forces on chromosomes at their kinetochores in order to silence the spindle assembly checkpoint (SAC) during metaphase and segregate the chromosomes during anaphase (McDonald et al. 1992). Between 10 and 30 kinetochore microtubules comprise k-fibers, bundles of microtubules that are attached at their plus ends to the kinetochores of chromosomes with their minus ends at or close to the spindle poles (McEwen, Ding, and Heagle 1998). Finally, astral microtubules attach at their minus ends to the centrosomes, but radiate outwards with their plus ends extended towards the cell cortex. Astral microtubules function to anchor the position of the spindle within the cell (Grill et al. 2003). Kinetochore microtubules are fairly stable and have a long half-life of up to several minutes, while interpolar and astral microtubules are much more dynamic and short-lived, with half-lives on the order of around 10 seconds (Maiato, Rieder, and Khodjakov 2004; Zhai, Kronebusch, and Borisy 1995). Recently, a fourth population of microtubules termed “bridging fibers” has been described (Kajtez et al. 2016). These microtubules comprise bundles of microtubules that span the overlap zone in the spindle equator and act as a bridge between pairs of sister kinetochores by interacting laterally with kinetochore microtubules. Bridging fibers are hypothesized to help balance the tension between kinetochores and give the spindle its rounded shape (Kajtez et al. 2016).

The spindle is home to a variety of microtubule-associated proteins (MAPs) that are crucial for regulating the structure and dynamics of spindle microtubules. Many of these MAPs are molecular motors, proteins that convert energy from ATP hydrolysis into mechanical force. These motors, which include the kinesin superfamily and cytoplasmic dynein, use this force to organize spindle microtubules into a bipolar array and regulate their dynamics. Non-motor MAPs include proteins that either stabilize or destabilize microtubules, and some that do both (Hélder Maiato, Sampaio, and Sunkel 2004). Proper

spindle organization depends on balancing the outward and inward forces of microtubule-associated motors. In mammalian cells, members of the Kinesin-5 and -12 families provide outward, plus-end-directed forces that separate the centrosomes and afford the spindle its bipolarity, while dynein and Kinesin-14 provide the inward, minus-end-directed forces that focus the spindle poles. Deletion or inhibition of one of these motors upsets the force-balance and impairs normal spindle assembly, which can be rescued by deletion or inhibition of another oppositely-directed motor (Saunders, Lengyel, and Hoyt 1997; T. J. Mitchison et al. 2005).

1.1.4 The kinesin superfamily

More than 40 microtubule-based motor proteins comprise the kinesin superfamily, which is subdivided into 14 families (Lawrence et al. 2004). All kinesins contain a highly conserved motor domain with the ability to bind both microtubules and ATP, and a tail domain that confers specific cargo-binding abilities to each motor. Most kinesins form homodimers with a pair of motor heads on one end of the motor, although some, such as members of the Kinesin-5 family, are homotetrameric in structure with two pairs of motors at opposite ends of the molecule (Kashina et al. 1996). The position of the motor within the polypeptide dictates directionality. Plus-end directed motors, or motors whose motility is directed mainly towards the plus-end of the microtubule, generally possess N-terminal motor domains (Kinesin families 1-12), whereas the motor domains of minus-end directed kinesins are located at the C-terminal (Kinesin-14). One exception is the Kinesin-13 family that possesses a centrally-located motor domain and function to destabilize microtubules (Moores and Milligan 2006). ATP hydrolysis powers conformational changes within the motor that enable stepping along microtubule tracks. Studies have shown that kinesins move via a “hand-over-hand” model, in which the motor heads take turns leading rather than one head always being in the lead (Yildiz et al. 2004).

1.2 Mitosis as a target for anticancer therapies

Cancer is one of the leading causes of death worldwide, resulting in nearly 10 million deaths in 2020 (Ferlay et al. 2021). Thus, the drive to develop new therapeutics to treat cancer is strong, and fuels a fast-growing pharmaceutical industry. As cancer is a group of diseases characterized by deregulated cell division, many currently used cancer

therapeutics target this increased proliferation, disrupting various stages of the cell cycle in tumor cells through a variety of mechanisms. Some drugs induce apoptosis in cancer cells by damaging their DNA and activating the DNA damage response, or by inhibiting the synthesis of DNA (Montecucco, Zanetta, and Biamonti 2015; Woods and Turchi 2013). Another class of anticancer therapies are anti-mitotic agents, which selectively block mitotic progression in cancer cells (Jordan and Wilson 2004). Anti-mitotic drugs activate the SAC in dividing cells, which typically results in a prolonged mitotic delay and subsequent apoptosis. Here, I will discuss the major classes of anti-mitotics that have been developed and the current outlook on their use as anti-cancer therapies.

1.2.1 Vinca Alkaloids

Vinca alkaloids (VAs) were discovered as compounds that arrest cells in mitosis with spindle defects, similar to colchicine (Palmer, 1960). Vinblastine was the first VA discovered, identified in 1958 from *Catharanthus roseus*, or periwinkle plant (Noble, Beer, and Cutts 1958). It is used clinically, often as part of a combination regimen, to treat lung cancer, breast cancer and several hematological cancers (Lucas et al. 2010; Martino et al. 2018). At high concentrations, they can induce depolymerization of microtubules, while at lower concentrations they alter microtubule dynamics and prevent microtubule polymerization. When treated with vinca alkaloids, cells arrest in metaphase. Cells often retain normal spindle organization and microtubule structure when low doses are used, although one or more chromosomes can frequently be found near the spindle poles (Jordan, Thrower, and Wilson 1991). Spindle structure becomes more disrupted with increasing concentrations of vinca alkaloids, culminating with total microtubule depolymerization at the highest doses. These drugs appear to have little effect on interphase cells or cell cycling other than the progression of metaphase to anaphase (Jordan, Thrower, and Wilson 1991).

Vinca alkaloids bind reversibly to β-tubulin at what is termed the "*Vinca* domain", which is known to bind a variety of other drugs (Bai, Pettit, and Hamel 1990). VAs bind to tubulin subunits at microtubule ends with higher affinity than subunits along the lattice; this difference in affinity can explain how VAs suppress dynamics at microtubule ends at low concentrations while completely destabilizing microtubules at higher concentrations

(M. A. Jordan et al. 1986; L. Wilson et al. 1982; Singer et al. 1989). At very high concentrations (> 10 μM), VAs can actually cause tubulin to self-aggregate into paracrystalline arrays (M. A. Jordan et al. 1986).

Five VAs are currently in use to treat a wide range of cancers. Vinblastine and vincristine are the two natural VAs identified in the late 1950's, and are currently used to treat both solid tumors and hematological malignancies. Three semisynthetic VA analogs have since been developed, including vindesine, vinorelbine, and vinflunine. Vindesine is only approved for use in a handful of countries due to its severe side effects (Dyke, Nelson, and Brade 1979). Vinorelbine is more potent and has fewer side effects compared to the natural VAs, and is used to treat advanced or metastatic breast and non-small-cell lung cancer (Budman 1997). Vinflunine is the most recently developed VA and is currently being evaluated, but has been approved in Europe to treat urothelial carcinoma (Bellmunt et al. 2009).

1.2.2 Taxanes

After the discovery of vinca alkaloids, screening of natural products led to the identification of several other types of tubulin poisons, most of which target the β-tubulin subunit. Perhaps the most clinically successful of these was taxol, which was isolated in 1971 from the Pacific yew *Taxus brevifolia* (Wani et al. 1971). Taxol binds reversibly to microtubules with high affinity, and with much lower affinity to soluble tubulin (Parness and Horwitz 1981; Manfredi, Parness, and Horwitz 1982). Photoaffinity studies have shown that taxol binds to the N-terminus of the B-subunit of tubulin dimers, binding along the inside surface of microtubule filaments (Rao et al. 1994, 1995). *In vitro*, taxol promotes microtubule polymerization, enhancing both nucleation and elongation and stabilizing the filaments such that they are resistant to cold temperatures. (Schiff and Horwitz 1981; Kumar 1981; Howard and Timasheff 1988). Interestingly, taxol-polymerized microtubules typically contain 12 protofilaments, whereas the semisynthetic taxol analog, Taxotere, induces normal 13-protofilament microtubules (Díaz and Andreu 1993).

At low concentrations of taxol, shortening of microtubule plus ends is reduced while the dynamics of minus ends are unaffected (Derry, Wilson, and Jordan 1998). At intermediate concentrations, microtubule growth rates are also decreased and the

filaments are stabilized in a state of pause. At very high doses, microtubule shortening is inhibited at both ends of the filament and polymerization is enhanced, causing a sharp increase in the mass of microtubule polymer (Caplow and Zeeberg 1982; L. Wilson et al. 1985). Much like VAs, low doses of taxol block cells in mitosis without producing significant spindle assembly defects (M. A. Jordan et al. 1993). Disruption in spindle organization characterized by chromosomes stuck at the poles and large bundles of stabilized microtubules become more apparent with increasing doses (De Brabander et al. 1981). Apoptosis following taxol treatment is common (M. A. Jordan et al. 1996).

Currently, three types of taxanes are used to treat cancer: paclitaxel, docetaxel, and cabazitaxel. Paclitaxel was first tested in clinical trials during the 1980's against advanced ovarian and breast cancers, and docetaxel showed efficacy against breast cancer soon after. Both drugs are currently used as frontline therapies for a variety of tumor types, including lung, bladder, breast, prostate, and ovarian cancer. Cabazitaxel was more recently approved for use to treat hormone-refractory metastatic prostate cancer in combination with prednisone (Mosca et al. 2021).

1.2.3 How do MTAs cause cell death?

Chemical inhibitors that impair stable kinetochore attachment, centrosome separation, or alter microtubule dynamics can arrest mitotic progression by preventing the SAC from being satisfied. Prolonged SAC activation can result in cell death at several points, whether during the disrupted mitosis, during the following interphase cycle, or following an abnormal cell division (Rieder and Maiato 2004). Several mechanisms for apoptosis following mitotic arrest have been proposed, and so the precise method remains unclear and controversial. Most likely, contradictory results have arisen from variation between studies in cell lines, drug types and doses, and experimental techniques and analysis. Additionally, the duration of mitotic arrest can vary between transformed and non-transformed cells (Brito and Rieder 2009).

After prolonged mitotic delay with an unsatisfied SAC, cells will typically either i) die before exiting mitosis; ii) exit mitosis as a 4N cell (i.e. containing both sets of replicated genetic material) and die in the subsequent G1 phase; iii) exit mitosis as a 4N cell that is metabolically viable but reproductively dead, and ultimately die through either

senescence or apoptosis; iv) exit mitosis as a 4N cell that enters another cell cycle; or v) abnormally segregate chromosomes into two or more aneuploid cells. There are many factors that determine which of these fates cells end up in, including the spindle poison and dosage used, the time spent in mitotic delay, and any genetic mutations the cell possesses, especially in the case of transformed or malignant cells. For example, whether or not cells have a functional p53 pathway can determine whether they will undergo senescence following mitotic delay or continue cycling despite aneuploidy (Andreassen et al. 2001). Some studies have found a correlation between time spent in mitosis and subsequent apoptosis (Masuda et al. 2003; Gajate et al. 2000), whereas others have found no correlation between these events (Gascoigne and Taylor 2008).

Cells exiting the cell cycle in a 4N state without satisfying the SAC or completing division is termed mitotic slippage. This can be mediated through gradual degradation of cyclin B1, where beyond a certain threshold cyclin B1 activity is not great enough to maintain the cell in a mitotic state (Brito and Rieder 2006). Normally degradation of Cyclin B via polyubiquitination by the anaphase-promoting complex (APC) occurs during anaphase and begins the process of mitotic exit, but low levels of polyubiquitination can occur even while the SAC is activated. In contrast, cells whose apoptotic signals reach the threshold before Cyclin B1 is sufficiently degraded will die during mitosis (Gascoigne and Taylor 2008). Intra- and inter-cell line variation in cell fate post-mitotic delay is hypothesized to occur due to cell to cell variation in network stability as well as differences in genetic background between cell-types (Gascoigne and Taylor 2008)

1.2.4 Resistance to MTAs

While MTAs are clearly very successful in the clinic, there remain several challenges that limit their use, namely resistance and off-target toxicity. One source of resistance stems from drug efflux. Both taxanes and vinca alkaloids are substrates of P-glycoprotein, a drug efflux pump often overexpressed in cancer cells that renders them multidrug-resistant (Cole et al. 1994; Lorico et al. 1996).

Another potential source of resistance is the mutations to the drug target, i.e. mutations arising in the genes encoding the β-tubulin isotypes. β-tubulin point mutations were identified in paclitaxel-resistant ovarian cancer cell lines (Giannakakou et al. 1997),

and similar mutations were linked to paclitaxel resistance in a genetic analysis of patients with non-small-cell lung cancer (Monzó et al. 1999). Similarly, a β-tubulin point mutation was identified in acute lymphoblastic leukemia cell lines resistant to either vincristine or vinblastine (Kavallaris et al. 2001). However, later studies have brought into question the presence of these mutations and the validity of their correlation with treatment response, and so it remains unclear whether β-tubulin mutations are clinically relevant for MTA resistance (Kelley, Li, and Harpole 2001; Berrieman, Lind, and Cawkwell 2004).

While β-tubulin mutations may have an ambiguous role in MTA resistance, changes in expression of certain tubulin isotypes have a more definitive role. Abnormal expression of βIII-tubulin, an isotype with expression typically limited to neurons and testicular Sertoli cells, is associated with resistance to several taxanes and vinca alkaloids in a range of cancers (Kavallaris et al. 1997; Sève and Dumontet 2005). Additionally, changes in expression or activity of several microtubule-associated proteins (MAPs), such as stathmin, MAP2c, and Tau, were also shown to be correlated with increased MTA resistance (Martello et al. 2003; Don et al. 2004; Neal and Yu 2006).

Epothilones are another natural product compound with a similar binding site and mechanism of action to taxanes (Nettles et al. 2004). Isolated from the myxobacterium *Sorangium cellulosum*, epothilones stabilize microtubules and induce mitotic arrest and subsequent apoptosis with higher levels of cytotoxicity that those of taxol. (Kowalski, Giannakakou, and Hamel 1997; Chou et al. 2001). Intriguingly, they have shown promising activity in drug-refractory cancers. Epothilones and their analogs are active against paclitaxel-resistant cancers, including those expressing high levels of βIII-tubulin, suggesting that epothilones and taxanes have non-overlapping mechanisms of resistance (Mozzetti et al. 2008; Dumontet, Jordan, and Lee 2009). Continued characterization of the sensitivity and resistance of various tumor types to epothilones is necessary, but this class of compound represents a promising alternative to classical taxane treatment and a potential way to side-step drug resistance.

In addition to resistance, these MTAs have been found to have severe side effects, including neutropenia and neurotoxicity. Neutropenia is a form of myelosuppression that occurs when a patient's neutrophil cell count is lowered, increasing their risk of infection, and stems from the drugs limiting cell division in neutrophils in addition to cancer cells.

While neutropenia is a serious condition that increases the patient's risk of infection, it is a common side effect of many chemotherapies and is reversible when treated (Pizzo 1993). Neurotoxicity, while less common, is irreversible and often more severe. Since MTAs do not target cancer cells specifically, but rather preferentially halt their proliferation, these drugs can have off-target effects on other cell types that depend on microtubules for functions other than proliferation such as neurons. Patients treated with paclitaxel can experience a dose-limiting sensory neuropathy, while treatment with vincristine can result in abdominal pain, jaw pain, and loss of reflexes (Lipton et al. 1989; Tuxen and Hansen 1994). Because of these undesirable side effects, it is imperative to develop inhibitors that disrupt mitosis in cancer cells without harming healthy cells.

1.3 Non-microtubule-targeting antimitotics

The high levels of neurotoxicity associated with classical MTAs necessitated the development of drugs that target proteins specific to mitosis. Promising mitosis-specific drug targets include kinases involved in mitotic progression as well as molecular motors essential for spindle assembly.

1.3.1 Cyclin-dependent kinase and checkpoint kinase inhibitors

Cyclin-dependent kinases (CDKs) and checkpoint kinases (CHKs) are two families of kinases involved in coordinating cell cycle progression. Various CDKs are responsible for regulating G1/S and G2/M transitions (Lim and Kaldis 2013). CHKs, on the other hand, arrest cell cycle progression in response to DNA damage, allowing the cell cycle to proceed once it has been repaired. Several CHK inhibitors have been developed and tested in clinical trials, but overall have shown poor selectivity and high toxicity. One CHK1 inhibitor, SRA737, has completed phase I clinical trials and is undergoing further testing (Banerji et al. 2019; Plummer et al. 2019).

The first CDK inhibitors developed were pan-CDK inhibitors (inhibitors that target multiple CDKs). While most of the first-generation pan-CDK inhibitors showed high toxicity, several second-generation inhibitors show better selectivity and efficacy with fewer side effects. For example, Dinaciclib has shown promising anti-tumor activity against breast and lung cancer as well as lymphocytic carcinoma in phase III clinical trials, and is even more powerful when combined with PD1 monocolonal antibody treatment

(Md Sakib Hossain et al. 2018). To improve specificity, inhibitors of specific CDKs are being developed that have fewer off-target effects than pan-CDK inhibitors. Palbociclib, Ribociclib, and Abemaciclib (produced by Pfizer, Novartis, and Eli Lilly, respectively) are three CDK4/6 inhibitors approved for use as first-line treatments for HR^+ breast cancer. Studies have shown that CDK4/6 inhibition arrests cells from G1 to S phase by reducing phosphorylation of the CDK4/6 target protein Rb, thus halting proliferation of Rb-positive cancer cells (Gelbert et al. 2014). However, recent research has shown that CDK inhibitors may exert anti-tumor activity through other non-cell-cycle related manners (Klein et al. 2018); thus, further understanding of the mechanisms by which these inhibitors cause cell death is necessary for improving their development and use.

1.3.2 Aurora A and B Kinase inhibitors

The Aurora family of kinases are Ser/Thr kinases involved in coordinating mitotic and meiotic progression. Aurora A localizes to the centrosomes in G2 phase and plays a central role in mitotic entry, and continues to regulate centrosomal proteins during mitosis (Sugimoto et al. 2002). Inhibition or depletion of Aurora A in cells inhibits centrosome maturation, delays mitotic entry, and induces monopolar spindle formation (Q. Liu and Ruderman 2006). Additionally, Aurora A is often overexpressed in tumor cells, and so inhibition inhibits proliferation of cancer cells both *in vitro* and *in vivo* (Sen, Zhou, and White 1997; Bischoff et al. 1998; Hata et al. 2005). Aurora B localizes to kinetochores early in mitosis, but then moves to the microtubules at the spindle equator at anaphase onset. It plays essential roles in regulating kinetochore function and chromosome attachment error correction, and is required for SAC function and cytokinesis. (Zeitlin, Shelby, and Sullivan 2001; Ditchfield et al. 2003). Inhibition of Aurora B causes defects in chromosome alignment and blocks cell division, causing aneuploidy (Ditchfield et al. 2003).

Numerous Aurora inhibitors are currently undergoing clinical trials. Due to high homology in the Aurora family, most inhibitors developed have overlapping activity; however inhibitors are now being developed to have higher specificity for one over the other. For instance, barasertib exhibits 1000-fold higher selectivity for Aurora B over A and has shown promise in a number of pre-clinical models of colon, lung, and

hematological cancers (Wilkinson et al. 2007). Several crystal structure of Aurora A and B have been reported recently which are likely to aid in the development of more potent and selective inhibitors (Nowakowski et al. 2002; Sessa et al. 2005; Bayliss et al. 2003). Additionally, it remains unclear exactly how Aurora inhibitors cause cell death; some studies have suggested cells without a functional p53 response are more sensitive to Aurora inhibition-induced polyploidy and are more likely to eventually undergo apoptosis, but a better understanding of these mechanisms is necessary for predicting response to Aurora inhibitors (Gizatullin et al. 2006).

1.3.3 Polo-like kinase inhibitors

The polo-like kinases (PLKs) are ser/thr kinases that play important roles in mitotic entry and exit as well as in events that occur during mitosis. PLK1 cooperates with many other cellular kinases and performs a variety of complex roles throughout the cell cycle and is necessary for process such as mitotic entry, spindle pole formation, chromosome separation, and mitotic exit. High expression of PLK1 can be found in several cancer types, including non-small-cell lung cancer, melanoma, and prostate cancer, and expression is typically correlated with worse prognosis (Cholewa, Liu, and Ahmad 2013). The roles of the other PLKs are less understood, and expression of PLK2-5 is often reduced in tumor cells (X. Liu 2015).

Preclinical studies have validated PLK1 as a promising drug target in both cancer cell lines and xenograft models (Spänkuch et al. 2004; Guan et al. 2005). Several PLK inhibitors have withgone or are currently going through clinical trials. The most successful so far is perhaps rigosertib, a compound that actually binds to Raf and inhibits its activation of PLK1, thus inhibiting downstream PLK1 activity (Fruman and Rommel 2014). Rigosertib is currently in Phase III trials in patients with myelodysplastic syndrome and metastatic pancreatic cancer. Clearly, PLKs are a promising antimitotic target, and an increased understanding of their complex functioning in cells will is needed to improve the development of PLK inhibitors.

1.3.4 CENP-E (Kinesin-7) inhibitors

CENP-E localizes to the kinetochores of chromosomes during mitosis and plays an essential role in mediating the proper congression and attachment of chromosomes

(Wood et al. 1997). Kinetochore-attached CENP-E transports laterally attached chromosomes to the plus-ends of kinetochore microtubules during prometaphase (Wood et al. 1997; Kapoor et al. 2006), and remains at the kinetochores of bioriented chromosomes throughout metaphase and into anaphase where it maintains stable attachments (Vitre et al. 2014). Two CENP-E inhibitors have shown promise in preclinical models: GSK923295, which allosterically inhibits the ATPase activity of CENP-E; and Cmpd-A, an ATP-competitive inhibitor. Both inhibitors are effective at blocking proliferation in tumor cells lines and xenograft models, and GSK923295 showed low levels of toxicity in a Phase I clinical trial (Wood et al. 2010; Ohashi et al. 2015; Chung et al. 2012). Further work is necessary to evaluate CENP-E as an effective drug target and the efficacy of CENP-E inhibitors in patient responses.

1.3.5 Eg5 (Kinesin-5) inhibitors

Eg5 is a plus end-directed motor essential for bipolar spindle assembly, although it is non-essential for bipolar spindle maintenance (Blangy et al. 1995; Kapoor et al. 2000). The current structural model of Eg5 suggests that it adopts a homotetrameric structure comprised of two antiparallel dimers; each dimer contains a long coiled-coil with two motor domains on the end, and coiled-coils of each dimer then assemble to form a central rod structure with the motor head pairs on each end of the molecule (Acar et al. 2013; Scholey et al. 2014). This conformation allows Eg5 to crosslink antiparallel microtubules and slide them apart via its plus-end directed motility on each microtubule (*Fig. 1.3*) (Kashina et al. 1996; Kapitein et al. 2005). Eg5 is activated by phosphorylation of Thr927 by cdc2 at the G2/M transition, enabling it to associate with spindle microtubules and drive centrosome separation in early prophase (Blangy et

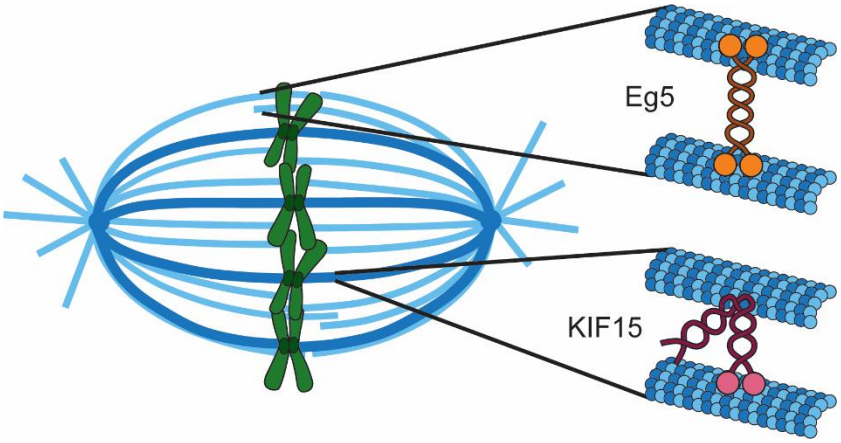

Fig. 1.3: Mitotic motors within the spindle. Eg5 (orange) localizes to the antiparallel overlap zone of interpolar microtubules. KIF15 (magenta) localizes to kinetochore microtubules. Both motors are capable of crosslinking and sliding apart antiparallel microtubules.

al. 1995). The plus-end directed force generated by Eg5 counteracts the minus-end directed action of the molecular motor protein dynein to assemble the bipolar spindle, and depletion of either Eg5 or dynein impairs proper spindle assembly (Gaglio et al. 1996).

The first Eg5 inhibitor, or K5I (**k**inesin-**5** **i**nhibitor) discovered was monastrol; treatment with monastrol causes cells to arrest in mitosis with a monopolar spindle structure, causing SAC activation and subsequent apoptosis (*Fig. 1.4*) (Mayer et al. 1999). Monastrol treatment is also reversible, and does not affect microtubule dynamics in interphase cells or cell cycle progression in G or S phase (Kapoor et al. 2000). These results highlighted Eg5 as a potential target for non-microtubule-targeting antimitotic compounds, as it is essential for cell division yet dispensable for non-proliferating cells. Furthermore, expression of Eg5 is typically elevated in tumor cells compared to normal human tissue, further widening the therapeutic window. Eg5 is overexpressed in several cancer types, including non-small-cell lung cancer, prostate cancer, and laryngeal squamous cell carcinoma (Saijo et al. 2006; Wissing et al. 2014; Lu et al. 2016). In patients, Eg5 overexpression and increased gene copy number is correlated with poor clinical outcome and increased tumorigenesis in pancreatic cancer and renal cell carcinoma (M. Liu et al. 2010; Sun et al. 2013). Transgenic mice that overexpress Eg5 displayed increased genomic instability stemming from chromosome mis-segregation and an increased number of tetraploid cells (Castillo et al. 2007). Additionally, tetraploid cells were significantly more sensitive to knockdown of Eg5 by siRNA than diploid cells, an important finding seeing as many cancer cells are tetraploid or aneuploid (Rello-Varona et al. 2009).

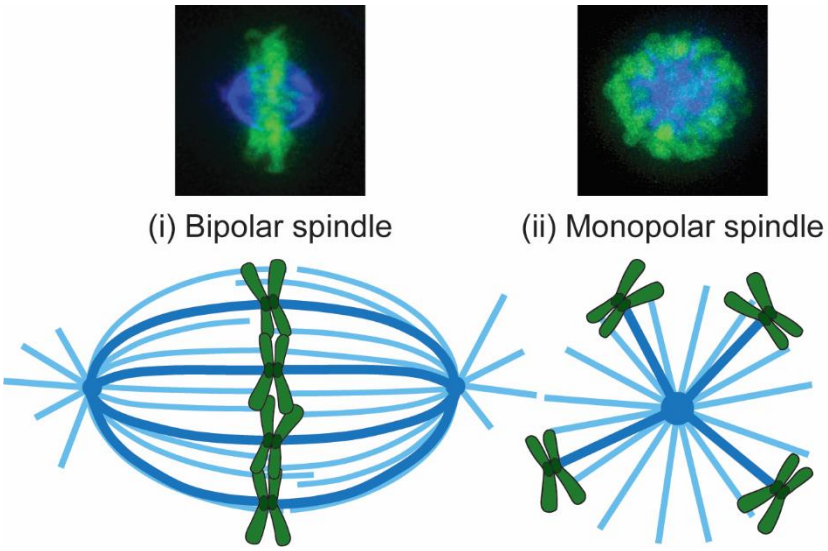

Fig. 1.4: Spindle morphology resulting from Eg5 inhibition. Representative images of RPE-1 cells and cartoons of (i) bipolar and (ii) monopolar spindle morphologies. Inhibition of Eg5 activity prevents centrosome separation and results in a monopolar array with microtubules emanating from one pole in the middle.

Over the last two decades, a multitude of K5Is

have been developed and tested in clinical trials. Most of these drugs target the Eg5 motor domain, either binding allosterically to Loop 5 of the motor head and trapping the motor in an ATP-bound state (Maliga et al. 2006; Talapatra, Schüttelkopf, and Kozielski 2012), or binding competitively near the ATP-binding pocket and interfering with nucleotide-binding (Luo et al. 2007; Peña et al. 2020). To this day, more than 40 clinical trials have been completed or are ongoing testing the safety and efficacy of K5Is in patients. Phase I trial results were encouraging as K5Is are well-tolerated and produce minimal toxicities; importantly, no neurotoxicity has been observed in patients, validating the search for non-microtubule-targeting antimitotic therapies.

However, Phase II studies have been largely disappointing, as little response to any K5Is tested has been reported. No complete or partial response was observed in Phase II trials tested in patients with squamous cell carcinoma (Tang et al. 2008), advanced renal cell cancer (Lee et al. 2008), prostate cancer (Beer et al. 2008), advanced urothelial cancer (Jones et al. 2013), or lymphoma (O'Connor et al. 2015), with the best result being several patients experiencing stable disease. Only one inhibitor, Arry-520 (filanesib), has shown any efficacy in producing partial responses in patients with multiple myeloma, either as a monotherapy or in combination with dexamethasone or a proteasome inhibitor (Owens 2013; Shah et al. 2017; Zonder et al. 2015). This large discrepancy between preclinical success and clinical failure of K5Is has prompted extensive research into potential mechanisms behind K5I resistance.

1.3.6 Mechanisms of K5I resistance

One reason for the low efficacy of most K5Is is likely due to the pharmacokinetics of the drugs with respect to their mechanism of action. Antimitotic inhibitors are only active against cells during mitosis, which comprises a relatively small portion of the cell cycle. The frequent dosing schedule of preclinical models compared to human patients, as well as the much longer half-life of Arry-520 relative to most other K5Is, is one potential explanation for the discrepancy between pre-clinical success and clinical failure and the unique response to Arry-520 (Komlodi-Pasztor et al. 2011; Rosenfeld 2015).

In addition to pharmacokinetic issues, several mechanisms of K5I resistance have been identified in cells that may be clinically relevant. Like MTAs, some K5Is are targets

of common drug efflux pumps that are often upregulated in cancer cells. One study found that ispinesib is a substrate for both the P-glycoprotein and breast cancer resistance protein (Brcp) drug efflux transporters; combination of ispinesib with elacridar, a potent inhibitor of both pumps, increased efficacy and drug permeation in an orthotopic glioblastoma model (Gampa et al. 2020).

Another potential mechanism of K5I resistance is the acquisition of mutations to Eg5 that reduce its sensitivity to K5Is. Mutations to the drug target itself that render drugs ineffective is a common theme in drug resistance (Wacker et al. 2012). Indeed, a study of acquired resistance to ispinesib, the most extensively tested clinical K5I, identified Eg5 mutations in all resistant clones that did not show resistance to other multidrug resistance substrates (Kasap, Elemento, and Kapoor 2014).

A third mechanism of K5I resistance centers on KIF15, another kinesin whose activity is partially redundant to Eg5. A member of the Kinesin-12 family, KIF15 is a plus-end directed kinesin whose normal functions include facilitating spindle elongation in prometaphase and maintaining spindle bipolarity (Tanenbaum et al. 2009). Unlike Eg5, KIF15 forms a homodimer in cells; however, it contains a second microtubule-binding site on its stalk that enable it to crosslink and slide apart antiparallel microtubules, much like Eg5 (Sturgill et al. 2014). KIF15 is dispensable for spindle assembly; as long as cells contain active Eg5, KIF15 depletion has little to no affect on the ability of cells to establish bipolar spindles (Tanenbaum et al. 2009).

Endogenous KIF15 is not capable of independently driving spindle assembly as it preferentially targets k-fibers rather than interpolar microtubules. Additionally, one of the main roles of Eg5 in mitotic progression is to separate the centrosomes before NEB, which KIF15 cannot fully compensate for since it does not become activated until NEB. Studies have shown, however, that under the selective pressure of Eg5 inhibition, some cells accumulate mutations that enable them to utilize KIF15 instead of Eg5 in spindle assembly. In some K5I-resistant cell (KIRC) lines, simple overexpression of KIF15 is sufficient to mislocalize KIF15 to non-kinetochore microtubules and drive bipolar spindle assembly in an Eg5-independent manner (Tanenbaum et al. 2009; Sturgill and Ohi 2013). In other KIRC lines, a mutation to Eg5 was identified that transforms it into an immotile crosslinker capable of bundling microtubules, thus creating a better substrate for KIF15

to bind to (Sturgill et al. 2016). In both of these cases, cells display an intermediate monopolar microtubule array before achieving bipolarity, indicative of a lack of pre-NEB centrosome separation. KIF15 activity on non-kinetochore microtubules during prometaphase is then capable of breaking the astral symmetry and establishing spindle bipolarity through a “reverse jackknifing” method (Sturgill and Ohi 2013). Similarly, studies have shown that hyperactivated nuclear envelope-associated dynein and elevated epidermal growth factor (EGF) levels are each capable of inducing centrosome separation in prophase independently of Eg5, which enables bipolar spindle establishment *via* endogenous levels of KIF15 (Raaijmakers et al. 2012; Mardin et al. 2013). EGF promotes weakening of centrosome cohesion via signaling events downstream of EGFR, facilitating KIF15-dependent spindle assembly (Mardin et al. 2013).

Importantly, KIF15 is central to all mechanisms that give rise to K5I resistance. Thus, removal of KIF15 *via* CRISPR-Cas9 technology would be predicted to eliminate the ability of HeLa cells to acquire resistance to K5Is; indeed this prediction was borne out experimentally (Sturgill et al. 2016). This reveals a fundamental requirement of KIF15 for K5I resistance, and suggests that the clinical efficacy of K5Is may be improved if paired with a KIF15 inhibitor.

1.4 Regulation of mitotic motors

Kinesins must be tightly regulated to control when and where in the cell they are exerting their various activities, and to prevent unnecessary energy loss in the absence of cargo-binding. The kinesin superfamily has evolved several mechanisms of regulation, and many motors are regulated by more than one mechanism. In this section, I will discuss several common mechanisms of regulation of mitotic kinesins and how they work together to coordinate cell division.

1.4.1 Autoinhibition

Kinsin-1 motors were discovered to adopt two different conformation: an extended, linear shape and a folded, more compact conformation (Hirokawa et al. 1989). Motors in the folded conformation were later found to be inactive and unable to bind microtubules (Verhey et al. 1998; Stock et al. 1999; Friedman and Vale 1999). This mechanism was

termed “autoinhibition”, characterizing a method of regulation in which the kinesin intrinsically inactivates itself. Autoinhibition via conformational folding has been proposed as a mechanism of regulation for members of the kinesin-2, -3, and -7 families in addition to Kinesin-1 (Imanishi et al. 2006; Hammond et al. 2009; Espeut et al. 2008). When kinesins are in an autoinhibited state, non-motor regions are able to contact the motor domain and disable microtubule-binding and ATPase activity. Studies of Kinesin-1 identified a hinge in its coiled-coil stalk, folding of which enables the tail to physically interact with the head and trap it in an ADP-bound state (Dietrich et al. 2008; Hackney and Stock 2000).

CENP-E is a member of the Kinesin-7 family and plays a vital role in chromosome congression during mitosis (Schaar et al. 1997; Wood et al. 1997). Similar to Kinesin-1, the C-terminal tail domain of CENP-E directly interacts with the motor domain. Unlike Kinesin-1, however, autoinhibited CENP-E can still bind microtubules; autoinhibition instead blocks processive motility along microtubules, thus disabling its activity (Espeut et al. 2008). KIF15 is another mitotic motor hypothesized to autoinhibit. Addition of the C-terminal coiled-coil in *trans* inhibits motility of KIF15 *in vitro*, and both size-exclusion chromatography and negative stain experiments suggest that KIF15 can adopt both open and compact conformations (Sturgill et al. 2014).

While autoinhibition partly answers the question of how some mitotic kinesins are regulated, it brings up the question of what governs the regulation of autoinhibition itself. Cargo-binding is one method of releasing autoinhibition; with Kinesin-1 or -2 motors, binding of kinesin-specific cargo to the tails releases the autoinhibited state and allows processive motility on microtubules to resume (Coy et al. 1999; Imanishi et al. 2006). Post-translational modifications may also play a role in autoinhibition release; phosphorylation of CENPE by either MPS1 or CDK1/Cyclin B stimulates unfolding of the molecule and enables microtubule motility (Espeut et al. 2008).

1.4.2 Cellular sequestration and Ran-GTP

Another method of regulation is to isolate motors from microtubules and/or cargo in a cell-cycle-dependent way. For mitotic motors, this typically involves sequestration in the nucleus. Members of the Kinesin-6, -8, -10, and -14 family contain nuclear localization

signals (NLSs) which mediate their localization to the nucleus during interphase; upon nuclear envelope breakdown at the beginning of mitosis, these motors are released to perform their mitotic duties (Trieselmann et al. 2003; Goshima and Vale 2005; X. Liu and Erikson 2007; Du, English, and Ohi 2010). As these motors act on microtubules either with either crosslinking activity or by affecting microtubule dynamics, sequestering them in the nucleus during interphase is critical to prevent aberrant microtubule organization in interphase cells. CENP-E, on the other hand, is excluded from the nucleus during interphase and is only able to bind its kinetochore targets on chromosomes after nuclear envelope breakdown (Brown, Wood, and Cleveland 1996).

Nuclear sequestration of these mitotic motors is typically mediated by the importin proteins (Ems-McClung, Zheng, and Walczak 2004; Tahara et al. 2008), which are in turn regulated by the small GTPase Ran. During interphase, importin-α/β bind their protein targets in the cytoplasm and transport them into the nucleus through the nuclear pores. In the nucleus, Ran-GTP binds importin-α/β, stimulating release of the cargos and facilitating movement of the importins back to the cytoplasm (Kutay et al. 1997). The presence of RanGAP (a GTPase-activating protein) in the cytoplasm and RCC1 (a guanine nucleotide exchange factor) in the nucleus maintain Ran-GTP levels high in the nucleus and low in the cytoplasm, which in turn regulates cargo-binding and release of the importin proteins spatiotemporally (Melchior 2001).

Ran-GTP also plays a role in kinesin localization and activation during mitosis. After nuclear envelope breakdown, importin-α/β are still able to bind their kinesin targets via their NLSs; while this clearly doesn't induce nuclear localization during mitosis, binding by importins holds the kinesins in an inactive state. However, during mitosis a gradient of RanGTP is generated with highest levels near the chromosomes; Ran-GTP-binding of importin-α/β at the chromosomes stimulates release and activation of their kinesin cargos (Trieselmann et al. 2003; Ems-McClung, Zheng, and Walczak 2004; Tahara et al. 2008). In this way, the activity of NLS-containing kinesins, among other spindle assembly factors, is restricted both spatially and temporally throughout the cell cycle.

1.4.3 Regulatory binding partners

Localization and activity of multiple mitotic kinesins is controlled *via* interactions with regulatory binding partners. For example, in yeast, the Kinesin-14 homolog Kar3 is targeted to the spindle poles by binding partner Vik1, and to overlapping microtubules in the central spindle by Cik1 (Allingham et al. 2007; Benanti et al. 2009). Similarly, studies have shown that localization of CENP-E to kinetochores requires direct interactions with several binding partners, including SEPT7, a member of the GTP-binding septin family of proteins, and NUF2, a component of the kinetochore-associated NDC80 complex (D. Liu et al. 2007; Zhu et al. 2008).

On the other hand, kinesin-binding protein (KIFBP) is a negative regulator of a subset of kinesins in cells. KIFBP binds members of the Kinesin-2, -3, -8, and -12 families, including the mitotic kinesins KIF15 and KIF18A, and prevents their interactions with microtubules (Kevenaar et al. 2016). Knockdown of KIFBP increases the occurrence of lagging chromosomes in mitotic cells, a phenotype that can be reproduced by overexpression of either KIF15 or KIF18A; thus it is concluded that negative regulation *via* KIFBP is necessary for preventing overactivity of mitotic kinesins (Malaby et al. 2019).

1.4.4 Post-translational modifications

Lastly, the localization and activity of many mitotic kinesins are regulated by various post-translational modifications (PTMs). Phosphorylation of Eg5 by Cdc2 is required for robust microtubule-binding in mammalian cells (Blangy et al. 1995; Sawin and Mitchison 1995). CENP-E is also regulated by a different type of PTM, sumoylation, in which a SUMO (small ubiquitin-related modifier) is covalently conjugated to it. Unlike ubiquitination, which typically targets proteins for proteasomal degradation, sumoylation often enhances protein-protein interactions of its substrates with other macromolecules (Johnson 2004). Sumoylation by SUMO2/3 is required for proper localization of CENP-E to kinetochores (Zhang et al. 2008).

Some kinesins are regulated by a combination of several PTMs. The Kinesin-13 KIF2A, whose microtubule-depolymerase activity is essential for regulating spindle microtubule dynamics, is phosphorylated by both PLK1 and Aurora A. PLK1 targets KIF2a to spindle microtubules and poles, and increases its depolymerase activity, whereas phosphorylation by Aurora A disrupts its decreases its depolymerase activity (Jang et al.

2009). This antagonistic regulation of KIF2A spatially controls its activity on the spindle; Aurora A prevents KIF2A-mediated microtubule depolymerization on spindle microtubules, while centrosomal PLK1 activates KIF2A depolymerization at the spindle poles, which is required for establishing tension between sister kinetochores (Sumara et al. 2004; Jang et al. 2009).

It is clear that regulation of mitotic kinesins is complex, and motor activity is often orchestrated by a variety of regulatory mechanisms. Consider, for instance, CENP-E, whose location and activity throughout the cell cycle is controlled by a combination of PTMs, binding partners, and autoinhibition. Another interesting example is KIFBP; many of its substrates are regulated by one or more additional mechanisms, and so the evolutionary purpose of regulation by KIFBP in addition to these other mechanisms remains uncertain. Furthermore, it is not always clear whether localization completely corresponds to activity, and additional work is necessary to elucidate the relationships between location and activity of the mitotic motors.

1.5 KIFBP: a regulatory kinesin binding partner

As briefly discussed, KIFBP binds to a subset of kinesins in cells and inhibits their interactions with microtubules. KIFBP was originally discovered as a binding partner of the Kinesin-3 KIF1Bα (Wozniak et al. 2005), and was later shown to bind to eight kinesins in cells, including members of the Kinesin-2, -3, -8, and -12 families (Kevenaar et al. 2016). KIFBP interacts directly with the motor domains of these kinesins and decreases their landing rate on microtubules *in vitro*.

KIFBP is especially critical for mitotic cells. Overexpression of KIFBP induces defects in metaphase spindle length and chromosome alignment, whereas KIFBP depletion increases the occurrence of lagging chromosomes during anaphase, an issue that can lead to genomic instability in cells. Immunofluorescence experiments revealed that excess KIFBP in cells disrupts normal spindle localization of the two mitotic motors KIF15 and KIF18A, and overexpression of either motor can reproduce the phenotypes seen in KIFBP-depleted cells (Malaby et al. 2019). This supports a model in which KIFBP is necessary to “buffer”, or prevent overactivity, of mitotic kinesins in dividing cells. As noted above, KIFBP-binding kinesins are regulated through a variety of other mechanisms in cells, and so an interesting question remains as to the purpose of KIFBP

as an additional form of regulation. Additionally, it is not yet known why or how KIFBP specifically binds only a subset of eight kinesins, as there is no obvious structural or sequence similarity that set those eight apart from other kinesins in cells.

1.5.1 KIFBP in disease

KIFBP is also pathologically relevant. Around the same time it was identified as a kinesin binding partner, the gene that encodes KIFBP was identified as a disease-causing gene for Goldberg-Shprintzen syndrome, an autosomal recessive neurological disorder characterized by defects in neuronal development, mental retardation, facial dysmorphism, heart defects, and often Hirschsprung disease (H. Tanaka et al. 1993; Valence et al. 2013; Dafsari et al. 2015). 16 KIFBP mutations that cause GOSHS have been identified to date; most mutations results in either a reduction or complete loss of protein expression (MacKenzie et al. 2020; Cubuk 2021).

While the exact causes of GOSHS are poorly understood, KIFBP activity is indeed important for neuronal development. Studies in zebrafish showed that *KIFbp* expression increases during neuronal differentiation and that *KIFbp* is expressed in both the central and enteric nervous systems, confirming a role in the development of both (Alves et al. 2010). Zebrafish harboring a truncation mutation in *KIFbp* exhibit delayed axonal outgrowth and less organized axonal MTs (Lyons et al. 2008). Similarly, when KIFBP was knocked down in embryonic mouse cortices, mice displayed defects in migration of neural progenitor cells, simplified dendritic structures with fewer branches, defects in axonal extension, and an increase in neuronal apoptosis (Chang et al. 2019).

Several KIFBP functions in neurons are directly linked to GOSHS symptoms. For example, reduction in neuronal migration has been previously linked to polymicrogyria (Chang et al. 2019). *KIFbp*$^{-/-}$ mice also exhibit reduced size of the brain and olfactory bulbs, which may reflect the microcephaly commonly observed in GOSHS patients (Faheem et al. 2015; Hirst et al. 2017). Lastly, dendritic abnormalities are implicated in multiple neurological disorders characterized by mental retardation similar to GOSHS, including Autism spectrum disorders, Fragile X syndrome, and Down syndrome (Hutsler and Zhang 2010; Rudelli et al. 1985; Takashima et al. 1989).

As KIFBP regulates a subset of kinesin motors, we hypothesize that GOSHS phenotypes arise due to dysregulation of KIFBP-binding kinesins in the absence of KIFBP activity. Supporting this hypothesis, several KIFBP-binding kinesins have roles in neuronal development and regulating MT dynamics. For example, KIF18A regulates MT dynamics, which is necessary for effective axonal elongation; inhibition of MT dynamics by MT stabilizing or destabilizing drugs disrupts axonal outgrowth (Letourneau and Ressler 1984; E. Tanaka, Ho, and Kirschner 1995). Depleting KIF18A in post-mitotic neurons increases the growth rate and catastrophe frequency of axonal MTs, while reducing the overall axon length, phenotypes that can be reproduced by KIFBP overexpression (Kevenaar et al. 2016). KIF1A and KIF3A are involved in regulating neuronal migration; thus, dysregulation of these motors in the absence of KIFBP activity may cause the neuronal migration defects observed in mice (Tsai et al. 2010; Chen, Chang, and Tsai 2019). Lastly, KIF13B transports PIP3 to neurite tips to mediate axonal differentiation and extension (Horiguchi et al. 2006). Overactivity of KIF13B leads to accumulation of PIP3 at multiple neurite tips and impairs axonal differentiation, another potential result of loss of KIFBP function.

1.6 Overview of dissertation

In this dissertation, I present the development of a new resources with which to assay KIF15's role in cellular organization, and describe the characterization of a novel method of kinesin regulation. In Chapter II, I describe the pipeline our lab has established to screen for and evaluate small molecule inhibitors of kinesin inhibitors. In Chapter III, I describe the identification of two KIF15 inhibitors, and show that KIF15 inhibitors can synergize with K5Is to prevent resistance. In Chapter IV, I describe the mechanism by which KIFBP prevents KIF15, among a subset of other kinesins, from binding to microtubules in cells.

1.7 References

Acar, S., Carlson, D. B., Budamagunta, M. S., Yarov-Yarovoy, V., Correia, J. J., Niñonuevo, M. R., … Scholey, J. M. (2013). The bipolar assembly domain of the mitotic motor kinesin-5. Nature Communications, 4. https://doi.org/10.1038/ncomms2348

Allen, C., & Borisy, G. G. (1974). Structural polarity and directional growth of microtubules of Chlamydomonas flagella. Journal of Molecular Biology, 90(2), 381–402. https://doi.org/10.1016/0022-2836(74)90381-7

Allingham, J. S., Sproul, L. R., Rayment, I., & Gilbert, S. P. (2007). Vik1 Modulates Microtubule-Kar3 Interactions through a Motor Domain that Lacks an Active Site. Cell, 128(6), 1161–1172. https://doi.org/10.1016/j.cell.2006.12.046

Alves, M. M., Burzynski, G., Delalande, J. M., Osinga, J., van der Goot, A., Dolga, A. M., … Hofstra, R. M. W. (2010). KBP interacts with SCG10, linking Goldberg-Shprintzen syndrome to microtubule dynamics and neuronal differentiation. Human Molecular Genetics, 19(18), 3642–3651. https://doi.org/10.1093/hmg/ddq280

Andreassen, P. R., Lohez, O. D., Lacroix, F. B., & Margolis, R. L. (2001). Tetraploid state induces p53-dependent arrest of nontransformed mammalian cells in G1. Molecular Biology of the Cell, 12(5), 1315–1328. https://doi.org/10.1091/mbc.12.5.1315

Bai, R., Pettit, G. R., & Hamel, E. (1990). Binding of dolastatin 10 to tubulin at a distinct site for peptide antimitotic agents near the exchangeable nucleotide and vinca alkaloid sites. Journal of Biological Chemistry, 265(28), 17141–17149. https://doi.org/10.1016/s0021-9258(17)44880-0

Banerji, U., Plummer, E. R., Moreno, V., Ang, J. E., Quinton, A., Drew, Y., & Hernandez, T. (2019). A phase I/II first-in-human trial of oral SRA737 (a Chk1 inhibitor) given in combination with low-dose gemcitabine in subjects with advanced cancer. Journal of Clinical Oncology, 37, 3095–3095.

Bayliss, R., Sardon, T., Vernos, I., & Conti, E. (2003). Structural basis of Aurora-A activation by TPX2 at the mitotic spindle. Molecular Cell, 12(4), 851–862. https://doi.org/10.1016/S1097-2765(03)00392-7

Beer, T. M., Goldman, B., Synold, T. W., Ryan, C. W., Vasist, L. S., Van Veldhuizen, P. J., … Crawford, E. D. (2008). Southwest oncology group phase II study of ispinesib in androgen-independent prostate cancer previously treated with taxanes. Clinical Genitourinary Cancer, 6(2), 103–109. https://doi.org/10.3816/CGC.2008.n.016

Bellmunt, J., Théodore, C., Demkov, T., Komyakov, B., Sengelov, L., Daugaard, G., … Von Der Maase, H. (2009). Phase III trial of vinflunine plus best supportive care compared with best supportive care alone after a platinum-containing regimen in patients with advanced transitional cell carcinoma of the urothelial tract. Journal of Clinical Oncology, 27(27), 4454–4461. https://doi.org/10.1200/JCO.2008.20.5534

Benanti, J. A., Matyskiela, M. E., Morgan, D. O., & Toczyski, D. P. (2009). Functionally Distinct Isoforms of Cik1 Are Differentially Regulated by APC/C-Mediated Proteolysis. Molecular Cell, 33(5), 581–590. https://doi.org/10.1016/j.molcel.2009.01.032

Berrieman, H. K., Lind, M. J., & Cawkwell, L. (2004). Do β-tubulin mutations have a role in resistance to chemotherapy? Lancet Oncology, 5(3), 158–164. https://doi.org/10.1016/S1470-2045(04)01411-1

Bischoff, J. R., Anderson, L., Zhu, Y., Mossie, K., Ng, L., Souza, B., … Plowman, G. D. (1998). A homologue of Drosophila aurora kinase is oncogenic and amplified in human

colorectal cancers. EMBO Journal, 17(11), 3052–3065. https://doi.org/10.1093/emboj/17.11.3052

Blangy, A., Lane, H. A., D'Hérin, P., Harper, M., Kress, M., & Nigg, E. A. (1995). Phosphorylation by p34cdc2 regulates spindle association of human Eg5, a kinesin-related motor essential for bipolar spindle formation in vivo. Cell, 83(7), 1159–1169. https://doi.org/10.1016/0092-8674(95)90142-6

Brito, D. A., & Rieder, C. L. (2006). Mitotic Checkpoint Slippage in Humans Occurs via Cyclin B Destruction in the Presence of an Active Checkpoint. Current Biology, 16(12), 1194–1200. https://doi.org/10.1016/j.cub.2006.04.043

Brito, D. A., & Rieder, C. L. (2009). The ability to survive mitosis in the presence of microtubule poisons differs significantly between human nontransformed (RPE-1) and cancer (U2OS, HeLa) cells. Cell Motility and the Cytoskeleton, 66(8), 437–447. https://doi.org/10.1002/cm.20316

Brown, K. D., Wood, K. W., & Cleveland, D. W. (1996). The kinesin-like protein CENP-E is kinetochore-associated throughout poleward chromosome segregation during anaphase-A. Journal of Cell Science, 109(5), 961–969. https://doi.org/10.1242/jcs.109.5.961

Budman, D. R. (1997). Vinorelbine (Navelbine®): A third-generation vinca alkaloid. Cancer Investigation, 15(5), 475–490. https://doi.org/10.3109/07357909709047587

Caplow, M., & Zeeberg, B. (1982). Dynamic Properties of Microtubules at Steady State in the Presence of Taxol. European Journal of Biochemistry, 127(2), 319–324. https://doi.org/10.1111/j.1432-1033.1982.tb06873.x

Castillo, A., Iii, H. C. M., Godfrey, V. L., Naeem, R., & Justice, M. J. (2007). Overexpression of Eg5 Causes Genomic Instability and Tumor Formation in Mice. Cancer Res, 67(21), 10138–10185. https://doi.org/10.1158/0008-5472.CAN-07-0326

Chang, H., Cheng, H., Tsao, A., Liu, C., & Tsai, J. (2019). Multiple Functions of KBP in Neural Development Underlie Brain Anomalies in Goldberg-Shprintzen Syndrome. Frontiers in Molecular Neuroscience, 12(November), 1–12. https://doi.org/10.3389/fnmol.2019.00265

Chen, J. L., Chang, C. H., & Tsai, J. W. (2019). Gli2 Rescues Delays in Brain Development Induced by Kif3a Dysfunction. Cerebral Cortex, 29(2), 751–764. https://doi.org/10.1093/cercor/bhx356

Cholewa, B. D., Liu, X., & Ahmad, N. (2013). The role of polo-like kinase 1 in carcinogenesis: Cause or consequence? Cancer Research, 73(23), 6848–6855. https://doi.org/10.1158/0008-5472.CAN-13-2197

Chou, T. C., O'Connor, O. A., Tong, W. P., Guan, Y., Zhang, Z. G., Stachel, S. J., … Danishefsky, S. J. (2001). The synthesis, discovery, and development of a highly promising class of microtubule stabilization agents: Curative effects of desoxyepothilones B and F against human tumor xenografts in nude mice. Proceedings of the National Academy of Sciences of the United States of America, 98(14), 8113–8118. https://doi.org/10.1073/pnas.131153098

Chung, V., Heath, E. I., Schelman, W. R., Johnson, B. M., Kirby, L. C., Lynch, K. M., … Holen, K. D. (2012). First-time-in-human study of GSK923295, a novel antimitotic inhibitor of centromere-associated protein e (CENP-E), in patients with refractory cancer. Cancer Chemotherapy and Pharmacology, 69(3), 733–741. https://doi.org/10.1007/s00280-011-1756-z

Cimini, D., Howell, B., Maddox, P., Khodjakov, A., Degrassi, F., & Salmon, E. D. (2001). Merotelic kinetochore orientation is a major mechanism of aneuploidy in mitotic mammalian tissue cells. Journal of Cell Biology, 152(3), 517–527. https://doi.org/10.1083/jcb.153.3.517

Cole, S. P. C., Sparks, K. E., Fraser, K., Loe, D. W., Grant, C. E., Wilson, G. M., & Deeley, R. G. (1994). Pharmacological Characterization of Multidrug Resistant MRP-transfected Human Tumor Cells. Cancer Research, 54, 5902–5910.

Coy, D. L., Hancock, W. O., Wagenbach, M., & Howard, J. (1999). Kinesins Tail Domain Is an Inhibitors Regulator of the Otor Region. Nature Cell Biology, 1(September), 288–292.

Cubuk, P. O. (2021). Goldberg-Shprintzen Syndrome Associated with a Novel Variant in the KIFBP Gene. Molecular Syndromology. https://doi.org/10.1159/000514531

Dafsari, H. S., Byrne, S., Lin, J. P., Pitt, M., Jongbloed, J. D., Flinter, F., & Jungbluth, H. (2015). Goldberg-Shprintzen megacolon syndrome with associated sensory motor axonal neuropathy. American Journal of Medical Genetics, Part A, 167(6), 1300–1304. https://doi.org/10.1002/ajmg.a.36873

De Brabander, M., Geuens, G., Nuydens, R., Willebrords, R., & De Mey, J. (1981). Taxol induces the assembly of free microtubules in living cells and blocks the organizing capcity of the centrosomes and kinetochores. Proceedings of the National Academy of Sciences, 78(9), 5608–5612. https://doi.org/10.1073/pnas.78.9.5608

Derry, W. B., Wilson, L., & Jordan, M. A. (1998). Low potency of Taxol at microtubule minus ends: Implications for its antimitotic and therapeutic mechanism. Cancer Research, 58, 1177–1184.

Díaz, J. F., & Andreu, J. M. (1993). Assembly of Purified GDP-Tubulin into Microtubules Induced by Taxol and Taxotere: Reversibility, Ligand Stoichiometry, and Competition. Biochemistry, 32(11), 2747–2755. https://doi.org/10.1021/bi00062a003

Dietrich, K. A., Sindelar, C. V, Brewer, P. D., Downing, K. H., Cremo, C. R., & Rice, S. E. (2008). The kinesin-1 motor protein is regulated by a direct interaction of its head and tail. Retrieved from www.pnas.org/cgi/content/full/

Ditchfield, C., Johnson, V. L., Tighe, A., Ellston, R., Haworth, C., Johnson, T., … Taylor, S. S. (2003). Aurora B couples chromosome alignment with anaphase by targeting BubR1, Mad2, and Cenp-E to kinetochores. Journal of Cell Biology, 161(2), 267–280. https://doi.org/10.1083/jcb.200208091

Don, S., Verrills, N. M., Liaw, T. Y. E., Liu, M. L. M., Norris, M. D., Haber, M., & Kavallaris, M. (2004). Neuronal-associated microtubule proteins class III β-tubulin ad MAP2c in

neuroblastoma: Role in resistance to microtubule-targeted drugs. Molecular Cancer Therapeutics, 3(9), 1137–1146.

Du, Y., English, C. A., & Ohi, R. (2010). The Kinesin-8 Kif18A Dampens Microtubule Plus-End Dynamics. Current Biology, 20(4), 374–380. https://doi.org/10.1016/j.cub.2009.12.049

Dumontet, C., Jordan, M. A., & Lee, F. F. Y. (2009). Ixabepilone: Targeting βIII-tubulin expression in taxane-resistant malignancies. Molecular Cancer Therapeutics, 8(1), 17–25. https://doi.org/10.1158/1535-7163.MCT-08-0986

Dyke, R. W., Nelson, R. L., & Brade, W. P. (1979). Vindesine a short review of preclinical and first clinical data. Cancer Chemotherapy and Pharmacology, 2, 229–232. https://doi.org/10.1007/BF00257185

Ems-McClung, S. C., Zheng, Y., & Walczak, C. E. (2004). Importin α/β and Ran-GTP Regulate XCTK2 Microtubule Binding through a Bipartite Nuclear Localization Signal. Molecular Biology of the Cell, 15, 46–57. https://doi.org/10.1091/mbc.E03

Espeut, J., Gaussen, A., Bieling, P., Morin, V., Prieto, S., Fesquet, D., … Abrieu, A. (2008). Phosphorylation Relieves Autoinhibition of the Kinetochore Motor Cenp-E. Molecular Cell, 29(5), 637–643. https://doi.org/10.1016/j.molcel.2008.01.004

Faheem, M., Naseer, M. I., Rasool, M., Chaudhary, A. G., Kumosani, T. A., Ilyas, A. M., … Jamal, H. S. (2015). Molecular genetics of human primary microcephaly: An overview. BMC Medical Genomics, 8(Suppl 1), S4. https://doi.org/10.1186/1755-8794-8-S1-S4

Ferlay, J., Colombet, M., Soerjomataram, I., Parkin, D. M., Piñeros, M., Znaor, A., & Bray, F. (2021). Cancer statistics for the year 2020: An overview. International Journal of Cancer, 149(4), 778–789. https://doi.org/10.1002/ijc.33588

Forer, A. (1965). Local reduction of spindle fiber birefringence in living Nephrotoma suturalis (Loew) spermatocytes induced by ultraviolet microbeam irradiation. J Cell Biol, 25, 95–117.

Friedman, D. S., & Vale, R. D. (1999). Single-molecule analysis of kinesin motility reveals regulation by the cargo-binding tail domain. NATURE CELL BIOLOGY | (Vol. 1).

Fruman, D. A., & Rommel, C. (2014). PI3K and cancer: Lessons, challenges and opportunities. Nature Reviews Drug Discovery, 13(2), 140–156. https://doi.org/10.1038/nrd4204

Fygenson, D. K., Flyvbjerg, H., Sneppen, K., Libchaber, A., & Liebler, S. (1995). Spontaneous nucleation of microtubules. Physical Review, 51(5), 5058–5063.

Gaglio, T., Saredi, A., Bingham, J. B., Hasbani, M. J., Gill, S. R., Schroer, T. A., & Compton, D. A. (1996). Opposing Motor Activities Are Required for the Organization of the Mammalian Mitotic Spindle Pole. Retrieved from https://www.ncbi.nlm.nih.gov/pmc/articles/PMC2121053/pdf/jc1352399.pdf

Gajate, C., Barasoain, I., Andreu, J. M., & Mollinedo, F. (2000). Induction of Apoptosis in Leukemic Cells by the Reversible Microtubule-disrupting Agent 2-Methoxy-5-(2′,3′,4′-

trimethoxyphenyl)-2,4,6-cycloheptatrien-1-one: Protection by Bcl-2 and Bcl-XL and Cell Cycle Arrest. Experimental Therapeutics, 60(10), 2651–2659.

Gampa, G., Kenchappa, R. S., Mohammad, A. S., Parrish, K. E., Kim, M., Crish, J. F., … Elmquist, W. F. (2020). Enhancing Brain Retention of a KIF11 Inhibitor Significantly Improves its Efficacy in a Mouse Model of Glioblastoma. Scientific Reports, 10(1), 1–13. https://doi.org/10.1038/s41598-020-63494-7

Gascoigne, K. E., & Taylor, S. S. (2008). Cancer Cells Display Profound Intra- and Interline Variation following Prolonged Exposure to Antimitotic Drugs. Cancer Cell, 14(2), 111–122. https://doi.org/10.1016/j.ccr.2008.07.002

Gelbert, L. M., Cai, S., Lin, X., Sanchez-Martinez, C., Prado, M. Del, Lallena, M. J., … De Dios, A. (2014). Preclinical characterization of the CDK4/6 inhibitor LY2835219: In-vivo cell cycle-dependent/independent anti-tumor activities alone/in combination with gemcitabine. Investigational New Drugs, 32(5), 825–837. https://doi.org/10.1007/s10637-014-0120-7

Giannakakou, P., Sackett, D. L., Kang, Y. K., Zhan, Z., Buters, J. T. M., Fojo, T., & Poruchynsky, M. S. (1997). Paclitaxel-resistant human ovarian cancer cells have mutant β-tubulins that exhibit impaired paclitaxel-driven polymerization. Journal of Biological Chemistry, 272(27), 17118–17125. https://doi.org/10.1074/jbc.272.27.17118

Gizatullin, F., Yao, Y., Kung, V., Harding, M. W., Loda, M., & Shapiro, G. I. (2006). The Aurora kinase inhibitor VX-680 induces endoreduplication and apoptosis preferentially in cells with compromised p53-dependent postmitotic checkpoint function. Cancer Research, 66(15), 7668–7677. https://doi.org/10.1158/0008-5472.CAN-05-3353

Goshima, G., & Vale, R. D. (2005). Cell Cycle-dependent Dynamics and Regulation of Mitotic Kinesins in Drosophila S2 Cells. Molecular Biology of the Cell, 16, 3896–3907. https://doi.org/10.1091/mbc.E05

Grill, S. W., Howard, J., Schäffer, E., Stelzer, E. H. K., & Hyman, A. A. (2003). The distribution of active force generators controls mitotic spindle position. Science, 301(5632), 518–521. https://doi.org/10.1126/science.1086560

Guan, R., Tapang, P., Leverson, J. D., Albert, D., Giranda, V. L., & Luo, Y. (2005). Small interfering RNA-mediated polo-like kinase 1 depletion preferentially reduces the survival of p53-defective, oncogenic transformed cells and inhibits tumor growth in animals. Cancer Research, 65(7), 2698–2704. https://doi.org/10.1158/0008-5472.CAN-04-2131

Hackney, D. D., & Stock, M. F. (2000). Kinesin's IAK tail domain inhibits initial microtubule-stimulated ADP release. NATURE CELL BIOLOGY (Vol. 2). Retrieved from www.nature.com/ncb

Hammond, J. W., Cai, D., Blasius, T. L., Li, Z., Jiang, Y., Jih, G. T., … Verhey, K. J. (2009). Mammalian Kinesin-3 motors are dimeric in vivo and move by processive motility upon release of autoinhibition. PLoS Biology, 7(3), 0650–0663. https://doi.org/10.1371/journal.pbio.1000072

Hata, T., Furukawa, T., Sunamura, M., Egawa, S., Motoi, F., Ohmura, N., … Horii, A. (2005). RNA interference targeting aurora kinase A suppresses tumor growth and enhances the taxane chemosensitivity in human pancreatic cancer cells. Cancer Research, 65(7), 2899–2905. https://doi.org/10.1158/0008-5472.CAN-04-3981

Hirokawa, N., Pfister, K. K., Yorifuji, H., Wagner, M. C., Brady, S. T., & Bloom, G. S. (1989). Submolecular domains of bovine brain kinesin identified by electron microscopy and monoclonal antibody decoration. Cell, 56(5), 867–878. https://doi.org/10.1016/0092-8674(89)90691-0

Hirst, C. S., Stamp, L. A., Bergner, A. J., Hao, M. M., Tran, M. X., Morgan, J. M., … Young, H. M. (2017). Kif1bp loss in mice leads to defects in the peripheral and central nervous system and perinatal death. Scientific Reports, 7(1), 1–14. https://doi.org/10.1038/s41598-017-16965-3

Horiguchi, K., Hanada, T., Fukui, Y., & Chishti, A. H. (2006). Transport of PIP3 by GAKIN, a kinesin-3 family protein, regulates neuronal cell polarity. Journal of Cell Biology, 174(3), 425–436. https://doi.org/10.1083/jcb.200604031

Howard, W. D., & Timasheff, S. N. (1988). Linkages between the effects of taxol, colchicine, and GTP on tubulin polymerization. Journal of Biological Chemistry, 263(3), 1342–1346. https://doi.org/10.1016/s0021-9258(19)57307-0

Hutsler, J. J., & Zhang, H. (2010). Increased dendritic spine densities on cortical projection neurons in autism spectrum disorders. Brain Research, 1309, 83–94. https://doi.org/10.1016/j.brainres.2009.09.120

Imanishi, M., Endres, N. F., Gennerich, A., & Vale, R. D. (2006). Autoinhibition regulates the motility of the C. elegans intraflagellar transport motor OSM-3. Journal of Cell Biology, 174(7), 931–937. https://doi.org/10.1083/jcb.200605179

Jang, C. Y., Coppinger, J. A., Seki, A., Yates, J. R., & Fang, G. (2009). Plk1 and aurora A regulate the depolymerase activity and the cellular localization of Kif2a. Journal of Cell Science, 122(9), 1334–1341. https://doi.org/10.1242/jcs.044321

Johnson, E. S. (2004). Protein modification by SUMO. Annual Review of Biochemistry, 73, 355–382. https://doi.org/10.1146/annurev.biochem.73.011303.074118

Jones, R., Vuky, J., Elliott, T., Mead, G., Arranz, J. A., Chester, J., … Hudes, G. (2013). Phase II study to assess the efficacy, safety and tolerability of the mitotic spindle kinesin inhibitor AZD4877 in patients with recurrent advanced urothelial cancer. Investigational New Drugs, 31(4), 1001–1007. https://doi.org/10.1007/s10637-013-9926-y

Jordan, M. A., Margolis, R. L., Himes, R. H., & Wilson, L. (1986). Identification of a distinct class of vinblastine binding sites on microtubules. Journal of Molecular Biology, 187(1), 61–73. https://doi.org/10.1016/0022-2836(86)90406-7

Jordan, M. A., Thrower, D., & Wilson, L. (1991). Mechanism of Inhibition of Cell Proliferation by Vinca Alkaloids. Cancer Research, 51(8), 2212–2222.

Jordan, M. A., Toso, R. J., Thrower, D., & Wilson, L. (1993). Mechanism of mitotic block and inhibition of cell proliferation by taxol at low concentrations. Proceedings of the

National Academy of Sciences, 90, 9552–9556. https://doi.org/10.1073/pnas.90.20.9552

Jordan, M. A., Wendell, K., Gardiner, S., Derry, W. B., Copp, H., & Wilson, L. (1996). Mitotic block induced in HeLa cells by low concentrations of paclitaxel (taxol) results in abnormal mitotic exit and apoptotic cell death. Cancer Research, 56, 816–825.

Jordan, M. A., & Wilson, L. (2004). Microtubules as a target for anticancer drugs. Nat. Rev. Cancer, 4(4), 253–265. https://doi.org/10.1038/nr1317

Kajtez, J., Solomatina, A., Novak, M., Polak, B., Vukušić, K., Rüdiger, J., … Tolić, I. M. (2016). Overlap microtubules link sister k-fibres and balance the forces on bi-oriented kinetochores. Nature Communications, 7. https://doi.org/10.1038/ncomms10298

Kapitein, L. C., Peterman, E. J. G., Kwok, B. H., Kim, J. H., Kapoor, T. M., & Schmidt, C. F. (2005). The bipolar mitotic kinesin Eg5 moves on both microtubules that it crosslinks. Nature, 435(7038), 114–118. https://doi.org/10.1038/nature03503

Kapoor, T. M., Lampson, M. A., Hergert, P., Cameron, L., Cimini, D., Salmon, E. D., … Khodjakov, A. (2006). Chromosomes Can Congress to the Metaphase Plate Before Biorientation. Science, 311, 388–391.

Kapoor, T. M., Mayer, T. U., Coughlin, M. L., & Mitchison, T. J. (2000). Probing Spindle Assembly Mechanisms with Monastrol, a Small Molecule Inhibitor of the Mitotic Kinesin, Eg5 7. The Journal of Cell Biology (Vol. 150). Retrieved from http://www.jcb.org

Kasap, C., Elemento, O., & Kapoor, T. M. (2014). DrugTargetSeqR: A genomics- and CRISPR-Cas9-based method to analyze drug targets. Nature Chemical Biology, 10(8), 626–628. https://doi.org/10.1038/nchembio.1551

Kashina, A. S., Baskin, R. J., Cole, D. G., Wedaman, K. P., Saxton, W. M., & Scholey, J. M. (1996). A bipolar kinesin. Nature, 379(6562), 270–272. https://doi.org/10.1038/379270a0

Kavallaris, M., Kuo, D. Y. S., Burkhart, C. A., Regl, D. L., Norris, M. D., Haber, M., & Horwitz, S. B. (1997). Taxol-resistant epithelial ovarian tumors are associated with altered expression of specific β-tubulin isotypes. Journal of Clinical Investigation, 100(5), 1282–1293. https://doi.org/10.1172/JCI119642

Kavallaris, M., Tait, A. S., Norris, M. D., Haber, M., Walsh, B. J., He, L., & Horwitz, S. B. (2001). Multiple microtubule alterations are associated with Vinca alkaloid resistance in human leukemia cells. Cancer Research, 61(15), 5803–5809.

Kelley, M. J., Li, S., & Harpole, D. H. (2001). Genetic Analysis of the β-Tubulin Gene, TUBB, in Non-Small-Cell Lung Cancer. Journal of the National Cancer Institute, 93(24), 1886–1888.

Kevenaar, J. T., Bianchi, S., Van Spronsen, M., Olieric, N., Lipka, J., Frias, C. P., … Hoogenraad, C. C. (2016). Kinesin-Binding Protein Controls Microtubule Dynamics and Cargo Trafficking by Regulating Kinesin Motor Activity. Current Biology, 26(7), 849–861. https://doi.org/10.1016/j.cub.2016.01.048

Klein, M. E., Kovatcheva, M., Davis, L. E., Tap, W. D., & Koff, A. (2018). CDK4/6 Inhibitors: The Mechanism of Action May Not Be as Simple as Once Thought. Cancer Cell, 34(1), 9–20. https://doi.org/10.1016/j.ccell.2018.03.023

Komlodi-Pasztor, E., Sackett, D. L., Wilkerson, J., & Fojo, T. (2011). Mitosis is not a key target of microtubule agents in patient tumors. Nature Reviews Clinical Oncology, 8, 244–250.

Kowalski, R. J., Giannakakou, P., & Hamel, E. (1997). Activities of the microtubule-stabilizing agents epothilones A and B with purified tubulin and in cells resistant to paclitaxel (Taxol®). Journal of Biological Chemistry, 272(4), 2534–2541. https://doi.org/10.1074/jbc.272.4.2534

Kumar, N. (1981). Taxol-induced polymerization of purified tubulin. Mechanism of action. Journal of Biological Chemistry, 256(20), 10435–10441. https://doi.org/10.1016/s0021-9258(19)68639-4

Kutay, U., Ralf Bischoff, F., Kostka, S., Kraft, R., & Görlich, D. (1997). Export of importin α from the nucleus is mediated by a specific nuclear transport factor. Cell, 90(6), 1061–1071. https://doi.org/10.1016/S0092-8674(00)80372-4

Lawrence, C. J., Dawe, R. K., Christie, K. R., Cleveland, D. W., Dawson, S. C., Endow, S. A., … Wordeman, L. (2004). A standardized kinesin nomenclature. Journal of Cell Biology, 167(1), 19–22. https://doi.org/10.1083/jcb.200408113

Lee, R. T., Beekman, K. E., Hussain, M., Davis, N. B., Clark, J. I., Thomas, S. P., … Stadler, W. M. (2008). A University of Chicago Consortium Phase II trial of SB-715992 in advanced renal cell cancer. Clinical Genitourinary Cancer, 6(1), 21–24. https://doi.org/10.3816/CGC.2008.n.003

Letourneau, P. C., & Ressler, A. H. (1984). Inhibition of neurite initiation and growth by taxol. Journal of Cell Biology, 98(4), 1355–1362. https://doi.org/10.1083/jcb.98.4.1355

Lim, S., & Kaldis, P. (2013). Cdks, cyclins and CKIs: Roles beyond cell cycle regulation. Development (Cambridge), 140(15), 3079–3093. https://doi.org/10.1242/dev.091744

Lipton, R. B., Apfel, S. C., Dutcher, J. P., Rosenberg, R., Kaplan, J., Berger, A., … Schaumburg, H. H. (1989). Taxol produces a predominantly sensory neuropathy. Neurology, 39(3), 368–373.

Liu, D., Ding, X., Du, J., Cai, X., Huang, Y., Ward, T., … Yao, X. (2007). Human NUF2 interacts with centromere-associated protein E and is essential for a stable spindle microtubule-kinetochore attachment. Journal of Biological Chemistry, 282(29), 21415–21424. https://doi.org/10.1074/jbc.M609026200

Liu, M., Wang, X., Yang, Y., Li, D., Ren, H., Zhu, Q., … Zhou, J. (2010). Ectopic expression of the microtubule-dependent motor protein Eg5 promotes pancreatic tumourigenesis. Journal of Pathology, 221(2), 221–228. https://doi.org/10.1002/path.2706

Liu, Q., & Ruderman, J. V. (2006). Aurora A, mitotic entry, and spindle bipolarity. Proceedings of the National Academy of Sciences of the United States of America, 103(15), 5811–5816. https://doi.org/10.1073/pnas.0601425103

Liu, X. (2015). Targeting polo-like kinases: A promising therapeutic approac for cancer treatment. Translational Oncology, 8(3), 185–195. https://doi.org/10.1016/j.tranon.2015.03.010

Liu, X., & Erikson, R. L. (2007). The nuclear localization signal of mitotic kinesin-like protein Mklp-1: Effect on Mklp-1 function during cytokinesis. Biochemical and Biophysical Research Communications, 353(4), 960–964. https://doi.org/10.1016/j.bbrc.2006.12.142

Lorico, A., Rappa, G., Flavell, R. A., & Sartorelli, A. C. (1996). Double knockout of the MRP gene leads to increased drug sensitivity in vitro. Cancer Research, 56, 5351–5355.

Lu, M., Zhu, H., Wang, X., Zhang, D., Xiong, L., Xu, L., & You, Y. (2016). The prognostic role of Eg5 expression in laryngeal squamous cell carcinoma. Pathology, 48(3), 214–218. https://doi.org/10.1016/j.pathol.2016.02.008

Lucas, D. M., Still, P. C., Perez, L. B., Grever, M. R., & Kinghorn, A. D. (2010). Potential of Plant-Derived Natural Products in the Treatment of Leukemia and Lymphoma. Current Drug Targets, 11(7), 812–822. Retrieved from file:///C:/Users/ASUS/Desktop/Rujukan PhD/Dev of drug R cell line/nihms579608.pdf

Luo, L., Parrish, C. A., Nevins, N., McNulty, D. E., Chaudhari, A. M., Carson, J. D., … Auger, K. R. (2007). ATP-competitive inhibitors of the mitotic kinesin KSP that function via an allosteric mechanism. Nature Chemical Biology, 3(11), 722–726. https://doi.org/10.1038/nchembio.2007.34

Lyons, D. A., Naylor, S. G., Mercurio, S., Dominguez, C., & Talbot, W. S. (2008). KBP is essential for axonal structure, outgrowth and maintenance in zebrafish, providing insight into the cellular basis of Goldberg-Shprintzen syndrome. Development, 135(3), 599–608. https://doi.org/10.1242/dev.012377

MacKenzie, K. C., de Graaf, B. M., Syrimis, A., Zhao, Y., Brosens, E., Mancini, G. M. S., … Alves, M. M. (2020). Goldberg–Shprintzen syndrome is determined by the absence, or reduced expression levels, of KIFBP. Human Mutation. https://doi.org/10.1002/humu.24097

Maiato, H., Rieder, C. L., & Khodjakov, A. (2004). Kinetochore-driven formation of kinetochore fibers contributes to spindle assembly during animal mitosis. J Cell Biol, 167(5), 831–840. https://doi.org/10.1083/JCB.200407090

Maiato, H., Sampaio, P., & Sunkel, C. E. (2004). Microtubule-associated proteins and their essential roles during mitosis. International Review of Cytology, 241, 53–153. https://doi.org/10.1016/S0074-7696(04)41002-X

Malaby, H. L., Dumas, M. E., Ohi, R., & Stumpff, J. (2019). Kinesin-binding protein ensures accurate chromosome segregation by buffering KIF18A and KIF15. Journal of Cell Biology. https://doi.org/10.1083/jcb.201806195

Maliga, Z., Xing, J., Cheung, H., Juszczak, L. J., Friedman, J. M., & Rosenfeld, S. S. (2006). A pathway of structural changes produced by monastrol binding to Eg5.

Journal of Biological Chemistry, 281(12), 7977–7982. https://doi.org/10.1074/jbc.M511955200

Manfredi, J. J., Parness, J., & Horwitz, S. B. (1982). Taxoi binds to cellular microtubules. Journal of Cell Biology, 94, 688–696. https://doi.org/10.1083/jcb.94.3.688

Mardin, B. R., Isokane, M., Cosenza, M. R., Krämer, A., Ellenberg, J., Fry, A. M., & Schiebel, E. (2013). EGF-Induced Centrosome Separation Promotes Mitotic Progression and Cell Survival. Developmental Cell, 25(3), 229–240. https://doi.org/10.1016/j.devcel.2013.03.012

Martello, L. A., Verdier-pinard, P., Shen, H., He, L., Torres, K., Orr, G. A., & Horwitz, S. B. (2003). Advances in Brief Elevated Levels of Microtubule Destabilizing Factors in a Taxol-resistant / dependent. Cancer Research, 63, 1207–1213.

Martino, E., Casamassima, G., Castiglione, S., Cellupica, E., Pantalone, S., Papagni, F., … Collina, S. (2018). Vinca alkaloids and analogues as anti-cancer agents: Looking back, peering ahead. Bioorganic and Medicinal Chemistry Letters, 28(17), 2816–2826. https://doi.org/10.1016/j.bmcl.2018.06.044

Mastronarde, D. N., McDonald, K. L., Ding, R., & McIntosh, J. R. (1993). Interpolar spindle microtubules in PTK cells. Journal of Cell Biology, 123(6 I), 1475–1489. https://doi.org/10.1083/jcb.123.6.1475

Masuda, A., Maeno, K., Nakagawa, T., Saito, H., & Takahashi, T. (2003). Association between mitotic spindle checkpoint impairment and susceptibility to the induction of apoptosis by anti-microtubule agents in human lung cancers. American Journal of Pathology, 163(3), 1109–1116. https://doi.org/10.1016/S0002-9440(10)63470-0

Mayer, T. U., Kapoor, T. M., Haggarty, S. J., King, R. W., Schreiber, S. L., & Mitchison, T. J. (1999). Small molecule inhibitor of mitotic spindle bipolarity identified in a phenotype-based screen. Science, 286(5441), 971–974. https://doi.org/10.1126/science.286.5441.971

McDonald, K. L., O'Toole, E. T., Mastronarde, D. N., & McIntosh, J. R. (1992). Kinetochore microtubules in PTK cells. Journal of Cell Biology, 118(2), 369–383. https://doi.org/10.1083/jcb.118.2.369

McEwen, B. F., Ding, Y., & Heagle, A. B. (1998). Relevance of kinetochore size and microtubule-binding capacity for stable chromosome attachment during mitosis in PtK1 cells. Chromosome Research, 6(2), 123–132. https://doi.org/10.1023/A:1009239013215

Md Sakib Hossain, D., Javaid, S., Cai, M., Zhang, C., Sawant, A., Hinton, M., … Chackerian, A. (2018). Dinaciclib induces immunogenic cell death and enhances anti-PD1–mediated tumor suppression. Journal of Clinical Investigation, 128(2), 644–654. https://doi.org/10.1172/JCI94586

Melchior, F. (2001). Ran GTPase cycle: One mechanism - Two functions. Current Biology, 11(7), 257–260. https://doi.org/10.1016/S0960-9822(01)00132-4

Mitchison, T., Evans, L., Schulze, E., & Kirschner, M. (1986). Sites of microtubule assembly and disassembly in the mitotic spindle. Cell, 45(4), 515–527. https://doi.org/10.1016/0092-8674(86)90283-7

Mitchison, T. J., Maddox, P., Gaetz, J., Groen, A., Shirasu, M., Desai, A., … Kapoor, T. M. (2005). Roles of Polymerization Dynamics , Opposed Motors, and a Tensile Element in Governing the Length of Xenopus Extract Meiotic Spindles. Molecular Biology of the Cell, 16(June), 3064–3076. https://doi.org/10.1091/mbc.E05

Mitchison, T., & Kirschner, M. (1984). Dynamic instability of microtubule growth. Nature, 312(5991), 237–242. https://doi.org/10.1038/312237a0

Montecucco, A., Zanetta, F., & Biamonti, G. (2015). Molecular mechanisms of etoposide. EXCLI Journal, 14, 95–108. https://doi.org/10.17179/excli2014-561

Monzo, M., Rosell, R., Sanchez, J. J., Lee, J. S., O'Brate, A., Gonzalez-Larriba, J. L., … Martın, C. (1999). Paclitaxel Resistance in Non–Small-Cell Lung Cancer Associated With Beta-Tubulin Gene Mutations. Journal of Clinical Oncology, 17(6), 1786–1793.

Moores, C. A., & Milligan, R. A. (2006). Lucky 13 - Microtubule depolymerisation by kinesin-13 motors. Journal of Cell Science, 119(19), 3905–3913. https://doi.org/10.1242/jcs.03224

Mosca, L., Ilari, A., Fazi, F., Assaraf, Y. G., & Colotti, G. (2021). Taxanes in cancer treatment: Activity, chemoresistance and its overcoming. Drug Resistance Updates, 54(November 2020), 100742. https://doi.org/10.1016/j.drup.2020.100742

Mozzetti, S., Iantomasi, R., De Maria, I., Prislei, S., Mariani, M., Camperchioli, A., … Ferlini, C. (2008). Molecular mechanisms of patupilone resistance. Cancer Research, 68(24), 10197–10204. https://doi.org/10.1158/0008-5472.CAN-08-2091

Neal, C. L., & Yu, D. (2006). Microtubule-associated protein tau: A marker of paclitaxel sensitivity in breast cancer. Breast Diseases, 16(4), 374–375. https://doi.org/10.1016/S1043-321X(05)80306-6

Nettles, J. H., Li, H., Cornett, B., Krahn, J. M., Snyder, J. P., & Downing, K. H. (2004). The binding mode of epothilone A on α,β-tubulin by electron crystallography. Science, 305(5685), 866–869. https://doi.org/10.1126/science.1099190

Noble, R. L., Beer, C. T., & Cutts, J. H. (1958). Further biological activities of vincaleukoblastine - an alkaloid isolated from Vinca rosea (L.). Biochemical Pharmacology, 1, 347–348. https://doi.org/10.1016/0006-2952(59)90123-6

Nowakowski, J., Cronin, C. N., McRee, D. E., Knuth, M. W., Nelson, C. G., Pavletich, N. P., … Thompson, D. A. (2002). Structures of the cancer-related Aurora-A, FAK, and EphA2 protein kinases from nanovolume crystallography. Structure, 10(12), 1659–1667. https://doi.org/10.1016/S0969-2126(02)00907-3

O'Connor, O. A., Gerecitano, J., Van Deventer, H., Hainsworth, J., Zullo, K. M., Saikali, K., … Escandón, R. (2015). The addition of granulocyte-colony stimulating factor shifts the dose limiting toxicity and markedly increases the maximum tolerated dose and activity of the kinesin spindle protein inhibitor SB-743921 in patients with relapsed or

refractory lymphoma: Res. Leukemia and Lymphoma, 56(9), 2585–2591. https://doi.org/10.3109/10428194.2015.1004167

Ohashi, A., Ohori, M., Iwai, K., Nambu, T., Miyamoto, M., Kawamoto, T., & Okaniwa, M. (2015). A novel time-dependent CENP-E inhibitor with potent antitumor activity. PLoS ONE, 10(12), 1–19. https://doi.org/10.1371/journal.pone.0144675

Owens, B. (2013). Kinesin inhibitor marches toward first-in-class pivotal trial. Nature Medicine, 19(12), 1550–1550. https://doi.org/10.1038/nm1213-1550a

Parness, J., & Horwitz, S. B. (1981). Taxol binds to polymerized tubulin in vitro. Journal of Cell Biology, 91, 479–487. https://doi.org/10.1083/jcb.91.2.479

Peña, A., Sweeney, A., Cook, A. D., Topf, M., & Moores, C. A. (2020). Structure of Microtubule-Trapped Human Kinesin-5 and Its Mechanism of Inhibition Revealed Using Cryoelectron Microscopy. Structure, 28(4), 450–457.e5. https://doi.org/10.1016/j.str.2020.01.013

Pinsky, B. A., & Biggins, S. (2005). The spindle checkpoint: Tension versus attachment. Trends in Cell Biology, 15(9), 486–493. https://doi.org/10.1016/j.tcb.2005.07.005

Pizzo, P. A. (1993). Management of fever in patients with cancer and treatment induced neutropenia. N Engl J Med, 328(18), 1323–1332.

Plummer, E. R., Kristeleit, R. S., Cojocaru, E., Haris, N. M., Carter, L., & Jones, R. H. (2019). A first-in-human phase I/II trial of SRA737 (a Chk1 Inhibitor) in subjects with advanced cancer. Journal of Clinical Oncology, 37(3094–3094).

Raaijmakers, J. A., Van Heesbeen, R. G. H. P., Meaders, J. L., Geers, E. F., Fernandez-Garcia, B., Medema, R. H., & Tanenbaum, M. E. (2012). Nuclear envelope-associated dynein drives prophase centrosome separation and enables Eg5-independent bipolar spindle formation. EMBO Journal, 31(21), 4179–4190. https://doi.org/10.1038/emboj.2012.272

Rao, S., Krauss, N. E., Heerding, J. M., Swindell, C. S., Ringel, I., Orr, G. A., & Horwitz, S. B. (1994). 3'-(p-Azidobenzamido)taxol photolabels the N-terminal 31 amino acids of β-tubulin. Journal of Biological Chemistry, 269(5), 3132–3134. https://doi.org/10.1016/s0021-9258(17)41836-9

Rao, S., Orr, G. A., Chaudhary, A. G., Kingston, D. G. I., & Horwitz, S. B. (1995). Characterization of the taxol binding site on the microtubule: 2-(m-azidobenzoyl)taxol photolabels a peptide (amino acids 217-231) of β-tubulin. Journal of Biological Chemistry, 270(35), 20235–20238. https://doi.org/10.1074/jbc.270.35.20235

Rello-Varona, S., Vitale, I., Kepp, O., Senovilla, L., Jemaá, M., Métivier, D., … Kroemer, G. (2009). Preferential killing of tetraploid tumor cells by targeting the mitotic kinesin Eg5. Cell Cycle, 8(7), 1030–1035. https://doi.org/10.4161/cc.8.7.7950

Richard McIntosh, J. (1991). Structural and mechanical control of mitotic progression. Cold Spring Harbor Symposia on Quantitative Biology, 56, 613–619.

Rieder, C. L., & Maiato, H. (2004). Stuck in division or passing through: What happens when cells cannot satisfy the spindle assembly checkpoint. Developmental Cell, 7(5), 637–651. https://doi.org/10.1016/j.devcel.2004.09.002

Rogers, G. C., Rogers, S. L., Schwimmer, T. A., Ems-McClung, S. C., Walczak, C. E., Vale, R. D., … Sharp, D. J. (2004). Two mitotic kinesins cooperate to drive sister chromatid separation during anaphase. Nature, 427(6972), 364–370. https://doi.org/10.1038/nature02256

Rosenfeld, S. S. (2015). Clinical Trials of Mitotic Kinesin Inhibitors. In F. Kozielski FSB (Ed.), Kinesins and Cancer (pp. 63–76). Dordrecht: Springer Netherlands. https://doi.org/10.1007/978-94-017-9732-0_4

Rudelli, R. D., Brown, W. T., Wisniewski, K., Jenkins, E. C., Laure-Kamionowska, M., Connell, F., & Wisniewski, H. M. (1985). Adult fragile X syndrome - Clinico-neuropathologic findings. Acta Neuropathologica, 67(3–4), 289–295. https://doi.org/10.1007/BF00687814

Saijo, T., Ishii, G., Ochiai, A., Yoh, K., Goto, K., Nagai, K., … Saijo, N. (2006). Eg5 expression is closely correlated with the response of advanced non-small cell lung cancer to antimitotic agents combined with platinum chemotherapy. Lung Cancer, 54(2), 217–225. https://doi.org/10.1016/j.lungcan.2006.06.018

Saunders, W., Lengyel, V., & Hoyt, M. A. (1997). Mitotic spindle function in Saccharomyces cerevisiae requires a balance between different types of kinesin-related motors. Molecular Biology of the Cell, 8(6), 1025–1033. https://doi.org/10.1091/mbc.8.6.1025

Sawin, K. E., & Mitchison, T. J. (1995). Mutations in the kinesin-like protein Eg5 disrupting localization to the mitotic spindle. Cell Biology (Vol. 92). Retrieved from https://www.ncbi.nlm.nih.gov/pmc/articles/PMC41929/pdf/pnas01486-0225.pdf

Schaar, B. T., Chan, G. K. T., Maddox, P., Salmon, E. D., & Yen, T. J. (1997). CENP-E function at kinetochores is essential for chromosome alignment. Journal of Cell Biology, 139(6), 1373–1382. https://doi.org/10.1083/jcb.139.6.1373

Schiff, P. B., & Horwitz, S. B. (1981). Taxol Assembles Tubulin in the Absence of Exogenous Guanosine 5'-Triphosphate or Microtubule-Associated Proteins. Biochemistry, 20(11), 3247–3252. https://doi.org/10.1021/bi00514a041

Scholey, J. E., Nithianantham, S., Scholey, J. M., & Al-Bassam, J. (2014). Structural basis for the assembly of the mitotic motor kinesin-5 into bipolar tetramers. ELife, 2014(3), 1–19. https://doi.org/10.7554/eLife.02217

Sen, S., Zhou, H., & White, R. A. (1997). A putative serine/threonine kinase encoding gene BTAK on chromosome 20q13 is amplified and overexpressed in human breast cancer cell lines. Oncogene, 14(18), 2195–2200. https://doi.org/10.1038/sj.onc.1201065

Sessa, F., Mapelli, M., Ciferri, C., Tarricone, C., Areces, L. B., Schneider, T. R., … Musacchio, A. (2005). Mechanism of Aurora B activation by INCENP and inhibition by

hesperadin. Molecular Cell, 18(3), 379–391. https://doi.org/10.1016/j.molcel.2005.03.031

Sève, P., & Dumontet, C. (2005). Chemoresistance in non-small cell lung cancer. Current Medicinal Chemistry - Anti-Cancer Agents, 5(1), 73–88. https://doi.org/10.2174/1568011053352604

Shah, J. J., Kaufman, J. L., Zonder, J. A., Cohen, A. D., Bensinger, W. I., Hilder, B. W., … Lonial, S. (2017). A Phase 1 and 2 study of Filanesib alone and in combination with low-dose dexamethasone in relapsed/refractory multiple myeloma. Cancer, 123(23), 4617–4630. https://doi.org/10.1002/cncr.30892

Singer, W. D., Jordan, M. A., Wilson, L., & Himes, R. H. (1989). Binding of vinblastine to stabilized microtubules. Molecular Pharmacology, 36(3), 366–370.

Spänkuch, B., Matthess, Y., Knecht, R., Zimmer, B., Kaufmann, M., & Strebhardt, K. (2004). Cancer inhibition in nude mice after systemic application of U6 promoter-driven short hairpin RNAs against PLK1. Journal of the National Cancer Institute, 96(11), 862–872. https://doi.org/10.1093/jnci/djh146

Spiegelman, B. M., Penningroth, S. M., & Kirschner, M. W. (1977). Turnover of tubulin and the N site GTP in chinese hamster ovary cells. Cell, 12(3), 587–600. https://doi.org/10.1016/0092-8674(77)90259-8

Stock, M. F., Guerrero, J., Cobb, B., Eggers, C. T., Huang, T.-G., Li, X., & Hackney, D. D. (1999). Formation of the Compact Confomer of Kinesin Requires a COOH-terminal Heavy Chain Domain and Inhibits Microtubule-stimulated ATPase Activity*. Retrieved from http://www.jbc.org/

Sturgill, E. G., Das, D. K., Takizawa, Y., Shin, Y., Collier, S. E., Ohi, M. D., … Ohi, R. (2014). Kinesin-12 kif15 targets kinetochore fibers through an intrinsic two-step mechanism. Current Biology, 24(19), 2307–2313. https://doi.org/10.1016/j.cub.2014.08.022

Sturgill, E. G., Norris, S. R., Guo, Y., & Ohi, R. (2016). Kinesin-5 inhibitor resistance is driven by kinesin-12. Journal of Cell Biology, 213(2), 213–227. https://doi.org/10.1083/jcb.201507036

Sturgill, E. G., & Ohi, R. (2013). Kinesin-12 differentially affects spindle assembly depending on its microtubule substrate. Current Biology, 23(14), 1280–1290. https://doi.org/10.1016/j.cub.2013.05.043

Sugimoto, K., Urano, T., Zushi, H., Inoue, K., Tasaka, H., Tachibana, M., & Dotsu, M. (2002). Molecular dynamics of Aurora-A kinase in living mitotic cells simultaneously visualized with histone H3 and nuclear membrane protein importinα. Cell Structure and Function, 27(6), 457–467. https://doi.org/10.1247/csf.27.457

Sumara, I., Gimenez-Abian, J. F., Gerlich, D., Hirota, T., Kraft, C., de la Torre, C., … Peters, J. M. (2004). Roles of Polo-like Kinase 1 in the Assembly of Functional Mitotic Spindles. Current Biology, 14, 1712–1722. https://doi.org/10.1016/j

Sun, D., Lu, J., Ding, K., Bi, D., Niu, Z., Cao, Q., … Ding, S. (2013). The expression of Eg5 predicts a poor outcome for patients with renal cell carcinoma. Medical Oncology, 30(1). https://doi.org/10.1007/s12032-013-0476-0

Tahara, K., Takagi, M., Ohsugi, M., Sone, T., Nishiumi, F., Maeshima, K., … Imamoto, N. (2008). Importin-β and the small guanosine triphosphatase Ran mediate chromosome loading of the human chromokinesin Kid. Journal of Cell Biology, 180(3), 493–506. https://doi.org/10.1083/jcb.200708003

Takashima, S., Ieshima, A., Nakamura, H., & Becker, L. E. (1989). Dendrites, dementia and the down syndrome. Brain and Development, 11(2), 131–133. https://doi.org/10.1016/S0387-7604(89)80082-8

Talapatra, S. K., Schüttelkopf, A. W., & Kozielski, F. (2012). The structure of the ternary Eg5-ADP-ispinesib complex. Acta Crystallographica Section D: Biological Crystallography, 68(10), 1311–1319. https://doi.org/10.1107/S0907444912027965

Tanaka, E., Ho, T., & Kirschner, M. W. (1995). The role of microtubule dynamics in growth cone motility and axonal growth. Journal of Cell Biology, 128(1–2), 139–155. https://doi.org/10.1083/jcb.128.1.139

Tanaka, H., Ito, J., Cho, K., & Mikawa, M. (1993). Hirschsprung disease, unusual face, mental retardation, epilepsy, and congenital heart disease: Goldberg-Shprintzen syndrome. Pediatric Neurology, 9(6), 479–481. https://doi.org/10.1016/0887-8994(93)90029-C

Tanenbaum, M. E., Macůrek, L., Janssen, A., Geers, E. F., Alvarez-Fernández, M., & Medema, R. H. (2009). Kif15 Cooperates with Eg5 to Promote Bipolar Spindle Assembly. Current Biology, 19(20), 1703–1711. https://doi.org/10.1016/j.cub.2009.08.027

Tang, P. A., Siu, L. L., Chen, E. X., Hotte, S. J., Chia, S., Schwarz, J. K., … Winquist, E. (2008). Phase II study of ispinesib in recurrent or metastatic squamous cell carcinoma of the head and neck. Investigational New Drugs, 26(3), 257–264. https://doi.org/10.1007/s10637-007-9098-8

Trieselmann, N., Armstrong, S., Rauw, J., & Wilde, A. (2003). Ran modulates spindle assembly by regulating a subset of TPX2 and Kid activities including Aurora A activation. Journal of Cell Science, 116(23), 4791–4798. https://doi.org/10.1242/jcs.00798

Tsai, J. W., Lian, W. N., Kemal, S., Kriegstein, A. R., & Vallee, R. B. (2010). Kinesin 3 and cytoplasmic dynein mediate interkinetic nuclear migration in neural stem cells. Nature Neuroscience, 13(12), 1463–1472. https://doi.org/10.1038/nn.2665

Tuxen, M. K., & Hansen, S. W. (1994). Neurotoxicity secondary to antineoplastic drugs. Cancer Treatment Reviews, 20(2), 191–214. https://doi.org/10.1016/0305-7372(94)90027-2

Valence, S., Poirier, K., Lebrun, N., Saillour, Y., Sonigo, P., Bessières, B., … Bahi-Buisson, N. (2013). Homozygous truncating mutation of the KBP gene, encoding a

KIF1B-binding protein, in a familial case of fetal polymicrogyria. Neurogenetics, 14(3–4), 215–224. https://doi.org/10.1007/s10048-013-0373-x

Verhey, K. J., Lizotte, D. L., Abramson, T., Barenboim, L., Schnapp, B. J., & Rapoport, T. A. (1998). Light chain-dependent regulation of kinesin's interaction with microtubules. Journal of Cell Biology, 143(4), 1053–1066. https://doi.org/10.1083/jcb.143.4.1053

Vitre, B., Gudimchuk, N., Borda, R., Kim, Y., Heuser, J. E., Cleveland, D. W., & Grishchuk, E. L. (2014). Kinetochore-microtubule attachment throughout mitosis potentiated by the elongated stalk of the kinetochore kinesin CENP-E. Molecular Biology of the Cell, 25(15), 2272–2281. https://doi.org/10.1091/mbc.E14-01-0698

Wacker, S., Houghtaling, B., Elemento, O., & Kapoor, tarun M. (2012). Using transcriptome sequencing to identify mechanisms of drug action and resistance. Nature Chemical Biology, 8. https://doi.org/10.1038/nCHeMBIO.779

Wani, M. C., Taylor, H. L., Wall, M. E., Coggon, P., & McPhail, A. T. (1971). The Isolation and Structure of Taxol, a Novel Antileukemic and Antitumor Agent from Taxus brivifolia. Journal of the American Chemical Society, 93(9), 2325–2327.

Wilkinson, R. W., Odedra, R., Heaton, S. P., Wedge, S. R., Keen, N. J., Crafter, C., … Green, S. (2007). AZD1152, a selective inhibitor of Aurora B kinase, inhibits human tumor xenograft growth by inducing apoptosis. Clinical Cancer Research, 13(12), 3682–3688. https://doi.org/10.1158/1078-0432.CCR-06-2979

Wilson, L., Jordan, M. A., Morse, A., & Margolis, R. L. (1982). Interaction of vinblastine with steady-state microtubules in vitro. Journal of Molecular Biology, 159(1), 125–149. https://doi.org/10.1016/0022-2836(82)90035-3

Wilson, L., Miller, H. P., Farrell, K. W., Snyder, K. B., Thompson, W. C., & Purich, D. L. (1985). Taxol Stabilization of Microtubules in Vitro: Dynamics of Tubulin Addition and Loss at Opposite Microtubule Ends. Biochemistry, 24(19), 5254–5262. https://doi.org/10.1021/bi00340a045

Wissing, M. D., de Morrée, E. S., Dezentjé, V. O., Buijs, J. T., de Krijger, R. R., Smit, V. T. H. B. M., … van der Pluijm, G. (2014). Nuclear Eg5 (kinesin spindle protein) expression predicts docetaxel response and prostate cancer aggressiveness. Oncotarget, 5(17), 7357–7367. https://doi.org/10.18632/oncotarget.1985

Wood, K. W., Lad, L., Luo, L., Qian, X., Knight, S. D., Nevins, N., … Jackson, J. R. (2010). Antitumor activity of an allosteric inhibitor of centromere-associated protein-E. Proceedings of the National Academy of Sciences of the United States of America, 107(13), 5839–5844. https://doi.org/10.1073/pnas.0915068107

Wood, K. W., Sakowicz, R., Goldstein, L. S. B., & Cleveland, D. W. (1997). CENP-E is a plus end-directed kinetochore motor required for metaphase chromosome alignment. Cell, 91(3), 357–366. https://doi.org/10.1016/S0092-8674(00)80419-5

Woods, D., & Turchi, J. J. (2013). Chemotherapy induced DNA damage response Convergence of drugs and pathways. Cancer Biology and Therapy, 14(5), 379–389. https://doi.org/10.4161/cbt.23761

Wozniak, M. J., Melzer, M., Dorner, C., Haring, H. U., & Lammers, R. (2005). The novel protein KBP regulates mitochondria localization by interaction with a kinesin-like protein. BMC Cell Biology, 6, 1–15. https://doi.org/10.1186/1471-2121-6-35

Yildiz, A., Tomishige, M., Vale, R. D., & Selvin, P. R. (2004). Kinesin Walks Hand-Over-Hand. Science, 303(5658), 676–678. https://doi.org/10.1126/science.1093753

Zeitlin, S. G., Shelby, R. D., & Sullivan, K. F. (2001). CENP-A is phosphorylated by Aurora B kinase and plays an unexpected role in completion of cytokinesis. Journal of Cell Biology, 155(7), 1147–1157. https://doi.org/10.1083/jcb.200108125

Zhai, Y., Kronebusch, P. J., & Borisy, G. G. (1995). Kinetochore microtubule dynamics and the metaphase-anaphase transition. Journal of Cell Biology, 131(3), 721–734. https://doi.org/10.1083/jcb.131.3.721

Zhang, X. D., Goeres, J., Zhang, H., Yen, T. J., Porter, A. C. G., & Matunis, M. J. (2008). SUMO-2/3 Modification and Binding Regulate the Association of CENP-E with Kinetochores and Progression through Mitosis. Molecular Cell, 29(6), 729–741. https://doi.org/10.1016/j.molcel.2008.01.013

Zhou, J., Yao, J., & Joshi, H. C. (2002). Attachment and tension in the spindle assembly checkpoint. Journal of Cell Science, 115(18), 3547–3555. https://doi.org/10.1242/jcs.00029

Zhu, M., Wang, F., Yan, F., Yao, P. Y., Du, J., Gao, X., … Yao, X. (2008). Septin 7 interacts with centromere-associated protein E and is required for its kinetochore localization. Journal of Biological Chemistry, 283(27), 18916–18925. https://doi.org/10.1074/jbc.M710591200

Zonder, J. A., Usmani, S., Scott, E. C., Hofmeister, C. C., Lendvai, N., Berdeja, J. G., … Raje, N. S. (2015). Phase 2 Study of Carfilzomib (CFZ) with or without Filanesib (FIL) in Patients with Advanced Multiple Myeloma (MM). Blood, 126(23), 728–728. https://doi.org/10.1182/blood.v126.23.728.728

Chapter II:
Chemical Biology of Mitotic Spindle Assembly Motors

April Solon[1] and Ryoma Ohi[1†]

[1]Department of Cell and Developmental Biology, University of Michigan School of Medicine, Ann Arbor, MI, 48109

Previously published in part as:

Solon, A. L., and Ohi, R. (2021). Chemical Biology of Mitotic Spindle Assembly Motors. In E. H. Hinchcliffe (Ed.). *Mitosis : Methods and Protocols* (Chapter 11). New York, NY: Springer-Verlag New York Inc.

2.1 Abstract

Mitotic kinesins play essential roles during mitotic spindle assembly and in ensuring proper chromosome segregation. Chemical inhibitors of mitotic kinesins are therefore valuable tools to study kinesin function *in vitro* and in cells. Because cancer is a disease of unregulated cell division, inhibitors also represent potential chemotherapeutic agents. Here, we present assays that can be used to evaluate the potency and specificity of mitotic kinesin inhibitors identified from high-throughput screening. By evaluating their effects in a variety of *in vitro*, fixed-cell, and live-cell assays, screening hits can be prioritized and optimized to produce effective, on-target inhibitors.

2.2 Introduction

The kinesin superfamily is comprised of 14 distinct families of microtubule-dependent motor proteins, many of which use energy from ATP hydrolysis to transport cargoes along microtubule tracks in cells (Verhey and Hammond 2009). A subset of kinesins also regulate microtubule dynamics (Drummond 2011), or use their motility to organize microtubules in three-dimensional space (Akhmanova and Steinmetz 2015). While there is wide variation in domain organization and primary sequence between

subfamilies, all kinesins share a conserved motor head domain with an ATP binding site that binds the microtubule track (Hirokawa et al. 1989). Kinesins perform diverse functions in cells, and several kinesins are essential for cell division. These “mitotic kinesins” drive the assembly and maintenance of a bipolar mitotic spindle, the microtubule-based structure essential for chromosome segregation (Sawin et al. 1992).

Several small molecule inhibitors that target mitotic kinesins have been developed that are useful as tools to study kinesin function and elucidate mechanisms of mitosis. For example, the small molecule monastrol was discovered as an inhibitor of Eg5 (Mayer et al. 1999), a member of the kinesin-5 family (Sawin et al. 1992; Blangy et al. 1995; Ferenz, Gable, and Wadsworth 2010). Eg5 drives the separation of centrosomes during the early stages of mitosis (Sawin and Mitchison 1995). Eg5 inhibition with monastrol thus prevents centrosome separation, resulting in the formation of monopolar spindles and mitotic arrest (Mayer et al. 1999). As a specific and reversible inhibitor, monastrol has been used to probe processes involved in bipolar spindle assembly and maintenance, and the contribution of Eg5 to these processes (Kapoor et al. 2000).

Mitotic kinesin inhibitors can also be used as anticancer therapies, functioning to activate the mitotic checkpoint and selectively kill dividing cells (Jordan and Wilson 2004). Since cancer is characterized by deregulated proliferation, antimitotic drugs comprise an important class of anticancer therapies. Taxanes and Vinca alkaloids, drugs that disrupt microtubule dynamics and mitotic spindle assembly, have had clinical success against a wide range of cancers including breast and ovarian cancer and leukemia (Tuxen and Hansen 1994; Rowinsky 1997). Despite their success at reducing tumor burden in patients, these drugs also affect non-dividing cells that rely on microtubules to function, such as neurons, and can cause debilitating neurotoxicity (Tuxen and Hansen 1994; Lipton et al. 1989). Targeting proteins that are only utilized during cell division can reduce such off-target toxicities. Since Eg5 is necessary for spindle formation but is non-essential during interphase, inhibiting its activity prevents mitotic progression but has no known effects on non-dividing cells, creating a therapeutic window for treating proliferating cancer cells (Kapoor et al. 2000).

Many Eg5 inhibitors have been developed that are effective at halting mitosis *in vitro*, however none have been successful at reducing tumor burden in patients. One

hypothesis to explain this discrepancy is that a kinesin-12, KIF15, can compensate for loss of Eg5 activity (Dumas et al. 2019). Deletion of KIF15 by CRISPR-Cas9 technology renders cells completely sensitive to Eg5 inhibition, providing rationale for developing KIF15 inhibitors. We have developed a pipeline to identify novel KIF15 inhibitor scaffolds since there remains a lack of clinically available drugs to target KIF15 (Dumas et al. 2019; unpublished data). The methods presented in this chapter can be used to evaluate the potency and specificity of KIF15 inhibitors in any stage of development, and can be adapted to screen for and evaluate inhibitors of other kinesins. We first describe an ATPase assay that can be used to screen drug libraries for potential KIF15 inhibitors in a high-throughput, cell-free manner. We then detail several assays that are useful for prioritizing hit compounds by potency and evaluating off-target effects. When modifying inhibitor scaffolds *via* medicinal chemistry, these assays are critical for evaluating changes in effectiveness and specificity compared to the parent compound or other derivatives.

2.3 Materials

2.3.1 High-throughput screening for small molecules that inhibit the ATPase activity of KIF15

1. Taxol-stabilized microtubules: 20 μM tubulin, 1X BRB80 (see 2.2 for recipe), 1 mM GTP, 1 mM DTT. Incubate on ice for 5 min, then at 37° C for 1 hr. Add Taxol stepwise to a final concentration 20 μM. First add Taxol to 200 nM and incubate 10 min at 37° C, then to 2 μM and incubate 10 min, then to 20 uM and incubate for a final 15 min. Store at room temp for up to 72 hr.
2. Purified KIF15-N420
3. ADP-Glo Buffer Mix: 10 mM K-HEPES (pH 7.7), 100 mM KCl, 1 mM DTT, 10 mM $MgCl_2$, 5 μM. *Can be made fresh or stored at -20° C for up to 1 month prior to experiment.*
4. White polystyrene flat bottom non-binding 384-well microplates (Greiner Bio-One, 781904)
5. ADP-Glo™ Kinase Assay (Promega V6930)
6. DMSO

7. Library of small molecule inhibitors

2.3.2 Microtubule gliding assays

1. 5X BRB80: 400 mM K-PIPES (pH 6.8), 5 mM $MgCl_2$, 5 mM K-EGTA (pH 7.7) Dissolve PIPES, $MgCl_2$, and EGTA in water, and add KOH pellets until the PIPES fully dissolves. Measure pH after PIPES dissolves, bring up to 6.8 using 5M KOH, and adjust water volume.
2. 20 mg/mL Glucose Oxidase (Sigma G-2133) Dissolve in 12 mM K-PIPES, pH 6.8, 2 mM $MgCl_2$, 1 mM EGTA, aliquot and freeze in liquid nitrogen and store at -80° C.
3. GMPCPP-stabilized fluorescently labeled microtubules: 20 µM tubulin (*see* **Note 1**), BRB80, 1 mM GMPCPP, 1 mM DTT. *Incubate on ice for 5 min, then at 37° C for 1 hr. Store at room temp for up to 72 hr.*
4. Flow cells: place two strips of double-sided tape on a glass microscope slide about 7-10 mm apart and cover with a 18x18 or 22x22 mm glass coverslip
5. Whatman #1 filter paper, cut into small strips
6. Wash buffer: BRB80, 500 µg/mL casein, 1 mM MgATP
7. Oxygen-scavenging Mix: BRB80, 4.5 mg/mL glucose, 5% β-Mercaptoethanol, 200 µg/mL Glucose Oxidase, 10% catalase (Sigma C-3155)
8. Flow Cell Buffer: BRB80, 500 µg/mL casein, 1 mM MgATP, 1X Oxygen-scavenging Mix
9. 1% Pluronic F-127 in BRB80
10. Purified KIF15-N700
11. Fluorescence microscope capable of time-lapse imaging. We use the Eclipse Ni-E (Nikon).

2.3.3 Indirect immunofluorescence

1. Acid-washed round glass coverslips. Heat coverslips in container with 1 M HCl at 55° C for 4 hours. Rinse out with ddH_2O. Fill container with ddH_2O and sonicate in a water bath sonicator for 30 min; change water and repeat twice. Replace with 50% ethanol and sonicate 30 min. Replace with 70% ethanol and sonicate for 30 min, repeat once. Fill container with fresh 70% ethanol and store.

2. 6- or 12-well polystyrene tissue culture dishes (Falcon)
3. Humidified chamber for immunofluorescence (IF): line a 150 mm polystyrene tissue culture dish (Falcon) with parafilm and a damp paper towel.
4. PBS (Gibco)
5. 100% Methanol, chilled to -20° C
6. 3% formaldehyde
7. 1X TBS: 20 mM Tris-HCl, pH 7.6, 13.7 mM NaCl
8. TBST: 1X TBS, 0.1% Triton X-100
9. TBST + 2% BSA. Add 0.1% sodium azide if storing solution.
10. Mounting media: We use ProLong Diamond™ Antifade Mountant (Invitrogen)
11. Antibodies targeting proteins of interest
12. Fluorescence microscope: We use the DeltaVision Elite™ Imaging System (GE Healthcare) or the Eclipse Ni-E (Nikon)

2.3.4 Live cell imaging

1. 6-, 12-, or 24-well polystyrene tissue culture dishes (Falcon)
2. Glass bottom dishes (MatTek)
3. Leibovitz's L-15 Medium (Gibco), supplemented with 10% fetal bovine serum, 1% Penecillin-Streptomycin (10,000 U/mL, Gibco), and 7 mM K-HEPES
4. Microscope capable of time-lapse and DIC imaging. We use either the DeltaVision Elite, which requires glass-bottom dishes, or the EVOS FL Auto 2 microscope (Invitrogen), which can image through plastic dishes.

2.4 Methods

2.4.1 ATPase assay

Since kinesins generate force *via* ATP hydrolysis, many kinesin inhibitors block kinesin activity by inhibiting ATP hydrolysis, either by competing with ATP binding or hindering ATP hydrolysis through allosteric mechanisms. Thus, ATPase activity can be used to screen for molecules that block kinesin activity. We have used this assay in several high-throughput screens to identify novel KIF15 inhibitor scaffolds. We adapted the assay to a 384-well plate format, which is well-suited for screening a large panel of

drugs. Automation with robotics or liquid handling systems minimizes human error and increases the speed at which 384-well plates can be screened.

For our experiments, we use Promega's ADP-Glo™ Kinase Assay, which is a luminescent ADP-detection assay suitable for many different ATPases. To use ADP-Glo, a reaction is set up where an ADP-generating protein is incubated with its substrate and a set amount of ATP. ADP-Glo™ Reagent is then added to quench the reaction and deplete unhydrolyzed ATP, followed by adding the Kinase Detection Reagent to convert the hydrolyzed ADP back into ATP with a luciferase/luciferin reaction, resulting in luminescence that can be quantified and correlated with ATPase activity. Thus, higher luminescence readout signals higher ATPase activity. When screening small molecules, hits can be defined as compounds that decrease the luminescence readout below a certain threshold.

In the case of our KIF15 inhibitor screen, we used a recombinant dimeric construct (N420) comprised of the motor domain, neck linker, and a portion of the first coiled-coil to mediate dimerization (Dumas et al. 2019). It is important to test the specific activity of each KIF15 protein prep and use the same prep for the screen if possible, as activity may vary between preps. The substrate in our case is Taxol-stabilized microtubules. In our screen, we used a high concentration of ATP to bias our hits towards being allosteric inhibitors rather than ATP-competitive inhibitors; using a lower ATP concentration would increase the odds of isolating inhibitors that compete with the ATP-binding pocket.

Prior to conducting a high-throughput screen, it is critical to establish the robustness and dynamic range of the assay. A Z'-factor can be extracted using a 384-plate in which the locations of positive and negative controls are known. For our work with KIF15 inhibitors, we omit ATP as a positive control, representing complete inhibition of KIF15 activity. The compound GW406108X, a known sub-micromolar KIF15 inhibitor (Dumas et al. 2019), can also be used as a positive control. For a negative control, we use the same conditions as our regular assay (motor, substrate, ATP) but with DMSO added instead of a compound; this represents the baseline ATPase levels of our reaction. Using results from the positive and negative controls, the Z'-factor can be calculated to describe the dynamic range and variation of the assay, and thus the accuracy of the assay in identifying hits. The Z'-factor is calculated using the equation:

$$Z' = 1 - \frac{3 * \sigma_{C+} + 3 * \sigma_{C-}}{| \mu_{C+} - \mu_{C-} |}$$

where σ_{C+} and σ_{C-} represent the standard deviations of the positive and negative control data, and μ_{C+} and μ_{C-} represent the means (Zhang, Chung, and Oldenburg 1999). In general, larger Z'-factors signal higher quality of the assay and better confidence in the prediction of hits. We typically obtain Z'-factor scores of ~0.75, which is above a recommended cut-off of 0.5.

1. Polymerize taxol-stabilized microtubules following recipe in Materials section (*see* **Note 2**).
2. Make ADP-Glo Buffer Mix following recipe in Materials section (*see* **Note 3**) and thaw reagents from ADP-Glo kit (ATP, ADP-Glo reagent, Kinase Detection Reagent). Dilute microtubules to 5 μM and purified motor to appropriate concentration (*see* **Note 4**) in Buffer Mix to make Microtubule + Motor Mix.
3. Add 10 μL of Microtubule + Motor Mix to each well of a 384-well plate using a liquid dispenser (*see* **Note 5**), and quickly centrifuge for 30 sec at 1000 rpm to ensure liquids are in the bottom of the well.
4. Using a Pin Tool, add compound to each well to the desired concentration and incubate for 15 min. For negative control wells, add DMSO or another vehicle control. If necessary, compound can be added before M+M Mix, but we find it easier to add a small volume to the 10 μL of mix.
5. Add 10 μL of ATP Mix to each well of the plate *except* for the positive control wells. To these wells, just add 10 μL of ADP-Glo Buffer Mix with no ATP added. Gently shake plate to mix and incubate 20 min.
6. Add 5 μL of ADP-Glo reagent to each well of plate; gently shake and incubate 40 min.
7. Add 10 μL of KDR to each well of plate to quench the reaction. Gently shake and incubate 30 min.
8. After final incubation with KDR, image plate(s) as soon as possible on a plate-reading luminometer (*see* **Note 6**).
9. Analyze data, making sure to subtract the average background intensity from the negative control wells. The Z'-factor can be calculated from the positive and

negative control results as a measure of how accurate the assay is at detecting hits.

2.4.2 Microtubule gliding assay

This assay is a useful way to quantify on-target activity of KIF15 inhibitors in an *in vitro* setting. In this assay, KIF15 is first introduced into a flow cell, where it non-specifically associates with the slide and coverslip. Fluorescent microtubules are then infused into the flow cell, where they associate with the immobilized kinesin. Time-lapse imaging of flow cells using a fluorescence microscope enables visualization of microtubules being moved by stationary kinesin. Time lapse movies can be analyzed to quantify several parameters in response to drug treatment, including number of microtubules bound to the coverslip by motor, the percentage of bound microtubules that are moving, and the velocity of gliding microtubules. Reduction in any of these variables in response to drug treatment is an indication of on-target activity, and can provide information about the mechanism of action of the inhibitor. For example, high levels of stationary microtubules could indicate a rigor drug, whereas a reduction in microtubule binding might result from a drug that causes KIF15 to be trapped in an ADP-bound state, and therefore has a low affinity for microtubules. Since this is a cell-free assay, variables such as cell permeability or drug metabolism will not affect results.

In the case of KIF15, we use a different recombinant dimeric construct, N700, that includes the motor domain and the microtubule-binding Coil-1 region (Sturgill et al. 2014); both regions contribute to the recruitment of microtubules to the coverslip. KIF15-N700 lacks the C-terminal half of the full-length protein, eliminating autoinhibition (Sturgill et al. 2014). We find that our preps of KIF15-N700 typically produce a gliding velocity of 7 µM/min. We also use X-rhodamine-labeled GMPCPP-stabilized microtubules as our substrate.

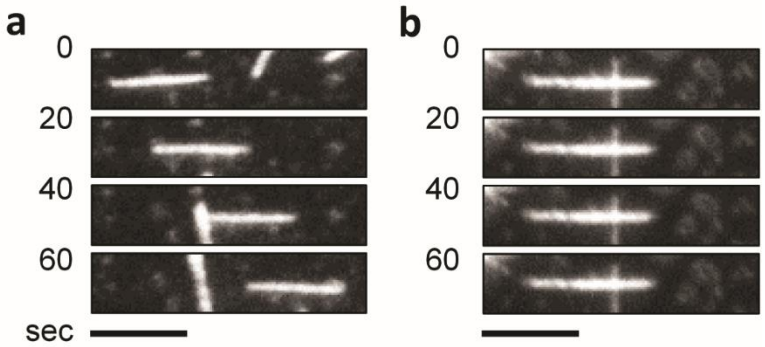

Fig. 2.1 Microtubule gliding assay. Images taken from a gliding assay using X-rhodamine-labeled microtubules and KIF15-N700. Assay was performed in the presence of (a) DMSO, or (b) a preliminary KIF15 inhibitor. Scale bar represents 5 µm.

We find that stabilizing with GMPCPP produces shorter microtubules than Taxol, which is better for visualizing gliding and reducing crowding on the coverslip. When incorporating labeled tubulin in the polymerization reaction, it is important to consider the labeling stoichiometry to obtain sufficient fluorescence. With our X-rhodamine-labeled tubulin that had a labeling stoichiometry of roughly 0.16 (one out of six tubulin subunits was labeled), we diluted this at a ratio of 1:4 with unlabeled tubulin when polymerizing our fluorescent microtubules.

This assay, as well as the previously described ATPase assay, can also be used to evaluate the specificity of kinesin inhibitors by testing against other kinesins rather than the kinesin targeted by the drug. If a drug is truly specific for the kinesin of interest, there should be little to no effect on ATPase activity or microtubule motility when tested against other motors.

1. Polymerize GMPCPP-stabilized microtubules following recipe in the Materials section.
2. Construct flow cells. Flow cells can be made several ways, but the most common way is to attach a coverslip to a glass microscope slide using double-sided tape. Place two narrow strips of double-sided tape on a glass slide about 7-10 mm apart, and cover with a 18x18 or 22x22 mm glass coverslip, pressing gently on coverslip edges to ensure a tight seal between the tape and glass. This results in a 15-20 µL flow cell with two open sides. Solutions should be pipetted in one side of the flow cell and removed from the other side by capillary action using Whatman filter paper.
3. Make the buffers needed for this assay (Wash Buffer, Flow Cell Buffer, and Oxygen-Scavenging Mix) as described in Materials section (*see* **Note 7**).
4. Dilute motor to the desired concentration in Wash Buffer (*see* **Note 8**) and pipette 20 µL into one side of the flow cell. Incubate for 3 min. Motor should be thawed immediately prior to assay and used fresh.
5. Wash excess motor out with 60 µL of Wash Buffer, removing buffer from the other side of the flow cell with a small piece of Whatman paper.
6. Block excess protein binding sites with 20 µL of 1% Pluronic F-127 in 1X BRB80. Incubate in flow cell for 1 min. Wash with 60 µL of Wash Buffer.

7. Dilute fluorescent microtubules to 1 µM in Flow Cell Buffer. Pipette 20 µL into flow cell and incubate for 3 min.
8. Wash excess microtubules out with 60 µL of Flow Cell Buffer. If testing a drug, first dilute it to the desired concentration Flow Cell Buffer and then pipette in 60 µL of the solution.
9. Immediately following, image microtubule gliding on a fluorescence microscope using a 100X oil objective. We find that doing time lapse imaging over 1 minute taking images every 5 seconds results in data for easy quantifications of velocity. **Fig. 2.1** shows representative images taken from gliding assays with rhodamine-labeled microtubules and KIF-N700, tested with a DMSO control and a KIF15 inhibitor that completely stops gliding.

2.4.3 Immunofluorescence assay

Staining fixed cells with fluorescent antibodies and analyzing them under the microscope is a useful way to quantify changes in protein levels and localization of the target protein in response to drug treatment, as well as observing spindle assembly defects. Drugs that inhibit kinesins necessary for spindle assembly, such as Eg5 and KIF15, should result in an increase in monopolar mitotic spindles rather than bipolar arrays (**Fig. 2.2**). Thus, staining for tubulin and DNA allows easy characterization of spindle geometries and quantification of the monopolarity index, and enables visualization of other mitotic errors such as lagging chromosomes or micronuclei. Additionally, staining for the

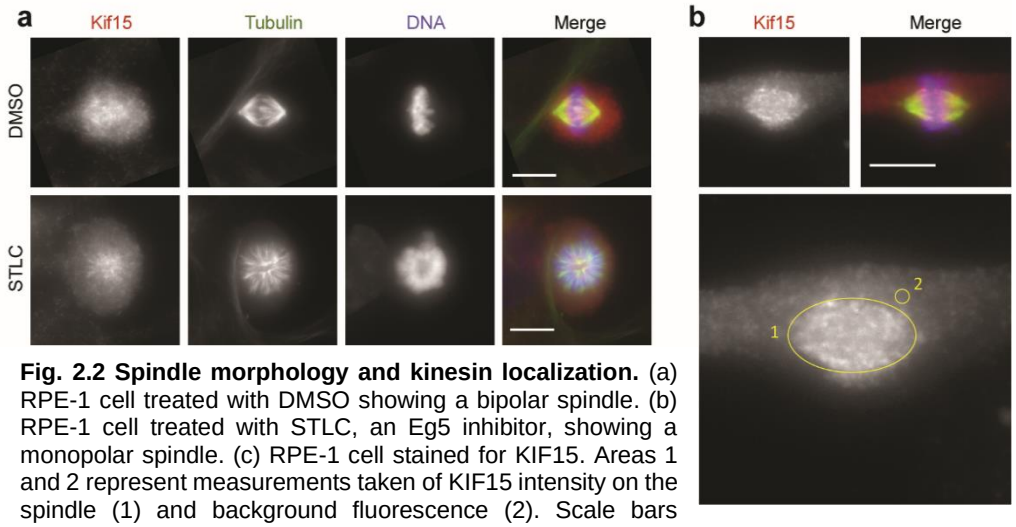

Fig. 2.2 Spindle morphology and kinesin localization. (a) RPE-1 cell treated with DMSO showing a bipolar spindle. (b) RPE-1 cell treated with STLC, an Eg5 inhibitor, showing a monopolar spindle. (c) RPE-1 cell stained for KIF15. Areas 1 and 2 represent measurements taken of KIF15 intensity on the spindle (1) and background fluorescence (2). Scale bars represent 10 µm.

targeted kinesin itself can report changes in kinesin localization. Some kinesin inhibitors may decrease levels of kinesin on the spindle, whereas others might lock it onto the spindle in an immotile state.

In the case of KIF15 inhibitors, it is necessary to test inhibitors in cells that divide in an Eg5 independent manner since KIF15 is not necessary for spindle assembly in the presence of Eg5 (Tanenbaum et al. 2009). We have developed Eg5-independent cell lines called KIRCs (Kinesin-5 Inhibitor Resistant Cells) from both HeLa and RPE-1 parental lines that are cultured in the presence of 10 μM S-trityl-L-cysteine, a well-characterized Eg-5 inhibitor (Debonis et al. 2004; Sturgill et al. 2016). In the absence of Eg5, these cells use KIF15 to drive spindle assembly. Thus, treating KIRCs with KIF15 inhibitors results in an increase in the prevalence of monopolar spindle arrays. KIRCs typically have a baseline monopolarity index (MPI) that is roughly 50% since KIF15 is less efficient than Eg5, but a potent KIF15 inhibitor can increase the MPI to 100%. Treating the parental cell line with the same inhibitor can serve as a readout on inhibitor specificity as well, as cells with functional Eg5 should show little to no change in spindle assembly when KIF15 is inhibited.

1. Seed cells onto acid-washed coverslips. When roughly 70% confluent, place into 6-12 well plates and treat as necessary (with compound of interest or control) for desired time, usually overnight.
2. On the day of the experiment, prepare a humid chamber lined with Parafilm by fixing a sheet of Parafilm to the bottom of a 150 mm dish, and placing a damp paper towel around the side of the dish. The dish should be covered by a lid during all washing and incubation steps to prevent dehydration of coverslips.
3. Remove coverslips from plate with forceps and wash with PBS. If fixing with methanol, place coverslips cell-side up in a 6-12 well plate containing 100% methanol. Incubate at -20 °C for 10 minutes and then place cell-side up on parafilm in a 150 mm dish. If fixing with formaldehyde, place coverslips cell-side up on parafilm in a 150 mm dish and cover with 3% formaldehyde for 10 min at room temperature. Aspirate formaldehyde solution and permeabilize with TBS + 0.5% Triton X-100 for 10 min at room temperature (*see* **Note 9**). The remainder of steps all occur at room temperature unless specified for a certain antibody.

4. Rehydrate coverslips by rinsing 3 times quickly with TBST, then washing 3 x 5 min with TBST.
5. Block coverslips with 2% BSA in TBST for 10 min.
6. Dilute primary antibodies in 2% BSA in TBST to desired concentration. Rinse coverslips 3x and wash 3 x 5 min with TBST. Add 75 µL primary antibody solution to each coverslip and incubate for 1 hr at room temperature.
7. Dilute secondary antibodies 1:2000 in 2% BSA in TBST. Rinse coverslips 3x and wash 3 x 5 min with TBST. Add 75 uL secondary antibody solution to each coverslip and incubate for 45 min at room temperature.
8. Dilute conjugated primary/secondary antibody 1:500 in 2% BSA in TBST. For our experiments, we use a mouse monoclonal anti-α Tubulin antibody (DM1α) conjugated to FITC. Rinse coverslips 3x and wash 3 x 5 min with TBST. Add 75 uL primary/secondary antibody solution to each coverslip and incubate for 30 min at room temperature.
9. Dilute counterstain 1:2000 in 2% BSA in TBST. For our experiments, we use Hoechst 33342. Rinse coverslips 3x and wash 3 x 5 min with TBST. Add 75 uL counterstain solution to each coverslip and incubate for 5 min at room temperature.
10. Prepare glass slides for mounting. Clean with 75% ethanol and place a small drop of mounting solution on slide. For our experiments, we use ProLong Diamond Antifade Mountant and mount two coverslips per slide.
11. Rinse coverslips 3x and wash 3 x 5 min with TBST. Aspirate as much TBST as possible. Pick up coverslips with forceps and blot excess TBST with the edge of a Kimwipe. Gently place cell-side down onto drop of mounting solution on slide. Carefully aspirate excess mountant from edges of coverslip. Let slides cure overnight protected from light before analyzing on microscope.
12. Image coverslips using a fluorescence microscope. To measure the monopolarity index of cells treated with kinesin inhibitor, it is easier and more efficient to view cells under the microscope and categorize mitotic spindles as monopolar or bipolar while viewing, rather than taking images and categorizing cells from the images. View cells using the 60x objective at 488 nm (using the FITC channel) and scan back and forth across the coverslip, making sure to not double count cells, and

categorize the spindles of mitotic cells as “monopolar”, “bipolar”, or “multipolar/other”. Examples of monopolar and bipolar spindles of RPE-1 cells treated with an Eg5 inhibitor can be seen below in **Fig. 2.2**.

13. To measure kinesin localization on the spindle, view cells and select a mitotic cell in metaphase. Using the 60x objective, acquire a z-stack image from the bottom to the top of the cell taking images every 0.2-3 µm and using the three fluorescent channels corresponding to the antibodies used. Images can be opened using a software such as ImageJ and relative amounts of kinesin on the spindle can be quantified by measuring fluorescence intensity part of the spindle and subtracting the background fluorescence intensity from an area adjacent to the spindle, as shown in **Fig. 2.2b**. It is important to use fluorescence from the same number of pixels for the spindle and background regions. This can be accomplished computationally, for example, by multiplying the fluorescence intensity of a smaller background region-of-interest (ROI) with a correction factor that equates the background ROI with that used to measure the fluorescence intensity of the target protein.

2.4.4 Live cell imaging

Live cell imaging is a powerful tool to characterize dynamic cellular processes such as cell division. By following individual dividing cells over the course of multiple hours, various aspects of mitosis can be characterized and quantified, such as metaphase duration, spindle dynamics and oscillations, or failed mitosis. Assessing these characteristics in cells can be instrumental in characterizing on- and off-target effect of kinesin inhibitors and selecting compounds to prioritize when evaluating hits from a screen. For example, we found that treating RPE-1 cells with one of our preliminary KIF15 inhibitors resulted in increased metaphase duration and spindle oscillations during this stall, suggesting off-target effects that we had not observed with our previous immunofluorescence

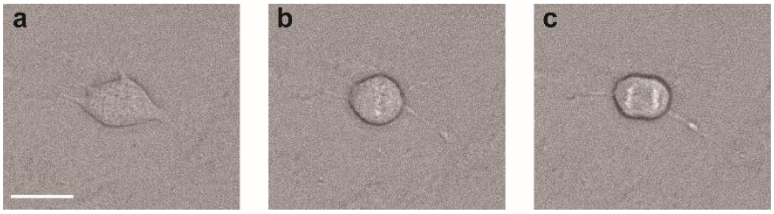

Fig. 2.3 Representative images of distinct mitotic phases of an RPE-1 cell. (a) Interphase cell beginning to round up. (b) Beginning of metaphase directly after nuclear envelope breakdown (c) Anaphase onset. Scale bar represents 10 µm.

assays. This assay can also be adapted to track the localization or expression of fluorescently-tagged or photoactivatable proteins.

1. Seed cells in an appropriate container to perform live cell imaging on your microscope (*see* **Note 10**). Grow cells to 70-80% confluency.
2. On the day of the experiment, replace media on cells with one suitable for long-term imaging, such as Leibovitz's L-15 media with no phenol red, supplemented with 10% FBS and 7 mM HEPES. L-15 is formulated to support cell growth without CO_2 equilibration.
3. Warm microscope to 37°C.
4. Place plate or dish on the microscope and focus using transmitted light with the appropriate objective (*see* **Note 11**). If only imaging mitotic progression, transmitted light or differential interference contrast (DIC) imaging is sufficient.
5. Set up an automated scan protocol. Mark points or areas to be imaged that contain ~70-80% confluent cells. If cells are too sparse or overgrown, the likelihood of multiple cells in the field of view going through mitosis during the imaging time decreases. If imaging multiple wells in a dish, mark points in each well. If you want to collect images from multiple focal planes, mark the top and bottom of the cells in the field of view to set a Z-stack.
6. Set the time lapse and total imaging duration and run the imaging protocol (*see* **Note 12**).
7. Analyze images to quantify mitotic duration. If time-lapse images are not automatically compiled into a video format, they can be concatenated using an image analysis software such as ImageJ. Select cells to analyze that are entirely in the field of view and that are captured entering and exiting mitosis. Measure the time from the cell entering mitosis to the beginning of anaphase when the chromosomes start to separate. **Fig. 2.3** shows representative images of a cell before entering mitosis, just after nuclear envelope breakdown, and at anaphase onset.

2.5 Notes

1. We incorporate X-rhodamine-labeled tubulin, diluted with unlabeled tubulin, into our microtubules to render them fluorescent. Tubulin can be labeled by a variety of dyes, but the labeling stoichiometry of tubulin should be taken into account when determining the optimal ratio of labeled to unlabeled tubulin. For tubulin that is labeled to a stoichiometry of ~0.5, we use a ratio of 1 part labeled tubulin to 9 parts unlabeled tubulin.
2. Microtubules should be polymerized at least one day prior to performing the assay; microtubules will be good for 1-3 days following polymerization, but may increase in length over time through end-to end annealing.
3. ADP-Glo Buffer Mix may be made fresh or stored at -20° C for up to 1 month and thawed immediately before using.
4. We use KIF15-N420 at a final concentration of 100 nM. Protein prep should be tested for specific activity prior to screen as activity may vary between preps and concentration may need to be modulated.
5. We use the Multidrop™ Combi Reagent Dispenser (ThermoFisher Scientific).
6. We use the 2104 Envision Multilabel Plate Reader (PerkinElmer).
7. Oxygen-Scavenging mix should be made fresh and added to FCB right before beginning the assay and will last for 1-2 hr.
8. We use undiluted KIF15-N700 from a protein prep that was 0.4 mg/mL. If concentration is much higher, it should be diluted to ~0.5 mg/mL, or titrated to find an optimal concentration that results in sufficient microtubule binding without generating fields of view that are overcrowded with microtubules.
9. The fixation method should be chosen based on the antibodies being used and the structures being imaged. Alcohol fixation is advantageous for immunofluorescence as it can result in high immunoreactivity paired with low levels of background or non-specific staining, but can alter cellular structures such as microtubules. Aldehyde fixation is better at preserving structures, but can have higher background reactivity and is inefficient at permeabilizing membranes (Hobro and Smith 2017). Additionally, certain primary antibodies work better with one method, thus optimization of fixation method is key.

10. For microscopes that can image through plastic, 6- or 12-well dishes work well for collecting data from multiple test conditions. For instruments that can only image though glass, MatTek glass-bottom dishes can be used, but multiple conditions must be split into individual experiments.
11. We use a 20X objective to retain enough resolution to identify mitotic phases, but increase the number of cells that can be imaged in the field of view.
12. The total imaging time should account for how long it will take for cells to progress from prometaphase through cytokinesis. For example, in our experiments cells are often stalled in metaphase for 4-5 hours; thus, imaging for at least 6 hours total is appropriate. When setting the time lapse, or duration between images, consider how many images must be acquired per time point and how photodamaging the imaging is. We find that imaging every 5 minutes using DIC is often enough to visualize distinct mitotic phases minimizing photodamage.

2.6 Acknowledgements

We would like to thank the Ohi lab that made this work possible, as well as Emma Sturgill, Megan Dumas, and George Xu for doing extensive optimization of these assays. We would also like to acknowledge NIH grant R01 GM086610, pilot project funding from Michigan Drug Discovery, and start-up funds from the University of Michigan.

2.7 References

Akhmanova, A., & Steinmetz, M. O. (2015). Control of microtubule organization and dynamics: two ends in the limelight. Nature Reviews | Molecular Cell Biology, 16(12): 711-716.

Blangy, A., Lane, H. A., d'Hérin, P., Harper, M., Kress, M., & Niggt, E. A. (1995). Phosphorylation by p34cdc2 regulates spindle association of human Eg5, a kinesin-related motor essential for bipolar spindle formation in vivo. Cell, 83(7), 1159-1169.

Debonis, S., Skoufias, D. A., Lebeau, L., Lopez, R., Robin, G., Margolis, R. L., Wade, R. H., Kozielski, F. (2004). In vitro screening for inhibitors of the human mitotic kinesin Eg5 with antimitotic and antitumor activities. Molecular Cancer Therapeutics, 3(9): 1079-1090.

Drummond, D. R. (2011). Regulation of microtubule dynamics by kinesins. Seminars in Cell and Developmental Biology, 22(9): 927-934.

Dumas, M. E., Chen, G.-Y., Kendrick, N. D., Xu, G., Larsen, S. D., Jana, S., Waterson, A. G., Bauer, J. A., Hancock, W., Sulikowski, G. A., Ohi, R. (2019). Dual inhibition of

KIF15 by oxindole and quinazolinedione chemical probes. Bioorganic & Medicinal Chemistry Letters, 29(2): 148–154.

Ferenz, N. P., Gable, A., & Wadsworth, P. (2010). Mitotic functions of kinesin-5. Seminars in Cell and Developmental Biology, 21(3): 255-259.

Hirokawa, N., Pfister, K. K., Yorifuji, H., Wagner, M. C., Brady, S. T., & Bloom, G. S. (1989). Submolecular domains of bovine brain kinesin identified by electron microscopy and monoclonal antibody decoration. Cell, 56(5): 867–878.

Hobro, A. J., & Smith, N. I. (2017). An evaluation of fixation methods: Spatial and compositional cellular changes observed by Raman imaging. Vibrational Spectroscopy, 91: 31–45.

Jordan, M. A., & Wilson, L. (2004). Microtubules as a target for anticancer drugs. Nat. Rev. Cancer, 4(4): 253–265.

Kapoor, T. M., Mayer, T. U., Coughlin, M. L., & Mitchison, T. J. (2000). Probing Spindle Assembly Mechanisms with Monastrol, a Small Molecule Inhibitor of the Mitotic Kinesin, Eg5. The Journal of Cell Biology, 150(5): 975-988.

Lipton, R. B., Apfel, S. C., Dutcher, J. P., Rosenberg, R., Kaplan, J., Berger, A., Einzig, A. I., Wiernik, P., Schaumburg, H. H. (1989). Taxol produces a predominantly sensory neuropathy. Neurology, 39(3): 368–373.

Mayer, T. U., Kapoor, T. M., Haggarty, S. J., King, R. W., Schreiber, S. L., & Mitchison, T. J. (1999). Smart molecule inhibitor of mitotic spindle bipolarity identified in a phenotype-based screen. Science, 286(5441): 971–974.

Rowinsky, E. K. (1997). The development and clinical utility of the taxane class of antimicrotubule chemotherapy agents. Annu. Rev. Med 48(1): 353-374.

Sawin, K. E., & Mitchison, T. J. (1995). Mutations in the kinesin-like protein Eg5 disrupting localization to the mitotic spindle. Proceedings of the National Academy of Sciences, 92(10): 4289-4293.

Sawin, K. E., Leguellect, K., Philippet, M., & Mitchison, T. J. (1992). Mitotic spindle organization by a plus-end-directed microtubule motor. Nature, 359(6395): 540-543.

Sturgill, E. G., Das, D. K., Takizawa, Y., Shin, Y., Collier, S. E., Ohi, M. D., Hwang, W., Lang, M. J., Ohi, R. (2014). Report Kinesin-12 KIF15 Targets Kinetochore Fibers through an Intrinsic Two-Step Mechanism. Current Biology, 24: 2307–2313.

Sturgill, E. G., Norris, S. R., Guo, Y., & Ohi, R. (2016). Kinesin-5 inhibitor resistance is driven by kinesin-12. Journal of Cell Biology, 213(2): 213–227.

Tanenbaum, M. E., Macůrek, L., Janssen, A., Geers, E. F., Alvarez-Fernández, M., & Medema, R. H. (2009). KIF15 Cooperates with Eg5 to Promote Bipolar Spindle Assembly. Current Biology, 19(20): 1703–1711.

Tuxen, M. K., & Hansen, S. W. (1994). Neurotoxicity secondary to antineoplastic drugs. Cancer Treatment Reviews, 20(2): 191–214.

Verhey, K. J., & Hammond, J. W. (2009). Traffic control: regulation of kinesin motors. Nature Reviews Molecular Cell Biology, 10(11): 765-777.

Zhang, J. H., Chung, T. D. Y., & Oldenburg, K. R. (1999). A simple statistical parameter for use in evaluation and validation of high throughput screening assays. Journal of Biomolecular Screening, 4(2): 67–73.

Chapter III
Synergy Between Inhibitors of Two Mitotic Spindle Assembly Motors Undermines an Adaptive Response

April L. Solon[1], Taylor M. Zaniewski[2], Patrick O'Brien[3], Martin Clasby[3], William O. Hancock[4], and Ryoma Ohi[1]

[1]Department of Cell and Developmental Biology, University of Michigan, Ann Arbor, MI; [2]Department of Chemistry, Pennsylvania State University, University Park, PA; [3]Vahlteich Medicinal Chemistry Core, University of Michigan, Ann Arbor, MI; [4]Department of Biomedical Engineering, Pennsylvania State University, University Park, PA

3.1 Abstract

Mitosis is the cellular process that ensures accurate segregation of the cell's genetic material into two daughter cells. It is often deregulated in cancer, and as such drugs that target mitosis-specific proteins represent attractive targets for anticancer therapy. Numerous inhibitors have been developed targeting Eg5, a kinesin essential for bipolar spindle assembly; however, these drugs have been largely ineffective in the clinic, possibly due to the activity of a second kinesin, KIF15, that can suppress the cytotoxic effect of Eg5 inhibitors by driving spindle assembly through an Eg5-independent pathway. We hypothesize that pairing inhibitors of Eg5 and KIF15 will be more cytotoxic than either inhibitor alone. Here, we present the results of a high-throughput screen from which we identified two inhibitors that potently inhibit the motor activity of KIF15 both in vitro and in cells. These inhibitors selectively inhibit KIF15 over other molecular motors, and show different effects on the ability of KIF15 to bind microtubules. Finally, we find that chemical inhibition of KIF15 reduces the ability of cells to acquire resistance to K5Is, highlighting the centrality of KIF15 to K5I resistance and the value of these inhibitors as tools with which to study KIF15 in a physiological context.

3.2 Introduction

Mitosis is the process by which chromosomes are segregated into two daughter cells. The complexity of cytoskeletal dynamics and signaling pathways during mitosis make it challenging to understand its molecular underpinnings and how forces within the spindle are integrated to promote accurate chromosome segregation. For example, although it is clear that a mitotic kinesin, Kif11/Eg5 (Eg5), and cytoplasmic dynein are the primary motors that organize microtubules into the mitotic spindle, other molecular motors can substitute for Eg5 and dynein; simultaneous inhibition of both Eg5 and dynein leads to the formation of a bipolar spindle that can segregate chromosomes, albeit with reduced fidelity (Mitchison et al. 2005). In this case, two additional mitotic kinesins - KIF15 and KifC1/HSET - substitute for Eg5 and dynein, respectively (Tanenbaum et al. 2009; Vanneste et al. 2009; Mountain et al. 1999; Hentrich and Surrey 2010). Moreover, motors and other microtubule-associated proteins (MAPs) link spindle microtubules in ways that are poorly understood, creating a network of interactions that collectively define systems-level properties of the mitotic spindle. These aspects of mitosis prevent conventional approaches such as RNA interference or gene deletion from painting a complete picture of mitotic mechanisms, and underscore the importance of orthogonal approaches, e.g., laser microsurgery(Maiato, Rieder, and Khodjakov 2004) and small molecules (Kapoor et al. 2000), in the study of mitosis. In addition, the complexity of mitosis has made it a challenging process to target in the context of cancer.

The importance of Eg5 during spindle assembly has made it a major target for anti-mitotic drugs. Eg5, a member of the kinesin-5 family, is a homo-tetrameric plus-end-directed motor that participates in spindle assembly by sliding anti-parallel microtubules apart (Kashina et al. 1996; Kapitein et al. 2005). The archetypal Eg5 inhibitor (K5I) monastrol blocks centrosome separation, yielding a preponderance of monopolar spindles (Mayer et al. 1999). Studies with monastrol and other K5Is have uncovered fundamental knowledge of mitosis including the correction of flawed kinetochore-microtubule attachments (Khodjakov et al. 2003; Lampson et al. 2004), the basis of spindle bipolarity maintenance in mammalian cells (Kapoor et al. 2000), and the discovery that KIF15 can substitute for Eg5 during spindle assembly (Tanenbaum et al. 2009; Vanneste et al. 2009). In the realm of cancer therapy, >50 K5Is have been developed and

many of them have been subjected to both pre-clinical studies and clinical trials. Although K5Is induce apoptosis of cultured cells as a result of failed mitoses (Kapoor et al. 2000), K5Is have performed poorly in Phase I and II clinical trials, failing to induce tumor regression (Marzo and Naval 2013). Several hypotheses have been posed to explain this disparity in results, including problems with drug uptake or efflux(Gampa et al. 2020), dosing schedules that were too infrequent to effectively treat the tumors (Komlodi-Pasztor et al. 2011), or the ability of cells to use an alternative spindle assembly pathway that depends on KIF15 (Tanenbaum et al. 2009).

An ability of mammalian cells to switch to KIF15-dependent spindle assembly pathway in the presence of K5Is is supported by several lines of evidence. Tanenbaum *et al* showed that overexpression of the mitotic kinesin KIF15 is sufficient to restore bipolar spindle assembly in Eg5-inhibited or -depleted cells (Tanenbaum et al. 2009). In addition, we and others showed that cells can accumulate genetic changes that allow KIF15 to substitute for Eg5 in spindle assembly when cultured in the presence of K5Is. Known changes that drive resistance to K5Is include 1) Mutation of Eg5 itself (Kasap, Elemento, and Kapoor 2014), 2) Overexpression of KIF15 (Tanenbaum et al. 2009; Sturgill and Ohi 2013), and 3) Mutations in protein factors that allow KIF15 to bind the spindle more efficiently (Raaijmakers et al. 2012; Sturgill et al. 2016). The central role of KIF15 in mediating these resistance pathways suggests that KIF15 is essential for cells to acquire resistance to K5Is. Indeed, removal of *KIF15 via* CRISPR-Cas9 technology completely abrogates K5I resistance in HeLa cells, an effect that can be rescued by overexpression of exogenous *KIF15* (Sturgill et al. 2016). This provides evidence that KIF15 is both sufficient and necessary for spindle assembly in the absence of functional Eg5, which in turn creates a therapeutic window for KIF15 inhibitors as a potential chemotherapeutic when paired with a K5I.

Unfortunately, the field lacks a well-characterized selective chemical inhibitor of KIF15 with which to test this hypothesis. We previously described a pipeline to screen for KIF15 inhibitors, and utilized this platform to identify GW108X, an oxindole that inhibits multiple kinases as well as KIF15 (Dumas et al. 2019). Although GW108X has already proven useful to investigate kinetochore-microtubule organization in the mitotic spindle (Begley et al. 2021), we have continued our efforts to identify new KIF15 inhibitor scaffolds

by high throughput screening. Here, we report two new KIF15 inhibitors, Munesib-1 and Fiftin. We show that these molecules selectively block KIF15 activity *in vitro*, as well as in cells that rely on KIF15 to progress through mitosis. Similar to GW108X, our new inhibitors work *via* an allosteric mechanism rather than by targeting the ATP-binding pocket, but they offer the advantage that they do not suffer from off-target effects that we observe with GW1086, which presumably stem from its anti-kinase activity. Lastly, we show that Fiftin synergizes a K5I to reduce the occurrence of K5I resistance. Collectively, Munesib-1 and Fiftin represent valuable tools for the scientific community with which to assay spindle mechanics in real-time.

3.3 Results

3.3.1 Identification of two potent KIF15 inhibitors via high-throughput screening

To identify new small molecule inhibitors of KIF15, we screened the Maybridge 24K Library of Small Molecule Inhibitors using a pipeline we described previously(Dumas et al. 2019). In brief, this *in vitro* cell-free assay uses a luciferase reaction to couple ATPase activity to luminescence that is quantifiable by a plate-reader (Fig. 31A). We used KIF15-N420, a minimal dimer construct that exhibits microtubule-stimulated ATPase activity (Fig. S3.1A-B), as the ATPase and taxol-stabilized microtubules as the substrate. In this assay, exclusion of ATP provides an idealized upper limit of 100% inhibition that would result from exposure to a perfect inhibitor. For a negative control, we included ATP but no compounds, a condition that yields the baseline ATPase activity of uninhibited motor.

Before screening, we ran several initial tests to determine the robustness of our assay. First, we determined that the final luminescence signal was adequately stable over 60 min (Fig. S3.1C). Next, we tried varying the concentration of motor used in the assay (Fig. S3.1D). Higher concentrations of KIF15 produced higher luminescence and greater separation between the readouts of the positive and negative controls. We thus, we elected to use a high concentration of enzyme (100 nM) for screening. Lastly, we tested our previously identified KIF15 inhibitor, GW108X (Dumas et al. 2019), in this assay (Fig. S3.1D). As expected, addition of 20 μM GW108X to 100 nM KIF15 resulted in a 41% decrease in luminescence compared to the control, validating our assay. Lastly, we

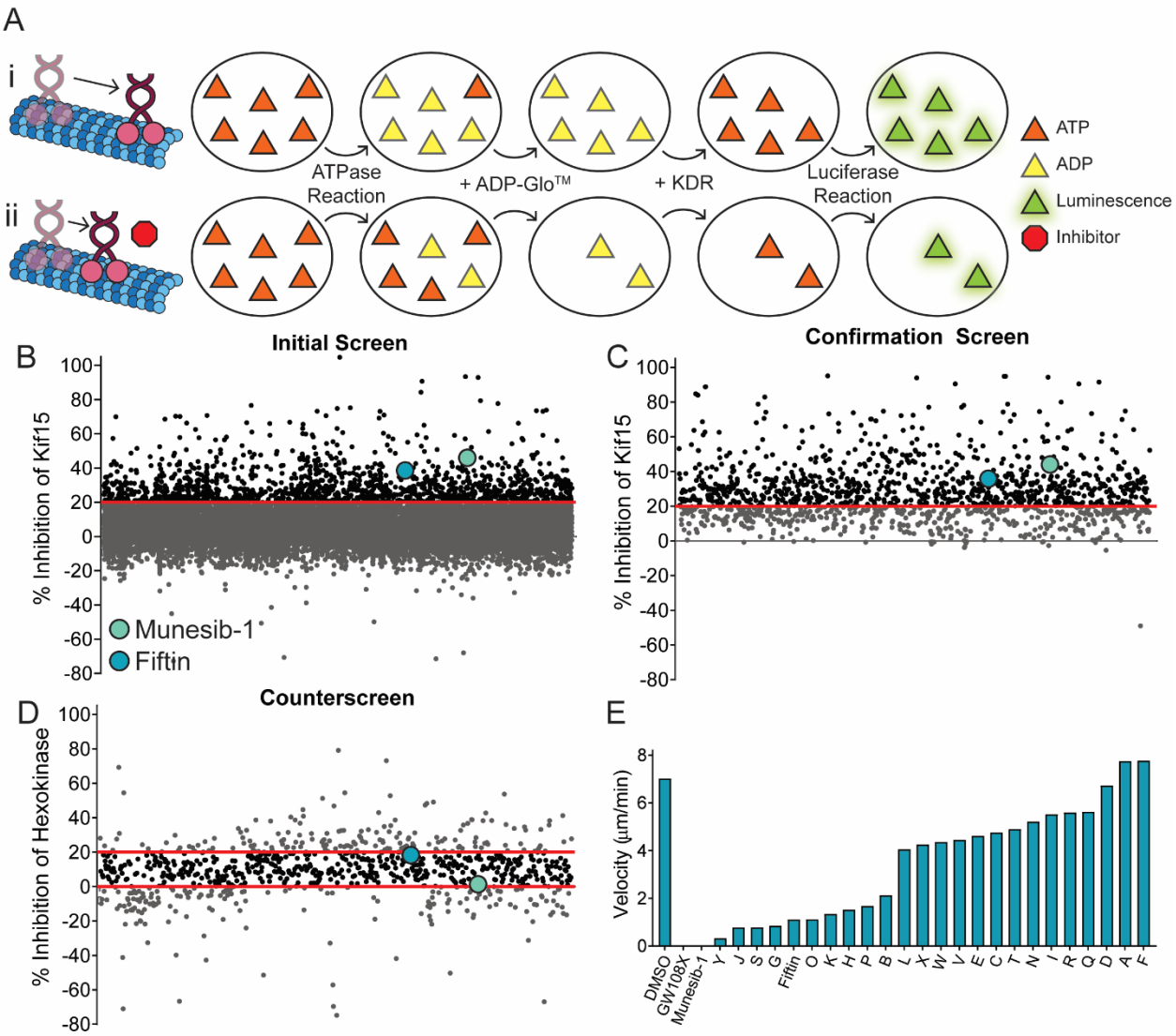

Fig. 3.1: Overview of KIF15 inhibitor screen. A) Schematic of ADP-Glo™ Kinase Assay used for screening. (i) KIF15-N420 is incubated with taxol-stabilized microtubules and 20 µM ATP (orange); ATP is hydrolyzed to ADP (yellow) via KIF15's ATPase activity; unhydrolyzed ATP is depleted by the ADP-Glo™ reagent; ADP is converted back into ATP by the Kinase Detection Reagent (KDR), which is coupled to a luciferase reaction to produce quantifiable luminescence (green). (ii) In the presence of a KIF15 inhibitor, KIF15's ATPase activity is reduced, resulting in less luminscence produced downstream. B) Results of the initial round of screening of 23,552 compounds from the MB 24K library, quantifying the % inhibition of KIF15 compared to the control. Each dot represents one compound. The red bar represents the 20% inhibition threshold above which hits were deemed active against KIF15. The results of Munesib-1 and Fiftin are indicated in green and blue, respectively. C) Results of the confirmation screen of 1,330 compounds. Each dot represents the average % inhibition of three replicates for each compound. As in B, the red bar indicates the threshold above which hits were deemed active. D) Results of the counterscreen of 864 compounds tested against Hexokinase. Compounds that resulted in between 0 to 20% inhibition of Hexokinase were deemed inactive, indicated by the red bars. E) Average microtubule gliding velocity of KIF15-N700 for each of the 25 compounds tested. DMSO was used as a negative control, 30 µM GW108X was used as a positive control. Each compound was tested in singlicate with n=10.

calculated the Z' value of the assay, a statistical measure of effect size used to quantify the robustness of an assay. By running roughly 200 samples each of positive and negative controls, we determined the Z' value to be 0.71 (Fig. S3.1E); as a Z' between

0.5 and 1 is interpreted as an excellent assay, a Z' of 0.71 indicates our assay is suitable for identifying KIF15 inhibitors.

In the first round of screening, we queried 23,552 compounds from the Maybridge 24K library, a collection containing chemically diverse small molecule compounds (Fig. 3.1B). As our positive control GW108X showed roughly 40% inhibition in this assay (Fig. S3.1D), we set the threshold above which to define "hits" at a conservative 20% inhibition of KIF15's ATPase activity, indicated by the red bar in Fig. 3.1B. The average Z' value for the assay plates was 0.82, indicating that our screening data were reliable. 1,330 compounds showed 20% or greater inhibition of KIF15 and were then screened in triplicate in a "confirmation screen" (Fig. 3.1C). Of 1,330 compounds re-tested, 864 confirmed an average percent inhibition of greater or equal to 20%.

Compounds that passed the confirmation screen were then subjected to a "counter-screen", wherein they were tested against a different ATPase using the same ADP-Glo assay (Fig. 3.1D). We selected hexokinase, an enzyme that phosphorylates six-sugar carbons in the first step of glycolysis (Wilson 2003), as a non-specific ATPase due to its highly distinct structure and function compared to KIF15. The purpose of counter-screening was to eliminate any promiscuous compounds that have non-specific activity against ATPases; thus, we set the criteria for this round to include any compounds showing between 0 and 20% inhibition of hexokinase activity. Of 864 compounds tested, 502 exhibited no inhibitory activity against hexokinase.

From this list of 502 compounds that showed specific activity against KIF15, we further eliminated any compounds known for binding promiscuously or containing residues that are reactive or toxic *in vivo*. We then ranked the remaining compounds that passed the counter-screen by their activity against KIF15 and selected the 120 most potent compounds for concentration-response analysis testing. 95 of the 120 compounds tested showed a concentration response relationship suggesting that the molecules were not inhibiting KIF15 through a non-specific mechanism, *e.g.*, enzyme sequestration. 25 of these compounds were then selected for further testing using microtubule gliding assays.

For gliding assays, we used a longer dimeric KIF15 construct, KIF15-N700, which powers robust microtubule movement (Sturgill et al. 2014). Of the 25 compounds tested,

we identified several that robustly inhibit the microtubule gliding ability of KIF15 at 30 μM (Fig. 3.1E). We selected two compounds for further testing and designated them as Munesib-1 and Fiftin (Fig. 3.2A). These two compounds were chosen due to their strong activity and their favorable concentration response curves using the ATPase assay; the IC_{50} values of Munesib-1 and Fiftin were 2 and 26 μM, respectively.

3.3.2 Munesib-1 and Fiftin are potent and specific KIF15 inhibitors

Concentration-response analysis *via* microtubule gliding assays yielded IC_{50} values of 0.4 and 5 μM for Munesib-1 and Fiftin (Fig. 3.2B-D), which are lower than those from the ATPase assay but still reflect an order of magnitude of difference between the two compounds. Since the ATPase assay tests the properties of single motors whereas the microtubule gliding assay tests ensembles of motors, it is not unexpected to obtain different estimated IC_{50} values from these two methods.

Both compounds have a relatively low 'lead like' molecular weight (351 and 312 respectively). This makes them both amenable to Medicinal Chemistry optimization, thus allowing significant headroom for incorporation or modification of functional groups. From a purely structural point of view, compound Munesib-1 is the preferable scaffold for optimization due to its already low ClogP (2.14 vs. 5.68, calculated vis ChemDraw®) and readily modifiable carboxylic ester and 2-thiomethyl substituted pyrimidine. Compound Fiftin is significantly more lipophilic, and thus is more limited in selection of modifications due to the need to, at the very least, maintain lipophilicity at its current level.

To assess the reversibility of Munesib-1 and Fiftin, we performed washout experiments using the microtubule gliding assay. We imaged microtubule-gliding of KIF15-N700 for one minute, then added either DMSO or a KIF15 inhibitor to the flow-cell and imaged gliding for another minute, and then washed out the inhibitor and imaged for one final minute (Fig. 3.2E). Microtubule gliding velocity was unaffected by the addition or removal of DMSO. Gliding was fully abrogated by the addition of Munesib-1 to the flow cell, but gliding velocity was nearly restored to baseline after its removal, indicating that Munesib-1 is a reversible inhibitor. However, gliding was still inhibited by >90% after washout of Fiftin, which suggests that Fiftin is not reversible. From this assay, it is not

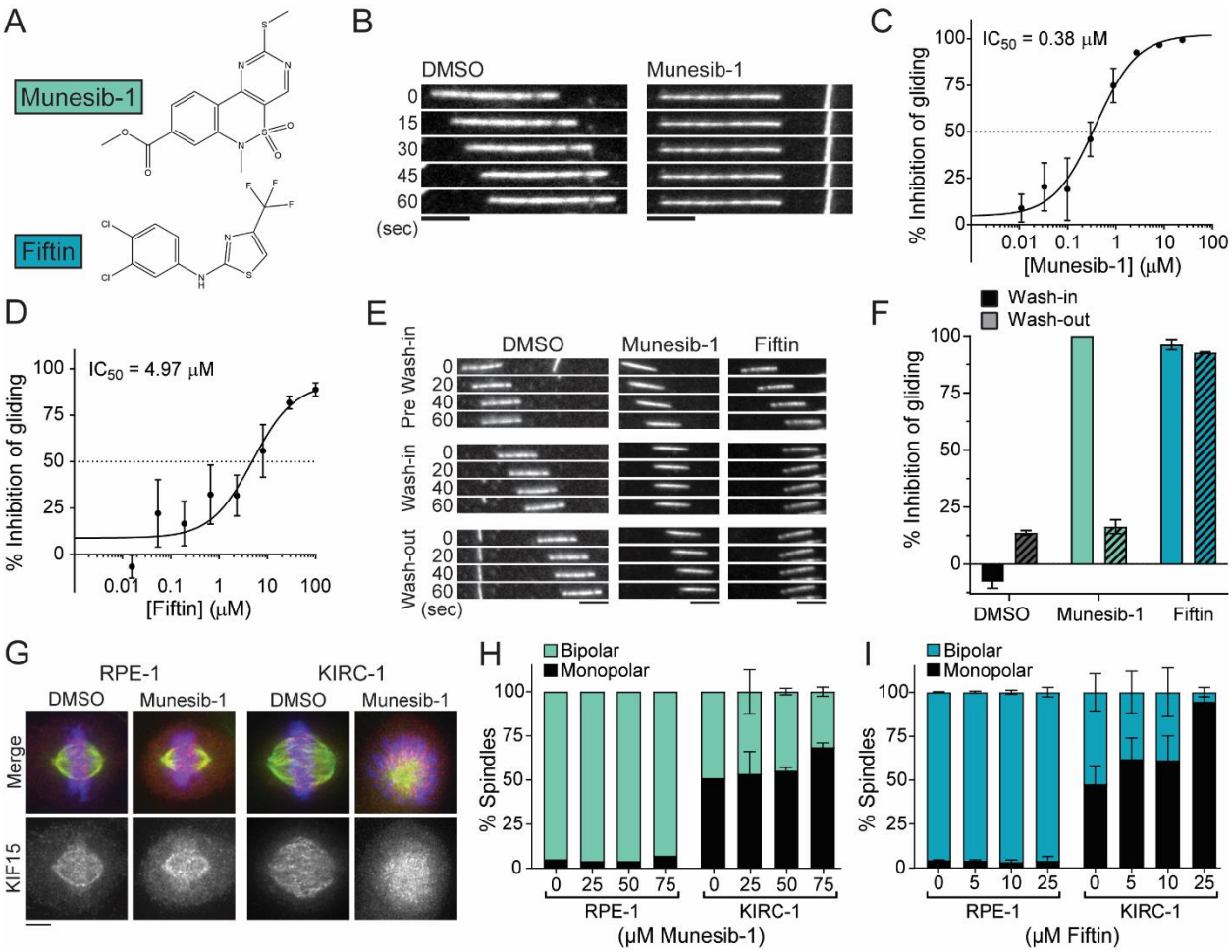

Fig. 3.2: Munesib-1 and Fiftin potently inhibit Kif15 both in vitro and in cells. A) Chemical structures of Munesib-1 (top) and Fiftin (bottom). B) Representative montage of a fluorescently-labeled stabilized microtubule in gliding assay utilizing KIF15-N700, treated with either DMSO (left) or 24 μM Munesib-1 (right). Time of each frame is indicated on the left in seconds. Scale bar, 5 μm. C) Concentration response curve (CRC) generated from microtubule gliding assays with Munesib-1 over a range of 8 concentrations from 10 nM to 30 μM. Each concentration was repeated in triplicate, n ≥ 50 for each replicate. D) CRC generated from gliding assays with Fiftin over a range of 8 concentrations from 10 nM to 100 μM. Each concentration was repeated in triplicate, n ≥ 50 for each replicate. E) Representative montage of a microtubule from a washout assay with the addition of either DMSO (left), 24 μM Munesib-1 (middle), or 100 μM Fiftin (right). Microtubule motility is shown before drug was added (”Pre Wash-in”, top), after drug was added (”Wash-in”, middle), and after drug was washed out (”Wash-out”, bottom). Time elapsed from the first frame of each phase is indicated on the left in seconds. Scale bar, 5 μm. F) Quantification of washout experiment showing % inhibition of gliding velocity of KIF15 after addition of drug (”Wash-in”, solid bars) and after washout of drug (”Wash-out”, hatched bars) for the addition and washout of DMSO, 24 μM Munesib-1, or 100 μM Fiftin. Each compound was tested in duplicate, n ≥ 20 for each replicate. G) Max intensity z-projections of RPE-1 cells (left) and KIRCI-1 cells (right) treated with either DMSO or 50 μM Munesib-1. Cells were stained with antibodies targeting KIF15 (red) and tubulin (green), and were counterstained with Hoecsht-33342 (blue). Scale bar, 5 μm. H) Quantification of pre-anaphase spindles in either monopolar or bipolar states in RPE-1 (left) or KIRC-1 (right) cells treated with increasing concentrations of Munesib-1. Concentration is indicated on the bottom of each bar in μM. Each concentration was tested in triplicate, n = 100 for each replicate. Error bars show SEM. I) Quantification of pre-anaphase spindles in either monopolar or bipolar states in RPE-1 (left) or KIRC-1 (right) cells treated with increasing concentrations of Fiftin. Concentration is indicated on the bottom of each bar in μM. Each concentration was tested in triplicate, n = 100 for each replicate. Error bars show SEM.

possible to determine whether Fiftin actually binds to KIF15 in a chemically irreversible way, or if it dissociates very slowly from its target site on the motor.

We next analyzed the effects of Munesib-1 and Fiftin on spindle assembly in cells by quantifying the number of monopolar spindles in *TP53*$^{-/-}$ RPE-1 and KIRC-1 cells (Sturgill and Ohi 2013) that have been treated with the compounds. KIF15 is non-essential in cells when Eg5 is present, and KIF15 inhibitors should therefore have little to no effect on RPE-1 cells. However, RPE-1-derived KIRC-1 cells are cultured in saturating amounts of a K5I, and depend on KIF15 for their Eg5-independent spindle assembly pathway (Sturgill and Ohi 2013). Thus, inhibition of KIF15 should block spindle assembly in KIRC-1 cells, resulting in an increase in monopolar pre-anaphase structures (Fig. 3.2E). Both compounds had little effect on spindle morphology in RPE-1 cells (Fig. 3.2F-G), but caused KIRC-1 cells to have a concentration-dependent increase in the monopolar index relative to cells treated with DMSO. Notably, treatment with Fiftin produced nearly 100% monopolar spindles at 25 µM (Fig. 3.2G), whereas the effects of Munesib-1 were comparatively modest, even when the compound was present at 75 µM (Fig. 3.2F). This behavior is opposite of the trend we observed *in vitro*, and we hypothesized that Munesib-1 may be less effective in cells due to reduced solubility. Indeed, we noted that Munesib-1 often precipitated in culture media while assessing its effects on cells.

3.3.3 Munesib-2 is more potent in cells due to increased solubility

To increase the solubility of Munesib-1, we made changes to the structure that are predicted to increase solubility, resulting in 6 chemical derivatives that we designated M-201 – M-206 [edit] (Fig. 3.3A). Munesib-1 (purchased from MolPort) was hydrolyzed with Lithium Hydroxide in aqueous DMF to give M-201 in 71% yield. Amide coupling of compound I using HATU/N,N-diisopropylethylamine in DMF gave M-202, M-203, M-204, and I in moderate to good yields. The Boc group of compound I was removed by treatment with TFA in methylene chloride to give M-205. Finally M-201 was reduced via sequential treatment with oxalyl chloride in methylene chloride followed by reduction with Lithium Aluminum Hydride in THF to give compound M-206 .

We first assessed the potency of these chemical derivatives using the microtubule gliding assay, selecting 25 µM as a starting point since the parent compound completely eliminates KIF15-driven microtubule gliding at this concentration. While all compounds

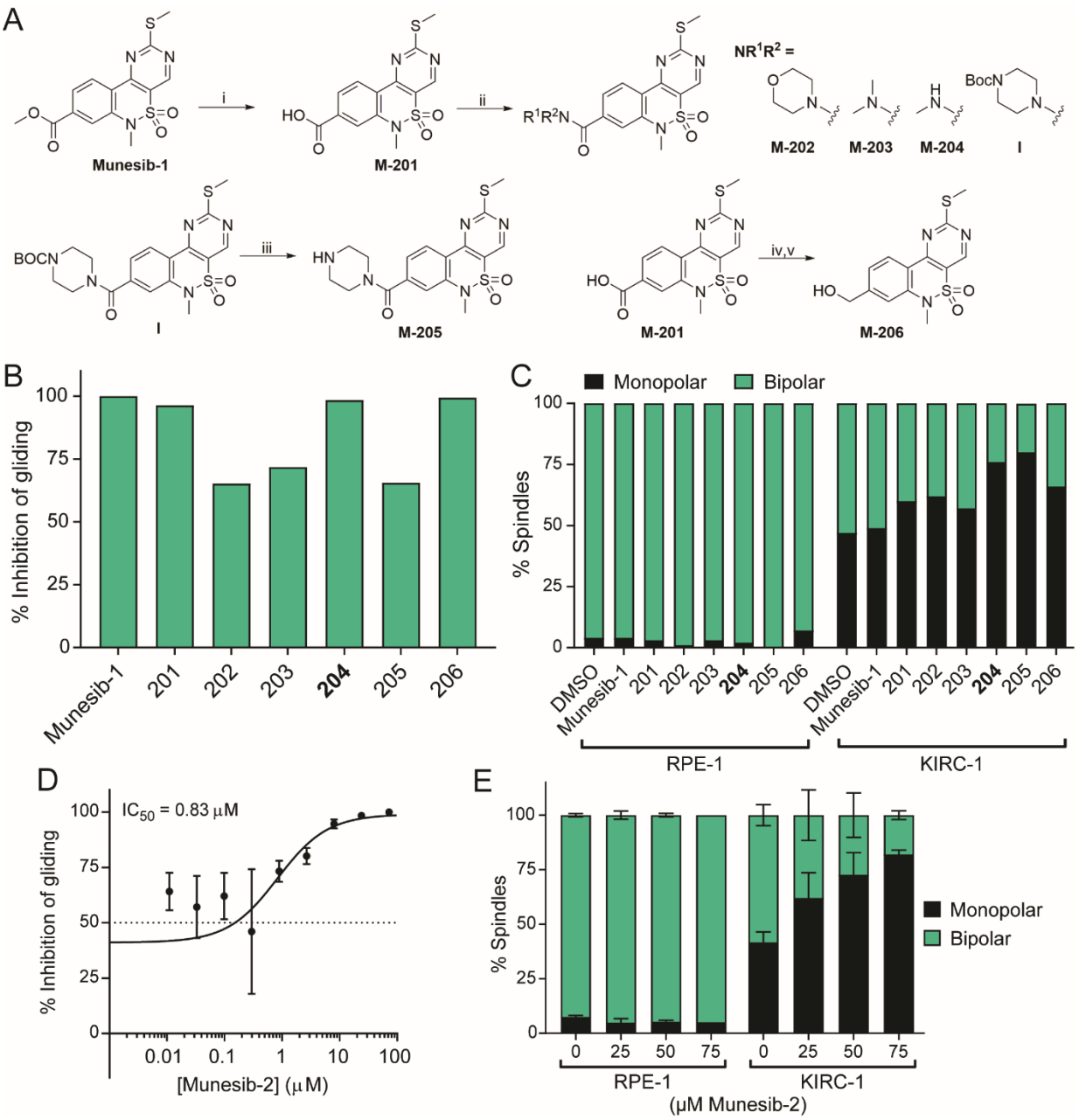

Fig. 3.3: Chemical derivatives of Munesib-1 increase potency against KIF15 in cells. A) Overview of chemical derivatives of Munesib-1 that were synthesized and tested. Reagents and conditions are as follows: i) LiOH, DMF/H2O, 25°C. ii) HATU, DIPEA, R1R2NH, DMF, 60°C. iii) TFA, CH2Cl2, room temperature. iv) Oxalyl chloride, CH2Cl2, room temperature. v) LAH, THF, 0° C, room temperature. B) Quantification of the % inhibition of KIF15 microtubule gliding activity induced by each chemical derivative tested at 25 µm. Each compound was tested in singlicate, n ≥ 50 for each replicate. C) Quantification of pre-anaphase spindles as either monopolar or bipolar in RPE-1 (left) or KIRC-1 (right) cells treated with each chemical derivative, as well as the parent compound. Each compound was tested at 25 µM in duplicate, n = 100 for each replicate. D) CRC generated from microtubule gliding assays with Munesib-2 (M-204) over a range of 9 concentrations from 10 nM to 30 µM. Each concentration was repeated in triplicate, n ≥ 50 for each replicate. E) Quantification of pre-anaphase spindles in either monopolar or bipolar states in RPE-1 (left) or KIRC-1 (right) cells treated with increasing concentrations of Munesib-2. Concentration is indicated on the bottom of each bar in µM. Each concentration was tested in triplicate, n = 100 for each replicate. Error bars show SEM.

displayed greater than 50% inhibition of KIF15 when tested at 25 µM, 3 derivatives (M-

201, M-204, and M-206) blocked KIF15 activity as effectively as Munesib-1 (Fig. 3.3B). We then tested all 6 derivatives in cells, again using all compounds at 25 μM. While none of the compounds produced a change in spindle morphology in RPE-1 cells, we observed that two derivatives (M-204 and M-205) substantially increased the monopolarity index in KIRC-1 cells compared to the parent compound (Fig. 3.3C). We thus selected compound M-204, designated as Munesib-2, for further evaluation since it matched Munesib-1 in the gliding assay and improved upon Munesib-1's effects in cells. Munesib-2 is slightly less potent than the parent compound Munesib-1 *in vitro*, with an IC_{50} of around 0.8 μM compared to Munesib-1's IC_{50} of roughly 0.4 μM. However, Munesib-2 substantially increased efficacy in cells; 75 μM Munesib-2 resulted in more than 80% monopolar spindles in KIRC-1 cells, while an equal concentration of Munesib-1 yielded less than 70% monopolar spindles. Evidently, Munesib-2 has increased potency in cells without losing much efficacy *in vitro*.

3.3.4 Munesib-1 and Fiftin show reduced off-target effects compared to GW108X

After evaluating the potency of Munesib-1 and Fiftin against KIF15, we assessed their specificity. We first tested the compounds against three other motors using the microtubule gliding assay using concentrations of Munesib-1 and Fiftin that completely abrogate KIF15-driven microtubule gliding. We selected HSET and Eg5, two other mitotic kinesins that are structurally distinct from KIF15 despite performing similar functions, and K560, a truncated form of Kinesin-1. While both compounds robustly inhibited KIF15 at the selected concentrations, neither substantially inhibited the microtubule gliding ability of the three other motors, indicating that these compounds are specific for KIF15 (Fig. 3.4A).

We next evaluated the effects of Munesib-1 and Fiftin on mitotic progression in RPE-1 cells by filming the progression of drug-treated cells through mitosis with differential interference contrast microscopy. We performed this analysis because we observed that the KIF15 inhibitor GW108X, a known kinase inhibitor, increased the time needed for cells to enter anaphase following chromosome alignment at the metaphase plate. GW108X-treated RPE-1 cells also exhibited a peculiar spindle oscillation phenotype, in which the spindle rocked back-and-forth prior to anaphase onset (Fig. 3.4B-

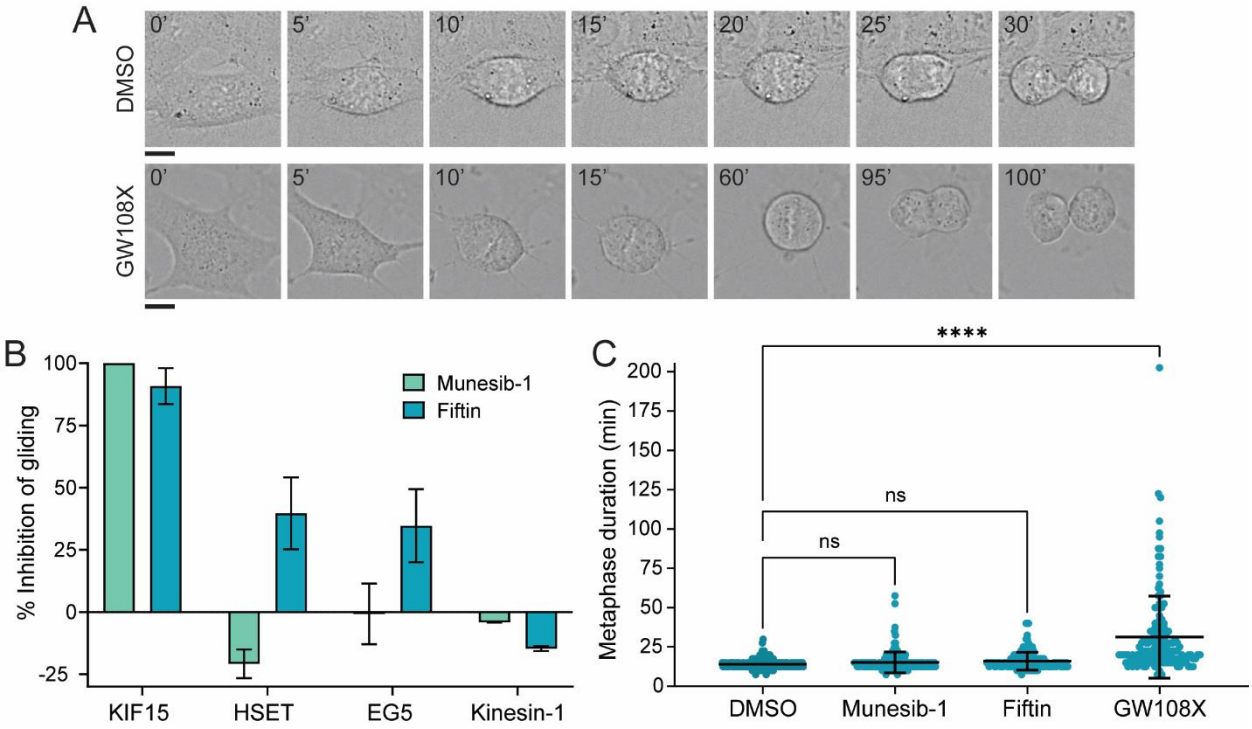

Fig. 3.4: Munesib-1 and Fiftin are selective KIF15 inhibitors. A) Schematic of mitotic progression of RPE-1 cells treated either with DMSO (top) or 25 µM GW108X (bottom). Images were collected via time-lapse microscopy. Time in minutes is indicated relative to the first frame. Scale bar, 5 µm. B) Quantification of % inhibition of microtubule gliding compared to DMSO control, for each of the motors indicated when treated with either 24 µM Munesib-1 or 100 µM Fiftin. Error bars, ±SEM. C) Quantification of metaphase duration for RPE-1 cells treated with the indicated inhibitor (Munesib-1 used at 50 µM, Fiftin and GW108X used at 25 µM). Time was quantified in minutes from metaphase plate formation until anaphase onset. Error bars, ±SEM; ****, $P < 0.0001$; $N \geq 50$ cells for each replicate of triplicate experiments.

C). We speculate that these effects are a result of promiscuous kinase inhibition. We imaged RPE-1 cells treated with saturating doses of Munesib-1 or Fiftin and quantified the time between metaphase plate formation and anaphase onset (Fig. 3.4B). Compared to the significant increase in metaphase duration with GW108X treatment, we observed no significant change in metaphase timing with treatment of either Munesib-1 or Fiftin. Combined with the gliding assay utilizing other motors, these results suggest that Munesib-1 and Fiftin are selective KIF15 inhibitors and improve upon the limited specificity of GW108X.

3.3.5 Fiftin decreases microtubule-binding activity of KIF15

To determine whether Munesib-1 and Fiftin affect the ability of KIF15 to bind to microtubules, we analyzed the effect on microtubule-binding immediately after the addition of each compound during microtubule gliding assays (Fig. 3.5A). Compared to

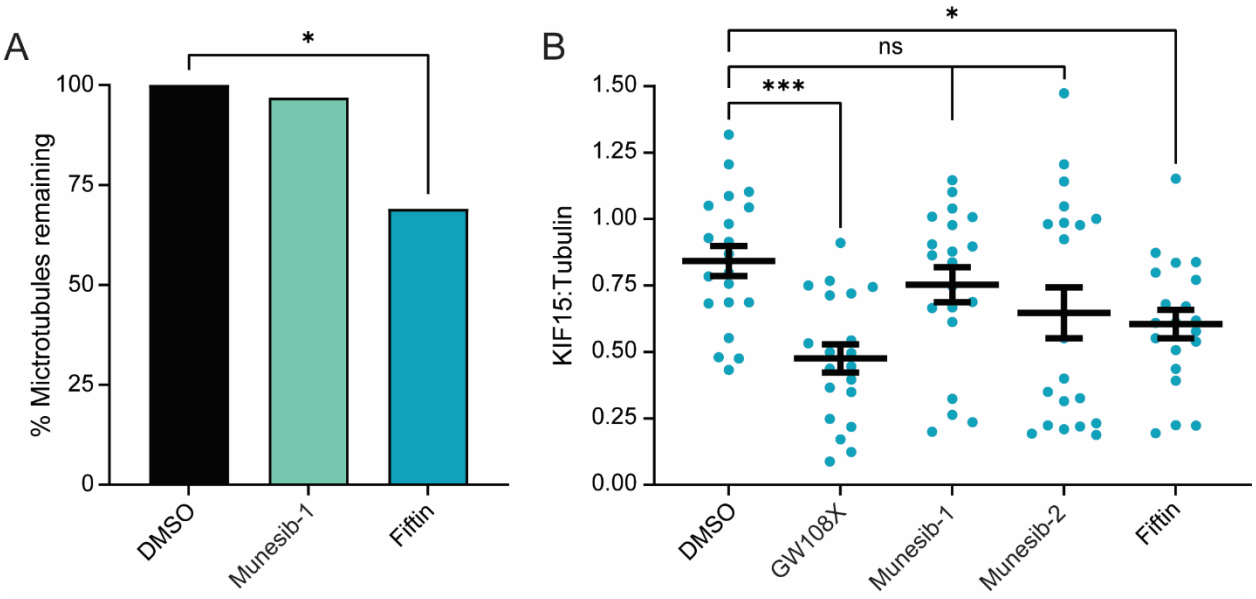

Fig. 3.5: Munesib and Fiftin have distinct mechanisms of inhibition of KIF15. A) Quantification of the % of microtubules that remain bound to the coverslip after 1 minute post-drug addition for either DMSO, 24 µM Munesib or 100 µM Fiftin. Experiment was repeated in duplicate; n ≥ 50 for each replicate; *, P < 0.05. B) Quantification of KIF15 on metaphase spindles in RPE-1 cells treated with either DMSO or the indicated compound (GW108X and Fiftin used at 25 µM, Munesib-1 and -2 used at 50 µM). Each dot represents one measurement. Experiment was repeated in duplicate; n = 10 for each replicate; ns, no significance; *, P < 0.001.

the DMSO control, addition of Fiftin induced a significant reduction in the number of microtubules bound to the coverslip *via* KIF15, whereas Munesib-1 had little effect on binding. We looked at this further in cells by measuring the relative amounts of KIF15 on spindle microtubules in RPE-1 cells in metaphase (Fig. 3.5B). Similar to our *in vitro* results, treatment of cells with a saturating dose of Fiftin significantly reduced the amount of KIF15 on the spindle, while Munesib-1 again had little effect. This effect on spindle binding with Fiftin was similar to the effect seen with the addition of GW108X, which is consistent with its known allosteric inhibition of microtubule binding (Dumas et al. 2019). These results suggest that Fiftin also competes with microtubule binding, whereas it is unclear how Munesib-1 inhibits KIF15 activity. The putative difference in mechanism of inhibition implies that Munesib-1 and Fiftin may have distinct binding sites on the motor domain of KIF15.

3.3.6 Fiftin synergizes with the K5I STLC to prevent the acquisition of drug resistance

Lastly, we analyzed the effect of KIF15 inhibition by Fiftin on the ability of cells to acquire resistance to STLC, a commonly-used K5I. *TP53*$^{-/-}$ RPE-1 cells were cultured for 24 days in either normal DMEM medium or medium containing 10 µM STLC, 10 µM Fiftin,

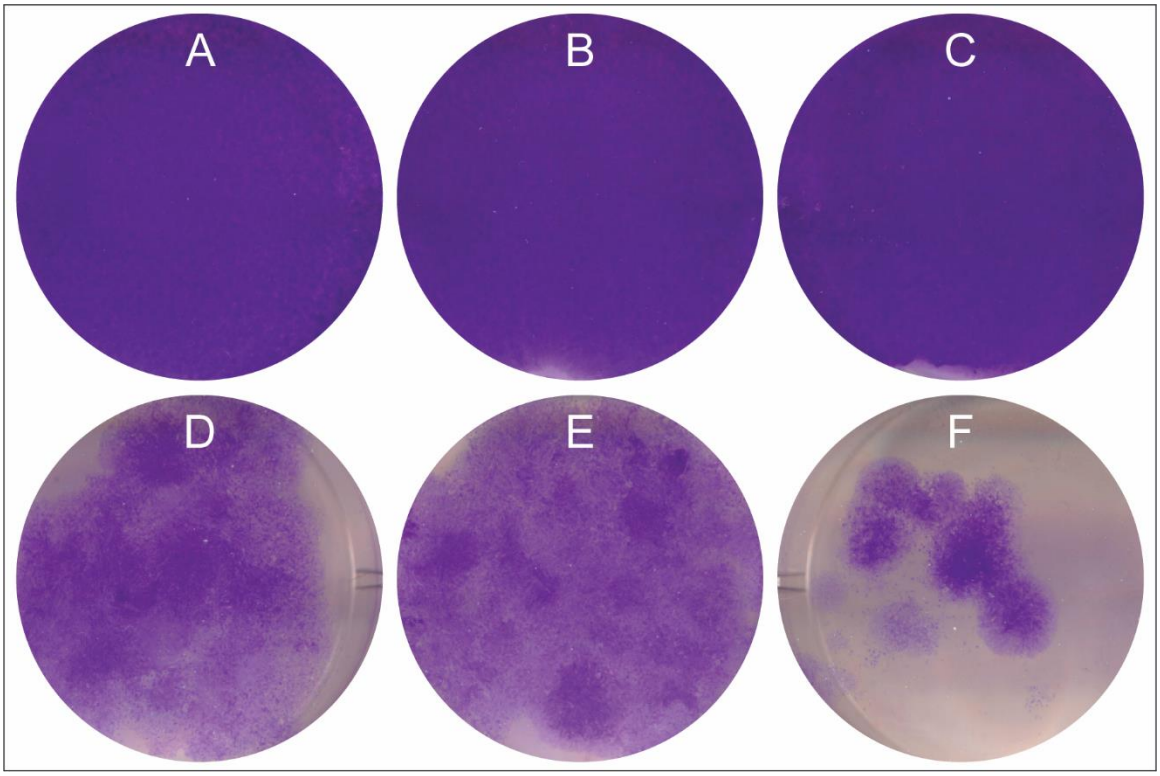

Fig. 3.6: STLC and Fiftin synergize to prevent K5I resistance. RPE-1 cells grown to 80% confluency and treated for 24 days with either A) no compound; B) 5 µM Fiftin; C) 10 µM Fiftin; D) 10 µM STLC; E) 10 µM STLC and 5 µM Fiftin; or F) 10 µM Fiftin and 10 µM Fiftin. Colonies were then stained with crystal violet.

or a combination of STLC and Fiftin together. As expected, Fiftin alone had little effect on cell growth compared to the control. STLC killed the majority of *TP53*$^{-/-}$ RPE-1 cells, but some cells acquired resistance to STLC and grew to form colonies. However, combined treatment of STLC and Fiftin substantially decreased the amount of resistant colonies that arose, showing that inhibition of KIF15 activity sensitizes cells to K5I treatment. This result is consistent with the notion that Fiftin is a small molecule that acts specifically to block KIF15 activity during mitosis.

3.4 Discussion

Chemical inhibitors of kinesins represent valuable tools for the cell biology community and can be used to improve our understanding of the mechanisms governing spindle assembly. Using high throughput screening, we identified two novel KIF15 inhibitor scaffolds that potently inhibit KIF15 activity both *in vitro* and *in vivo*. These compounds add to our growing toolbox of KIF15 inhibitors, which include the oxindole GW108X(Dumas et al. 2019) and KIF15-IN-1(Milic et al. n.d.). Kinesin inhibitors have proven to be valuable research tools that illuminate mitotic mechanisms, and a subset of

these have progressed towards clinical applications. Most recently, the kinesin-8 Kif18A has been postulated to be an Achilles' heel of cancer cells that are chromosomally unstable [REF] and the field awaits Kif18A inhibitors to evaluate the validity of this chemotherapeutic approach in patients. Our motivation to isolate KIF15 inhibitors is that human cells can escape the cytotoxic effects of K5Is by switching to an alternative spindle assembly pathway that depends on KIF15. We show here that, similar to genetic deletion of KIF15, Fiftin reduces the ability of human cells to acquire resistance to the K5I STLC. This result validates the hypothesis that combined treatment of cells with a K5I and KIF15 inhibitor will combat the ability of cells to acquire K5I resistance.

Although Munesib-1 and Fiftin both block KIF15 activity, the two molecules are structurally distinct. and while both molecules selectively target KIF15, Munesib-1 exhibits roughly 10-fold stronger inhibitory action against KIF15 in both in vitro ATPase and microtubule gliding assays. Intriguingly, the opposite trend is observed in cell-based assays, with Fiftin maximally abrogating bipolar spindle formation at much lower concentrations than Munesib-1. We hypothesized that this discrepancy in in vitro and cell-based effects of the two compounds could be due to Munesib-1's poor solubility. Indeed, substantial in vivo potency was gained by chemical modifications that increased solubility, as indicated by the results of Munesib-2. This increase in potency still did not outmatch the high activity of Fiftin in cells, and it remains unclear why Munesib-2 is not as good in cells. Future pharmacokinetics studies may elucidate whether the discrepancy in efficacy stems from differences in drug uptake or efflux between the two compounds. Furthermore, structural knowledge of the specific binding sites of each compound on the KIF15 motor domain will enable efficient optimization of Munesib-1 and Fiftin to further increase potency.

An important quality of Munesib-1 and Fiftin is their selectivity. Both compounds have little to no effect on three other kinesins, despite high sequence homology of kinesin motor domains. Additionally, both inhibitors appear to be more on-target compared to our previously published KIF15 inhibitor, GW108X, which inhibits several kinases in addition to KIF15. The most noticeable phenotype suggestive of GW108X's off-target activity is a significant increase in the time from metaphase plate formation to anaphase onset in RPE-1 cells; as mitotic arrest can increase the chances of cells undergoing apoptosis

(Gascoigne and Taylor 2009), this effect is undesirable for cells that should otherwise be unaffected by KIF15 inhibition. The metaphase duration of cells treated with either Munesib-1 or Fiftin was similar to that of DMSO-treated cells, and thus we conclude that these compounds act primarily on KIF15.

An open question remains regarding the mechanism of action of these inhibitors. Kinesin inhibitors typically work *via* one of two mechanisms, either i) impairing ATPase activity by inhibiting nucleotide binding, hydrolyzation, or release; or ii) impairing microtubule-binding. From analyzing *in vitro* microtubule-binding and spindle localization in cells, Fiftin appears to the inhibit microtubule-binding ability of KIF15. In contrast, Munesib-1 does not appear to have a strong effect on microtubule-binding in either setting. At this point it is difficult to say definitively through which mechanism each inhibitor works, and steady-state kinetics studies will be necessary to truly discern this. This potential difference in mechanism may also contribute to the discrepancy in *in vitro* and cell-based activity between the two compounds.

In summary, Munesib-1 and Fiftin represent powerful tools for the cell biology community with which to continue studying the complex forces involved in mitotic spindle assembly. Indeed, KIF15 inhibitors have already proven effective for studying microtubule organization in the spindle (Begley et al. 2021), and there are numerous potential applications for their use in studying KIF15's force contribution to spindle assembly and maintenance that thus far have relied upon genetic manipulation such as RNA interference. The difference in activity of Munesib-1 and Fiftin can also be harnessed for more specific applications; Munesib-1 is a potent inhibitor of KIF15 *in vitro*, whereas Fiftin robustly inhibits KIF15 activity in cells. The improvement of cell-based activity of Munesib-2 without significant loss of *in vitro* potency also makes it a good tool for use in both settings. Finally, these compounds will enable testing of Eg5 and KIF15 as a combined anticancer drug target. Combining Fiftin with STLC, a K5I, decreases the ability of cells to acquire resistance to STLC, highlighting the centrality of KIF15 to K5I resistance mechanisms. Future experiments with more *in vitro* cancer cell lines and *in vivo* tumor models can further illuminate the efficacy of combining K5Is and KIF15 inhibitors as an anticancer therapy.

3.5 Materials and Methods

3.5.1 ADP-Glo Kinase Reaction

The ADP Glo™ Kinase Assay kit (Promega) was used to quantify the ATPase activity of KIF15-N420 and was adapted for use in high throughput, as previously described (Dumas et al. 2019). 23,552 compounds were screened from the Maybridge 24k library of small molecules. Compounds were screened in 384 well plates; for each plate, one compound was added to each well in columns 3-22, just DMSO was added to wells in columns 1-2 to serve as a negative control (representing the baseline ATPase rate of KIF15), and ATP was excluded from wells in columns 23-24 to serve as a positive control (mimicking 100% inhibition of ATPase activity).

10 µL of Motor & MT solution (100 nM His_6-KIF15-N420 and 1 µM taxol-stabilized microtubules in screening buffer [10 mM K-HEPES (pH 7.7), 100 mM KCl, 1 mM DTT, 10 mM $MgCl_2$, and 5 µM Taxol]) was dispensed into each well of a 384 well-plate using a Multidrop Combi liquid dispenser (Thermo Fisher Scientific). 200 nL of each compound (2 mM stock in DMSO, final concentration of 20 µM) was added to wells in columns 3-22 of each plate using a Biomek FX pintool (Beckman Coulter); no compound was added to wells in columns 1-2 and 23-24. Plates were incubated for 15 min at room temperature (RT). 10 µL ATP solution (20 µM MgATP in screening buffer) was dispensed to wells in columns 1-22; 10 µL screening buffer was dispensed to wells in columns 23-24. Plates were incubated 20 min at RT. 5 µL of ADP-Glo™ reagent was added to every well, plate was incubated 40 min at RT. Finally, 10 µL Kinase Detection Reagent (KDR) was added to every well, and plate was incubated 30 min. Luminescence was quantified using an Envision 2104 Multilabel plate reader (Perkin Elmer). % inhibition of ATPase activity was calculated for each compound by normalizing to the average luminescence of the positive control wells for each plate.

To estimate the robustness of this assay, the Z' score was calculated using the equation $Z' = 1 - \frac{(3\sigma_{pos}+3\sigma_{neg})}{|\mu_{pos}-\mu_{neg}|}$. The average Z' score from the primary screen was 0.82, indicating a robust assay. Concentration response curves (CRCs) were performed as described above but with varying concentrations of compound added.

3.5.2 Protein Expression and Purification

His_6-KIF15-N420, His_6-Eg5, and His_6-EGFP-HSET purifications have been described previously (Dumas et al. 2019; Sturgill et al. 2016, 2014). His_6-KIF15-N700 was expressed in High Five insect cells for 72 hours, after which cells were pelleted and resuspended in lysis buffer (1X PNI [50 mM sodium phosphate, 500 mM NaCl, and 20 mM imidazole], 1% NP-40, 1 mM MgATP, 5 mM β-mercaptoethanol, and protease inhibitors [1 mM PMSF, 1 mM benzamidine, and LPC (10 µg/mL)]) and incubated on ice for 30 minutes followed by sonication. Lysate was clarified by centrifugation for 30 min at 35,000 rpm at 4°C in a Type 45 Ti rotor (Beckman). Cleared lysate was incubated with 2 mL of Ni-NTA (nitrilotriacetic acid) agarose (Qiagen) for 1 hour and washed with 50 mL of wash buffer (1X PNI, 100 µM MgATP, and 5 mM β-mercaptoethanol). Protein was eluted with elution buffer (1X PNI, 100 µM MgATP, 5 mM β-mercaptoethanol, and 200 mM imidazole), and peak fractions were combined and clarified by centrifugation for 5 min at 20,000 rpm at 4°C, after which they were subjected to size exclusion chromatography on a Superdex 200 column equilibrated in gel filtration buffer (10 mM K-Hepes [pH 7.7], 300 mM KCl, 1 mM DTT, and 0.2 mM MgATP). Protein concentration of fractions after gel filtration was estimated using a Bradford assay and purity of fractions was assessed by SDS-PAGE, after which peak fractions were combined and frozen with 10% sucrose.

3.5.3 Steady state ATPase assay

KIF15-N420 ATPase rates were measured by quantifying the rate of NADH conversion in an enzyme-coupled reaction, as described by Huang et al. (CITE). The reaction contained BRB80 with 50 nM KIF15-N420 dimers, 2 mM phosphoenolpyruvate (Alfa Aesar, B20358), 1 mM MgCl2 (Quality Biological, 340-034-721), 0.2 mg/ml casein (Sigma, C-7078), 10 mM Taxol (Sigma, T7191), 0.25 mM NADH (EMD, 48915), and 1.5/100 volume of pyruvate kinase/lactate dehydrogenase (Sigma, P-0294). In the ATP-dependent assay, ATP concentration was varied and microtubule concentration held at 3 µM. In the Mt-dependent assay, microtubule concentration was varied and ATP concentration held at 2 mM. In each assay, 30 uM of the drug or equal volume of DMSO for the control was included. Absorbance of NADH at 340 nm over time was measured on a Molecular Devices FlexStation 3 Multimode Microplate Reader, converted to an

ATPase rate, and divided by the active motor concentration to give the total hydrolysis cycle rate at 25 °C.

The same enzyme coupled reaction described for the ATPase assay was used to evaluate the IC50 for the drugs. This assay contained 2 mM ATP and 5 μM microtubules across all drug concentrations.

3.5.4 Microtubule gliding assays

Microtubule gliding assays were performed as previously described (Dumas et al. 2019). Images were captured using a Nikon Elements controlled Eclipse 90i (Nikon) with a 100X 1.4 NA (Nikon) objective and a Cool Snap HQ2 CCD camera (Roper). Time lapse image sequences spanned 1 min with acquisitions captured every 5 seconds. ImageJ was used for image analysis, and gliding velocity was quantified by measuring the distance a microtubule travelled in 1 min. For each condition of each assay, image sequences were acquired from three locations on the slide and velocities were calculated from ≥15 in each location for a total of n ≥ 50 from each slide.

For washout assays, image sequences were acquired for roughly 1 min pre-drug addition, 1 min post-drug addition, and 3 min post-drug washout for a total of 5 min captured. Gliding velocity for each time segment was quantified by measuring the distance a microtubule travelled over 1 min during each segment.

For analysis of microtubule binding, image sequences were captured before and after the addition of drug. The number of microtubules bound to the coverslip was quantified immediately before drug addition and after 1 min of drug incubation to calculate the % of microtubules that remained bound after drug addition.

3.5.5 Cell culture, immunofluorescence assays, and image analysis

TP53$^{-/-}$ RPE-1 cells were cultured in DMEM containing 10% fetal bovine serum (FBS), penicillin and streptomycin. KIRC-1 cells were cultured in the same medium with the addition of 10 μM STLC. For immunofluorescence assays, cells were grown on glass coverslips in 6-well dishes and then treated overnight with the desired drug concentrations added to their normal medium. Coverslips were rinsed with 1X PBS and fixed in 100% methanol at -20°C for 10 min, and then stained with the following primary antibodies: rabbit anti-KIF15 (Sturgill and Ohi 2013) at 1:2000 for 1 hour, and FITC-

conjugated mouse anti-α-tubulin (DM1α, Sigma-Aldrich) at 1:500 for 30 min. Alexa-594-conjugated anti-rabbit secondary antibodies were used at 1:2000 for 45 min. All antibodies were incubated at RT. DNA was counterstained with 5 µg/mL Hoechst 33342 and coverslips were mounted in Prolong Diamond (Thermo Fisher Scientific).

Images were acquired using a 60X 1.4 NA objective (Olympus) on a DeltaVision Elite imaging system (GE Healthcare) equipped with a Cool SnapHQ2 charge-coupled device (CCD) camera (Roper). Optical sections were collected at 200 nM intervals and processed using the ratio deconvolution in SoftWorx (GE Healthcare). Further image processing and analysis was done in ImageJ. Acquisition parameters were kept constant across cell lines and conditions.

To quantify levels of KIF15 and tubulin on the mitotic spindle, an ROI was drawn around the spindle to measure the integrated fluorescence of a single image frame for both the KIF15 and tubulin channels. A smaller oval ROI was drawn outside of the spindle to measure background fluorescence on the KIF15 and tubulin channels. Background intensity corrected for ROI size was subtracted from the spindle intensity of each channel, and corrected intensities were used to calculate the KIF15:tubulin ratio.

3.5.6 Live cell imaging and analysis

TP53$^{-/-}$ RPE-1 cells were plated in MatTek dishes (Thermo Fisher Scientific) and grown to ~70% confluency. Desired compounds were diluted in Leibovitz's L-15 medium (Invitrogen) supplemented with 10% FBS and 7 mM HEPES and applied to cells. Time lapse image sequences were captured using a 20X objective (Olympus) on the DeltaVision Elite imaging system using transmitted light microscopy. Optical sections were collected at 1.5 µm intervals every 2.5 min for 2-6 hours.

Image sequences were analysed in ImageJ to measure the time from metaphase plate formation to anaphase onset. Metaphase duration was quantified from 50 cells for each condition.

STLC selection

TP53$^{-/-}$ RPE-1 cells were plated in 6-well dishes and grown to ~80% confluency. Cells were then treated with the desired compounds added to DMEM medium supplemented with 10% FBS, penicillin and streptomycin. Media were changed every 2-

3 days for 24 days. At the endpoint, cells were rinsed with 1X PBS, fixed in 100% methanol at -20°C for 10 min, and stained with 0.1% crystal violet (Sigma Aldrich) in 25% methanol for 15 min at RT. Excess dye was removed by gentle washing with DI-H_2O. Images of dishes were acquired with a CanoScan 8800F (Cannon).

3.6 Compound synthesis methods

General techniques: All reactions requiring anhydrous conditions were conducted in flame dried glass apparatus under an atmosphere of argon. Preparative chromatographic separations were performed on silica gel (35-75 μm); reactions were followed by TLC analysis using silica plates with fluorescent indicator (254 nm) and visualized with a UV lamp or phosphomolybdic acid. All commercially available reagents were purchased from TCI or Aldrich and used as received unless stated otherwise. Optical rotations were measured with a polarimeter using a 1 mL capacity cell with 1 dm path length. 1H and 13C NMR spectra were recorded in Fourier transform mode at the field strength specified on either a 300 or 400 spectrometer. Spectra were obtained on CDCl3 or DMSO-d6 solutions in 5 mm diameter tubes, and chemical shifts in ppm are quoted relative to the residual signal of chloroform (δH 7.26 ppm). Multiplicities in the 1H NMR spectra are described as: s = singlet, d = doublet, t = triplet, q = quartet, m = multiplet, br = broad; coupling constants are reported in Hz. Low (MS) and high (HRMS) resolution mass spectra are reported with ion mass/charge (m/z) ratios as values in atomic mass units.

3.6.1 Synthesis of M-201

Methyl 6-methyl-2-methylsulfanyl-5,5-dioxopyrimido[5,4-c][2,1]benzothiazine-8-carboxylate 1 (Munesib-1) (100 mg, 0.28 mmol) was suspended in 4:1 DMF/H2O (10 mL) followed by the addition of LiOH (34 mg, 1.4 mmol) in one portion. Dissolution eventually occurred and the solution was stirred at room temperature for overnight. The solution was diluted with 10 mL of H2O and made acetic (pH=1) with 2M HCl. The precipitate was collected by filtration and washed with 2 portions of H2O. The solid was then suspended in acetonitrile and filtered (2X). The filter cake was triturated with hexane and concentrated in vacuo to afford 68 mg (71%) of M-201 (6-Methyl-2-(methylthio)-6H-benzo[c]pyrimido[4,5-e][1,2]thiazine-8-carboxylic acid 5,5-dioxide) as a beige solid.

HPLC: >98%, Rt=6.23 min.; ES-MS m/z 338.03 [M+H]+; HNMR (DMSO-d6, 400 MHz) 9.16 (s, 1H), 8.53 (d, J=8 Hz, 1H), 7.95-7.86 (m, 2H), 3.15 (s, 3H), 2.68 (s, 3H) ppm.

3.6.2 Synthesis of M-202

A mixture of M-201 (25 mg, 0.074 mmol) and HATU (56 mg, 0.15 mmol) was treated with DMF (3 mL) followed by the addition of diisopropylethylamine (19 mg, 0.15 mmol). The solution was stirred at room temperature for 20 minutes at which time morpholine (14 mg, 0.16 mmol) was added. The solution was then stirred at 60o C for 2 hours and evaluated by TLC (EtOAc): new product. The solution was stirred at 60o C for an additional 45 minutes, then cooled to room temperature and diluted with 10 mL H2O and 25 mL of EtOAc. The organic phase was separated, washed with brine, dried (Na2SO4), and concentrated to an orange liquid. The liquid was taken up in DCM and passed through a pad of silica gel eluting with ethyl acetate. Fractions containing the new product were combined and concentrated to afford M-202 ((6-Methyl-2-(methylthio)-5,5-dioxido-6H-benzo[c]pyrimido[4,5-e][1,2]thiazin-8-yl)(morpholino)methanone) as a yellow solid. Yield: 19 mg, 63%; HPLC: >95%, Rt=6.06 min; HNMR (CDCl3, 400 MHz) 9.0 (d, J=0.6Hz, 1H), 8.67 (d, J=7.8 Hz, 1H), 7.39-7.28 (m, 2H), 3.82 (s, 4H), 3.66 (s, 2H), 3.53 (d, J=0.7 Hz, 3H), 3.47 (s, 2H), 2.70 (d, J=0.7 Hz, 3H) ppm; ES-MS m/z 407.08 [M+H]+

3.6.3 Synthesis of M-203

A mixture of M-201 (30 mg, 0.089 mmol) and HATU (68 mg, 0.18 mmol) was treated with DMF (3 mL) followed by the addition of diisopropylethylamine (34 mg, 0.26 mmol). The solution was stirred at room temperature for 20 minutes at which time dimethylamine hydrochloride (46 mg, 0.56 mmol) was added. The solution was then stirred at 60o C for 2 hours and evaluated by TLC (EtOAc): new product. The solution was stirred at 60o C for an additional 45 minutes, then cooled to room temperature and diluted with 10 mL H2O and 25 mL of EtOAc. The organic phase was separated, washed with brine, dried (Na2SO4), and concentrated to an orange liquid. The liquid was taken up in DCM and passed through a pad of silica gel eluting with ethyl acetate. Fractions containing the new product were combined and concentrated to a yield M-203 (N,N-6-trimethyl-2-(methylthio)- 6H-benzo[c]pyrimido[4,5-e][1,2]thiazin-8-carboxamide 5,5-dioxide) as a beige solid. The product was dried under high vacuum for 2 hours. Yield: 25

mg, 77%; HNMR (CDCl3, 400 MHz): □ 9.0 (s, 1H), 8.66 (dd, J=7.9, 0.6Hz, 1H), 7.37 (dd, J=9.3, 1.2 Hz, 2H), 3.53 (s, 3H), 3.16 (s, 3H), 3.02 (s, 3H), 2.7 (s, 3H) ppm; HPLC: 95%, Rt=6.095 min.; ES-MS m/z 365.07 [M+H]+

3.6.4 Synthesis of M-204

A mixture of M-201 (30 mg, 0.089 mmol) and HATU (68 mg, 0.18 mmol) was treated with DMF (3 mL) followed by the addition of diisopropylethylamine (34 mg, 0.26 mmol). The solution was stirred at room temperature for 20 minutes at which time methylamine hydrochloride (38 mg, 0.56 mmol) was added. The solution was then stirred at 60o C for 2 hours and evaluated by TLC (EtOAc): new product. The solution was stirred at 60o C for an additional 45 minutes, then cooled to room temperature and diluted with 10 mL H2O and 25 mL of EtOAc. The organic phase was separated, washed with brine, dried (Na2SO4), and concentrated to an orange liquid. The liquid was taken up in DCM and passed through a pad of silica gel eluting with ethyl acetate. Fractions containing the new product were combined and concentrated to a yield M-204 (N- 6-dimethyl-2-(methylthio)-6H-benzo[c]pyrimido[4,5-e][1,2]thiazine-8-carboxamide 5,5-dioxide) as a yellow solid. The product was dried under high vacuum for 2 hours. Yield: 13 mg, 42%; HNMR (DMSO-d6, 400 MHz): □ 9.20 (s, 1H), 8.78 (d, J=4.8 Hz, 1H), 8.61 (d, J=8.3 Hz, 1H), 7.91 (d, J=1.5Hz, 1H), 7.86 (dd, J=8.2, 1.6 Hz, 1H), 3.49 (s, 3H), 2.83 (d, J=4.5 Hz, 3H), 2.69 (s, 3H) ppm; HPLC: 90%, Rt=5.9936 min.; ES-MS m/z 351.05 [M+H]+

3.6.5 Synthesis of compound I

A mixture of M-201 (32 mg, 0.095 mmol) and HATU (72 mg, 0.19 mmol) was treated with DMF (3.5 mL) followed by the addition of diisopropylethylamine (25 mg, 0.19 mmol). The solution was stirred at room temperature for 20 minutes at which time BOC-piperazine (39 mg, 0.21 mmol) was added. The solution was then stirred at 60o C for 2 hours and evaluated by TLC (EtOAc): new product. The solution was stirred at 60o C for an additional 45 minutes, then cooled to room temperature and diluted with 10 mL H2O and 25 mL of EtOAc. The organic phase was separated, washed with brine, dried (Na2SO4), and concentrated to a yellow liquid. The liquid was taken up in DCM and passed through a pad of silica gel eluting with ethyl acetate. Fractions containing the new product were combined and concentrated to afford compound I (tert-butyl 4-(6-methyl-2-

(methylthio)-5,5-dioxido-6H-benzo[c]pyrimido[4,5-e][1,2]thiazine-8-carbonyl)piperazine-1-carboxylate) (43 mg, 90%) as a yellow solid. HPLC: 95%, Rt=7.23 min.

3.6.6 Synthesis of M-205

The BOC-protected piperazine derivative I (29.5 mg, 0.058 mmol) was taken up in 4 mL of DCM followed by the dropwise addition of TFA (0.4 mL). The solution was stirred at room temperature for overnight, then diluted with 30 mL of DCM and washed with 12 mL of 10% sodium carbonate, brine, and dried over Na2SO4. The solvent was concentrated in vacuo affording M-205 ((6-Methyl-2-(methylthio)-5,5-dioxido-6H-benzo[c]pyrimido[4,5-e][1,2]thiazin-8-yl)(piperazin-1-yl)methanone) (23 mg, 97%) as a yellow solid. HPLC: 95%, Rt=4.94 min.; HNMR (CDCl3, 400 MHz) □ 9.0 (s, 1H), 8.66 (d, J=8.3Hz, 1H), 7.34 (td, J=4.2, 1.5Hz, 2H), 3.80 (s, 2H), 3.53 (s, 3H), 3.41 (s, 2H), 2.99 (s, 2H), 2.84 (s, 2H), 2.70 (s, 3H), 1.25 (s, 1H) ppm ; ES-MS m/z 406.09 [M+H]+ .

3.6.7 Synthesis of M-206

M-201 (30 mg, 0.089 mmol) was suspended in DCM (5 mL) followed by the addition of oxalyl chloride (41 mg, 0.32 mmol) and one drop of DMF. The mixture became a solution after stirring at room temperature for 30 minutes. The solution was stirred for an additional 30 minutes at which time it was concentrated in vacuo. The solid obtained (32 mg, 100%) was used in the next step without further purification. The crude acid chloride (32 mg, 0.090 mmol) was taken up in 4 mL of THF and cooled in an ice bath to approximately 0o C. To the solution was added in several portions LAH (10 mg, 0.27 mmol). The mixture gradually warmed to room temperature and was quenched with sat. aq. NaHPO4. The mixture was diluted with ethyl acetate and filtered through celite. The filtrate was washed with brine, dried (MgSO4), and concentrated to a solid. The crude product was passed through a pad of silica gel eluting with 9:1 DCM/EtOAc. Fractions containing the product were combined and concentrated to give M-206 (8-(hydroxymethyl)-6-methyl-2-(methylthio)-6H-benzo[c]pyrimido[4,5-e][1,2]thiazine 5,5-dioxide) as a yellow solid (9 mg, 30%). HNMR (CDCl3, 400 MHz): □ 8.97 (s, 1H), 8.59 (d, J=8.1Hz, 1H), 7.39-7.29 (m, 2H), 4.87 (d, J=5.2Hz, 2H), 3.52, s, 3H), 2.70 (s, 3H), 1.95 (t, J=5.9Hz, 1H) ppm ; HPLC: Rt=5.96 min., 99%; ES-MS m/z 324.047 [M+H]+

3.7 Acknowledgements

We would like to thank the Ohi lab that made this work possible, as well as Emma Sturgill, Megan Dumas, and George Xu for doing extensive optimization of these assays. We thank Steve Vander-Roest and Dr. Andrew Alt from the Center for Chemical Genomics, Dr. Peter Toogood and Dr. Pil Lee from Michigan Drug Discovery, and Dr. Martin Clasby and Dr. Patrick O'Brien from the Vahlteich Medicinal Chemistry Core for all of their invaluable effort, expertise, and advice on screening methods and medicinal chemistry. The research reported in this chapter was supported by NIH grant R01 GM086610, pilot project funding from Michigan Drug Discovery, and start-up funds from the University of Michigan.

3.8 References

Begley, M. A., Solon, A. L., Davis, E. M., Sherrill, M. G., Ohi, R., & Elting, M. W. (2021). K-fiber bundles in the mitotic spindle are mechanically reinforced by KIF15. Molecular Biology of the Cell, 32(22), br11. https://doi.org/10.1091/mbc.E20-06-0426

Dumas, M. E., Chen, G.-Y., Kendrick, N. D., Xu, G., Larsen, S. D., Jana, S., … Ohi, R. (2019). Dual inhibition of KIF15 by oxindole and quinazolinedione chemical probes. Bioorganic & Medicinal Chemistry Letters, 29(2), 148–154. https://doi.org/10.1016/j.bmcl.2018.12.008

Gampa, G., Kenchappa, R. S., Mohammad, A. S., Parrish, K. E., Kim, M., Crish, J. F., … Elmquist, W. F. (2020). Enhancing Brain Retention of a KIF11 Inhibitor Significantly Improves its Efficacy in a Mouse Model of Glioblastoma. Scientific Reports, 10(1), 1–13. https://doi.org/10.1038/s41598-020-63494-7

Gascoigne, K. E., & Taylor, S. S. (2009). How do anti-mitotic drugs kill cancer cells? Journal of Cell Science, 122(15), 2579–2585. https://doi.org/10.1242/jcs.039719

Hentrich, C., & Surrey, T. (2010). Microtubule organization by the antagonistic mitotic motors kinesin-5 and kinesin-14. Journal of Cell Biology, 189(3), 465–480. https://doi.org/10.1083/jcb.200910125

Kapitein, L. C., Peterman, E. J. G., Kwok, B. H., Kim, J. H., Kapoor, T. M., & Schmidt, C. F. (2005). The bipolar mitotic kinesin Eg5 moves on both microtubules that it crosslinks. Nature, 435(7038), 114–118. https://doi.org/10.1038/nature03503

Kapoor, T. M., Mayer, T. U., Coughlin, M. L., & Mitchison, T. J. (2000). Probing Spindle Assembly Mechanisms with Monastrol, a Small Molecule Inhibitor of the Mitotic Kinesin, Eg5 7. The Journal of Cell Biology (Vol. 150). Retrieved from http://www.jcb.org

Kasap, C., Elemento, O., & Kapoor, T. M. (2014). DrugTargetSeqR: A genomics- and CRISPR-Cas9-based method to analyze drug targets. Nature Chemical Biology, 10(8), 626–628. https://doi.org/10.1038/nchembio.1551

Kashina, A. S., Baskin, R. J., Cole, D. G., Wedaman, K. P., Saxton, W. M., & Scholey, J. M. (1996). A bipolar kinesin. Nature, 379(6562), 270–272. https://doi.org/10.1038/379270a0

Khodjakov, A., Copenagle, L., Gordon, M. B., Compton, D. A., & Kapoor, T. M. (2003). Minus-end capture of preformed kinetochore fibers contributes to spindle morphogenesis. Journal of Cell Biology, 160(5), 671–683. https://doi.org/10.1083/jcb.200208143

Komlodi-Pasztor, E., Sackett, D. L., Wilkerson, J., & Fojo, T. (2011). Mitosis is not a key target of microtubule agents in patient tumors. Nature Reviews Clinical Oncology, 8, 244–250.

Lampson, M. A., Renduchitala, K., Khodjakov, A., & Kapoor, T. M. (2004). Correcting improper chromosomes-spindle attachments during cell division. Nature Cell Biology, 6(3), 232–237. https://doi.org/10.1038/ncb1102

Maiato, H., Rieder, C. L., & Khodjakov, A. (2004). Kinetochore-driven formation of kinetochore fibers contributes to spindle assembly during animal mitosis. J Cell Biol, 167(5), 831–840. https://doi.org/10.1083/JCB.200407090

Marzo, I., & Naval, J. (2013). Antimitotic drugs in cancer chemotherapy: Promises and pitfalls. Biochemical Pharmacology, 86(6), 703–710. https://doi.org/10.1016/j.bcp.2013.07.010

Mayer, T. U., Kapoor, T. M., Haggarty, S. J., King, R. W., Schreiber, S. L., & Mitchison, T. J. (1999). Small molecule inhibitor of mitotic spindle bipolarity identified in a phenotype-based screen. Science, 286(5441), 971–974. https://doi.org/10.1126/science.286.5441.971

Milic, B., Chakraborty, A., Han, K., Bassik, M. C., & Block, S. M. (n.d.). KIF15 nanomechanics and kinesin inhibitors, with implications for cancer chemotherapeutics. https://doi.org/10.1073/pnas.1801242115

Mitchison, T. J., Maddox, P., Gaetz, J., Groen, A., Shirasu, M., Desai, A., … Kapoor, T. M. (2005). Roles of Polymerization Dynamics , Opposed Motors, and a Tensile Element in Governing the Length of Xenopus Extract Meiotic Spindles. Molecular Biology of the Cell, 16(June), 3064–3076. https://doi.org/10.1091/mbc.E05

Mountain, V., Simerly, C., Howard, L., Ando, A., Schatten, G., & Compton, D. A. (1999). Cross-links Microtubules in the Mammalian Mitotic Spindle. J. Cell Biol., 147(2), 351–365.

Raaijmakers, J. A., Van Heesbeen, R. G. H. P., Meaders, J. L., Geers, E. F., Fernandez-Garcia, B., Medema, R. H., & Tanenbaum, M. E. (2012). Nuclear envelope-associated dynein drives prophase centrosome separation and enables Eg5-independent bipolar spindle formation. EMBO Journal, 31(21), 4179–4190. https://doi.org/10.1038/emboj.2012.272

Sturgill, E. G., Das, D. K., Takizawa, Y., Shin, Y., Collier, S. E., Ohi, M. D., … Ohi, R. (2014). Kinesin-12 KIF15 targets kinetochore fibers through an intrinsic two-step

mechanism. Current Biology, 24(19), 2307–2313. https://doi.org/10.1016/j.cub.2014.08.022

Sturgill, E. G., Norris, S. R., Guo, Y., & Ohi, R. (2016). Kinesin-5 inhibitor resistance is driven by kinesin-12. Journal of Cell Biology, 213(2), 213–227. https://doi.org/10.1083/jcb.201507036

Sturgill, E. G., & Ohi, R. (2013). Kinesin-12 differentially affects spindle assembly depending on its microtubule substrate. Current Biology, 23(14), 1280–1290. https://doi.org/10.1016/j.cub.2013.05.043

Tanenbaum, M. E., Macůrek, L., Janssen, A., Geers, E. F., Alvarez-Fernández, M., & Medema, R. H. (2009). KIF15 Cooperates with Eg5 to Promote Bipolar Spindle Assembly. Current Biology, 19(20), 1703–1711. https://doi.org/10.1016/j.cub.2009.08.027

Vanneste, D., Takagi, M., Imamoto, N., & Vernos, I. (2009). The Role of Hklp2 in the Stabilization and Maintenance of Spindle Bipolarity. Current Biology, 19(20), 1712–1717. https://doi.org/10.1016/j.cub.2009.09.019

Wilson, J. E. (2003). Isozymes of mammalian hexokinase: Structure, subcellular localization and metabolic function. Journal of Experimental Biology, 206(12), 2049–2057. https://doi.org/10.1242/jeb.00241

Chapter IV:
Kinesin-Binding Protein Remodels the Kinesin Motor to Prevent Microtubule-Binding

April L. Solon[1]†, Zhenyu Tan[2,3]†, Katherine L. Schutt[4], Lauren Jepsen[5], Sarah E. Haynes[6], Alexey I. Nesvizhskii[6,7], David Sept[5], Jason Stumpff[4], Ryoma Ohi[1]*, and Michael A. Cianfrocco[3,8]*

[1]Department of Cell and Developmental Biology, University of Michigan.

[2]Department of Biophysics, University of Michigan.

[3]Life Sciences Institute, University of Michigan.

[4]Department of Molecular Physiology and Biophysics, University of Vermont.

[5]Department of Biomedical Engineering, University of Michigan.

[6]Department of Pathology, University of Michigan.

[7]Department of Computational Medicine and Bioinformatics, University of Michigan.

[8]Department of Biological Chemistry, University of Michigan.

†These authors contributed equally to this work.

Previously published in part as:

Solon, A. L., et al. (2021). Kinesin-binding protein remodels the kinesin motor to prevent microtubule binding. Science advances, 7(47).

4.1 Abstract

Kinesins are regulated in space and time to ensure activation only in the presence of cargo. Kinesin-binding protein (KIFBP), which is mutated in Goldberg-Shprintzen syndrome (GOSHS), binds to and inhibits the catalytic motor heads of 8 of 45 kinesin superfamily members but the mechanism remains poorly defined. Here, we used cryo-electron microscopy and crosslinking mass spectrometry to determine high-resolution structures of KIFBP alone and in complex with two mitotic kinesins, revealing structural remodeling of kinesin by KIFBP. We find that KIFBP remodels kinesin motors and blocks microtubule-binding via 1) allosteric changes to kinesin and 2) by sterically blocking access to the microtubule. We identified two regions of KIFBP necessary for kinesin-

binding as well as cellular regulation during mitosis. Taken together, this work further elucidates the molecular mechanism of KIFBP-mediated kinesin inhibition and supports a model in which structural rearrangement of kinesin motor domains by KIFBP abrogates motor protein activity.

4.2 Introduction

Kinesins comprise a superfamily of microtubule-based motor proteins that play essential roles in virtually every aspect of cell physiology, including mitotic spindle assembly, regulation of microtubule dynamics, ciliogenesis, and transportation of cargoes throughout the cell (Hirokawa et al. 2009; Cross and McAinsh 2014; Walczak, Gayek, and Ohi 2013; Verhey, Dishinger, and Lee 2011). A signature protein fold shared among all members of the kinesin superfamily is a catalytic “motor” domain. The kinesin motor domain contains binding sites for both microtubules and ATP, enabling these proteins to convert energy from ATP hydrolysis into mechanical force (Vale and Milligan 2000). In most kinesin motors, this catalytic cycle powers motility of the proteins along microtubule tracks. While the motor domain exhibits structural and high sequence conservation among the superfamily, sequence differences imbue each kinesin with unique characteristics and are responsible for diversifying motor functions within the cell. In addition, the non-motor regions of different kinesin family members have diverged to confer specificity for cargo binding and regulation.

Kinesins are regulated at many levels to ensure that they become activated at the right time and place. Auto-inhibition, wherein kinesins adopt a conformation that prevents microtubule-binding(Verhey and Hammond 2009; Cheng et al. 2014; van der Vaart et al. 2013); sequestration within the nucleus (Goshima and Vale 2005; Walczak, Verma, and Mitchison 1997; Mayr et al. 2007; Lee et al. 2010; Kuriyama et al. 1995; Du, English, and Ohi 2010); and cell cycle-dependent protein expression (Brown et al. 1994) are common strategies to prevent untimely motor-track interactions. Kinesins are also regulated by post-translational modifications, *e.g.*, phosphorylation, which can serve to activate microtubule-binding (Blangy et al. 1995; Cahu et al. 2008; Espeut et al. 2008). Lastly, kinesin-interacting proteins such as adaptor proteins and light chains, and their phosphorylation, can regulate the ability of transport kinesins to engage cargo (Hirokawa et al. 2009; Blasius et al. 2007; Cho et al. 2009; Twelvetrees et al. 2019; Seeger and Rice

2013; Siddiqui et al. 2019; Henrichs et al. 2020), or target them to specific locations within the cell (Bouchet et al. 2016; Santamaria et al. 2008). KIFBP, a unique class of kinesin-binding protein, has emerged as an important negative regulator of a subset of kinesin motors (Kevenaar et al. 2016; Malaby et al. 2019).

KIFBP was discovered as a disease-causing gene associated with the neurological disorder Goldberg-Shprintzen syndrome (GOSHS (Brooks et al. 2005; Dafsari et al. 2015; Valence et al. 2013)), an autosomal disease characterized by facial dysmorphism, mental retardation, and congenital heart disease (OMIM #609460). In mice and zebrafish, loss of KIFBP function leads to neuronal migration and maturation defects in the developing brain (Hirst et al. 2018; Lyons et al. 2008). Emerging data demonstrate a compelling role for KIFBP in regulating motor-microtubule interactions for 8 of the 45 kinesin motors encoded by the human genome. KIFBP interacts directly with the motor head of Kinesin-2 (KIF3A), Kinesin-3 (KIF1A, KIF1B, KIF1C, KIF13B, and KIF14), Kinesin-8 (KIF18A), and Kinesin-12 (KIF15) family members, resulting in inhibition of motor-microtubule binding both *in vitro* and in cells (Kevenaar et al. 2016; Malaby et al. 2019). How the regulation of kinesin motors by KIFBP is linked to specific biological processes is largely unexplored, although neuronal microtubule dynamics appear to be controlled through KIFBP-dependent regulation of KIF18A (Kevenaar et al. 2016). Moreover, recent work has shown that KIFBP is critical for ensuring proper mitotic spindle assembly by regulating the mitotic kinesins KIF15 and KIF18A (Malaby et al. 2019).

Recently, a 4.6 Å structure for KIFBP and a 6.9 Å structure for KIFBP bound to KIF15 were reported (Atherton et al. 2020). These studies indicated that KIFBP alters the KIF15 kinesin motor to prevent microtubule binding (Atherton et al. 2020). Despite the advances afforded by this study, many open questions remain. First, the resolution of the published structures did not fully define the KIFBP-interaction interface with KIF15 given the large degree of uncertainty for the atomic model. For example, at the resolutions reported, the atomic models may have incorrect helical placement or helical registries. Without an accurate atomic model of KIFBP, the molecular mechanism of kinesin regulation by KIFBP remains unclear. Second, the generality of the previously proposed inhibition mechanism is unknown. The earlier work also included an analysis of KIFBP in complex with KIF1A, but the low resolution of the KIFBP-KIF1A complex and

heterogeneity of binding poses did not allow firm conclusions regarding the binding mechanism. Third, the previous study did not address the importance of residue-residue contacts between KIFBP and kinesin motors (KIF15 and KIF1A) in the context of the specific biological processes in which these motors participate.

To understand how KIFBP engages kinesin motors, we leveraged an interdisciplinary approach to generate a high-confidence atomic model of the KIFBP-kinesin motor interface by combining cryo-electron microscopy (cryo-EM) with crosslinking mass spectrometry (XL-MS). We show that KIFBP is a tandem repeat protein constructed of 9 helix pairs that assemble into a solenoid-like structure. When complexed with KIF15 and KIF18A, three helices in KIFBP (helical pairs (HP) 4a/b-HP5) associate closely with the kinesin α4 helix, an interaction that requires a 15 Å displacement of α4 from its resting position. Using molecular dynamics simulations, we find that kinesin α4 is immobile when a motor head is not bound to KIFBP, suggesting that allosteric changes drive the repositioning of α4 required for binding HP4a/b-HP5. Using our high-confidence KIFBP:kinesin atomic model, we identify two regions in KIFBP that are responsible for the interaction *in vitro*, and show that mutations in these regions disable the ability of KIFBP to regulate KIF15 and KIF18A during mitosis. Collectively, our work describes the molecular mechanism of KIFBP-mediated inhibition of KIF15 and KIF18A via binding to and stabilizing a conformation of the kinesin motor head that is incompatible with microtubule binding.

4.3 Results

4.3.1 KIFBP adopts a solenoid structure composed of TPR motifs

To determine an atomic model of KIFBP, we utilized cryo-EM to determine the overall structure of KIFBP and a higher-resolution structure of the N-terminus of KIFBP (Fig. 4.1). Reconstructions of the full KIFBP molecule at 4.6Å showed that KIFBP is almost entirely α-helical, possessing nine helical pairs along with one long helix throughout the 621 amino acid sequence, similar to previous reports (Atherton et al. 2020) (Fig. 4.1A, Fig. S4.1 & S4.2, Table S4.1). The α helices are arranged into a right-handed superhelical twist, giving KIFBP an appearance analogous to other tetratricopeptide repeat (TPR) proteins (Perez-Riba and Itzhaki 2019).

Given that the resolution of 4.6Å is not sufficient to build an atomic model, we wanted to improve the resolution of our reconstruction. To this end, we performed masking and 3D classification on the N-terminal two-thirds of KIFBP to obtain a higher-resolution structure at 3.8Å (Fig. 4.1B). We could unambiguously identify amino acid side chains at this resolution, allowing us to construct an atomic model for amino acids 5 to 403 (Fig. 4.1C, Fig. S4.1, S4.3, S4.4, & S4.5, Table S4.2). Our atomic model provides a high-confidence positioning of KIFBP residues, allowing us to map the structure onto the KIFBP sequence (Fig. 4.1D), confirming α-helical positions and showing the locations of loops connecting helical pairs throughout the structure.

4.3.2 KIFBP inhibits KIF15 microtubule-binding and remodels the motor domain of KIF15

After determining the structure of KIFBP alone, we used cryo-EM to determine the structure of KIFBP bound to KIF15. To prepare cryo-EM samples, we incubated the purified KIF15 motor domain (amino acids 1-375) with KIFBP and subjected the sample to size exclusion chromatography in the presence of ATP (Fig. S4.6). SDS-PAGE analysis determined that KIF15 co-migrated with KIFBP in a 1:1 complex, and fractions containing the complex were utilized for cryo-EM sample preparation.

We used cryo-EM to determine a ~4.8Å resolution structure of KIFBP bound to KIF15 (Fig. 4.2A, Fig. S4.7 & S4.8, Table S4.3). At this resolution, we could unambiguously identify the regions of density corresponding to KIFBP in addition to the

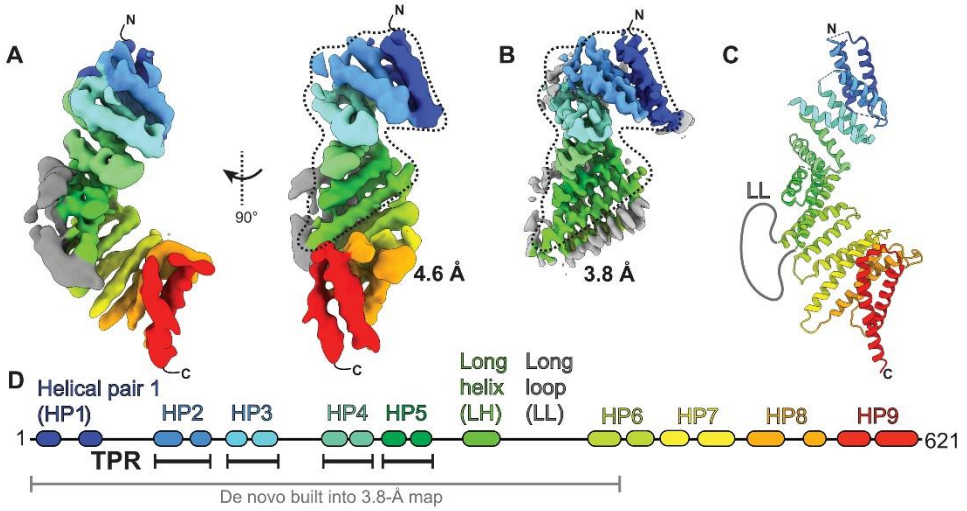

Fig. 4.1. KIFBP adopts a solenoid structure composed of TPR motifs. A) Overview of KIFBP structure at 4.6Å. Dotted lines indicate the masked region for the higher-resolution KIFBP core. (B) Structure of KIFBP core at 3.8Å. (C) Combined atomic model of KIFBP. (D) Structural features and nomenclature for KIFBP.

motor domain of KIF15 (Fig. 4.2A). Unexpectedly, when we docked the structure of KIF15 into the reconstruction, we noticed that the α4 helix of KIF15 was missing. Instead, we noticed the presence of an additional α-helical density within a cleft of KIFBP, suggesting the displacement of KIF15-α4 into this cleft during complex formation (Fig. 4.2B). In the structure, KIFBP occupies the microtubule-binding surface of KIF15, sterically blocking access to the microtubules by KIF15.

To understand how KIFBP affected the overall architecture of KIF15, we utilized both manual building and Rosetta comparative modeling (Song et al. 2013) to develop a model for the KIFBP-engaged KIF15 motor (Fig. 4.2C). Our analysis of KIFBP:KIF15 revealed structural rearrangements of the KIF15 motor by KIFBP to disrupt KIF15's microtubule-binding interface. The most notable structural change involved the repositioning of KIF15-α4 away from the kinesin motor domain, placing KIF15-α4 15Å away from the location found in the crystal structure of KIF15 (Klejnot et al. 2014). Notably, kinesin motors require the α4 helix for engaging microtubules during the kinesin mechanochemical cycle (Wang et al. 2015). The adjoining loops on each side of KIF15-

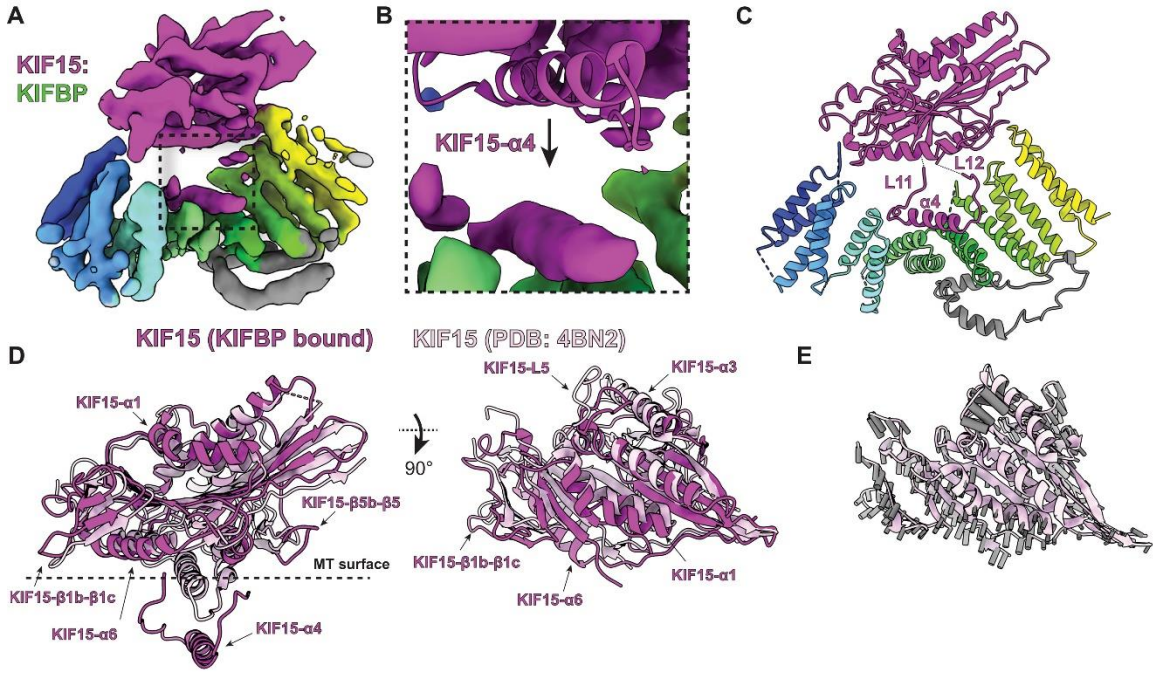

Fig. 4.2. KIFBP stabilizes KIF15 in a conformation that blocks microtubule-binding. (A) KIF15:KIFBP reconstruction. (B) Zoom-in on additional density present in KIF15:KIFBP reconstruction (purple) alongside docked crystal structure (PDB: 4BN2). (C) Atomic model of KIF15:KIFBP. (D) Superposition of KIF15 bound to KIFBP (dark purple) with apo-KIF15 (light purple) (PDB: 4BN2) relative to KIF15-α2. Structural elements that differ are indicated by arrows. (E) Vectors (gray) calculated from Cα differences between KIF15 (KIFBP-bound) vs. KIF15 superimposed on the apo KIF15 crystal structure (PDB: 4BN2).

α4, Loop-11 (“KIF15-L11”) and Loop-12 (“KIF15-L12”), accommodated the repositioning of KIF15-α4 by facilitating the extension of KIF15-α4 away from the body of the motor domain (Fig. 4.2C). Whereas KIF15-L12 remains extended in solution, the KIF15-L11 is positioned away from the motor domain and binds along KIFBP-HP4a.

In addition to seeing changes in KIF15-L11, KIF15-α4, and KIF15-L12, we saw that the overall structure of KIF15 adopted a more open conformation (Fig. 4.2D & E). The structure showed the shift of α-helices KIF15-α1, -α3, and -α6 away from the core of the motor. We observed large movements for beta-strand pairs KIF15-β1b-β1c and KIF15-β5b-β5 in addition to loop KIF15-L5. These changes indicate that KIFBP stabilizes several structural changes in KIF15 to block microtubule-binding. Thus, KIFBP blocks microtubule binding by sterically preventing microtubule interaction in addition to allosterically altering the KIF15 motor.

4.3.3 KIFBP binds to KIF15-α4 in a distinct manner relative to αβ-tubulin

Given that KIFBP binds along the microtubule-binding interface of KIF15, we sought to compare the interaction interface between KIF15:KIFBP and KIF15:αβ-tubulin (Atherton et al. 2020). First, we noticed that the length of the α4 helix is shorter for KIF15-KIFBP compared to the microtubule-engaged α4 helix (Fig. 4.3A-F). The length of α4 in KIFBP:KIF15 is similar to the crystal structure of KIF15 when not bound to microtubules (Klejnot et al. 2014). Second, KIF15-L11 is bent relative to α4 at an angle of ~120° (Fig. 4.3B), whereas KIF15-L11 on the microtubule adopts a helical structure to extend the length of α4 (Fig. 4.3E) (Atherton et al. 2020). These two observations indicate that KIFBP holds KIF15-α4 in a conformation that is incompatible with microtubule-binding.

Comparing the hydrophobicity and electrostatic charge surfaces on KIFBP vs. αβ-tubulin shows that KIFBP binds KIF15-α4 via hydrophilic and hydrophobic helices (Fig. 4.3B, C, E, & F). The strong electrostatic nature of αβ-tubulin results in minimal hydrophobic residues contributing to KIF15 binding. Unlike β-tubulin, KIFBP utilizes a composite binding site stretching across three helices to bind both hydrophobic and polar residues to interact with KIF15-α4. Comparing the overall hydrophobicity and charge distribution indicates that KIFBP binds KIF15-α4 in a manner distinct from αβ-tubulin.

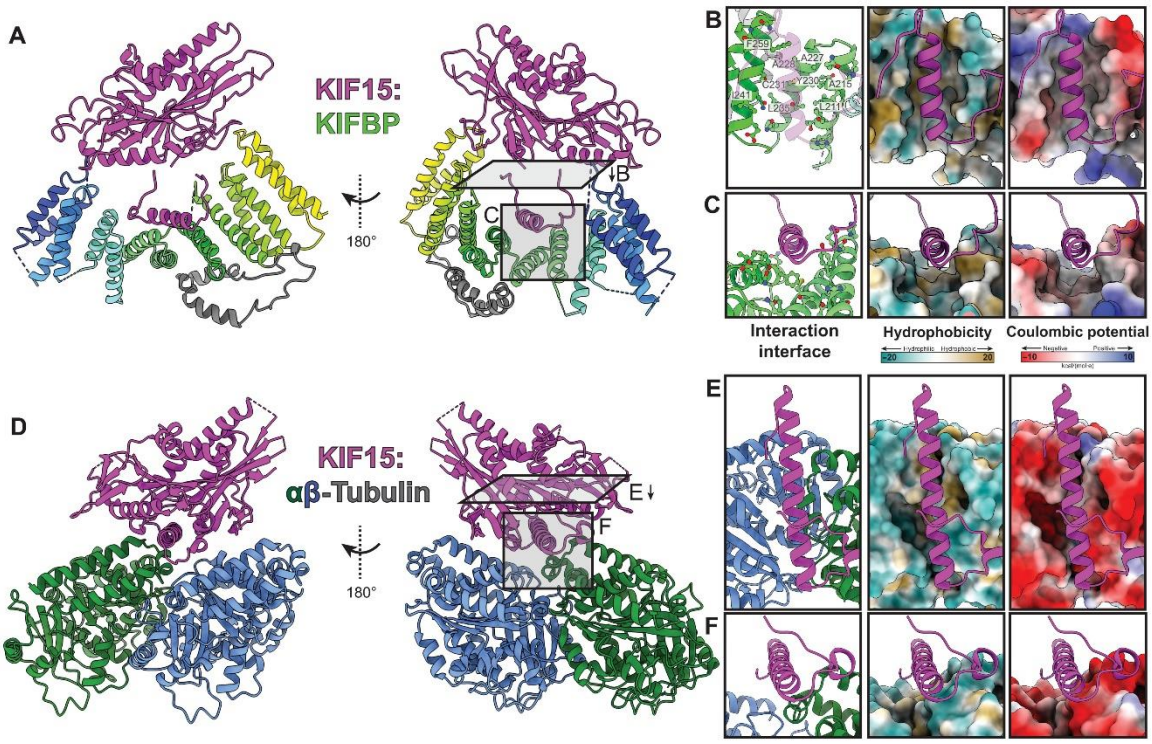

Fig. 4.3. KIFBP binds to KIF15-α4 in a distinct manner relative to tubulin. Comparison of KIFBP- and αβ-tubulin-bound KIF15. (A) KIF15:KIFBP atomic model. (Right) Gray rectangles indicate viewing directions for panels (B) & (C). (B) & (C) Top and side views of KIF15-α4 interface (left), hydrophobicity (center), and Coulombic potential (right). KIFBP binding residues for KIF15-α4 are shown in ball and stick mode and hydrophobic residues are labeled in (B). (D) KIF15:αβ-tubulin structure (PDB: 6ZPI)[34] shown relative to KIF15:KIFBP (A). (Right) Gray rectangles indicate viewing directions for (E) & (F). (E) & (F) Top and side views of KIF15-α4 interface (left), hydrophobicity (center), and Coulombic potential (right).

4.3.4 KIFBP engages the microtubule-binding interface of KIF15 using multiple contact points

To obtain further insight into the regions of KIFBP and KIF15 that interact with each other, we performed crosslinking mass spectrometry (XL-MS). Recombinant KIFBP and KIF15 (1-375) were incubated with the 11 Å lysine-targeting crosslinker BS3, digested with trypsin, and analyzed using tandem mass spectrometry. We identified crosslinked peptides using pLink software (see Materials and Methods). We present all high-confidence crosslinks between KIFBP and KIF15 peptides (e-value >0.05) in Table S5, and have displayed them on the primary and secondary structures of KIFBP:KIF15 as well (Fig. 4A & 4B, Movie S1).

We observed the highest density of crosslinks between three residues of KIFBP-L1 (K26, K30, and K36) and the microtubule-binding interface of KIF15 (K273, K283, K319, and K361) (Fig. 4.4A & C). Interestingly, these same KIF15 residues also

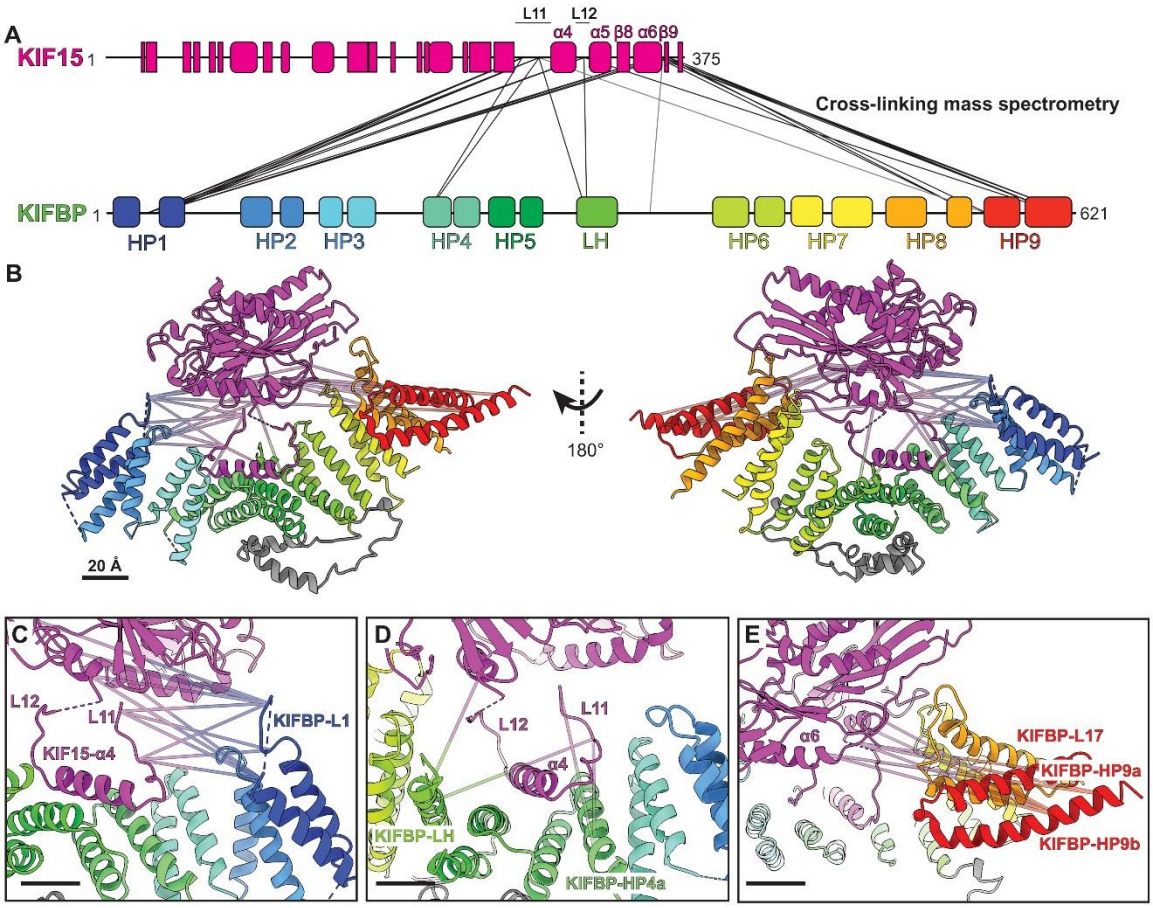

Fig. 4.4. KIFBP physically contacts multiple sites along the microtubule-binding interface of KIF15. (A) Schematic representing the location of identified crosslinks between the KIF15 motor domain (top) and KIFBP (bottom). Secondary structure elements of the two proteins are represented by rectangles (β-sheets), rounded rectangles (α-helices), and lines (unstructured regions). (B) Crosslinks shown in panel (A) have been superimposed on the cryo-EM structure of KIF15:KIFBP. (C) Zoomed-in view of the crosslinks between KIFBP-L1 and KIF15. (D) Zoomed-in view of the crosslinks between KIFBP-HP4a and -LH and KIF15. (E) Zoomed-in view of the crosslinks between KIFBP-L17 and -HP9a/b and KIF15. Scale bars are 20Å.

crosslinked to regions in the middle of KIFBP (HP4a, LH, and LL) (Fig. 4.4D) and towards the C-terminus (L17, HP9a, and HP9b) (Fig. 4.4E). Two KIF15 residues that crosslinked multiple KIFBP sites (K273 and K283) are located in KIF15-L11, adjacent to KIF15-α4. Additionally, residues KIF15-K273 and KIF15-K319 form the kinesin motor microtubule-binding interface (Atherton et al. 2020). The high density of crosslinks involving these KIF15 residues supports a mechanism of inhibition where KIFBP directly binds the microtubule-binding domain of kinesins, occluding interactions with the microtubule lattice.

KIFBP:KIF15 crosslinks span nearly the entire length of KIFBP to bind the KIF15 microtubule-binding surface. When superimposed onto the KIFBP:KIF15 structure (Fig. 4.4B-E), these crosslinks bridge distances greater than the 11 Å BS3 can reach. This

suggests that the crosslinked regions of KIFBP may associate transiently with the microtubule-binding interface of KIF15 at different time points during complex formation (see Discussion).

4.3.5 KIFBP inhibits KIF18A via a similar mechanism as KIF15

After characterizing how KIFBP inhibits KIF15 (kinesin-12 family), we next aimed to establish whether KIFBP utilizes the same mode of inhibition for a kinesin motor from a different kinesin family, KIF18A (kinesin-8 family). To determine how KIFBP inhibits KIF18A, we first purified recombinant KIF18A (1-363) motor domain, incubated KIF18A with KIFBP, and performed size exclusion chromatography to confirm the formation of a 1:1 complex (Fig. S4.9). After preparing cryo-EM grids with the complex, we obtained 2D class averages that appeared similar in shape and features as seen previously for KIF15 (Fig. S4.10), further confirming the formation of a KIFBP:KIF18A complex.

After performing further single particle analysis, the cryo-EM structure of KIFBP:KIF18A revealed that KIFBP binds KIF18A like KIF15 (Fig. 4.5A-B, Fig. S4.11, Table S4.4). In the structure, KIFBP N- and C-terminal domains engage both sides of the motor domain while KIF18A-α4 is displaced away from the motor into the central cavity

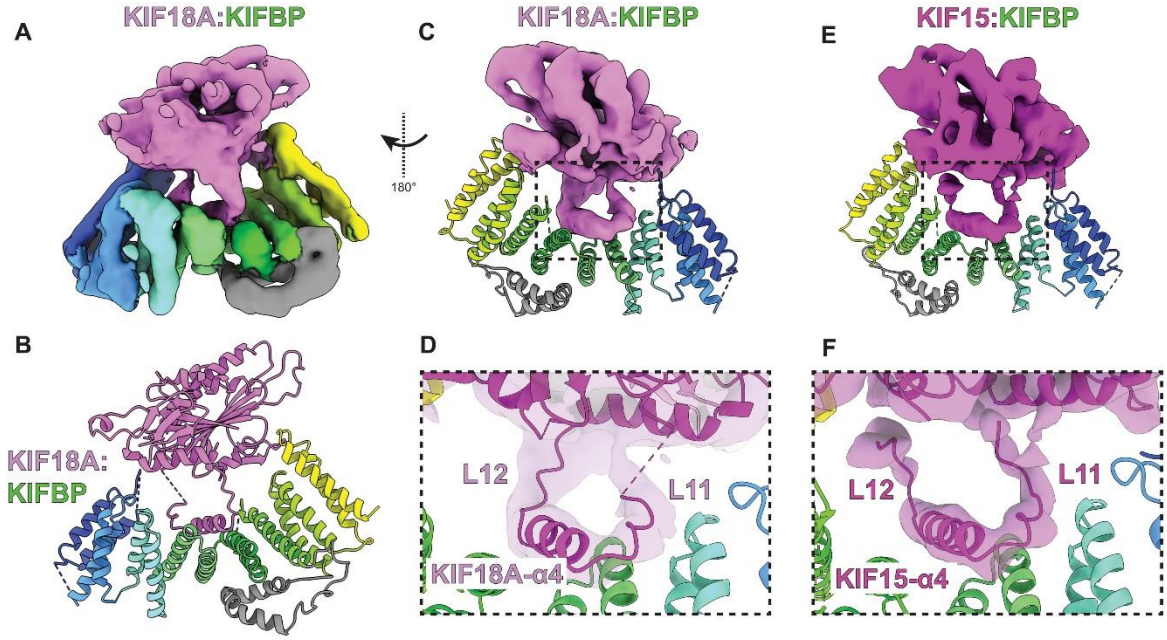

Fig. 4.5. KIFBP inhibits KIF18A *via* a similar mechanism as KIF15. (A) Cryo-EM reconstruction of KIF18A:KIFBP. (B) Atomic model of KIF18A:KIFBP. (C) Segmented KIF18A density shown alongside KIFBP atomic model, rotated 180° from (A). (D) Zoomed-in view of KIF18A density and model on KIFBP interface. (E) Segmented KIF15 density shown in a similar orientation as (C). (F) Zoomed-in view of KIF15:KIFBP interface.

of KIFBP. To highlight the similarities between KIFBP engagement of KIF15 and KIF18A, we segmented the motor density from either KIFBP:KIF18A (Fig. 4.5C-D) or KIFBP:KIF15 (Fig. 4.5E-F). This comparison shows for both motors that 1) α4 is held within the central cleft of KIFBP, 2) Loops-11 & -12 are extended away from the motor, and 3) KIFBP-L11 adopts a curved shape as it makes a ~120° turn to follow helix KIFBP-HP4a within the KIFBP cleft. Thus, KIFBP stabilization of kinesin α4 helix away from the motor is a shared mode of kinesin inhibition by KIFBP for KIF18A and KIF15.

4.3.6 KIFBP utilizes Loop-1 and Loop-14 to bind kinesin in vitro

Our structural data and XL-MS results identified multiple KIFBP:motor interactions that may be important for robust binding and inhibition of motor activity. In particular, our XL-MS results revealed that the most extensively crosslinked residues in KIFBP occurred

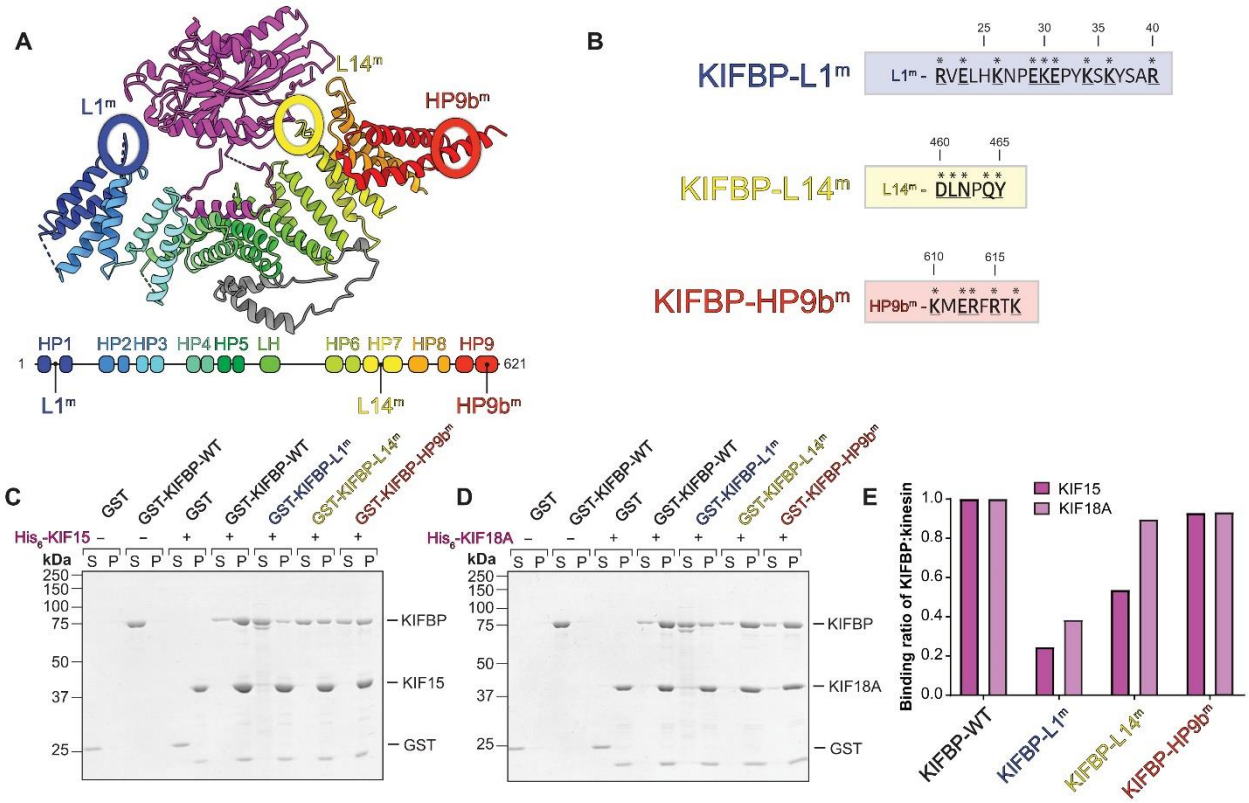

Fig. 4.6. KIFBP utilizes Loop-1 and Loop-14 to bind kinesins *in vitro*. (A) Schematic showing the locations of the three mutations on the cryo-EM structure of KIF15:KIFBP (top) and the secondary structure of KIFBP (bottom). Mutations were made to Loop-1, Loop-14, and HP9b of KIFBP. (B) Mutated residues in each mutant are indicated with asterisks; residue position is indicated above each sequence. (C and D) Representative Coomassie gels showing results of *in vitro* pull-down assays where KIFBP proteins were pulled down by either KIF15 (C) or KIF18A (D). Supernatant and pellet samples, as well as the presence or absence of kinesin, are indicated at the top of each gel. (E) Quantifications of pull-down assays shown in panels (C) and (D) are graphed as the ratio of each KIFBP protein to KIF15 or KIF18A in the pellet.

within Loop-1 and the C-terminal helix pairs of KIFBP (Fig. 4.4A, Table S4.5). Our cryo-EM structure of KIFBP complexed with the motor domains of both KIF15 and KIF18A support a prominent role for Loop-1 in motor engagement. We therefore targeted both KIFBP-L1 and KIFBP-HP9b for mutagenesis, selecting positively and negatively charged residues in those regions and substituting them with alanine or glycine residues (Fig. 4.6B). We also constructed a third KIFBP mutant by mutating residues 460-465 in KIFBP-L14 to alanine (Fig. 4.6B) because of the proximity of KIFBP-L14 to KIF15 and previous work indicating that it is important for kinesin motor binding (Atherton et al. 2020). All proteins were purified for *in vitro* binding studies (Fig. S4.12).

First, we tested the ability of these three KIFBP mutants to bind the motor domains of KIF15 and KIF18A *in vitro*. We performed *in vitro* pull-down assays using hexahistidine-tagged motor domains of either KIF15 (1-375) or KIF18A (1-363) immobilized on nickel resin, and analyzed the ratio of recombinant wildtype or mutant KIFBP to kinesin motor domain in the pellet. We used GST as a negative control, which showed little to no nonspecific interaction with nickel resin or immobilized kinesin. When incubated with KIF15, we observed a four-fold reduction in binding of the KIFBP-L1^{m} mutant and a two-fold reduction in binding of the KIFBP-L14^{m} mutant compared to KIFBP-WT, indicating that mutations in these regions abrogate the ability of KIFBP to interact with the motor robustly. Surprisingly, the KIFBP-HP9b^{m} showed no difference in binding compared to KIFBP-WT, suggesting that the charged residues mutated are not essential for motor binding. Thus, although both Loop-1 and the C-terminus of KIFBP were implicated as potentially important for binding in our XL-MS experiment (Fig. 4.4C & E), mutations to only one of these regions, Loop-1, affected binding biochemically.

Next, we repeated pull-down assays with KIF18A immobilized on the resin and analyzed binding of the same panel of mutants. Similar to KIF15, the KIFBP-L1^{m} mutant showed a three-fold reduction in binding compared to KIFBP-WT. Intriguingly, the KIFBP-L14^{m} mutant showed only a slight 10% reduction in binding to KIF18A compared to KIFBP-WT, in contrast to the 50% decrease in binding to KIF15.

4.3.7 Mutations in KIFBP-L1 and KIFBP-L14 disrupt the regulation of mitotic kinesins

Overexpression of KIFBP in HeLa cells leads to defects in chromosome alignment and an increase in spindle length (Malaby et al. 2019). To determine whether mutations that block KIFBP interaction *in vitro* also reduce KIFBP effects during mitosis, we transfected N-terminally mCherry-tagged KIFBP constructs into HeLa Kyoto cells and measured chromosome alignment and spindle length in metaphase arrested cells. Consistent with previous results, overexpression of mCherry-KIFBP-WT decreased chromosome alignment, quantified by an increase in full-width at half maximum (FWHM) of centromere fluorescence distribution along the length of the spindle (Fig. 4.7A & B)

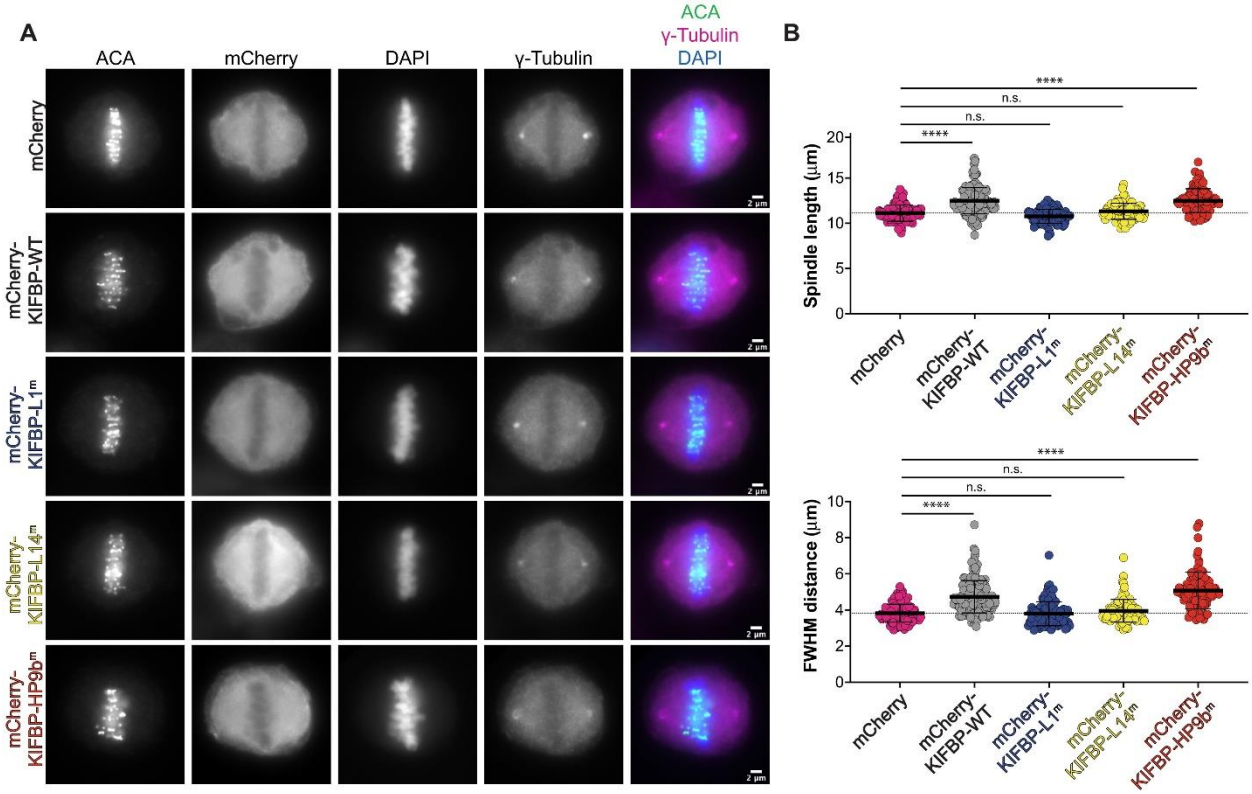

Fig. 4.7. Mutations in KIFBP-L1 and -L14 diminish KIFBP-mediated regulation of spindle length and chromosome alignment during mitosis. (A) MG132-arrested HeLa Kyoto cells overexpressing mCherry or indicated mCherry-KIFBP construct. Scale bar 2 µm. (B) Top: Graph of spindle lengths measured in cells overexpressing mCherry or indicated mCherry-KIFBP construct. Each dot represents a single cell. Mean ± standard deviation is displayed. Statistical results are shown for a one-way ANOVA with Tukey's Multiple Comparisons test. N.S. indicated not significant, **** indicates adjusted p-value < 0.0001 with 95% confidence interval. See Figure S13 for spindle length versus average mCherry expression for individual cells. Bottom: Graph of full-width at half maximum (FWHM) of centromere fluorescence distribution along the length of the spindle measured in cells overexpressing mCherry of indicated mCherry-KIFBP construct. Each dot represents a single cell. Mean ± standard deviation is displayed. Statistical results are shown for a one-way ANOVA with Tukey's Multiple Comparisons test. N.S. indicated not significant, **** indicates adjusted p-value < 0.0001 with 95% confidence interval. See Figure S13 for FWHM distance versus average mCherry expression for individual cells. Data were obtained from a minimum of three independent experiments. The following cell numbers were analyzed for the mCherry and mCherry-KIFBP constructs: (1) mCherry (control) = 132 cells; (2) mCherry-KIFBP-WT = 165 cells; (3) mCherry-KIFBP-L1^{m} = 102 cells; (4) mCherry-KIFBP-L14^{m} = 99 cells; and (5) mCherry-KIFBP-HP9b^{m} = 89 cells.

(Malaby et al. 2019; Fonseca and Stumpff 2016). Overexpression of mCherry-KIFBP-WT also increased spindle lengths, as shown previously (Malaby et al. 2019) (Fig. 4.7A & B). These mitotic effects scaled with the mCherry-KIFBP-WT expression level, where cells expressing higher levels of mCherry-KIFBP-WT had longer spindles and more severe chromosome alignment defects (Fig. S4.13).

To test the mitotic effects of the KIFBP mutants, we generated mCherry-KIFBP overexpression mutant constructs mCherry-KIFBP-L1^{m}, mCherry-KIFBP-L14^{m}, and mCherry-KIFBP-HP9b^{m} (Fig. 4.6B). Cells expressing mCherry-KIFBP-L1^{m} and mCherry-KIFBP-L14^{m} mutants displayed similar chromosome alignment and spindle lengths as cells overexpressing the mCherry control (Fig. 4.7A & B). In contrast to mCherry-KIFBP-WT, mitotic effects of mCherry-KIFBP-L1^{m} did not scale with expression level, suggesting that mCherry-KIFBP-L1^{m} does not inhibit kinesin activity even when expressed at higher levels (Fig. S4.13). Spindle length and chromosome alignment defects increased at high expression levels of mCherry-KIFBP-L14^{m}, suggesting mCherry-KIFBP-L14^{m} may inhibit kinesin activity at high expression levels (Fig. S4.13). In contrast to mCherry-KIFBP-L1^{m} and mCherry-KIFBP-L14^{m}, mCherry-KIFBP-HP9b^{m} showed similar effects as mCherry-KIFBP-WT overexpression, decreasing chromosome alignment and increasing spindle length (Fig. 4.7A & B). Interestingly, mitotic defects did not scale with expression level for mCherry-KIFBP-HP9b^{m}, in contrast to mCherry-KIFBP-WT (Fig. S4.13). Cells expressing lower levels of mCherry-KIFBP-HP9b^{m} displayed mitotic defects, suggesting that mCherry-KIFBP-HP9b^{m} may be a more potent inhibitor than mCherry-KIFBP-WT. These findings are consistent with the *in vitro* observations that KIFBP-L1^{m} and KIFBP-L14^{m} reduce KIFBP's interaction with KIF15 and KIF18A, whereas the KIFBP-HP9b^{m} does not block interaction (Fig. 4.6C-E).

To further investigate the cellular effects of the KIFBP mutations, we measured KIF18A localization in HeLa Kyoto cells overexpressing wild type KIFBP or the KIFBP mutants. KIF18A accumulates at the plus-ends of microtubules during metaphase, and we have previously shown that overexpression of mCherry-KIFBP-WT alters KIF18A spindle localization (Malaby et al. 2019). Overexpression of mCherry-KIFBP-WT abolishes KIF18A plus-end enrichment and leads to a more uniform spindle localization (Fig. 4.8A), consistent with previous observations (Malaby et al. 2019). Line-scan analysis

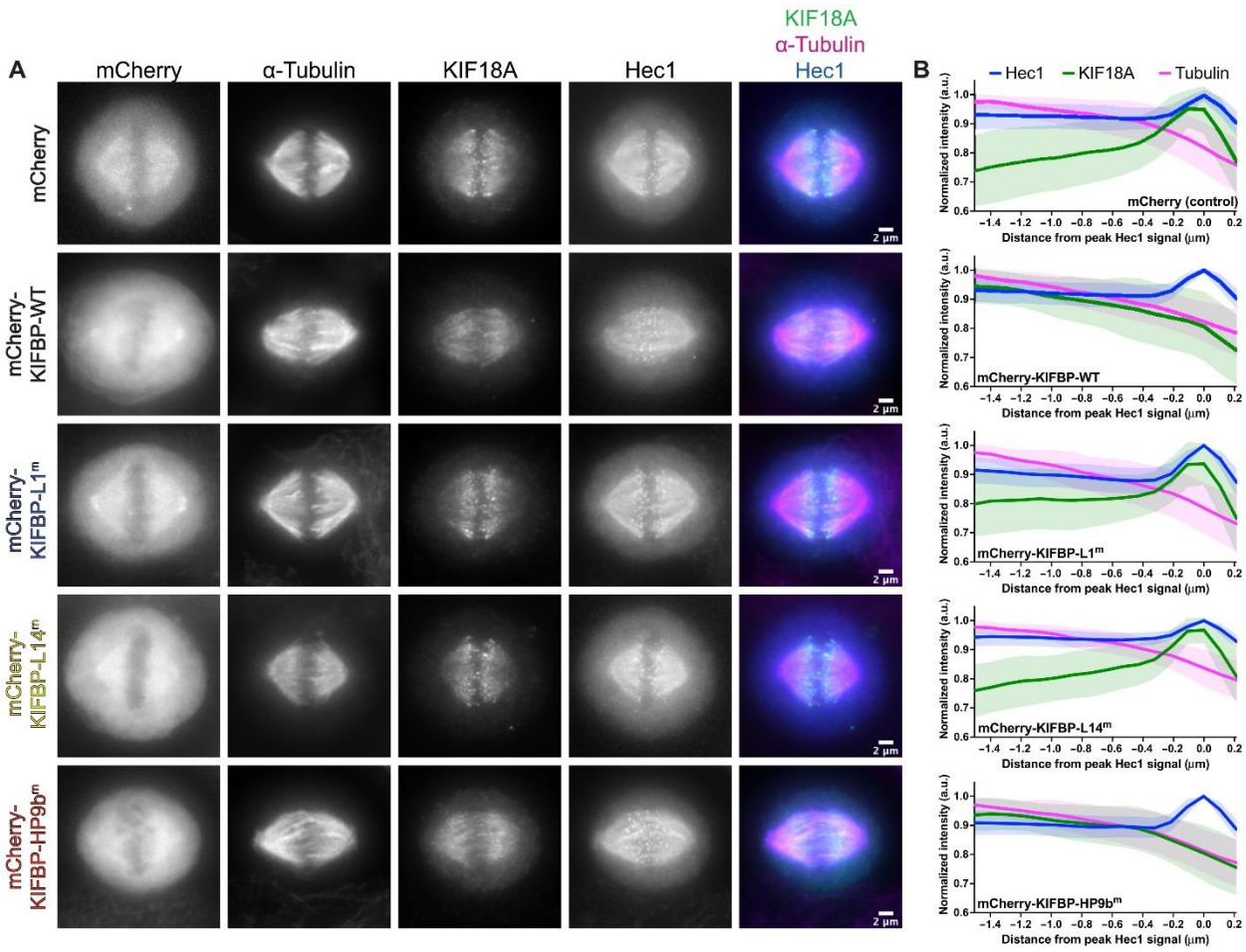

Fig. 4.8. Mutations in KIFBP-L1 and -L14 disrupt KIFBP-regulation of KIF18A localization. (A) KIF18A localization in MG132-arrested HeLa Kyoto cells overexpressing mCherry or indicated mCherry-KIFBP construct. Hec1 is used as a marker for the kinetochore. Scale bar 2 µm. (B) Line scan analyses of KIF18A distribution along kinetochore microtubules. Fluorescence values were normalized, aligned by peak Hec1 intensity, and averaged across multiple line scans. Hec1, blue; KIF18A, green; Tubulin, magenta. Solid lines indicate the means, shaded areas indicate standard deviation. A.U. indicates arbitrary units. The following cell numbers and line scans were analyzed for the mCherry and mCherry-KIFBP constructs: (1) mCherry (control) = 40 cells (64 lines); (2) mCherry-KIFBP-WT = 34 cells (64 lines); (3) mCherry-KIFBP-L1^{m} = 34 cells (64 lines); (4) mCherry-KIFBP-L14^{m} = 32 cells (68 lines); and (5) mCherry-KIFBP-HP9b^{m} = 33 cells (63 lines).

confirmed the loss of KIF18A from microtubule plus-end enrichment along individual kinetochore microtubules (Fig. 4.8B).

We predicted that mutations that abolished KIFBP interaction with kinesins *in vitro* would not disrupt KIF18A localization. Overexpression of mCherry-KIFBP-L1^{m} and mCherry-KIFBP-L14^{m} did not disrupt KIF18A plus-end enrichment on kinetochore microtubules (Fig. 4.8A & B). In contrast, overexpression of mCherry-KIFBP-HP9b^{m} showed similar effects to overexpression of mCherry-KIFBP-WT (Fig. 4.8A & B). This is especially interesting considering that KIFBP-L14^{m} binds KIF18A *in vitro*, suggesting that the interaction is not necessarily equivalent to inhibition. Even a 10% reduction in binding

may be sufficient to impair regulation by KIFBP beyond a cellular threshold. Taken together, these results support the conclusion that KIFBP Loop-1 and Loop-14 are critical regions for kinesin interaction and indicate that both regions are necessary for KIFBP to limit KIF15 and KIF18A activity during mitosis.

4.3.8 KIFBP-binding kinesins adopt conformations that are distinct from non-KIFBP binding kinesins

To gain insight into how KIFBP inhibits particular kinesins, we performed a series of molecular dynamics (MD) simulations using a number of kinesin family members. We selected two members that bind KIFBP (KIF15 and KIF18A) as well as two that show little or no interaction with KIFBP (KIF5C and KIF11) (Kevenaar et al. 2016). Using only the motor domains, we performed 500+ nanosecond simulations of all-atom MD for each protein in the unbound, ADP state (see Methods).

To analyze the dynamics and conformational spaces explored by these proteins, we compared MD trajectories between KIFBP-binding motors (KIF15 and KIF18A) and motors that do not bind KIFBP (KIF5C and KIF11). We performed principal component analysis (PCA) using the KIF15 simulation as the reference for the other proteins to reduce dimensionality. To minimize noise in the PCA analysis that comes from fluctuations in unstructured regions of the protein, we only analyzed amino acids that were in stable secondary structure elements (α-helices of β-strands) at least 80% of the time. Finally, we removed α4 from the PCA analysis since this helix remained stably bound to the motors in the simulations (Fig. S4.14), but is extended in the cryo-EM structure and would thus skew the PCA results.

Comparison of PCA analysis for these kinesin motors shows that 1) all four proteins have similar ranges of motion and explore comparable regions of conformational space and 2) there are specific motions that are only present in KIFBP-binding kinesins (KIF15 and KIF18A) (Fig. 4.9A). Close inspection of the amino acids that contribute to PC1 (*i.e.*, the largest motions of KIF15) revealed that splaying of both the C-terminal end of α3 and the N-terminal end of α6 are the dominant contributors to this mode. These structural differences are consistent with the KIFBP:KIF15 cryo-EM structure (Fig. 4.2D) where movements of these helices are a defining feature of the bound complex. Thus,

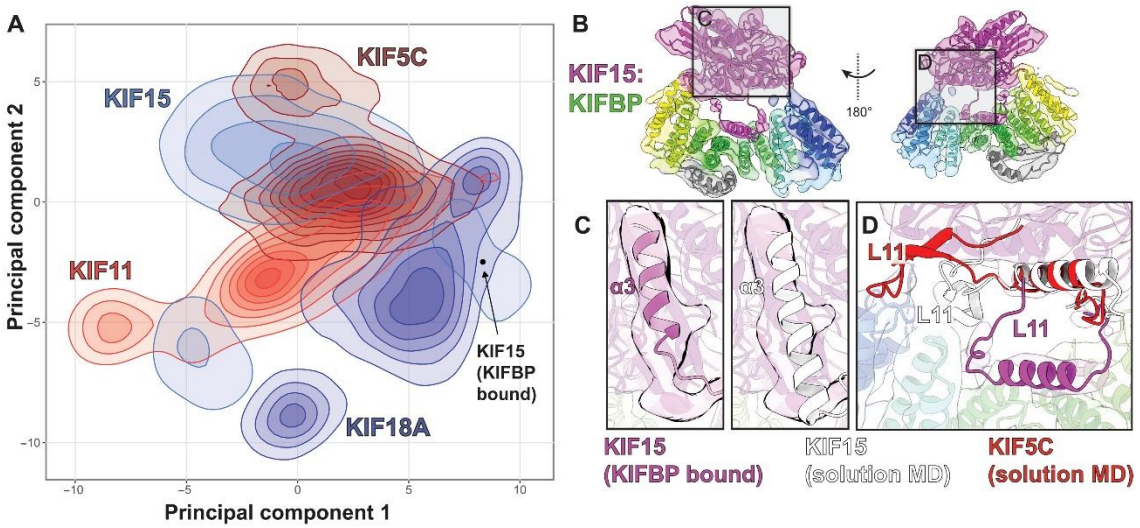

Fig. 4.9. Molecular dynamics reveals specific conformations adopted by KIF15 and KIF18A that may promote KIFBP-binding. (A) Principal Component Analysis of the MD simulations for all four kinesin motors (KIF15, KIF18A, KIF5C, and KIF11). The two KIFBP binders (KIF15 and KIF18A in shades of blue) can reach the conformation of the cryo-EM complex, but the non-binders (KIF5C and KIF11 in shades of red) do not. (B) Overview of KIF15:KIFBP structure. (C) Comparison of KIF15-α3 between MD simulations and cryo-EM. (D) Differences in Loop-11 between KIF15 and KIF5C. For KIF15, Loop-11 fits within the KIFBP pocket while the extended Loop-11 structure of KIF5C clashes with KIFBP.

MD simulations indicate that only KIF15 and KIF18A are able to reach the conformation found in the bound complex (Fig. 4.9A).

The MD KIF15 solution structure differs in specific structural regions with KIFBP-bound KIF15. First, the KIF15 solution structure shows that KIF15-α4 remains closely bound to the motor body throughout each simulation. This would suggest that the release and translocation of KIF15-α4 would only occur upon interaction with KIFBP, or on a much longer time scale than that sampled during the simulation. Second, even though we saw that the movement of KIF15-α3 was a key feature from the PCA analysis, we see in the cryo-EM structure that the C-terminal end of KIF15-α3 loses its structure over the final 8-9 residues, forming an extended loop with a short antiparallel β-sheet (Fig. 4.9B & C). This part of KIF15 makes contact with KIFBP and it appears that this structural change would allow better contact between KIF15 and KIFBP.

Lastly, even though α4 has a nearly identical conformation for all kinesins, L11 is much more dynamic and its conformation is kinesin-dependent. For KIF5C, L11 tends to be extended away from α4, and when superimposed on the cryo-EM complex, L11 has a steric clash with KIFBP (Fig. 4.9B & D). Conversely, both KIF15 and KIF18A adopt more compact L11 structures and these fit well within the cavity of the KIFBP structure (KIF15

structure shown in Fig. 4.9D). Taken together, this suggests that the overall conformation of the motor head as well as the dynamics or conformation of more flexible parts of each protein may act in concert to determine which kinesins will bind to KIFBP and which will not.

4.4 Discussion

Our work presents a previously undescribed mode of kinesin motor protein regulation *via* a multivalent interaction between KIFBP and the kinesin motor domain. Using a combination of cryo-EM, XL-MS, MD simulations, biochemical assays, and cell biology, we describe a model in which KIFBP stabilizes the microtubule-binding α4 helix (Vale and Milligan 2000; Sosa et al. 1997; Woehlke et al. 1997; Kull et al. 2013) away from the kinesin motor domain in addition to sterically inhibiting the microtubule-binding interface. Interestingly, KIFBP does not mimic the negatively-charged microtubule surface (Nogales et al. 1995) to engage kinesin motors. Instead, KIFBP utilizes a hydrophobic cleft to hold α4 and Loop-11 in a conformation that is incompatible with microtubule-binding, while simultaneously engaging and sterically inhibiting the kinesin microtubule-binding interface (Fig. 4.3).

Determining the binding mechanism of KIFBP relied on cryo-EM structural data for relatively small macromolecular samples. We determined a near-atomic structure of KIFBP corresponding to ~40kDa out of 72 kDa, using this reconstruction for *de novo* model building. This places the KIFBP reconstruction and model among the smallest molecular weight macromolecules to be built *de novo* by cryo-EM. The relatively small size of KIFBP may be the driving factor limiting the overall resolution of KIFBP alone to ~3.8Å instead of obtaining higher-resolution reconstructions.

During the preparation of this work, another study utilized cryo-EM and cell biology assays to propose a mechanism of KIFBP-mediated kinesin inhibition (Atherton et al. 2020). In this study, Atherton et al. determined lower resolution structures of KIFBP (4.8Å) and KIFBP-KIF15 (6.9Å) to arrive at a similar model of kinesin motor inhibition, where KIFBP stabilizes the α4 helix away from KIF15. In our work, our higher-resolution structures of KIFBP alone (3.8Å) and KIFBP-KIF15 (4.8Å) allowed us to 1) build a high-confidence atomic model for KIFBP and 2) map conformational changes in the KIF15 motor when bound to KIFBP. Importantly, we showed that KIFBP utilizes a similar mode

of inhibition for KIF18A, indicating that our proposed model is likely a general mode of kinesin inhibition. Finally, we used our structures alongside XL-MS to map the interaction of KIFBP with kinesin motors and showed that blocking the interaction between KIFBP with KIF15 and KIF18A *via* mutagenesis minimizes its ability to regulate motor activity in the physiologically-relevant context of mitosis (Fig. 4.7 & 4.8).

4.4.1 Kinesin motor recognition by KIFBP

Our cryo-EM reconstruction of KIFBP reveals that KIFBP contains a 9-TPR array, which folds into a solenoid with a concave kinesin-interacting surface. Unlike continuous TPR proteins like LGN (Mapelli and Gonzalez 2012), KIFBP is punctuated by a centrally located helix and loop (Fig. 4.1). The binding of KIFBP to kinesin motor heads is strikingly different from the interaction of many TPR proteins to their ligands (Perez-Riba and Itzhaki 2019). Many TPR proteins bind a short sequence, e.g. HOP binds the motif MEEVD in Hsp90 (Scheufler et al. 2000). In contrast, our cryo-EM and XL-MS show that the interaction of KIFBP with kinesin motors is highly multivalent. First, KIFBP-L1, localized at its N-terminus, engages α3 and β6 of the kinesin motor head. Second, KIFBP-L14 contacts β4-β5 of KIF15 and KIF18A with amino acid E168 in the KIF15 motor domain (or E161 in KIF18A) positioned to play a key role in this interaction. Third, α4 helices of KIF15 and KIF18A become nestled into a multi-helix groove created by KIFBP-HP4a, -HP4b, and -HP5a. The binding of KIF15/KIF18A-α4 to KIFBP is striking because it requires a 15 Å displacement of the helix from its resting position within the kinesin motor head.

Our structure- and XL-MS-guided mutagenesis study of KIFBP revealed that KIFBP-L1 is especially important for motor binding. Charge-neutralization of Loop-1 renders KIFBP incompetent for binding both KIF15 and KIF18A *in vitro* (Fig. 4.6). Consistent with these data, the KIFBP-L1^{m} failed to produce phenotypes associated with KIFBP overexpression in cells, *i.e.*, disruption of chromosome alignment and increased spindle length (Fig. 4.7 & 4.8). Unlike KIFBP-WT, the KIFBP-L1^{m} mutant was also incapable of disrupting KIF18A localization.

In contrast to KIFBP-L1, the role of KIFBP-L14 in motor inhibition remains less clear. Previous work utilizing an artificial peroxisome transport assay suggested that

KIFBP-L14 is important for the ability of KIFBP to inhibit the motor activities of KIF1A and KIF15 (Atherton et al. 202). Interestingly, however, mutation of KIFBP-L14 more strongly affected the ability of KIFBP to retrieve KIF1A from cell lysates than KIF15. In our experiments with purified proteins, we observed reduced binding of KIFBP-L14^{m} to KIF15, but only minimal reduction in binding to KIF18A (Fig. 4.6). Surprisingly, in cells, KIFBP-L14^{m} reduced the ability of KIFBP to disrupt metaphase chromosome alignment, spindle length homeostasis and KIF18A localization (Fig. 4.7 & 4.8). However, high levels of KIFBP-L14^{m} did produce phenotypes associated with KIFBP overexpression, suggesting that KIFBP-L14^{m} is capable of weak interactions with KIF18A and/or KIF15. This discrepancy in binding is surprising since the region implicated in interaction with KIFBP-L14, kinesin Loop-8, is highly conserved between KIF15 and KIF18A. Furthermore, the precise binding site of KIFBP-L1 on KIF15/KIF18A is unclear, impeding a more detailed comparison between the KIFBP-L1 and -L14 interaction surfaces. Taken together, these data suggest KIFBP-L14 may be more important for binding some kinesins than others, but that binding for all three kinesins collectively tested (KIF15, KIF18A, and KIF1A) was reduced beyond some cellular threshold necessary for producing the observed phenotypes of mitotic defects or reduced peroxisome transport. More work is required to relate the ability of KIFBP to bind kinesin motors in vitro to its ability to regulate kinesins in cells.

Lastly, we observed a high density of crosslinks between KIFBP-HP9b (residues K610 and K617) and the microtubule-binding interface of KIF15 (Fig. 4.4). These structural elements are not within the crosslinking range of BS3 in our cryo-EM structures (Fig. 4.2 & 4.5), and the significance of these crosslinks is therefore not clear. Perhaps in line with this, our analysis of the charge-neutralization mutant KIFBP-HP9b^{m} revealed that this mutation had little effect on *in vitro* interaction with KIF15 or KIF18A or on the mitotic phenotypes we quantified, suggesting that electrostatic interactions with amino acids 610-617 of KIFBP are not critical for kinesin interaction. A role for the C-terminus in KIFBP-motor interactions should not be dismissed, as a recent study identified a novel nonsense KIFBP mutation in a GOSHS patient that truncates the protein at position 593 (Cubuk 2021). It will be interesting to determine if the C-terminus of KIFBP is generally important

for its interaction with all kinesins, or if it instead drives interactions with kinesins that are more clinically relevant to GOSHS.

4.4.2 KIFBP remodels the kinesin motor head to displace kinesin-α4

Kinesin α4 helix plays a critical role in motor-KIFBP binding. Lysine residues within KIFBP-HP4a (K205) and KIFBP-LH (K307) crosslink residues located in KIF15-L11 (K273 and K283). Surprisingly, residues in KIFBP-L1 (K26, K30, K36) also crosslinked KIF15 residues K273 and K283. The significance of these crosslinks is not clear, but these data may suggest that an intermediary complex between KIFBP and kinesin motor domains, driven by the interaction of KIFBP-L1 with kinesin Loop11, may form prior to the acquisition of the final bound state.

One outstanding question concerns the mechanism by which KIF15/KIF18A α4 undergoes long-range motion to achieve KIFBP binding. The simplest possibility is that α4 is positionally unstable. If sufficiently compliant, the adjacent loops, *i.e.*, Loops11 and 12, may allow α4 excursions that eventually result in “capture” of α4 by KIFBP. Long-range motions of α4 are not without precedent. For example, Wang *et al.* (2016) observed by X-ray crystallography that α4 of KIF19 is positioned much farther from the motor head than is typical (Wang, Nitta, Hirokowa 2016). Our MD work, however, suggests that α4 remains closely associated with the motor head (Fig. S4.14), leading us to speculate that the binding of a motor head by KIFBP results in allosteric changes in the structure of both proteins, inducing motions of α4 that predispose it to KIFBP binding. Comparison of KIF15 in apo *versus* bound states supports this possibility (Fig. 4.2D-E). When bound to KIFBP, KIF15 showed a shift of several α helices (α1, α3, α6) away from the core of the motor as well as large movements of several beta-strand pairs. The movement of these structural elements causes the motor to assume a more open conformation.

Another unresolved issue is the functional relevance of α4 extraction by KIFBP. α4 is displaced a substantial distance from its position in the motor head (Fig. 4.2A-C), but it is unclear why this displacement is advantageous for the mechanism of action by KIFBP. In principle, steric inhibition of the KIF15/KIF18A microtubule-binding domain should be sufficient to prevent motor-microtubule binding. One possibility is that α4 extraction is necessary for the formation of a stable, long-lived complex; however, as mentioned

above, our MD analysis suggests that α4 is only available for extraction due to allosteric changes caused by KIFBP binding. Additionally, mutating KIFBP Loop-1 disables both *in vitro* interaction (Fig. 4.6) and motor inhibition in cells (Fig. 4.7 & 4.8), indicating that α4 displacement is not sufficient for complex formation. Another possibility is that α4 extraction is necessary for complex maintenance, perhaps serving to lock the motor in a bound conformation. It is also yet unknown how KIFBP dissociates from kinesin motor domains; it is possible that the interaction of α4 with HP4a/b-HP5 may be stable enough to require some form of active regulation for disengagement. Future work is required to elucidate the functional implications of α4 extraction.

In summary, our work establishes a structural mechanism by which KIFBP inactivates the microtubule-binding activity of mitotic kinesins KIF15 and KIF18A. Unlike common TPR tandem proteins, KIFBP uses multivalency to form a complex with the kinesin motor head. Multivalency may explain why it has not been possible to identify a consensus sequence for kinesin motors that bind KIFBP *versus* those that do not (Atherton et al. 2020). Our MD simulations and PCA analysis also indicate that motor-specific steric clashes may serve as a mechanism that prevents certain motors from binding KIFBP. Specifically, we observed that L11 of KIF5C would sterically clash with KIFBP-HP2, whereas L11 of KIF15 and KIF18A fits within the cavity between HP3 & HP4 of KIFBP. Further work is required to test the generality of this idea. An additional area for future work is to reveal the mechanism by which KIFBP dissociates from a kinesin motor. The multivalency with which KIFBP interacts with a kinesin motor, in particular the interaction of HP4a/b-HP5 with α4, suggests that a motor will not readily disengage from KIFBP. Motor recycling may require active regulation, e.g., phosphorylation, as proposed in earlier work (Kevenaar et al. 2016).

4.5 Materials and Methods

4.5.1 Plasmid construction

The following plasmids that were used in this study were previously described elsewhere: GST-KIFBP (Malaby et al. 2019), mCherry and mCherry-KIFBP expression plasmids (Malaby et al. 2019). The construction of the other plasmids used in this study is described as follows.

His_6-KIF15-N375 was created through isothermal assembly where the first 375 amino acids of the KIF15 open reading frame were amplified from pEGFP-C1-KIF15-FL (Sturgill et al. 2014) and inserted into the pET15b vector. Correct insertion was confirmed by sequencing.

His_6-KIF18A-N363 was created through isothermal assembly where a gBlock gene fragment of the first 363 amino acids of KIF18A codon-optimized for expression in E. coli (IDT) was inserted into the pET15b vector. Correct insertion was confirmed by sequencing.

GST-KIFBP-$L1^m$ was created by site-directed mutagenesis of GST-KIFBP, replacing amino acids 21-40 with the altered amino acid sequence described in **Fig. 6B**. Similarly, GST-KIFBP-$HP9b^m$ was created by site-directed mutagenesis of GST-KIFBP replacing amino acids 610-617 with the altered amino acids sequence described in **Fig. 6B**. Mutagenesis was confirmed by sequencing of the open reading frame. mCherry-KIFBP-$L1^m$ and mCherry-KIFBP-$HP9b^m$ were created in the same manner by site-directed mutagenesis of the mCherry-KIFBP wild-type plasmid using the primers described in the Key Resources Table. PCR products were circularized using the commercially available KLD Enzyme Mix (New England Biolabs). The resulting plasmids were confirmed by sequencing.

To create the mCherry-KIFBP-$L14^m$ plasmid, a GeneStrand containing KIFBP base pairs 1092-1588 with the $L14^m$ mutations was synthesized (Eurofins) (Sequence provided in Key Resources Table). This gene fragment was then inserted into the mCherry-KIFBP expression vector by isothermal assembly using the commercially available Gibson Assembly Master Mix (New England Biolabs) after PCR amplification of the mCherry-KIFBP expression vector with the primers described in the Key Resources Table. The resulting clones were confirmed by sequencing. GST-KIFBP-$L14^m$ was then created by isothermal assembly wherein the full KIFBP sequence containing the mutated residues was inserted into the pGEX-6P-1 vector. Correct insertion was confirmed via sequencing.

4.5.2 Protein expression and purification

Expression of GST-KIFBP, GST-KIFBP-L1^{m}, GST-KIFBP-L14^{m}, and GST-KIFBP-HP9b^{m} were induced in BL21-DE3 cells with 0.4 M IPTG overnight at 16° C. Cells were pelleted and resuspended in lysis buffer (1X PBS, 0.5 mM NaCl, 5 mM β-mercaptoethanol, 1% NP-40, and protease inhibitors [1 mM PMSF, 1 mM benzamidine, and 10 ug/mL LPC]), after which they were incubated with 1 mg/mL lysozyme for 30 minutes on ice followed by sonication. The lysate was clarified by centrifugation for 30 min at 35,000 rpm at 4°C in a Type 45 Ti rotor (Beckman). Cleared lysate was incubated with 2 mL glutathione-sepharose (Thermo Fisher Scientific) for 1 hr and washed with 50 mL [25 CV (column volume)] wash buffer (1X PBS, 0.5 M NaCl, 5 mM β-mercaptoethanol). Resin was incubated with 200 µL PreScission Protease (Cytiva) in 2 mL cleavage buffer (50 mM Tris-HCl, pH 7.0, 150 mM NaCl, 1 mM EDTA, 1 mM DTT) for 4 hr at 4° C to cleave the GST tag. Protein was eluted with 50 mM Tris-HCl, pH 8.0, and peak fractions were combined and clarified by centrifugation for 5 min at 20,000 rpm at 4°C, after which they were subjected to size exclusion chromatography on a Superdex 200 column (GE Healthcare) equilibrated in 10 mM K-HEPES, pH 7.7, 50 mM KCl, and 1 mM DTT. Protein concentration of fractions after gel filtration were estimated using a Bradford assay, after which peak fractions were combined, concentrated to >1 mg/mL using Amicon 10 kDa centrifugal filter units (Millipore), and either used immediately for cryo-EM or flash frozen and stored at -80°C.

Expression of His$_6$-KIF15-N375 and His$_6$-KIF18A-N363 was induced in BL21-DE3 cells with 0.4 M IPTG overnight at 16° C. Cells were pelleted and resuspended in lysis buffer (1X PNI [50 mM sodium phosphate, 500 mM NaCl, 20 mM imidazole], 1% NP-40, 1 mM MgATP, and protease inhibitors [1 mM PMSF, 1 mM benzamidine, and 10 ug/mL LPC]), after which they were incubated with 1 mg/mL lysozyme for 30 minutes on ice followed by sonication. The lysate was clarified by centrifugation for 30 min at 35,000 rpm at 4°C in a Type 45 Ti rotor (Beckman). Cleared lysate was incubated with 2 mL Ni-NTA agarose (Qiagen) for 1 hr and washed with 50 mL wash buffer (1X PNI, 100 µM MgATP, 5 mM β-mercaptoethanol). Protein was eluted with elution buffer (1X PNI, 100 µM MgATP, 5 mM β-mercaptoethanol, 200 mM imidazole) and peak fractions were combined and clarified by centrifugation for 5 min at 20,000 rpm at 4°C, after which they were subjected to size exclusion chromatography on a Superdex 200 column equilibrated in

gel filtration buffer (10 mM K-HEPES, pH 7.7, 50 mM KCl, 1 mM DTT, and 0.2 mM MgATP). Protein concentration of fractions after gel filtration were estimated using a Bradford assay, after which peak fractions were combined and concentrated to >1 mg/mL using Amicon 10 kDa centrifugal filter units (Millipore). Prior to cryo-EM grid preparation, the protein was then mixed with equimolar KIFBP and subjected to size exclusion chromatography a second time on a Superose 6 column (GE Healthcare) equilibrated with gel filtration buffer. Peak fractions were analyzed by SDS-PAGE and stained with Coomassie blue. Fraction(s) containing only the two proteins of interest were then combined, concentrated to >1 mg/mL, and used immediately for cryo-EM.

4.5.3 Cryo-EM grid preparation and data collection

For cryo-EM grid preparation, after size exclusion chromatography, KIFBP was concentrated to 4mg/ml whereas KIFBP:KIF15 and KIFBP:KIF18A complexes were each concentrated to 1mg/ml. Aliquots of 4µL were applied on glow-discharged UltrAuFoil R(1.2/1.3) 300 mesh gold grids (Electron Microscopy Sciences). The grids were then blotted with filter paper and plunge-frozen into liquid ethane cooled by liquid nitrogen using a Vitrobot Mark IV (Thermo Fisher Scientific) set to 4°C, 100% humidity, 1.5s blot, and a force of 20.

For KIFBP and KIFBP:KIF15 samples, datasets were collected using Leginon (Suloway et al. 2009) on a Thermo Fisher Scientific Glacios transmission electron microscope operating at 200keV equipped with a Gatan K2 Summit direct electron detector (Gatan Inc.) in counting mode. For KIFBP, a total of 11,086 micrographs were collected through 3 data collection sessions with total doses of 58-68$e^-/Å^2$ during exposure time of 7-9s, dose fractionated into 35-45 movie frames at defocus ranges of 1-2µm. The magnification used here is 45000x, resulting in a physical pixel size of 0.98 Å per pixel. For KIFBP:KIF15, 4 data collection sessions were performed with 45000x magnification and a physical pixel size of 0.98 Å per pixel. A total number of 6,184 micrographs were collected with a total dose of 60 $e^-/Å^2$ during 6-7s exposure time, dose fractionated into 30-35 movie frames.

Data collection for the KIFBP:KIF18A sample was automatically collected using Leginon(*49*) on an FEI Talos Arctica transmission electron microscope operating at

200keV equipped with a Gatan K2 Summit direct electron detector in counting mode. Three datasets were collected, resulting in a total 4,669 micrographs in a physical pixel size of 0.91 Å per pixel. The total dose ranges from 52-62 $e^-/Å^2$ in a 7-8s exposure time with dose fractionated into 35-40 movie frames.

4.5.4 Cryo-EM data processing

The data processing diagram for KIFBP is shown in **Fig.s S2 & S3**. Movie alignment, Contrast Transfer Function (CTF) parameter estimation, and particle picking were performed using Warp (Tegunov and Cramer 2019). The resulting particles were imported into cryoSPARC (Punjani et al. 2017) and underwent iterative 2D classification to remove incorrect particle picks. We initially analyzed sample heterogeneity in 'dataset3' using *ab-initio* reconstruction with 3 classes. Particles from the one higher-resolution class were then subjected to another round *ab-initio* reconstruction with 2 classes, resulting in two very similar classes. After careful examination, we believe that the first class is the full-length KIFBP map, while the other is the KIFBP lack of the C-terminal helices, explaining why some class averages are missing the C-terminal helices pairs of the KIFBP.

To resolve the structure of the full KIFBP, we deliberately selected the class averages from 'dataset1' and 'dataset2' that resemble the full KIFBP molecule using cryoSPARC (Punjani et al. 2017). These particles were then combined with the particles from the full-length KIFBP class in 'dataset3' and subjected to *ab-initio* reconstruction with 2 classes. Particles from the higher-resolution classes were selected for non-uniform refinement (Punjani. Zhang, and Fleet 2020) to obtain a 4.7Å resolution map. The map quality was improved to 4.6Å using local refinement with a static mask. The resulting map was manually sharpened for the visual inspection purpose using a B-factor of -50$Å^2$.

Next, we focused on analyzing the N-terminus of KIFBP lacking the C-terminal helices to try to improve the resolution. Particles from 'dataset2' were chosen since CTF fit resolution in 'dataset2' was the best among all three datasets. 913,455 particles from Warp (Tegunov and Cramer 2019) were imported into cryoSPARC (Punjani et al. 2017). We then performed iterative heterogeneous refinement with one class from the KIFBP lacking the C-terminal helices and two low-resolution classes from failed *ab-initio*

reconstruction jobs. 301,491 particles corresponding to KIFBP were enriched after extensive heterogeneous refinement and 2D classification. These particles were then subjected to homogeneous refinement and local refinement, resulting in a 3.8Å resolution map. However, the quality of the map was not satisfactory. To improve the map quality, the particles were exported into RELION-3.1 (Scheres 2012) and underwent one round of 3D auto-refinement to obtain a reconstruction at 4.2Å. Subsequently, two rounds of CTF refinement were performed to correct for beam tilt (Zivanov et al. 2018). 3D auto-refinement with refined beam-tilt yielded an estimated resolution of 4.1Å. We then exported micrograph motion trajectories from Warp and performed Bayesian polishing (Zivanov, Nakane, and Scheres 2019) to optimize per-particle motion tracks. 3D auto-refinement from the polished particles resulted in a 3.8Å map. Following this step, one round of 3D classification with 6 classes was performed to further remove heterogeneity. 5 classes corresponding to KIFBP lacking the C-terminus were selected and underwent another round of refinement, yielding a 3.8Å resolution map. The particles were then re-extracted and re-centered. The following 3D auto-refinement yielded a 4Å map. Bayesian polishing was performed on this particle stack, resulting in an improved map quality. 3D classification without alignment using T=12 resulted in one high-resolution class. 3D auto-refinement using the 128,190 particles from this high-resolution class gave a 3.8Å map with improved map quality.

For KIFBP:KIF15, all the data processing steps were performed in cryoSPARC (Punjani et al. 2017), as presented in **Fig. S8**. To generate an initial map for the KIFBP:KIF15 complex, 1,007 movies from dataset1 were imported into cryoSAPRC (Punjani et al. 2017). Patch motion correction and patch CTF estimation were used to correct beam-induced motion and estimate CTF parameters. 235,721 particles were automatically picked using the Topaz general model (Bepler et al. 2019). These particles were then subjected to iterative 2D classification to remove incorrect particle picks. The resulting 32,262 particles were used for *ab-initio* reconstruction with one class and also retraining Topaz. The model from the ab-initio reconstruction was refined to ~7Å and used as a template for the heterogeneous refinement in the following steps.

Movies from dataset1, 2, 3, and 4 were imported into cryoSPARC (Punjani et al. 2017) and processed separately at the beginning steps. Movies were aligned using patch

motion correction with dose weighting. CTF parameters were estimated with patch CTF estimation. Micrographs with CTF fit resolution below 5Å were selected and subjected to particle picking using a restrained Topaz model. The picked particles underwent one round 2D classification to remove incorrect particle picks. We then performed iterative heterogeneous refinement with one class from the initial template and two low-resolution classes from the early-terminated *ab-initio* reconstruction jobs to enrich particles corresponding to KIFBP:KIF15 complex. The resulting particles were further cleaned by 2D classification and *ab-initio* reconstruction with multi-classes. Particles from the individual dataset were then re-extracted, re-centered and combined, resulting in 189,984 particles. These particles were subsequently classified into three classes using *ab-initio* reconstruction. Two classes showing KIFBP and KIF15 density were merged and further classified into two classes with *ab-initio* reconstruction. One class with the better KIF15 motor domain density was selected and subjected to homogenous refinement, resulting in a 4.8Å resolution map. Then local refinement with a user-defined mask was performed to improve the map quality.

For KIFBP:KIF18A, the data processing diagram is presented in **Fig. S11.** A total 4,669 micrographs were collected through three datasets. For each dataset, motion correction, CTF estimation and particle picking was performed in Warp (Tegunov and Cramer 2019), resulting in 71,529 particles (dataset1), 94,716 particles (dataset2) and 638,186 particles (dataset3). These particles were imported into cryoSPARC(*51*) and underwent interactive 2D classification to remove incorrect particle picks. The remaining 156,159 particles were used for *ab-initio* reconstruction into four classes in cryoSPARC. 54,801 particles from the class with clear KIF18A density were selected for homogeneous refinement to obtain a 5 Å resolution structure of the KIFBP:KIF18A complex. The quality of the map was further improved by local refinement in cryoSPARC with a user-defined mask.

4.5.5 Model building

To construct an atomic model of KIFBP, first, we began by *de novo* building of the 3.8Å KIFBP reconstruction using Coot (Emsley et al. 2012) on the RELION (Scheres 2012) post-processed reconstruction. To guide model building, we used density

modification with DeepEMhancer (Sanchez-Garcia et al. 2020) that was run on the COSMIC^2 science gateway (Cianfrocco et al. 2017) to help interpret the cryo-EM density. From this process, we built amino acids 5-403 of KIFBP and the RELION post-processed map was used for model refinement and validation using Phenix (Liebschner et al. 2019). After building this high-resolution part of our reconstruction, we built poly-alanine models for the C-terminal helices KIFBP-HP6b, -HP7, -HP8, and HP9 using Coot (Sanchez-Garcia et al. 2020). The manual build model was then subjected to real-space refinement in Phenix (Liebschner et al. 2019).

Due to the moderate resolution (4.8Å) of KIF15:KIFBP, we built the model of KIF15:KIFBP using a combination of Rosetta-CM (Song et al. 2013), Rosetta-Relax, and manual building in Coot (Emsley et al. 2010). For the KIFBP model, we manually docked the KIFBP model into the density using Chimera (Pettersen et al. 2004) after which we fit the model into the density Rosetta-Relax. To fit KIF15 into the density, we manually docked KIF15 (PDB: 4BN2) (Klejnot et al. 2014) into the cryo-EM density, removing KIF15-L11,-α4, and -L12 from the model. With this docking, we then ran Rosetta-CM (Song et al. 2013), using atomic models 1V8K (Chain A) (Ogawa et al. 2004), 2OWM (Chain B) (Marx et al. 2008), 3U06 (Chain A) (Liu, Pemble, and Endow 2012), 4BN2 (Chain C) (Kleijnot et al. 2014), 5GSZ (Chain A) (Wang et al. 2016), 5MIO (Chain C) (Wang et al. 2017), 5MLV (Chain D) (von Loeffelholz et al. 2019a), 5MM4 (Chain K) (von Loeffelholz et al. 2019b), 5MM7 (Chain K) (von Loeffelholz et al. 2019b), 6B0I (Chain K) (Benoit, Asenjo, and Sosa 2018) as the library of fragments for rebuilding. After running Rosetta-CM to calculate 5000 models, we used the lowest scoring model for the final step of Rosetta-Relax. To build KIF15-L11,-α4, and -L12, we built a polyalanine model manually using Coot (Emsley et al. 2010).

For the KIF18A:KIFBP model, we used Rosetta-Relax to fit the KIFBP model into the density. The KIF18A motor, we manually docked the crystal structure of KIF18A (PDB: 3LRE) (Peters et al. 2010) into the density with the exception of KIF18A-L11,-α4, and -L12. To build KIF18A-L11,-α4, and -L12, we built a polyalanine model manually using Coot (Emsley et al. 2010).

The efficiency (cryoEF) (Navdenova and Russo 2017) for each reconstruction was calculated on the COSMIC^2 science gateway (Cianfrocco et al. 2017). Fig.s were prepared using Chimera (Pettersen et al. 2004) and ChimeraX (Pettersen et al. 2021).

4.5.6 Crosslinking mass spectrometry

His_6-KIF15-N375 and KIFBP were purified as described above. An equimolar solution of both proteins was prepared in a crosslinking buffer (40 mM HEPES pH 7.4) where the total protein concentration was 10 uM and the amount of each protein was at least 20 ug. A 50 mM solution of the 11 Å lysine-targeting crosslinker BS3 was prepared in water and added to the reaction in a 100-molar excess. The reaction proceeded for 30 min while rotating at 4° C, after which it was quenched with Tris-HCl pH 7.5 at a final concentration of 50 mM. As an un-crosslinked control, a separate reaction was prepared and quenched the same way but no crosslinker was added.

The crosslinking reactions were resuspended in 50 µL of 0.1M ammonium bicarbonate buffer (pH~8). Cysteines were reduced by adding 50 µL of 10 mM DTT and incubating at 45°C for 30 min. Samples were cooled to room temperature and alkylation of cysteines was achieved by incubating with 65 mM 2-Chloroacetamide, under darkness, for 30 min at room temperature. Overnight digestion with 1:50 enzyme:substrate modified trypsin was carried out at 37°C with constant shaking in a Thermomixer. Digestion was stopped by acidification and peptides were desalted using SepPak C18 cartridges using the manufacturer's protocol (Waters). Samples were completely dried via Vacufuge. Resulting peptides were dissolved in 9 µL of 0.1% formic acid/2% acetonitrile solution, and 2 µL of the peptide solution were resolved on a nano-capillary reverse phase column (Acclaim PepMap C18, 2 micron, 50 cm, ThermoScientific) using a 0.1% formic acid/2% acetonitrile (Buffer A) and 0.1% formic acid/95% acetonitrile (Buffer B) gradient at 300 nl/min over a period of 180 min (2-25% buffer B in 110 min, 25-40% in 20 min, 40-90% in 5 min followed by holding at 90% buffer B for 10 min and equilibration with Buffer A for 30 min). The eluent was directly introduced into a Q exactive HF mass spectrometer (Thermo Scientific, San Jose CA) using an EasySpray source. MS1 scans were acquired at 60K resolution [automatic gain control (AGC) target, $3x10^6$; max injection time (IT), 50 ms]. Data-dependent collision-induced dissociation MS/MS spectra were acquired using

the Top speed method (3 seconds) following each MS1 scan (NCE ~28%; 15K resolution; AGC target $1x10^5$; max IT 45 ms).

pLink v2.3.9 was used to perform database searching against a FASTA protein sequence file containing full-length KIF15, KIFBP, and 292 common contaminant proteins. Raw data files were searched with BS3 as the crosslinker, Trypsin_P allowing up to 3 missed cleavages, peptide mass between 500 and 6000, peptide length between 5 and 60, precursor and fragment tolerances set to 20 ppm, fixed carbamidomethyl cysteine, variable methionine oxidation, 10 ppm filter tolerance, and separate 5% peptide spectrum match (PSM) false discovery rate (FDR). pLabel v2.4.1 was used to visualize crosslinked MS/MS spectra. Of the resulting FDR-filtered list of crosslinked peptides, we filtered out all intra-KIFBP and intra-KIF15 crosslinks, as well as crosslinks with contaminant proteins and crosslinks with an e-value >0.05.

4.5.7 In vitro pull-down assays

100 µL of Ni-NTA Agarose resin (Qiagen) per condition was equilibrated with binding buffer (10 mM HEPES pH 7.4, 50 mM KCl, 10 mM imidazole) and incubated with 250 µg of either His_6-KIF15-N375 or His_6-KIF18A-N363 for 30 min at 4°C. The kinesin-bound resin was then washed 3 times in batch with 10 CV of binding buffer, split into 20 µL aliquots, and incubated with 20 µg of either KIFBP-WT, KIFBP-$L1^m$, KIFBP-$L14^m$, KIFBP-$HP9b^m$, or GST in a total volume of 200 µL for 30 min at 4°C. To control for non-specific binding to the resin, 20 µL of resin was incubated with either 20 µg of WT-KIFBP or GST with no previous kinesin-incubation step. After incubation with GST or KIFBP proteins, the resin was pelleted and the supernatant was removed and saved for analysis. The resin was then washed 5 times with 10 CV of wash buffer (binding buffer with 0.05% Tween-20). After the final wash, each resin sample was resuspended in 80 µL of binding buffer, and samples were taken for analysis. 5% of each supernatant and pellet sample was boiled in 5X SDS-sample dye and loaded onto a 10% SDS-PAGE gel. Gels were stained with Coomassie-blue and quantifications of band intensities were done with ImageJ. Images for publication were enhanced with ImageJ, while quantification was done from raw images.

4.5.8 Cell culture and transfections

HeLa Kyoto cells were cultured at 37ºC with 5% CO_2 in MEM-α medium (Gibco) containing 10% Fetal Bovine Serum (FBS) (Gibco). For plasmid transfections in a 24-well plate format, ~75,000 cells in 500 µl MEM-α medium were seeded onto acid-washed glass coverslips and subsequently transfected with 375 ng mCherry alone or mCherry-KIFBP plasmid DNA (containing wild type KIFBP sequence or indicated KIFBP mutant). Cells were treated with mCherry and indicated mCherry-KIFBP plasmids that were preincubated for 10 minutes in 50 µl Opti-MEM (Gibco) and 1 µl Lipofectamine LTX reagent (Invitrogen). Plasmid transfections were incubated for 24 hours before fixation for immunofluorescence.

4.5.9 Cell fixation and immunofluorescence

For metaphase observations of spindle length and chromosome alignment, cells expressing mCherry and mCherry-KIFBP (wild type or indicated mutants) were treated with 20 µM MG132 (Selleck Chemicals) for 2 hours before fixation. Cells were fixed on coverslips in -20ºC methanol (Thermo Fisher Scientific) with 1% paraformaldehyde (Electron Microscopy Sciences) for 10 minutes on ice. Coverslips were then washed three times for 5 minutes each in Tris-Buffered Saline (TBS; 150 mM NaCl, 50 mM Tris base, pH 7.4). Coverslips were blocked for 1 hour at room temperature in 20% goat serum in antibody dilution buffer (Abdil: TBS pH 7.4, 1% Bovine Serum Albumin (BSA), 0.1% Triton X-100, and 0.1% sodium azide). Coverslips were then washed two times in TBS for 5 minutes each prior to the addition of primary antibodies. Primary antibodies were diluted in Abdil. For KIF18A localization analyses the following primary antibodies were used at the indicated dilutions: rat anti-α-tubulin 1:500 (MAB1864; Sigma Aldrich), rabbit anti-KIF18A 1:100 (A301-080A; Bethyl), and mouse anti-Hec1 1:500 (GTX70268; GeneTex). All mCherry images for KIF18A localization analyses are direct mCherry fluorescence. For KIF18A localization analyses the following secondary antibodies were used at 1:500 dilution: Goat anti-Rabbit IgG conjugated to Alexa Fluor 488 (A11034; Invitrogen), Goat anti-Mouse IgG conjugated to Alexa Fluor 405 (A31553; Invitrogen), and Goat anti-Rat IgG conjugated to Alexa Fluor 647 (A21247, Invitrogen). For spindle length and chromosome alignment analyses, the following primary antibodies were used at the indicated dilutions: mouse anti-γ-tubulin 1:500 (T5326; Sigma Aldrich), rabbit anti-

mCherry 1:500 (ab167453; Abcam), human anti-centromere antibody (ACA) 1:250 (15-235; Antibodies Inc.). All primary antibodies were incubated for 1 hour at room temperature with the exception of the human ACA antibody, which was incubated at 4^{o}C overnight. For spindle length and chromosome alignment analyses the following secondary antibodies were used at 1:500 dilution: Goat anti-Human IgG conjugated to Alexa Fluor 488 (A11013; Invitrogen), Goat anti-Mouse IgG conjugated to Alexa Fluor 647 (A21236; Invitrogen), and Goat anti-Rabbit IgG conjugated to Alexa Fluor 594 (A11037; Invitrogen). Coverslips were washed two times in TBS for 5 minutes each between primary and secondary antibody incubations. Coverslips were washed three times in TBS for 5 minutes each prior to mounting coverslips with Prolong Gold anti-fade mounting medium with DAPI (spindle length and chromosome alignment analyses) (P36935, Invitrogen) or Prolong Gold anti-fade mounting medium without DAPI (KIF18A localization analyses) (P36934, Invitrogen). Coverslips were imaged on a Ti-E inverted microscope (Nikon Instruments) using a Plan Apo λ 60x 1.42 NA objective, environmental chamber at 37^{o}C, a Clara cooled charge-coupled device (CCD) camera (Andor), and Nikon Elements Software (Nikon Instruments).

4.5.10 Chromosome Alignment Analysis

Cells expressing mCherry or indicated mCherry-KIFBP constructs were fixed and stained for mCherry, γ-tubulin, and ACA as described above. As described previously(Malaby et al. 2019; Wang et al. 2015), single focal plane images with both spindle poles in focus were acquired. A boxed region of interest with a fixed height and width defined by the length of the spindle was used to measure the distribution of ACA-labeled kinetochore fluorescence using the Plot Profile command in Fiji. The ACA signal intensity was normalized internally to its highest value and plotted as a function of distance along the pole-to-pole axis. These plots were then fitted to a Gaussian curve and the FWHM for the Gaussian fit as well as the spindle length are reported for each cell analyzed. Mean and standard deviations are reported from a minimum of three independent experiments for each construct. The following cell numbers were analyzed for the indicated mCherry and mCherry-KIFBP constructs: (1) mCherry (control) = 132

cells, (2) mCherry-KIFBP-WT = 165 cells, (3) mCherry-KIFBP-L1^{m} = 102 cells, (4) mCherry-KIFBP-L14^{m} = 99 cells, (5) mCherry-KIFBP-HP9b^{m} = 89 cells.

4.5.11 KIF18A Line Scan Analysis

Cells expressing mCherry or indicated mCherry-KIFBP constructs were fixed and stained for endogenous KIF18A, α-tubulin, and Hec1 as described above. Cells were imaged with 0.2 μm z-stacks throughout the entire cell. Within these z-sections, 2 μm line scans were manually drawn in Fiji for individual kinetochore microtubules (1-3 line scans per cell) and the profile intensities along those lines were measured and recorded for the KIF18A, α-tubulin, and Hec1 channels. Each of these profile intensities for KIF18A, α-tubulin, and Hec1 were normalized internally to its highest value. These normalized line scans were then aligned by peak Hec1 intensity and averaged for each pixel distance. Mean and standard deviations are reported from a minimum of three independent experiments for each construct. The following cell numbers and line scans were analyzed for the indicated mCherry and mCherry-KIFBP constructs: (1) mCherry (control) = 40 cells (64 lines), (2) mCherry-KIFBP-WT = 34 cells (64 lines), (3) mCherry-KIFBP-L1^{m} = 34 cells (64 lines), (4) mCherry-KIFBP-L14^{m} = 32 cells (68 lines), (5) mCherry-KIFBP-HP9b^{m} = 33 cells (63 lines).

4.5.12 Molecular Dynamics Simulations and Analysis

The structures of KIF5C, KIF15, KIF18A, and KIF11 bound to ADP and Mg^{2+} were taken from PDB structures 1BG2 (Kull et al. 1996), 4BN2 (Klejnot et al. 2014), 3LRE (Peters et al. 2010), and 1II6 (Turner et al. 2001), respectively. The missing residues of KIF5C were filled in as previously described (Budaitis et al. 2019). For all other proteins, I-TASSER was used to fill in the gaps of the remaining structures using the PDBs as primary template (Roy, Kucukural, and Zhang 2010; Yang et al. 2015a; Yang et al. 2015b). AmberTools was then used to prepare all systems for simulation (Case et al. 2021). Each system was solvated with a box of TIP3P water molecules with 10-Å padding around the protein. Na^{+} and Cl^{-} were added to both neutralize the systems and set the ionic concentration to 50 mM. NAMD was used to carry out the MD simulations with the amber ff19SB force field (Phillips et al. 2005; Tian et al. 2020). Force field parameters for the ADP nucleotide were obtained from the AMBER parameter database (Meagher,

Redman, and Carlson 2003). Following minimization, heating and equilibration, the systems were simulated at 300 K and 1 atm of pressure in an NpT ensemble. To allow for 2-fs time steps, bonded hydrogens were fixed. For long-range electrostatics, Particle Mesh Ewald was employed with a 10-Å cutoff and 8.5-Å switch distance for van der Waals interactions (Essmann et al. 1995). MD simulations were completed in 100 ns replicates starting from random velocities for a total simulation time of 500 ns for KIF5C, KIF11 and KIF18A, and 600 ns for KIF15.

All analysis was carried out using the Bio3d package (v 2.4.1) in R (Gran, Skjaerven, and Yao 2021). We first aligned our 4 kinesins of interest and then restricted analysis to the amino acids that appeared in all the motors. In order to focus on large-scale rearrangements in the motor head and remove the noise from fluctuating loops, we next restricted analysis to amino acids in stable secondary structures, leaving us with 154 amino acid positions in each protein. We performed Principal Component Analysis (PCA) using KIF15 as the reference structure. The remaining three kinesins simulations were then projected onto this KIF15 PCA space for direct comparison with each other and the cryo-EM structure.

4.6 Acknowledgments

We thank members of the Michigan Cytoskeleton Supergroup for helpful discussions and critical feedback. The authors thank Dr. Venkatesha Basrur of the Proteomics Resource Facility at the University of Michigan Medical School for providing technical expertise in mass spectrometry. Research reported in this publication was supported by the University of Michigan Cryo-EM Facility (U-M Cryo-EM). U-M Cryo-EM is grateful for support from the U-M Life Sciences Institute and the U-M Biosciences Initiative.

Funding: Start-up funds from the University of Michigan (R.O., M.A.C.); National Institutes of Health grant GM094231 (A.I.N.); National Institutes of Health grant GM136822 (D.S.); National Institutes of Health grant GM121491 (J.S.); National Institutes of Health grant GM086610 (R.O.); National Institutes of Health grant K12 GM111725 (L.J.); National Institutes of Health grant S10OD020011.

4.6.1 Author contributions

Conceptualization: R.O., M.A.C., A.L.S., J.S.; Methodology: A.L.S., Z.T., K.S., L.J., S.E.H.; Visualization: M.A.C., A.L.S., Z.T., K.L.S., D.S., S.E.H., A.I.N.; Supervision: R.O., M.A.C., J.S., D.S.; Writing—original draft: R.O., M.A.C., A.L.S., K.L.S., D.S., J.S.; Writing—review & editing: R.O., M.A.C., A.L.S., K.L.S., D.S., J.S.

4.7 References

Atherton, J., Hummel, J. J., Olieric, N., Locke, J., Peña, A., Rosenfeld, S. S., Steinmetz, M. O., Hoogenraad, C. C., & Moores, C. A. (2020). The mechanism of kinesin inhibition by kinesin-binding protein. eLife, 9. https://doi.org/10.7554/eLife.61481

Benoit, M. P. M. H., Asenjo, A. B., & Sosa, H. (2018). Cryo-EM reveals the structural basis of microtubule depolymerization by kinesin-13s. Nature Communications, 9(1), 1662.

Bepler, T., Morin, A., Rapp, M., Brasch, J., Shapiro, L., Noble, A. J., & Berger, B. (2019). Positive-unlabeled convolutional neural networks for particle picking in cryo-electron micrographs. Nature Methods, 16(11), 1153–1160.

Blangy, A., Lane, H. A., d'Hérin, P., Harper, M., Kress, M., & Nigg, E. A. (1995). Phosphorylation by p34cdc2 regulates spindle association of human Eg5, a kinesin-related motor essential for bipolar spindle formation in vivo. Cell, 83(7), 1159–1169.

Blasius, T. L., Cai, D., Jih, G. T., Toret, C. P., & Verhey, K. J. (2007). Two binding partners cooperate to activate the molecular motor Kinesin-1. The Journal of Cell Biology, 176(1), 11–17.

Bouchet, B. P., Gough, R. E., Ammon, Y.-C., van de Willige, D., Post, H., Jacquemet, G., Altelaar, A. M., Heck, A., Jr, Goult, B. T., & Akhmanova, A. (2016). Talin-KANK1 interaction controls the recruitment of cortical microtubule stabilizing complexes to focal adhesions. eLife, 5. https://doi.org/10.7554/eLife.18124

Brooks, A. S., Bertoli-Avella, A. M., Burzynski, G. M., Breedveld, G. J., Osinga, J., Boven, L. G., Hurst, J. A., Mancini, G. M. S., Lequin, M. H., de Coo, R. F., Matera, I., de Graaff, E., Meijers, C., Willems, P. J., Tibboel, D., Oostra, B. A., & Hofstra, R. M. W. (2005). Homozygous nonsense mutations in KIAA1279 are associated with malformations of the central and enteric nervous systems. American Journal of Human Genetics, 77(1), 120–126.

Brown, K. D., Coulson, R. M., Yen, T. J., & Cleveland, D. W. (1994). Cyclin-like accumulation and loss of the putative kinetochore motor CENP-E results from coupling continuous synthesis with specific degradation at the end of mitosis. The Journal of Cell Biology, 125(6), 1303–1312.

Budaitis, B. G., Jariwala, S., Reinemann, D. N., Schimert, K. I., Scarabelli, G., Grant, B. J., Sept, D., Lang, M. J., & Verhey, K. J. (2019). Neck linker docking is critical for Kinesin-1 force generation in cells but at a cost to motor speed and processivity. eLife, 8. https://doi.org/10.7554/eLife.44146

Cahu, J., Olichon, A., Hentrich, C., Schek, H., Drinjakovic, J., Zhang, C., Doherty-Kirby, A., Lajoie, G., & Surrey, T. (2008). Phosphorylation by Cdk1 increases the binding of

Eg5 to microtubules in vitro and in Xenopus egg extract spindles. PloS One, 3(12), e3936.

Cheng, L., Desai, J., Miranda, C. J., Duncan, J. S., Qiu, W., Nugent, A. A., Kolpak, A. L., Wu, C. C., Drokhlyansky, E., Delisle, M. M., Chan, W.-M., Wei, Y., Propst, F., Reck-Peterson, S. L., Fritzsch, B., & Engle, E. C. (2014). Human CFEOM1 mutations attenuate KIF21A autoinhibition and cause oculomotor axon stalling. Neuron, 82(2), 334–349.

Cho, K., Yi, H., Desai, R., Hand, A. R., Haas, A. L., & Ferreira, P. A. (2009). RANBP2 is an allosteric activator of the conventional kinesin-1 motor protein, KIF5B, in a minimal cell-free system. In EMBO reports (Vol. 10, Issue 5, pp. 480–486). https://doi.org/10.1038/embor.2009.29

Cianfrocco, M. A., Wong-Barnum, M., Youn, C., Wagner, R., & Leschziner, A. E. (2017, July 9). COSMIC2: A Science Gateway for Cryo-Electron Microscopy Structure Determination. Practice & Experience in Advanced Research Computing. Practice & Experience in Advanced Research Computing 2017 , New Orleans, LA.

Cross, R. A., & McAinsh, A. (2014). Prime movers: the mechanochemistry of mitotic kinesins. Nature Reviews. Molecular Cell Biology, 15(4), 257–271.

Cubuk, P. O. (2021). Goldberg-Shprintzen Syndrome Associated with a Novel Variant in the KIFBPGene. Molecular Syndromology, 1–4.

D.A. Case, H.M. Aktulga, K. Belfon, I.Y. Ben-Shalom, S.R. Brozell, D.S. Cerutti, T.E. Cheatham, III, V.W.D. Cruzeiro, T.A. Darden, R.E. Duke, G. Giambasu, M.K. Gilson, H. Gohlke, A.W. Goetz, R. Harris, S. Izadi, S.A. Izmailov, C. Jin, K. Kasavajhala, M.C. Kaymak, E. King, A. Kovalenko, T. Kurtzman, T.S. Lee, S. LeGrand, P. Li, C. Lin, J. Liu, T. Luchko, R. Luo, M. Machado, V. Man, M. Manathunga, K.M. Merz, Y. Miao, O. Mikhailovskii, G. Monard, H. Nguyen, K.A. O'Hearn, A. Onufriev, F. Pan, S. Pantano, R. Qi, A. Rahnamoun, D.R. Roe, A. Roitberg, C. Sagui, S. Schott-Verdugo, J. Shen, C.L. Simmerling, N.R. Skrynnikov, J. Smith, J. Swails, R.C. Walker, J. Wang, H. Wei, R.M. Wolf, X. Wu, Y. Xue, D.M. York, S. Zhao, and P.A. Kollman. (n.d.). Amber 2021.

Dafsari, H. S., Byrne, S., Lin, J.-P., Pitt, M., Jongbloed, J. D., Flinter, F., & Jungbluth, H. (2015). Goldberg-Shprintzen megacolon syndrome with associated sensory motor axonal neuropathy. American Journal of Medical Genetics. Part A, 167(6), 1300–1304.

Du, Y., English, C. A., & Ohi, R. (2010). The kinesin-8 Kif18A dampens microtubule plus-end dynamics. Current Biology: CB, 20(4), 374–380.

Emsley, P., Lohkamp, B., Scott, W. G., & Cowtan, K. (2010). Features and development of Coot. Acta Crystallographica. Section D, Biological Crystallography, 66(Pt 4), 486–501.

Espeut, J., Gaussen, A., Bieling, P., Morin, V., Prieto, S., Fesquet, D., Surrey, T., & Abrieu, A. (2008). Phosphorylation relieves autoinhibition of the kinetochore motor Cenp-E. Molecular Cell, 29(5), 637–643.

Essmann, U., Perera, L., Berkowitz, M. L., Darden, T., Lee, H., & Pedersen, L. G. (1995). A smooth particle mesh Ewald method. The Journal of Chemical Physics, 103(19), 8577–8593.

Fonseca, C., & Stumpff, J. (2016). Quantification of Mitotic Chromosome Alignment. Methods in Molecular Biology , 1413, 253–262.

Goshima, G., & Vale, R. D. (2005). Cell Cycle-dependent Dynamics and Regulation of Mitotic Kinesins in Drosophila S2 Cells. Molecular Biology of the Cell, 16(8), 3896–3907.

Grant, B. J., Skjaerven, L., & Yao, X.-Q. (2021). The Bio3D packages for structural bioinformatics. Protein Science: A Publication of the Protein Society, 30(1), 20–30.

Henrichs, V., Grycova, L., Barinka, C., Nahacka, Z., Neuzil, J., Diez, S., Rohlena, J., Braun, M., & Lansky, Z. (2020). Mitochondria-adaptor TRAK1 promotes kinesin-1 driven transport in crowded environments. Nature Communications, 11(1), 3123.

Hirokawa, N., Noda, Y., Tanaka, Y., & Niwa, S. (2009). Kinesin superfamily motor proteins and intracellular transport. Nature Reviews. Molecular Cell Biology, 10(10), 682–696.

Hirst, C. S., Stamp, L. A., Bergner, A. J., Hao, M. M., Tran, M. X., Morgan, J. M., Dutschmann, M., Allen, A. M., Paxinos, G., Furlong, T. M., McKeown, S. J., & Young, H. M. (2018). Publisher Correction: Kif1bp loss in mice leads to defects in the peripheral and central nervous system and perinatal death. Scientific Reports, 8(1), 9085.

Kevenaar, J. T., Bianchi, S., van Spronsen, M., Olieric, N., Lipka, J., Frias, C. P., Mikhaylova, M., Harterink, M., Keijzer, N., Wulf, P. S., Hilbert, M., Kapitein, L. C., de Graaff, E., Ahkmanova, A., Steinmetz, M. O., & Hoogenraad, C. C. (2016). Kinesin-Binding Protein Controls Microtubule Dynamics and Cargo Trafficking by Regulating Kinesin Motor Activity. Current Biology: CB, 26(7), 849–861.

Klejnot, M., Falnikar, A., Ulaganathan, V., Cross, R. A., Baas, P. W., & Kozielski, F. (2014). The crystal structure and biochemical characterization of Kif15: a bifunctional molecular motor involved in bipolar spindle formation and neuronal development. Acta Crystallographica. Section D, Biological Crystallography, 70(Pt 1), 123–133.

Kull, F. J., & Endow, S. A. (2013). Force generation by kinesin and myosin cytoskeletal motor proteins. Journal of Cell Science, 126(1), 9–19.

Kull, F. J., Sablin, E. P., Lau, R., Fletterick, R. J., & Vale, R. D. (1996). Crystal structure of the kinesin motor domain reveals a structural similarity to myosin. Nature, 380(6574), 550–555.

Kuriyama, R., Kofron, M., Essner, R., Kato, T., Dragas-Granoic, S., Omoto, C. K., & Khodjakov, A. (1995). Characterization of a minus end-directed kinesin-like motor protein from cultured mammalian cells. The Journal of Cell Biology, 129(4), 1049–1059.

Lee, Y. M., Kim, E., Park, M., Moon, E., Ahn, S.-M., Kim, W., Hwang, K. B., Kim, Y. K., Choi, W., & Kim, W. (2010). Cell cycle-regulated expression and subcellular localization of a kinesin-8 member human KIF18B. Gene, 466(1-2), 16–25.

Liebschner, D., Afonine, P. V., Baker, M. L., Bunkóczi, G., Chen, V. B., Croll, T. I., Hintze, B., Hung, L. W., Jain, S., McCoy, A. J., Moriarty, N. W., Oeffner, R. D., Poon, B. K., Prisant, M. G., Read, R. J., Richardson, J. S., Richardson, D. C., Sammito, M. D., Sobolev, O. V., … Adams, P. D. (2019). Macromolecular structure determination using X-rays, neutrons and electrons: recent developments in Phenix. Acta Crystallographica. Section D, Structural Biology, 75(Pt 10), 861–877.

Liu, H.-L., Pemble, C. W., 4th, & Endow, S. A. (2012). Neck-motor interactions trigger rotation of the kinesin stalk. Scientific Reports, 2, 236.

Lyons, D. A., Naylor, S. G., Mercurio, S., Dominguez, C., & Talbot, W. S. (2008). KBP is essential for axonal structure, outgrowth and maintenance in zebrafish, providing insight into the cellular basis of Goldberg-Shprintzen syndrome. Development , 135(3), 599–608.

Malaby, H. L. H., Dumas, M. E., Ohi, R., & Stumpff, J. (2019). Kinesin-binding protein ensures accurate chromosome segregation by buffering KIF18A and KIF15. The Journal of Cell Biology, 218(4), 1218–1234.

Mapelli, M., & Gonzalez, C. (2012). On the inscrutable role of Inscuteable: structural basis and functional implications for the competitive binding of NuMA and Inscuteable to LGN. Open Biology, 2(8), 120102.

Marx, A., Müller, J., Mandelkow, E.-M., Woehlke, G., Bouchet-Marquis, C., Hoenger, A., & Mandelkow, E. (2008). X-ray structure and microtubule interaction of the motor domain of Neurospora crassa NcKin3, a kinesin with unusual processivity. Biochemistry, 47(7), 1848–1861.

Mayr, M. I., Hümmer, S., Bormann, J., Grüner, T., Adio, S., Woehlke, G., & Mayer, T. U. (2007). The human kinesin Kif18A is a motile microtubule depolymerase essential for chromosome congression. Current Biology: CB, 17(6), 488–498.

Meagher, K. L., Redman, L. T., & Carlson, H. A. (2003). Development of polyphosphate parameters for use with the AMBER force field. Journal of Computational Chemistry, 24(9), 1016–1025.

Naydenova, K., & Russo, C. J. (2017). Measuring the effects of particle orientation to improve the efficiency of electron cryomicroscopy. In Nature Communications (Vol. 8, Issue 1). https://doi.org/10.1038/s41467-017-00782-3

Nogales, E., Wolf, S. G., Khan, I. A., Ludueña, R. F., & Downing, K. H. (1995). Structure of tubulin at 6.5 A and location of the taxol-binding site. Nature, 375(6530), 424–427.

Ogawa, T., Nitta, R., Okada, Y., & Hirokawa, N. (2004). A common mechanism for microtubule destabilizers-M type kinesins stabilize curling of the protofilament using the class-specific neck and loops. Cell, 116(4), 591–602.

Perez-Riba, A., & Itzhaki, L. S. (2019). The tetratricopeptide-repeat motif is a versatile platform that enables diverse modes of molecular recognition. Current Opinion in Structural Biology, 54, 43–49.

Peters, C., Brejc, K., Belmont, L., Bodey, A. J., Lee, Y., Yu, M., Guo, J., Sakowicz, R., Hartman, J., & Moores, C. A. (2010). Insight into the molecular mechanism of the multitasking kinesin-8 motor. The EMBO Journal, 29(20), 3437–3447.

Pettersen, E. F., Goddard, T. D., Huang, C. C., Couch, G. S., Greenblatt, D. M., Meng, E. C., & Ferrin, T. E. (2004). UCSF Chimera--a visualization system for exploratory research and analysis. Journal of Computational Chemistry, 25(13), 1605–1612.

Pettersen, E. F., Goddard, T. D., Huang, C. C., Meng, E. C., Couch, G. S., Croll, T. I., Morris, J. H., & Ferrin, T. E. (2021). UCSF ChimeraX: Structure visualization for researchers, educators, and developers. Protein Science: A Publication of the Protein Society, 30(1), 70–82.

Phillips, J. C., Braun, R., Wang, W., Gumbart, J., Tajkhorshid, E., Villa, E., Chipot, C., Skeel, R. D., Kalé, L., & Schulten, K. (2005). Scalable molecular dynamics with NAMD. Journal of Computational Chemistry, 26(16), 1781–1802.

Punjani, A., Rubinstein, J. L., Fleet, D. J., & Brubaker, M. A. (2017). cryoSPARC: algorithms for rapid unsupervised cryo-EM structure determination. Nature Methods, 14(3), 290–296.

Punjani, A., Zhang, H., & Fleet, D. J. (2020). Non-uniform refinement: adaptive regularization improves single-particle cryo-EM reconstruction. Nature Methods, 17(12), 1214–1221.

Roy, A., Kucukural, A., & Zhang, Y. (2010). I-TASSER: a unified platform for automated protein structure and function prediction. Nature Protocols, 5(4), 725–738.

Sanchez-Garcia, R., Gomez-Blanco, J., Cuervo, A., Carazo, J. M., Sorzano, C. O. S., & Vargas, J. (2020). DeepEMhancer: a deep learning solution for cryo-EM volume post-processing. In bioRxiv (p. 2020.06.12.148296). https://doi.org/10.1101/2020.06.12.148296

Santamaria, A., Nagel, S., Sillje, H. H. W., & Nigg, E. A. (2008). The spindle protein CHICA mediates localization of the chromokinesin Kid to the mitotic spindle. Current Biology: CB, 18(10), 723–729.

Scheres, S. H. W. (2012a). A Bayesian view on cryo-EM structure determination. Journal of Molecular Biology, 415(2), 406–418.

Scheres, S. H. W. (2012b). RELION: implementation of a Bayesian approach to cryo-EM structure determination. Journal of Structural Biology, 180(3), 519–530.

Scheufler, C., Brinker, A., Bourenkov, G., Pegoraro, S., Moroder, L., Bartunik, H., Hartl, F. U., & Moarefi, I. (2000). Structure of TPR domain-peptide complexes: critical elements in the assembly of the Hsp70-Hsp90 multichaperone machine. Cell, 101(2), 199–210.

Seeger, M. A., & Rice, S. E. (2013). Intrinsic Disorder in the Kinesin Superfamily. Biophysical Reviews, 5(3). https://doi.org/10.1007/s12551-012-0096-5

Siddiqui, N., Zwetsloot, A. J., Bachmann, A., Roth, D., Hussain, H., Brandt, J., Kaverina, I., & Straube, A. (2019). PTPN21 and Hook3 relieve KIF1C autoinhibition and activate intracellular transport. Nature Communications, 10(1), 1–16.

Song, Y., DiMaio, F., Wang, R. Y.-R., Kim, D., Miles, C., Brunette, T., Thompson, J., & Baker, D. (2013). High-resolution comparative modeling with RosettaCM. Structure , 21(10), 1735–1742.

Sosa, H., Dias, D. P., Hoenger, A., Whittaker, M., Wilson-Kubalek, E., Sablin, E., Fletterick, R. J., Vale, R. D., & Milligan, R. A. (1997). A model for the microtubule-Ncd motor protein complex obtained by cryo-electron microscopy and image analysis. Cell, 90(2), 217–224.

Sturgill, E. G., Das, D. K., Takizawa, Y., Shin, Y., Collier, S. E., Ohi, M. D., Hwang, W., Lang, M. J., & Ohi, R. (2014). Kinesin-12 Kif15 targets kinetochore fibers through an intrinsic two-step mechanism. Current Biology: CB, 24(19), 2307–2313.

Suloway, C., Shi, J., Cheng, A., Pulokas, J., Carragher, B., Potter, C. S., Zheng, S. Q., Agard, D. A., & Jensen, G. J. (2009). Fully automated, sequential tilt-series acquisition with Leginon. Journal of Structural Biology, 167(1), 11–18.

Tegunov, D., & Cramer, P. (2019). Real-time cryo-electron microscopy data preprocessing with Warp. Nature Methods, 16(11), 1146–1152.

Tian, C., Kasavajhala, K., Belfon, K. A. A., Raguette, L., Huang, H., Migues, A. N., Bickel, J., Wang, Y., Pincay, J., Wu, Q., & Simmerling, C. (2020). ff19SB: Amino-Acid-Specific Protein Backbone Parameters Trained against Quantum Mechanics Energy Surfaces in Solution. Journal of Chemical Theory and Computation, 16(1), 528–552.

Turner, J., Anderson, R., Guo, J., Beraud, C., Fletterick, R., & Sakowicz, R. (2001). Crystal structure of the mitotic spindle kinesin Eg5 reveals a novel conformation of the neck-linker. The Journal of Biological Chemistry, 276(27), 25496–25502.

Twelvetrees, A. E., Lesept, F., Holzbaur, E. L. F., & Kittler, J. T. (2019). The adaptor proteins HAP1a and GRIP1 collaborate to activate the kinesin-1 isoform KIF5C. In Journal of Cell Science (Vol. 132, Issue 24). https://doi.org/10.1242/jcs.215822

Valence, S., Poirier, K., Lebrun, N., Saillour, Y., Sonigo, P., Bessières, B., Attié-Bitach, T., Benachi, A., Masson, C., Encha-Razavi, F., Chelly, J., & Bahi-Buisson, N. (2013). Homozygous truncating mutation of the KBP gene, encoding a KIF1B-binding protein, in a familial case of fetal polymicrogyria. Neurogenetics, 14(3-4), 215–224.

Vale, R. D., & Milligan, R. A. (2000). The way things move: looking under the hood of molecular motor proteins. Science, 288(5463), 88–95.

van der Vaart, B., van Riel, W. E., Doodhi, H., Kevenaar, J. T., Katrukha, E. A., Gumy, L., Bouchet, B. P., Grigoriev, I., Spangler, S. A., Yu, K. L., Wulf, P. S., Wu, J., Lansbergen, G., van Battum, E. Y., Pasterkamp, R. J., Mimori-Kiyosue, Y., Demmers, J., Olieric, N., Maly, I. V., … Akhmanova, A. (2013). CFEOM1-associated kinesin KIF21A is a cortical microtubule growth inhibitor. Developmental Cell, 27(2), 145–160.

Verhey, K. J., Dishinger, J., & Kee, H. L. (2011). Kinesin motors and primary cilia. Biochemical Society Transactions, 39(5), 1120–1125.

Verhey, K. J., & Hammond, J. W. (2009). Traffic control: regulation of kinesin motors. Nature Reviews. Molecular Cell Biology, 10(11), 765–777.

von Loeffelholz, O., & Moores, C. A. (2019). Cryo-EM structure of the Ustilago maydis kinesin-5 motor domain bound to microtubules. Journal of Structural Biology, 207(3), 312–316.

von Loeffelholz, O., Peña, A., Drummond, D. R., Cross, R., & Moores, C. A. (2019). Cryo-EM Structure (4.5-Å) of Yeast Kinesin-5-Microtubule Complex Reveals a Distinct Binding Footprint and Mechanism of Drug Resistance. Journal of Molecular Biology, 431(4), 864–872.

Walczak, C. E., Gayek, S., & Ohi, R. (2013). Microtubule-depolymerizing kinesins. Annual Review of Cell and Developmental Biology, 29, 417–441.

Walczak, C. E., Verma, S., & Mitchison, T. J. (1997). XCTK2: a kinesin-related protein that promotes mitotic spindle assembly in Xenopus laevis egg extracts. The Journal of Cell Biology, 136(4), 859–870.

Wang, D., Nitta, R., & Hirokawa, N. (2016). Crystal structure of the KIF19A motor domain complexed with mg-ADP. Worldwide Protein Data Bank. https://doi.org/10.2210/pdb5gsz/pdb

Wang, D., Nitta, R., Morikawa, M., Yajima, H., Inoue, S., Shigematsu, H., Kikkawa, M., & Hirokawa, N. (2016). Motility and microtubule depolymerization mechanisms of the Kinesin-8 motor, KIF19A. eLife, 5. https://doi.org/10.7554/eLife.18101

Wang, W., Cantos-Fernandes, S., Lv, Y., Kuerban, H., Ahmad, S., Wang, C., & Gigant, B. (2017). Insight into microtubule disassembly by kinesin-13s from the structure of Kif2C bound to tubulin. Nature Communications, 8(1), 70.

Wang, W., Cao, L., Wang, C., Gigant, B., & Knossow, M. (2015). Kinesin, 30 years later: Recent insights from structural studies. Protein Science: A Publication of the Protein Society, 24(7), 1047–1056.

Woehlke, G., Ruby, A. K., Hart, C. L., Ly, B., Hom-Booher, N., & Vale, R. D. (1997). Microtubule Interaction Site of the Kinesin Motor. In Cell (Vol. 90, Issue 2, pp. 207–216). https://doi.org/10.1016/s0092-8674(00)80329-3

Yang, J., Yan, R., Roy, A., Xu, D., Poisson, J., & Zhang, Y. (2015). The I-TASSER Suite: protein structure and function prediction. Nature Methods, 12(1), 7–8.

Yang, J., & Zhang, Y. (2015). I-TASSER server: new development for protein structure and function predictions. Nucleic Acids Research, 43(W1), W174–W181.

Zivanov, J., Nakane, T., Forsberg, B. O., Kimanius, D., Hagen, W. J., Lindahl, E., & Scheres, S. H. (2018). New tools for automated high-resolution cryo-EM structure determination in RELION-3. eLife, 7. https://doi.org/10.7554/eLife.42166

Zivanov, J., Nakane, T., & Scheres, S. H. W. (2019). A Bayesian approach to beam-induced motion correction in cryo-EM single-particle analysis. IUCrJ, 6(Pt 1), 5–17.

Chapter V:
Discussion and Future Directions

5.1 Discussion

Kinesins are molecular motor proteins that perform vitals roles in complex cellular processes. The mitotic kinesins are a group of motors that are essential for organizing the mitotic spindle and ensuring accurate chromosome segregation. Due to the centrality of these motors' functions, many overlapping pathways have evolved such that if one motor is impaired, another motor can fulfill a similar role. For example, while it is known that Eg5 and dynein provide the main outward and inward forces necessary for building a bipolar spindle, KIF15 and HSET have been shown to have functionally redundant roles and can provide the necessary forces for spindle assembly in the case of dual Eg5 and dynein inhibition (T J Mitchison et al. 2005; Tanenbaum et al. 2009; Vanneste et al. 2009; Mountain et al. 1999). Over the last several decades, our collective knowledge of the complex forces underlying mitotic progression has increased drastically, yet there is still much we don't yet understand about how these forces coalesce to ensure mitotic fidelity. The multiple mechanisms by which mitotic motors are regulated add yet another layer of complexity to this question.

In this dissertation, I present work identifying several chemical inhibitors of the Kinesin-12 KIF15, and elucidate a novel mechanism of regulation of KIF15, among a subset of other motors. We built upon an existing high-throughput screening pipeline to identify KIF15 inhibitors and evaluate hits using a combination of *in vitro* and cell-based assays. We then applied these methods to screen a library of 24,000 small molecules and discovered two potent, selective KIF15 inhibitors that inhibit the motor *via* distinct mechanisms. Lastly, we comprehensively characterized the structure and mechanism of action of a newly described form of kinesin regulation, kinesin-binding protein (KIFBP). We find that KIFBP binds to kinesin motors domains in cells and prevents microtubule-binding through a combination of steric inhibition and allosterically-induced conformational changes. Our work with the two mitotic motors KIF15 and KIF18A

suggests that KIFBP uses a universal method of interaction with all of its binding partners, and molecular dynamics simulations suggest a conformational basis for how KIFBP discriminates between motors. Collectively, this work provides insight into how the complex forces involved in mitotic progression are regulated in time and space, and provides a new tool with which to continue examining the relative contribution of KIF15 to spindle organization.

5.1.1 KIFBP: a novel regulator of kinesin activity

KIFBP is a known regulator of eight kinesins in cells and has therapeutic implications for a severe neurological disorder (Kevenaar et al. 2016; Brooks et al. 2005). In this work, I describe the mechanism by which KIFBP binds to and remodels kinesin motor domains to prevent their microtubule binding activity. Through a combination of cryo-electron microscopy and crosslinking mass spectrometry, we show that KIFBP binds the microtubule binding domains of KIF15 and KIF18A and displaces the α-helix-4 15 Å down into KIFBP's concave face. This substantial displacement is especially interesting, and brings up several additional questions.

Mutagenesis of several regions of KIFBP have revealed their respective importance for complex formation; loops 1 and 14 of KIFBP appear necessary for complex formation both *in vitro* and in cells. However, the role of α4 in complex formation has yet to be tested. The KIFBP:kinesin interaction is very stable; perhaps extraction and stabilization of α4 in the KIFBP binding pocket is necessary for maintaining complex stability. Mutagenesis of the residues involved in the α4 interaction will illuminate the role of this displacement in both complex formation and maintenance.

Molecular dynamics simulations indicate that two KIFBP-binding kinesins are able to reach a conformational state that two non-binders (Eg5 and KIF5C) are not able to reach. While α4 itself was excluded from these simulations, one of the unstructured loops adjacent to α4 was found to adopt different conformations when comparing the binding motors to the non-binders, and so differences in the ability of α4 to extend and bind KIFBP may help differentiate which kinesins are able to bind. Future experiments investigating these conformational differences between binders and non-binders will further reveal the

role of α4 in the KIFBP:kinesin interaction, and may uncover additional regions of the kinesin motor domain that enable discrimination in binding.

Lastly, we still lack an understanding of how KIFBP is released from kinesins and recycled in cells. As the KIFBP:kinesin complex is stable in solution and KIFBP is not an ATPase, it is likely that some form of post-translational modification or other mode of additional regulation is necessary for inducing complex dissolution. Interestingly, phosphorylation was shown to be implicated in the ability of KIFBP to pull down kinesins from cells (Kevenaar et al. 2016). Future experiments investigating putative phosphorylation sites on KIFBP that may govern unbinding will help complete our understanding of how KIFBP regulates kinesins in cells.

5.1.2 KIF15 inhibitors: a valuable tools and potential therapies

Kinesin inhibitors have been instrumental for cell biologists to uncover the molecular underpinnings of mitotic progression, and some are currently being evaluated as potential therapeutics. For example, numerous Kinesin-5 inhibitors (K5Is) have enabled the discovery of the critical role of Eg5 in bipolar spindle assembly, and many have been tested in preclinical studies and clinical trials against a range of cancers. In Chapter III, I describe two novel KIF15 inhibitors that were identified from a high-throughput screen of a large library of small molecules, and detail the methods used to screen for an evaluate the compounds. These methods mostly rely on cell-free assays which make them simple to scale up to a high-throughput screen, and they can be easily adapted to identify inhibitors of other molecular motor proteins.

While both inhibitors described in our studies were shown to be effective and selective for KIF15, they each have their advantages and disadvantages. Munesib-1 is a highly potent inhibitor of KIF15 activity *in vitro*, as shown by its sub-micromolar IC_{50} in microtubule gliding assays. However, it is less effective in cells, likely due its low solubility. A chemical derivative of Munesib-1 with increased solubility, Munesib-2, proved much more effective in cells without losing much potency *in vitro*. On the other hand, Fiftin is highly effective in cells, fully abrogating bipolar spindle assembly at low micromolar concentrations in K5I-resistant cells. Intriguingly, Fiftin is not nearly as potent as Munesib-1 *in vitro*, with an IC_{50} nearly 10-fold higher in gliding assays, and appears to be less

reversible than Munesib-1. Understanding these differences in potency will be useful for determining which compound to use for future studies; for instance, Munesib-1/2 might be better for cell-free biochemical assays, whereas Fiftin will be advantageous for studies in cells.

The solubility issues with Munesib-1 may explain part of the disparate *in vitro* and cell-based activity of the two scaffolds. Indeed, Munesib-2 still precipitates slightly in solution. It is also possible that differences in drug uptake or efflux by cells exist between the two compounds. Pharmacokinetics experiments will be necessary to evaluate this possibility. Additionally, a structural understanding of where on the KIF15 motor domain each compound binds will improve our understanding of their mechanism of action and facilitate efficient development of the next generation of KIF15 inhibitors.

Finally, these compounds will enable us to test the hypothesis that inhibition of both Eg5 and KIF15 in combination will be more clinically effective than treatment with K5Is alone. Several studies have shown that KIF15 plays a central role in the ability of cells to acquire resistance to K5Is (Tanenbaum et al. 2009; Sturgill and Ohi 2013; Raaijmakers et al. 2012; Mardin et al. 2013; Sturgill et al. 2016), and that deletion of KIF15 abrogates K5I resistance completely. In support of this hypothesis, my work showed that combination treatment of STLC and Fiftin reduce the occurrence of resistant colonies, compared to STLC treatment alone. Certainly, it will be interesting to further test this hypothesis in other tumor cell lines or xenograft models to evaluate the clinical efficacy of this combination treatment.

5.1.3 The future of antimitotic compounds in the clinic

As we continue optimizing mitotic kinesin inhibitors, the question still remains as to why they have not been as clinically successful as the classical microtubule-targeting agents (MTAs) such as taxanes and Vinca alkaloids. K5Is have been particularly disappointing in clinical trials compared to their success in preclinical models, and potential mechanisms of K5I resistance arising from activation of redundant pathways are discussed at length in Chapter 1.3.6. However, we must also consider whether targeting the proliferation of cancer cells is an effective strategy for inducing tumor regression; recent research suggests that this may not be the case.

High levels of myelosuppression experienced by patients in clinical trials suggest that antimitotics are indeed hitting their mitotic targets with good pharmacokinetic profiles. The problem arises from the relevancy of targeting mitosis in general. Recent studies have suggested that the proliferation rate of preclinical tumor models, such as immortalized cells lines and xenograft models, is actually much higher than the average proliferation rates of solid tumors in patients. For example, the doubling time of most human cell lines is somewhere between 1-3 days, however the average doubling time of a panel of tumor types was found to be almost 150 days (Komlodi-Pasztor et al. 2011). This indicates that the cells of most solid tumors are dividing much less frequently than typical cancer model systems, and that at any given time point only a small percentage of tumor cells are dividing (Timothy J. Mitchison 2012). With such a small therapeutic window in patients, it is clear how antimitotics may not be as effective as we though under the tolerated dose thresholds.

The question then remains as to why MTAs are so effective in patients. Several models have been proposed recently for how MTAs may be causing cell death in patient tumors through mechanisms other than inducing cell cycle arrest. One possibility is that MTAs also affect interphase cells by disrupting intracellular transport and signaling pathways that rely on microtubules (Komlodi-Pasztor et al. 2011). As mitosis-specific drugs would not have drastic effects on interphase cells, this could explain part of the difference in effectiveness between MTAs and other antimitotics. Another model suggests that MTAs might induce tumor regression mainly through the formation of micronuclei, which then activate the pro-inflammatory cGAS-STING pathway (MacKenzie et al. 2017), which has been shown separately to have strong anti-tumor effects. Paclitaxel treatment is known to cause micronuclei formation (Jordan et al. 1996), whereas K5Is typically do not. Indeed, a better understanding of the exact mechanisms by which MTAs induce tumor regression in patients is necessary to fully explain the discrepancy in effects between MTAs and other antimitotics.

So what is the future of antimitotic therapies? While arresting mitosis is perhaps not the general cure for cancer, there may still be room for clinical use of antimitotics. One consideration is tumor type. The K5I Arry-520 has shown potential in clinical trials of patients with multiple myeloma, a very rapidly dividing cancer (Shah et al. 2017). The

longer half-life of Arry-520 combined with the increased mitotic index of multiple myeloma may represent a promising way to use antimitotics therapeutically; continuing to increase the half-life of K5Is and using them against tumor types with high rates of proliferation may be two ways to increase their therapeutic potential. Increasing our understanding of how MTAs kill cancer cells may also reveal novel aspects of mitosis to target therapeutically. If activation of inflammatory signaling *via* micronuclei is indeed an effective way to kill tumor cells, then identifying other drug targets whose inhibition causes micronucleation is another potential therapeutic strategy. Lastly, improved targeting of antimitotic drugs to the desired tumor sites has proven an effective strategy for increasing their efficacy. Drugs can be conjugated to antibodies or aptamers that deliver them to cancer cells expressing specific cell-surface receptors. Brentuximab vedotin, a CD30-targeting MMAE (an antimitotic) conjugate, has been approved for treatment of Hodgkin's lymphoma and systemic anaplastic large cell lymphoma (ALCL) (Younes, Yasothan, and Kirkpatrick 2012), and numerous other conjugates using similar strategies are being tested for efficacy against a range of cancers (Tse et al. 2006; Kratschmer and Levy 2018).

5.2 Future Directions

5.2.1 The role of KIFBP in Goldberg-Shprintzen syndrome

While we made significant progress in elucidating the mechanism by which KIFBP inhibits kinesin activity in cells, how loss-of-function mutations in KIFBP cause GOSHS remains unknown. As discussed in Chapter I, GOSHS is the result of autosomal recessive loss-of-function mutations to KIFBP. KIFBP has been shown to be important for several features of neurodevelopment, including axonal extension and dendritic outgrowth, organization of axonal microtubules, and migration of neural progenitor cells (Lyons et al. 2008; Chang et al. 2019). Other neurological diseases, *e.g.*, Fragile X syndrome, are associated with similar neurite abnormalities (Rudelli et al. 1985), and it is thus clear how loss of KIFBP function can be linked to GOSHS symptoms overall.

Since KIFBP regulates a subset of kinesin motors, we hypothesize that GOSHS phenotypes arise due to dysregulation of KIFBP-binding kinesins in the absence of KIFBP activity. Supporting this hypothesis, several KIFBP-binding kinesins have roles in

neuronal development and the regulation of MT dynamics. For example, Kinesin-8 members are known to regulate MT dynamics (Lin, Wei, and She 2020), Kinesin-2 and -3 members regulate neuronal migration (Chen, Chang, and Tsai 2019; Tsai et al. 2010), and Kinesin-12 has been shown to affect axon extension and growth cone turning (Liu et al. 2010).

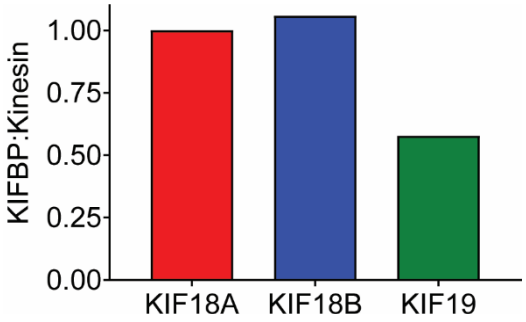

Fig. 5.1 KIFBP-binding of Kinesin-8 family. Quantification of in vitro pulldown results testing the binding of KIFBP with three members of the Kinesin-8 family: KIF18A, KIF18B, and KIF19. Binding ratios are normalized to the results of KIF18A, a known KIFBP-binder.

An important direction for future work is to define the neuronal kinesin(s) whose activity is mis-regulated in the absence of KIFBP. Published work provides a list of candidates, but my unpublished work suggests that this list is incomplete. First, KIFBP has been shown to bind Kif18A but not Kif18B (Kevenaar et al. 2016); however, I have shown that KIFBP binds both kinesins with similar affinity (*Fig. 5.1)*. Second, several studies have identified KIFBP interactors that cannot be reproduced in later papers, such as the MT dynamics regulator SCG10 (Alves et al. 2010; Kevenaar et al. 2016). Finally, previous IP-mass spectrometry experiments in our lab have failed to detect more than minimal levels of KIFBP bound to Kif15, despite our extensive work showing a robust in vitro interaction between them (*Brittany Salazar, unpublished data*). Thus, we believe that the KIFBP interactome may include binding partners with affinities too weak to be identified via IP-mass spectrometry. To improve identification of KIFBP binding partners, crosslinking mass spectrometry could be used to increase the chances of identifying less stable interactions during downstream analysis.

A second important point is that all previously published studies targeted at identifying KIFBP-binding partners have been done in non-neuronal cells and it is thus not clear whether disease-relevant KIFBP-binding proteins were identified (Wozniak et al. 2005; Alves et al. 2010; Kevenaar et al. 2016). To identify KIFBP-binders that may underlie GOSHS, it would be important to perform any crosslinking experiments in developing neurons. Stable inducible neurons (siNeurons) would be an appropriate and advantageous model to use for this experiment. siNeurons are derived from induced pluripotent stem cells (iPSCs) that conditionally express neurogenin 2, a transcription

factor that induces neuronal differentiation. When treated with doxycycline, these iPSCs differentiate into post-mitotic excitatory neurons (Zhang et al. 2013). siNeurons are easier to culture and differentiate than primary mouse neurons, and are more physiologically relevant to human disease than immortalized neuronal cell lines. Defining the KIFBP interactome in siNeurons and validating the effect of overactivity of identified KIFBP binders will significantly increase our understanding of the mechanisms underlying a serious, poorly characterized neurological disorder.

5.2.2 Regulation of Kif15 via autoinhibition

Although the precise mechanism(s) is not yet known, Kif15 is regulated *in cis* by autoinhibition *via* conformational folding. Hydrodynamic analysis of Kif15 shows that it adopts a small, compact conformation at low salt concentrations and an open, more extended conformation at high salt. Negative stain experiments have also shown what appears to be a flexible hinge in the stalk that might enable folding (Sturgill et al. 2014). These findings suggest that Kif15 can switch between open and closed conformations, and that the closed, autoinhibited state is likely mediated by intramolecular electrostatic interactions.

In vitro experiments show that self-repression of Kif15 is mediated by interactions between Coil-2 and either the motor domain and/or Coil-1. Full-length Kif15 is activated by the addition of Coil-2-targeting antibodies, as shown by an increase in microtubule gliding velocity with antibody addition. Conversely, the motility of Kif15-N700 (a Kif15 mutant truncated after Coil-1) is reduced with the addition of purified Coil-2 in *trans*. Furthermore, Kif15-N700 binds microtubules in interphase cells in the presence of AMPPNP much more robustly than full-length protein (Sturgill et al. 2014). Mutagenesis studies have narrowed down the region of Coil-2 that mediates the autoinhibitory interaction to the final 100 amino acids of Kif15. Truncation of this peptide (Kif15Δ100) enables interphase microtubule-binding to a similar extent as Kif15-N700, and the addition of this peptide in *trans* inhibits microtubule gliding *in vitro* in a concentration-dependent manner (*Megan Dumas, unpublished data*).

To further pinpoint the regions of Kif15 that mediate autoinhibition, I performed crosslinking mass spectrometry (XL-MS) on recombinant full-length Kif15. This work

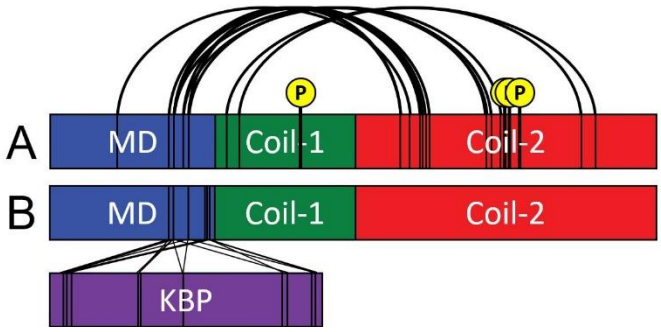

Fig. 5.2 Crosslinks within KIF15 and with KIFBP. A) Identified crosslinks (black lines) and phosphorylation sites (P) overlaid on the secondary structure of KIF15. B) Identified crosslinks between the motor domain of KIF15 and KIFBP.

revealed residues in Coil-2 that interact with the motor domain of Kif15 (*Fig. 5.2*). Several regions of Coil-2 were found to bind to residues that comprise the microtubule-binding domain of the motor head. Intriguingly, these were the same residues found to bind to KIFBP in a parallel XL-MS experiment, suggesting that these two interactions (autoinhibition and KIFBP-binding) are mutually exclusive. Another interesting but more puzzling finding was that no residues from the final 100 amino acids were identified in the XL-MS analysis, something we expected to find based on previous data. There are a variety of potential reasons that these residues were not identified. For example, the crosslinker I used, BS3, is an 11Å lysine-targeted crosslinker, and so functionally relevant regions could be missed if they are lysine-poor. Future work is necessary, perhaps through targeted mutagenesis to the final 100 amino acids as well as the identified crosslinked regions, to further elucidate the residues of KIF15 that are involved in autoinhibition.

Autoinhibition of Kif15 also appears to be controlled in a cell-cycle-dependent manner. Full-length Kif15 readily interacts with kinetochore microtubules during mitosis, but remains cytosolic during interphase. However, as previously mentioned, impairing autoinhibition by truncating Coil-2 of Kif15 enables it to robustly bind microtubules even in interphase cells (Sturgill et al. 2014). Taken together with the finding that KIFBP-binding and autoinhibition are likely mutually exclusive, we hypothesize that autoinhibition functions to restrict Kif15 from binding and crosslinking microtubules during interphase, while KIFBP fine-tunes levels of Kif15 on spindle microtubules during mitosis. This also raises the question of how autoinhibition of Kif15 is relieved, and how this release is controlled throughout the cell cycle.

Several mechanisms of autoinhibition release have been described for other kinesins, including cargo binding and post-translational modifications (PTMs) such as phosphorylation. We have shown that Kif15 preferentially binds bundled MTs, such as k-

fibers, and has little capability to bind single microtubules (Sturgill et al. 2014). This suggests that Kif15 may follow the cargo-binding model of autoinhibition release, where engagement of both microtubule-binding domains locks Kif15 in an open conformation and allows it to move within the microtubule bundle. This hypothesis could explain Kif15's preference for K-fibers and its lack of binding to non-bundled interphase MTs. However, we have shown that Kif15 still doesn't bind interphase MTs that are bundled (Sturgill et al. 2016), suggesting that an additional mechanism is required to relieve autoinhibition.

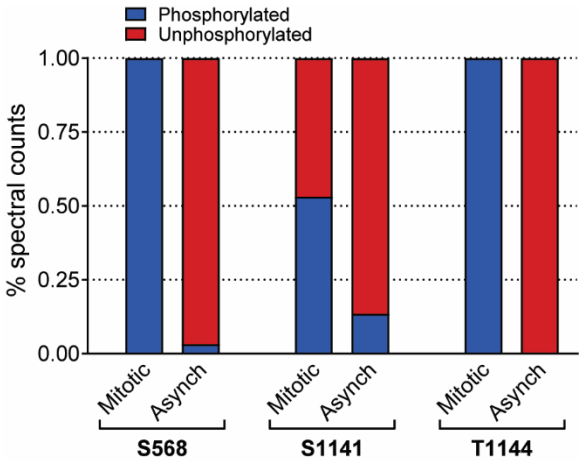

Fig. 5.3 Cell-cycle-dependent phosphorylation of KIF15. The relative abundance of phosphorylation on each CDK1 site in mitotic and asynchronous cells, as measured by mass spec.

In support of the PTM model of autoinhibition release, four putative phosphorylation sites have been identified on Kif15 with consensus sequences for Aurora A kinase and CDK1-Cyclin B, two mitotic kinases involved in mitotic entry and progression (*Fig. 5.3*) (Sugimoto et al. 2002; Lim and Kaldis 2013). One site is in Coil-1 of Kif15 and the other three are in Coil-2. We believe that the hinge in Kif15 exists between Coils 1 and 2, and thus predict that these phosphate groups may sterically hinder Kif15 from being in an autoinhibited state by disrupting intramolecular interactions between Coil-2 and Coil-1 and/or the motor domain. In support of this hypothesis, a phosphomimetic Kif15 mutant of one of the Coil-2 residues (S1169A) was shown to have increased spindle localization in mitotic cells compared to wildtype-Kif15, whereas a non-phosphorylatable mutant showed decreased spindle binding (Van Heesbeen et al. 2017). More recently, a mass spectrometry experiment performed by Brittany Salazar showed that the other three sites (S568, S1141, and T1144) are almost exclusively phosphorylated in mitotic cells (*Brittany Salazar, unpublished data*). This leads us to hypothesize that phosphorylation of Kif15 upon mitotic entry sterically inhibits interaction of the motor domain and C-terminus, releasing it from its autoinhibited state and allowing it to bind MT bundles.

A good way to test this hypothesis would be to express phosphomimetic and non-phosphorylatable mutant of the four identified phospho-sites on Kif15 in cells, and analyze

their microtubule localization patterns in both interphase and mitotic cells. If phosphorylation of one or more of these sites does indeed disrupt autoinhibition, phosphomimetic mutants should show increased binding to interphase microtubules as Kif15 regulation would be decoupled from the cell cycle. Conversely, non-phosphorylatable mutants should show decreased spindle binding in mitotic cells as Kif15 would likely be constitutively autoinhibited. It is difficult to predict whether single point mutations will have a measurable effect on Kif15 localization, and it is likely that combinations of two or more mutations would be necessary to produce a statistically significant change.

It is also unclear whether we have a comprehensive understanding of the phosphorylation sites that exist on Kif15. To test this, one could try to reconstitute activation of Kif15 *via* Cdk1 and/or Aurora A *in vitro*. If phosphorylation by either kinase is capable of releasing Kif15 from its autoinhibited state, it should increase the ability of full-length Kif15 to bind to and move along microtubules *in vitro*. Lastly, it would be interesting to test whether KIFBP and autoinhibition are truly mutually exclusive. Qualitative binding experiments using techniques such as size-exclusion chromatography or *in vitro* pulldowns could be used to determine whether phosphorylation status, and thus autoinhibition state, changes the ability of KIFBP to interact with Kif15.

5.2.3 Identification of novel mechanisms of K5I resistance

Since their development, K5Is have not passed clinical trials due to their inability to cause tumor regression in patients. It was shown that Kif15 is necessary and sufficient for driving spindle assembly in the absence of Eg5 activity, as deletion of KIF15 via CRISPR Cas9 technology prevents the formation of K5I-resistant clones (Raaijmakers et al. 2012; Sturgill and Ohi 2013; Sturgill et al. 2016). This strongly suggests that human cells adapt to K5Is by amassing genetic changes that promote alternative spindle assembly pathways, e.g. the Kif15 pathway. Several genetic alterations that enable K5I resistance have been uncovered, described in detail in Chapter 1.3.6. However, given the limited number of K5I-resistant clones analyzed in these experiments, it is likely that we have incomplete knowledge of the mechanisms that allow cells to overcome Eg5 inhibition. To address this, it would be advantageous to characterize the potential

mechanisms of K5I resistance more comprehensively using an unbiased screening approach.

I conceptualized an approach to identify mutations that drive drug resistance that lie outside of the gene encoding the drug target. This approach, which we term “extragenic suppressor sequencing” (ExSS), is designed to identify extragenic suppressors of a perturbing agent, i.e., genes that when mutated suppress the cytotoxic effects of a drug. In the case of K5Is, Kif15 is an extragenic suppressor of Eg5-inhibition; when Kif15 is overexpressed in K5I-treated cells, it can compensate for the loss of Eg5 activity and restore spindle assembly. Our ExSS approach is aimed at identifying other potential extragenic suppressors of Eg5 inhibition through a high-throughput screening method, and can be easily adapted to identify extragenic suppressors of other targets of chemical inhibition.

In this method, drug-resistant clones would be generated by treating cells with a chemical inhibitor (in our case, a K5I) of the desired drug target (Eg5); after resistant clones arise, genetic knockout of the drug target (Eg5) would be stimulated *via* an inducible CRISPR-Cas9 to kill any cells whose drug resistance is driven by mutations within the drug target itself. The remaining cells would be analyzed *via* RNA-sequencing to identify genetic alterations that decrease their sensitivity to the drug. The most common type of resistance-conferring mutations are often in the drug target that render the drug ineffective (Wacker et al. 2012). Thus, transcriptomics analysis would be complicated by a high occurrence of drug target mutations that may not be as biologically interesting. Removing the drug target post-selection would increase the chances of discovering novel pathways that drive K5I resistance rather than identifying mutations to Eg5 that desensitize it to K5I treatment. Additionally, the relative rate of occurrence of the identified mutations may provide information about their potential physiological relevance; extragenic suppressors that are present in the majority of clones may be more likely to drive resistance mechanisms in cells than ones that arise in a small percentage.

5.3 References

Alves, M. M., Burzynski, G., Delalande, J. M., Osinga, J., van der Goot, A., Dolga, A. M., … Hofstra, R. M. W. (2010). KBP interacts with SCG10, linking Goldberg-Shprintzen

syndrome to microtubule dynamics and neuronal differentiation. Human Molecular Genetics, 19(18), 3642–3651. https://doi.org/10.1093/hmg/ddq280

Brooks, A. S., Bertoli-Avella, A. M., Burzynski, G. M., Breedveld, G. J., Osinga, J., Boven, L. G., … Hofstra, R. M. W. (2005). Homozygous nonsense mutations in KIAA1279 are associated with malformations of the central and enteric nervous systems. American Journal of Human Genetics, 77(1), 120–126. https://doi.org/10.1086/431244

Chang, H., Cheng, H., Tsao, A., Liu, C., & Tsai, J. (2019). Multiple Functions of KBP in Neural Development Underlie Brain Anomalies in Goldberg-Shprintzen Syndrome. Frontiers in Molecular Neuroscience, 12(November), 1–12. https://doi.org/10.3389/fnmol.2019.00265

Chen, J. L., Chang, C. H., & Tsai, J. W. (2019). Gli2 Rescues Delays in Brain Development Induced by Kif3a Dysfunction. Cerebral Cortex, 29(2), 751–764. https://doi.org/10.1093/cercor/bhx356

Jordan, M. A., Wendell, K., Gardiner, S., Derry, W. B., Copp, H., & Wilson, L. (1996). Mitotic block induced in HeLa cells by low concentrations of paclitaxel (taxol) results in abnormal mitotic exit and apoptotic cell death. Cancer Research, 56, 816–825.

Kevenaar, J. T., Bianchi, S., Van Spronsen, M., Olieric, N., Lipka, J., Frias, C. P., … Hoogenraad, C. C. (2016). Kinesin-Binding Protein Controls Microtubule Dynamics and Cargo Trafficking by Regulating Kinesin Motor Activity. Current Biology, 26(7), 849–861. https://doi.org/10.1016/j.cub.2016.01.048

Komlodi-Pasztor, E., Sackett, D. L., Wilkerson, J., & Fojo, T. (2011). Mitosis is not a key target of microtubule agents in patient tumors. Nature Reviews Clinical Oncology, 8, 244–250.

Kratschmer, C., & Levy, M. (2018). Targeted Delivery of Auristatin-Modified Toxins to Pancreatic Cancer Using Aptamers. Molecular Therapy - Nucleic Acids, 10(March), 227–236. https://doi.org/10.1016/j.omtn.2017.11.013

Lim, S., & Kaldis, P. (2013). Cdks, cyclins and CKIs: Roles beyond cell cycle regulation. Development (Cambridge), 140(15), 3079–3093. https://doi.org/10.1242/dev.091744

Lin, Y., Wei, Y. L., & She, Z. Y. (2020). Kinesin-8 motors: regulation of microtubule dynamics and chromosome movements. Chromosoma, 129(2), 99–110. https://doi.org/10.1007/s00412-020-00736-7

Liu, M., Nadar, V. C., Kozielski, F., Kozlowska, M., Yu, W., & Baas, P. W. (2010). Kinesin-12, a mitotic microtubule-associated motor protein, impacts axonal growth, navigation, and branching. Journal of Neuroscience, 30(44), 14896–14906. https://doi.org/10.1523/JNEUROSCI.3739-10.2010

Lyons, D. A., Naylor, S. G., Mercurio, S., Dominguez, C., & Talbot, W. S. (2008). KBP is essential for axonal structure, outgrowth and maintenance in zebrafish, providing insight into the cellular basis of Goldberg-Shprintzen syndrome. Development, 135(3), 599–608. https://doi.org/10.1242/dev.012377

MacKenzie, K. J., Carroll, P., Martin, C. A., Murina, O., Fluteau, A., Simpson, D. J., … Jackson, A. P. (2017). CGAS surveillance of micronuclei links genome instability to innate immunity. Nature, 548(7668), 461–465. https://doi.org/10.1038/nature23449

Mardin, B. R., Isokane, M., Cosenza, M. R., Krämer, A., Ellenberg, J., Fry, A. M., & Schiebel, E. (2013). EGF-Induced Centrosome Separation Promotes Mitotic Progression and Cell Survival. Developmental Cell, 25(3), 229–240. https://doi.org/10.1016/j.devcel.2013.03.012

Mitchison, T. J. (2012). The proliferation rate paradox in antimitotic chemotherapy. Molecular Biology of the Cell, 23(1), 1–6. https://doi.org/10.1091/mbc.E10-04-0335

Mitchison, T. J., Maddox, P., Gaetz, J., Groen, A., Shirasu, M., Desai, A., … Kapoor, T. M. (2005). Roles of Polymerization Dynamics , Opposed Motors, and a Tensile Element in Governing the Length of Xenopus Extract Meiotic Spindles. Molecular Biology of the Cell, 16(June), 3064–3076. https://doi.org/10.1091/mbc.E05

Mountain, V., Simerly, C., Howard, L., Ando, A., Schatten, G., & Compton, D. A. (1999). Cross-links Microtubules in the Mammalian Mitotic Spindle. J. Cell Biol., 147(2), 351–365.

Raaijmakers, J. A., Van Heesbeen, R. G. H. P., Meaders, J. L., Geers, E. F., Fernandez-Garcia, B., Medema, R. H., & Tanenbaum, M. E. (2012). Nuclear envelope-associated dynein drives prophase centrosome separation and enables Eg5-independent bipolar spindle formation. EMBO Journal, 31(21), 4179–4190. https://doi.org/10.1038/emboj.2012.272

Rudelli, R. D., Brown, W. T., Wisniewski, K., Jenkins, E. C., Laure-Kamionowska, M., Connell, F., & Wisniewski, H. M. (1985). Adult fragile X syndrome - Clinico-neuropathologic findings. Acta Neuropathologica, 67(3–4), 289–295. https://doi.org/10.1007/BF00687814

Shah, J. J., Kaufman, J. L., Zonder, J. A., Cohen, A. D., Bensinger, W. I., Hilder, B. W., … Lonial, S. (2017). A Phase 1 and 2 study of Filanesib alone and in combination with low-dose dexamethasone in relapsed/refractory multiple myeloma. Cancer, 123(23), 4617–4630. https://doi.org/10.1002/cncr.30892

Sturgill, E. G., Das, D. K., Takizawa, Y., Shin, Y., Collier, S. E., Ohi, M. D., … Ohi, R. (2014). Kinesin-12 kif15 targets kinetochore fibers through an intrinsic two-step mechanism. Current Biology, 24(19), 2307–2313. https://doi.org/10.1016/j.cub.2014.08.022

Sturgill, E. G., Norris, S. R., Guo, Y., & Ohi, R. (2016). Kinesin-5 inhibitor resistance is driven by kinesin-12. Journal of Cell Biology, 213(2), 213–227. https://doi.org/10.1083/jcb.201507036

Sturgill, E. G., & Ohi, R. (2013). Kinesin-12 differentially affects spindle assembly depending on its microtubule substrate. Current Biology, 23(14), 1280–1290. https://doi.org/10.1016/j.cub.2013.05.043

Sugimoto, K., Urano, T., Zushi, H., Inoue, K., Tasaka, H., Tachibana, M., & Dotsu, M. (2002). Molecular dynamics of Aurora-A kinase in living mitotic cells simultaneously

visualized with histone H3 and nuclear membrane protein importinα. Cell Structure and Function, 27(6), 457–467. https://doi.org/10.1247/csf.27.457

Tanenbaum, M. E., Macůrek, L., Janssen, A., Geers, E. F., Alvarez-Fernández, M., & Medema, R. H. (2009). Kif15 Cooperates with Eg5 to Promote Bipolar Spindle Assembly. Current Biology, 19(20), 1703–1711. https://doi.org/10.1016/j.cub.2009.08.027

Tsai, J. W., Lian, W. N., Kemal, S., Kriegstein, A. R., & Vallee, R. B. (2010). Kinesin 3 and cytoplasmic dynein mediate interkinetic nuclear migration in neural stem cells. Nature Neuroscience, 13(12), 1463–1472. https://doi.org/10.1038/nn.2665

Tse, K. F., Jeffers, M., Pollack, V. A., McCabe, D. A., Shadish, M. L., Khramtsov, N. V., … LaRochelle, W. J. (2006). CR011, a fully human monoclonal antibody-auristatin E conjugate, for the treatment of melanoma. Clinical Cancer Research, 12(4), 1373–1382. https://doi.org/10.1158/1078-0432.CCR-05-2018

Van Heesbeen, R. G. H. P., Raaijmakers, J. A., Tanenbaum, M. E., Halim, V. A., Lelieveld, D., Lieftink, C., … Medema, R. H. (2017). Aurora A, MCAK, and Kif18b promote Eg5-independent spindle formation. Chromosoma, 126, 473–486. https://doi.org/10.1007/s00412-016-0607-4

Vanneste, D., Takagi, M., Imamoto, N., & Vernos, I. (2009). The Role of Hklp2 in the Stabilization and Maintenance of Spindle Bipolarity. Current Biology, 19(20), 1712–1717. https://doi.org/10.1016/j.cub.2009.09.019

Wacker, S., Houghtaling, B., Elemento, O., & Kapoor, tarun M. (2012). Using transcriptome sequencing to identify mechanisms of drug action and resistance. Nature Chemical Biology, 8. https://doi.org/10.1038/nCHeMBIO.779

Wozniak, M. J., Melzer, M., Dorner, C., Haring, H. U., & Lammers, R. (2005). The novel protein KBP regulates mitochondria localization by interaction with a kinesin-like protein. BMC Cell Biology, 6, 1–15. https://doi.org/10.1186/1471-2121-6-35

Younes, A., Yasothan, U., & Kirkpatrick, P. (2012). Brentuximab vedotin. Nature Reviews Drug Discovery, 11(1), 19–20. https://doi.org/10.1038/nrd3629

Zhang, Y., Pak, C., Han, Y., Ahlenius, H., Zhang, Z., Chanda, S., … Su, T. C. (2013). Rapid Single-Step Induction of Functional Neurons from Human Pluripotent Stem Cells. NeuroResource, 78, 785–798. https://doi.org/10.1016/j.neuron.2013.05.029

Appendix A

Appendix A.1: Supplemental Figures

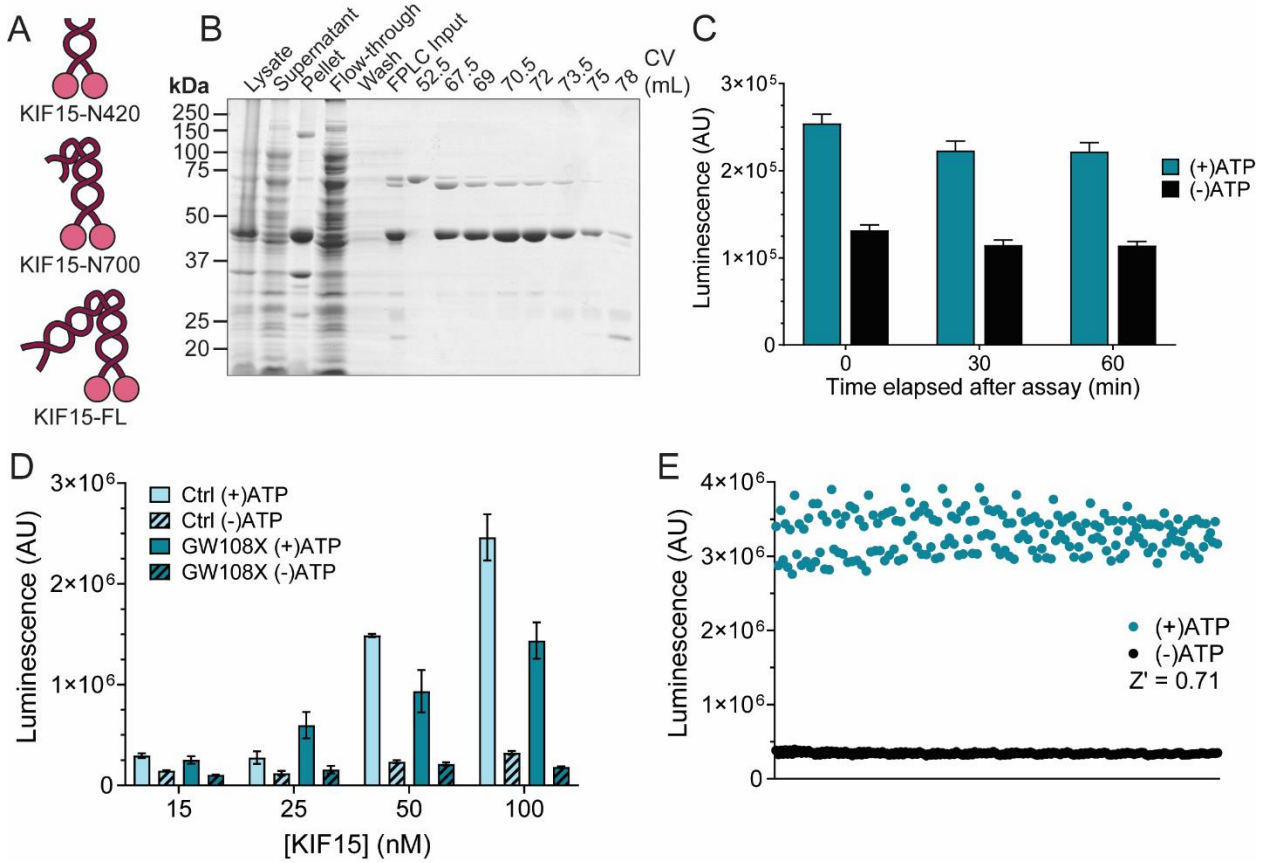

Fig. S3.1: Validation of the ADP-Glo assay for use in KIF15 inhibitor screen. A) Schematic showing the relative length of three constructs of KIF15. KIF15-N420 (top) is the minimal dimer construct and was used in all ATPase assays. KIF15-N700 (middle) contains the second microtubule-binding domain and was used in all gliding assays. KIF15-FL is the full-length protein; this construct was not used in any experiments in this paper. B) Representative Coomassie-stained SDS-PAGE of samples from each step of the purification process of KIF15-N420. C) Quantification of average luminescent signal from ADP-Glo assay in the presence or absence of 20 µM ATP at three time points after assay completion. D) Quantification of average luminescent signal from ADP-Glo assay in the presence or absence of 20 µM ATP, either with (dark blue) or without (light blue) 20 µM GW108X. Concentration of KIF15-N420 included in each condition is indicated below x-axis in nM. All samples were imaged 30 min after assay completion. Each condition was repeated in triplicate, error bars show ±SEM. E) Quantification of luminescent signal from ADP-Glo assay in either the presence (blue) or absence (black) of 20 µM ATP. Average Z' was calculated to be 0.71.

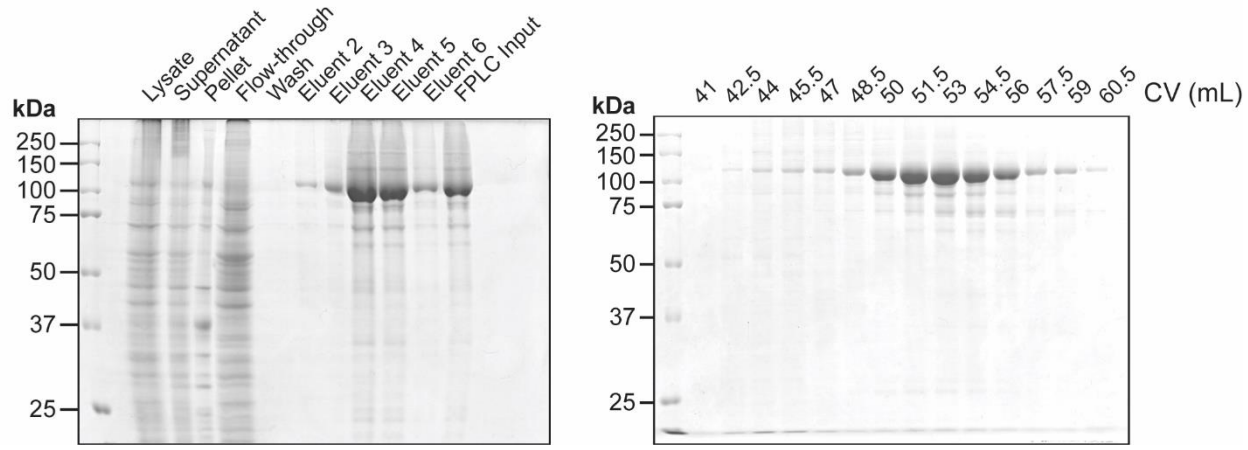

Fig. S3.2: Purification of KIF15-N700. Representative Coomassie-stained SDS-PAGE of samples from each step of the purification process of KIF15-N700.

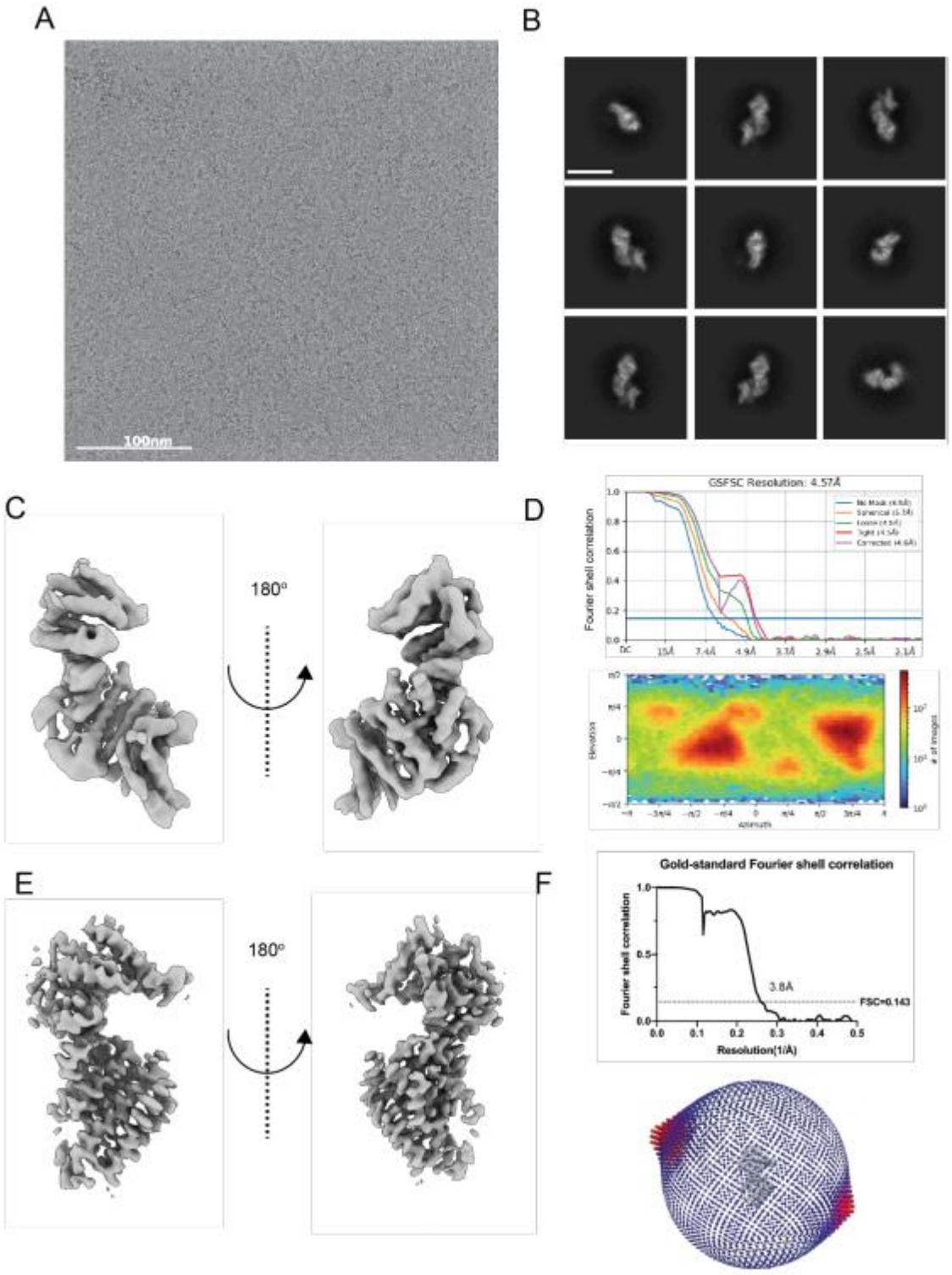

Fig. S4.1. Cryo-EM structures of KIFBP. (A) Representative cryo-EM micrograph. (B) Representative 2D class averages. Scale bar is 100Å. Full KIFBP reconstruction (C), FSC curves and Euler angle distribution (D). KIFBP core overview (E), FSC curves and Euler angle distribution (F).

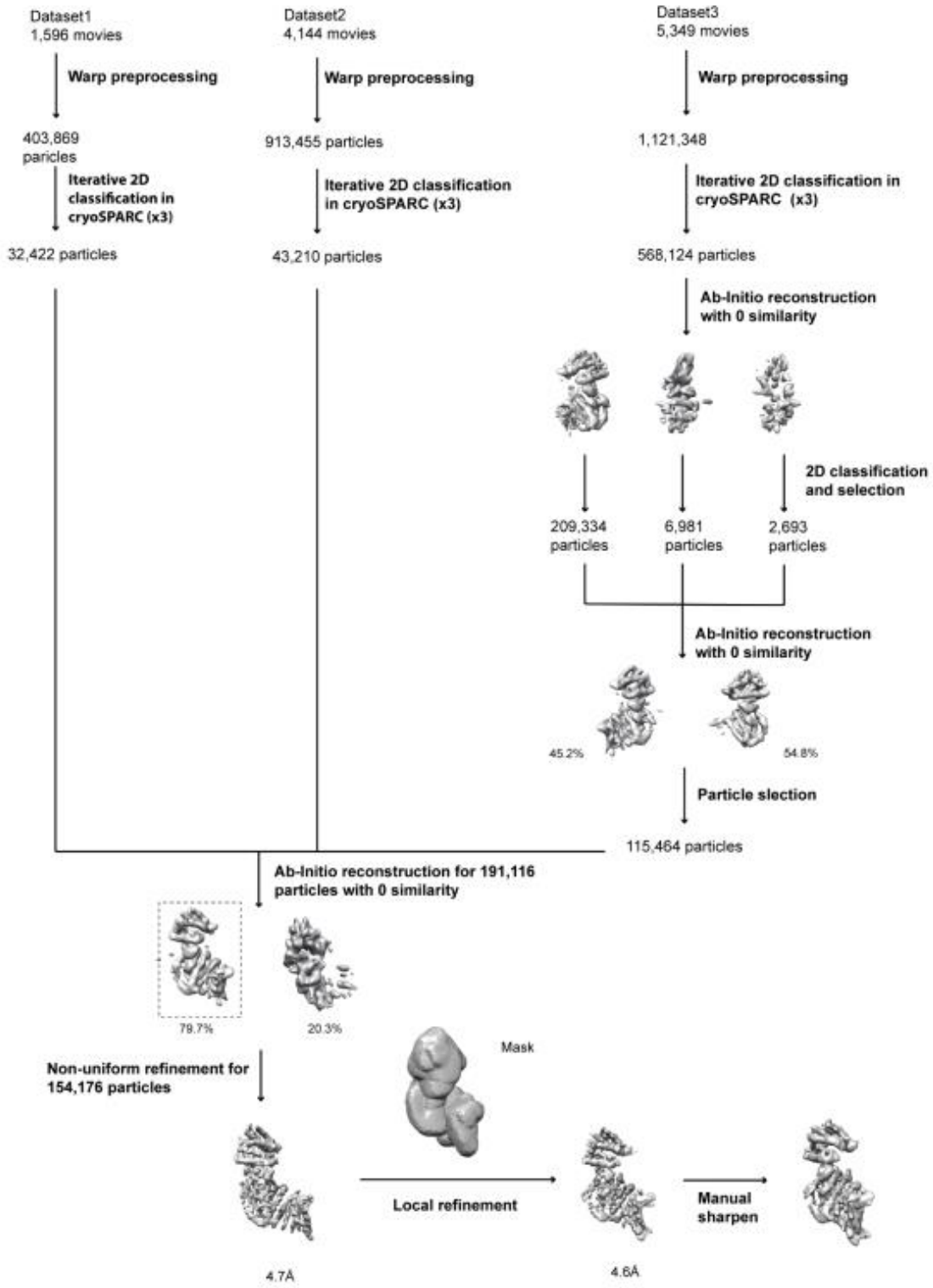

Fig. S4.2. Cryo-EM processing tree for 4.6Å full KIFBP reconstruction. Overview of data processing strategy for full KIFBP.

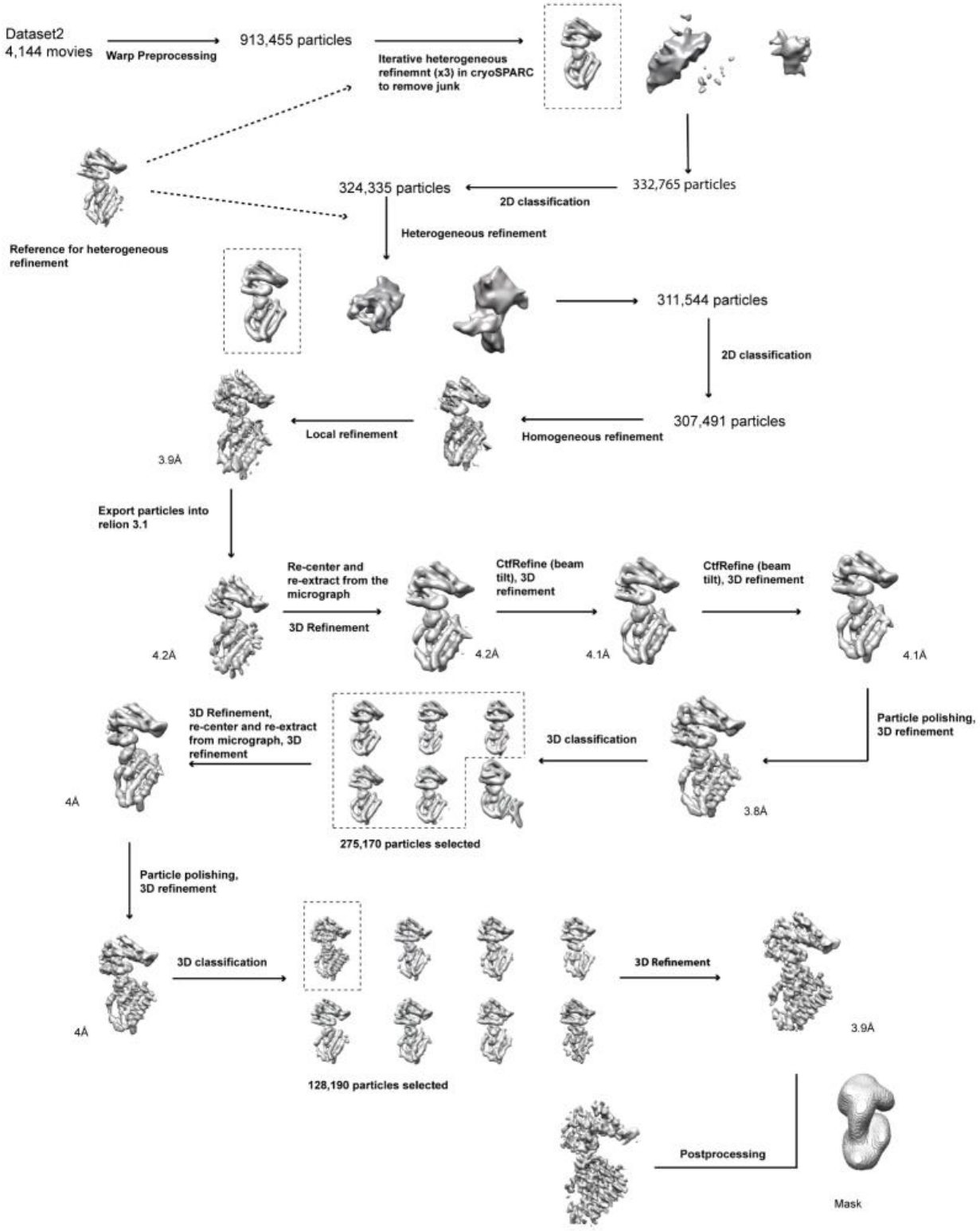

Fig. S4.3. Cryo-EM processing tree for 3.8Å core KIFBP reconstruction. Overview of data processing strategy for core KIFBP reconstruction.

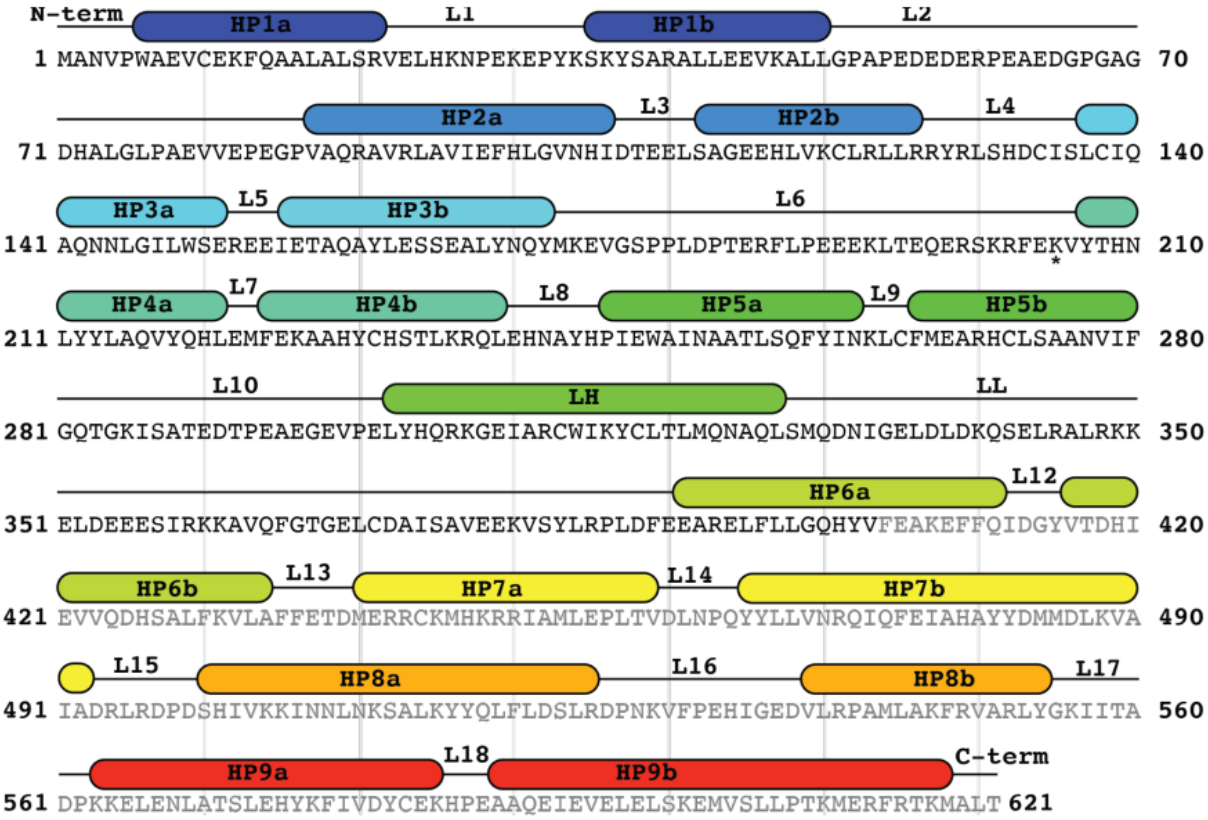

Fig. S4.4. Annotated KIFBP primary sequence using secondary structure information from the atomic model. Residues 5-403 were built de novo into the KIFBP core reconstruction at 3.8Å (black letters), whereas 404-621 were modeled into the 4.6Å reconstruction (gray letters).

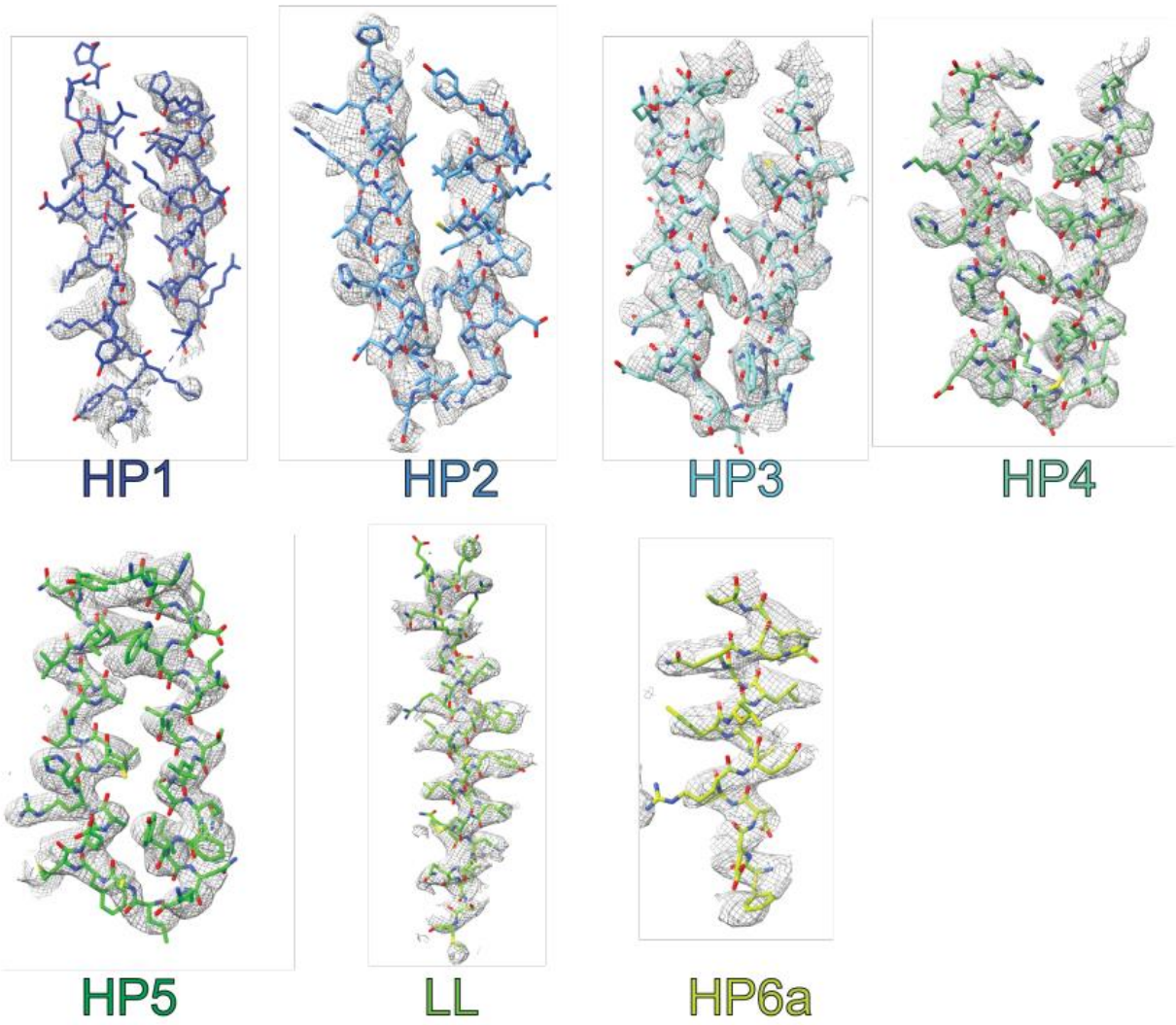

Fig. S4.5. Segmented density for 3.8Å core KIFBP reconstruction and atomic model. Helical pairs from core KIFBP reconstruction.

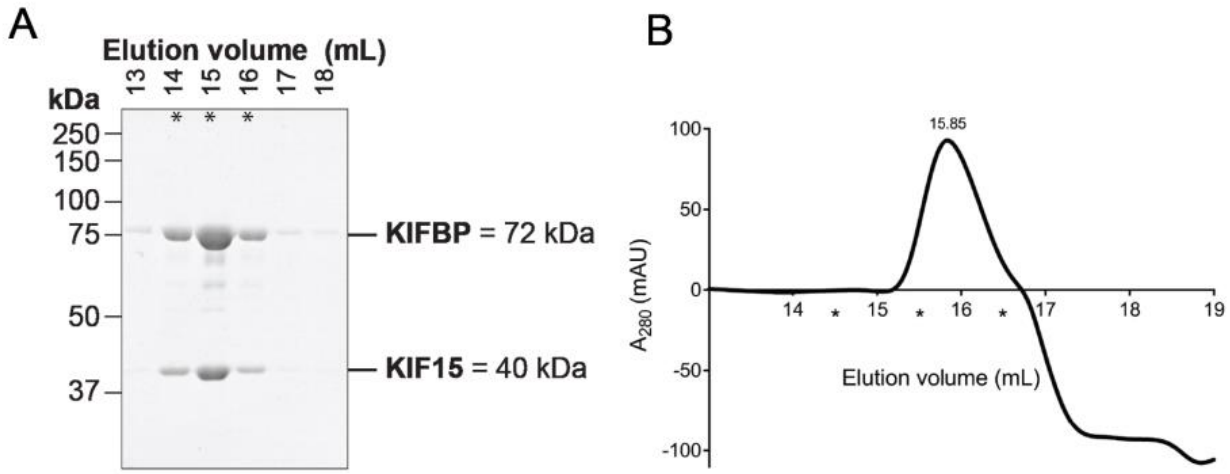

Fig. S4.6. Size exclusion chromatography of KIFBP:KIF15. KIFBP and KIF15 were purified, combined, and run over the Superose 6 column as described in methods. (A) Representative Coomassie-stained SDS-PAGE of peak fractions from elution profile shown in (B). Fractions 14, 15, and 16 were combined and used in subsequent cryo-EM experiments (indicated by asterisks). The molecular weight of each protein is indicated in kilodaltons.

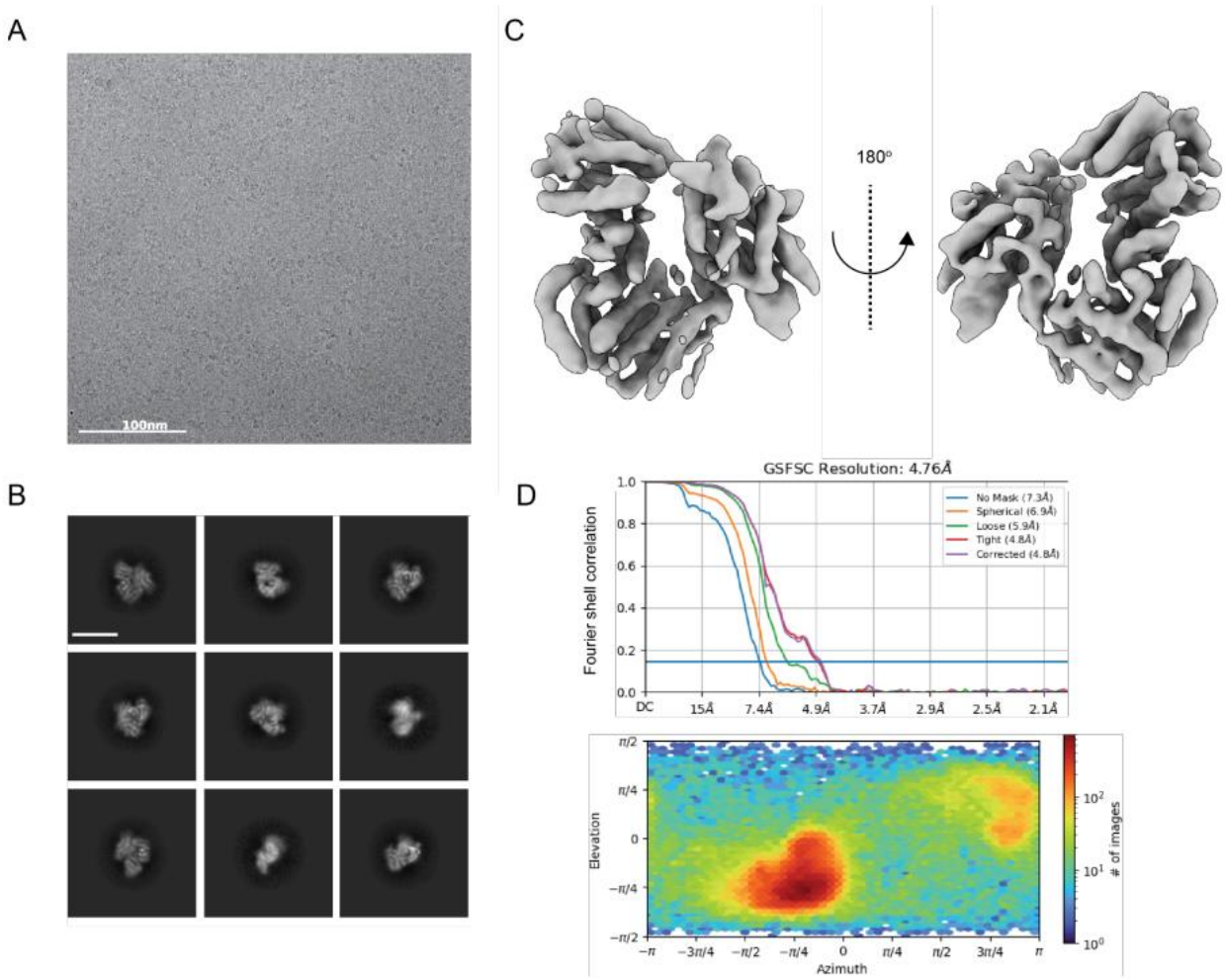

Fig. S4.7. Cryo-EM structure of KIFBP:KIF15. (A) Representative micrograph for KIFBP:KIF15. (B) Representative 2D class averages. The scale bar is 100Å. (C) Reconstruction overview. (D) FSC curves and Euler angle distribution.

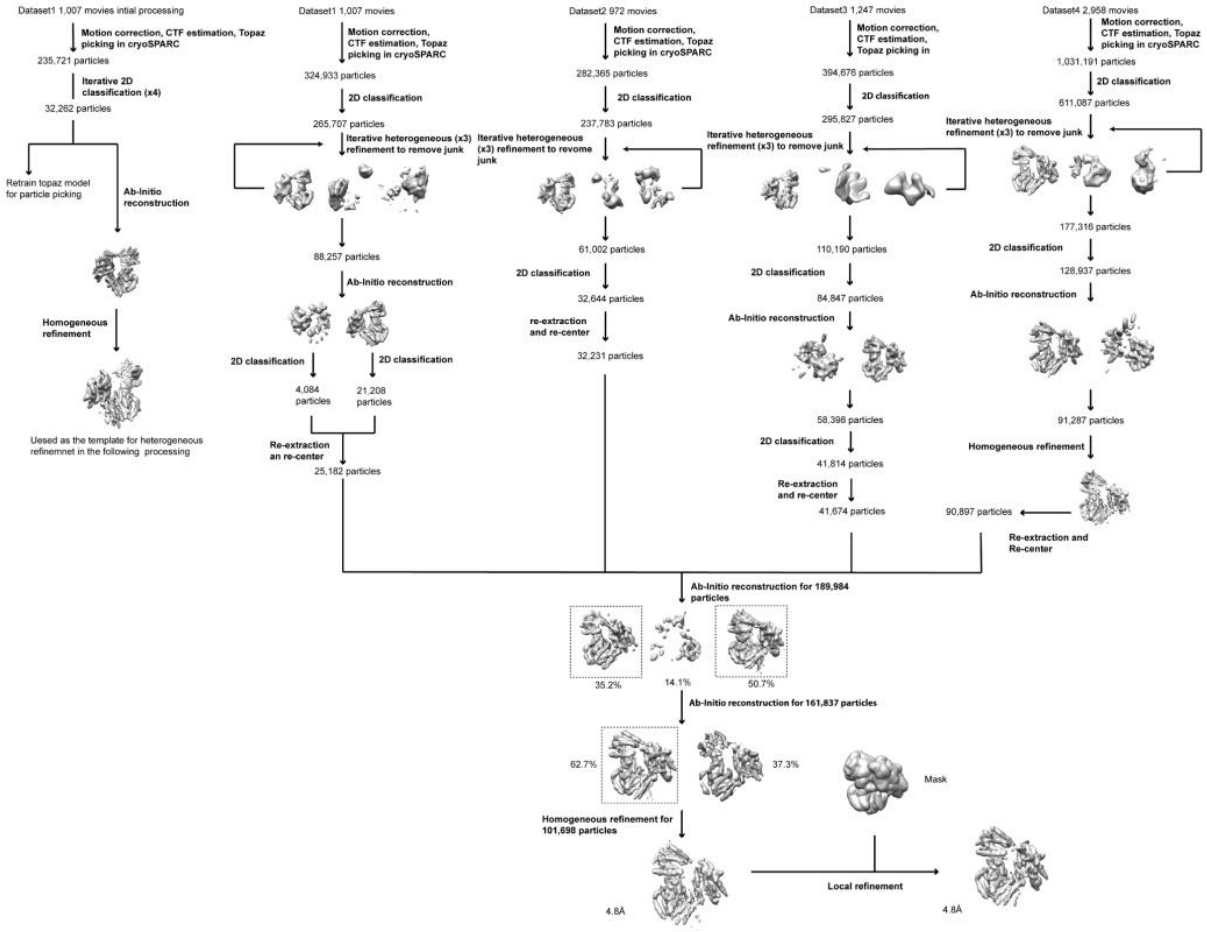

Fig. S4.8. Cryo-EM processing tree for KIFBP:KIF15. Overview of processing steps for KIFBP:KIF15.

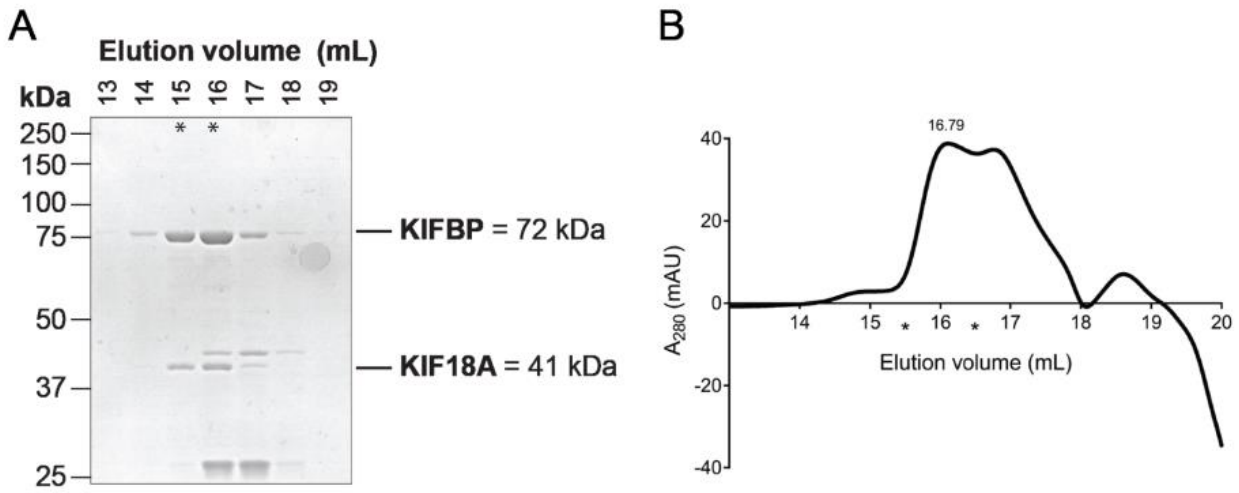

Fig. S4.9. Size exclusion chromatography of KIFBP:KIF18A. KIFBP and KIF18A were purified, combined, and run over the Superose 6 column as described in methods. (A) Representative Coomassie-stained SDS-PAGE of peak fractions from elution profile shown in (B). Fractions 15 and 16 were combined and used in subsequent cryo-EM experiments (indicated by asterisks). The molecular weight of each protein is indicated in kilodaltons.

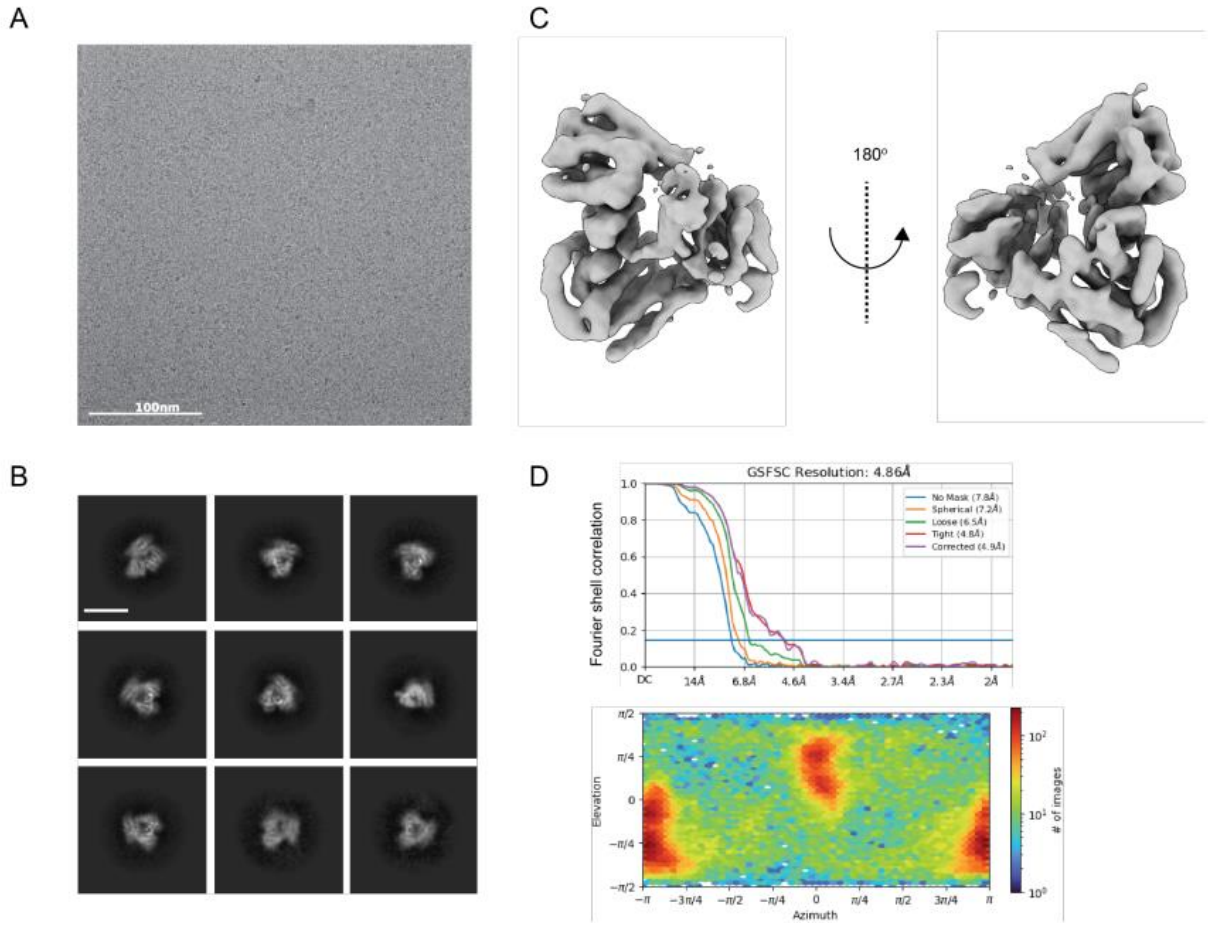

Fig. S4.10. Cryo-EM structure of KIFBP:KIF18A. (A) Representative micrograph for KIFBP:KIF18A. (B) Representative 2D class averages. Scale bar is 100Å. (C) Reconstruction overview. (D) FSC curves and Euler angle distribution.

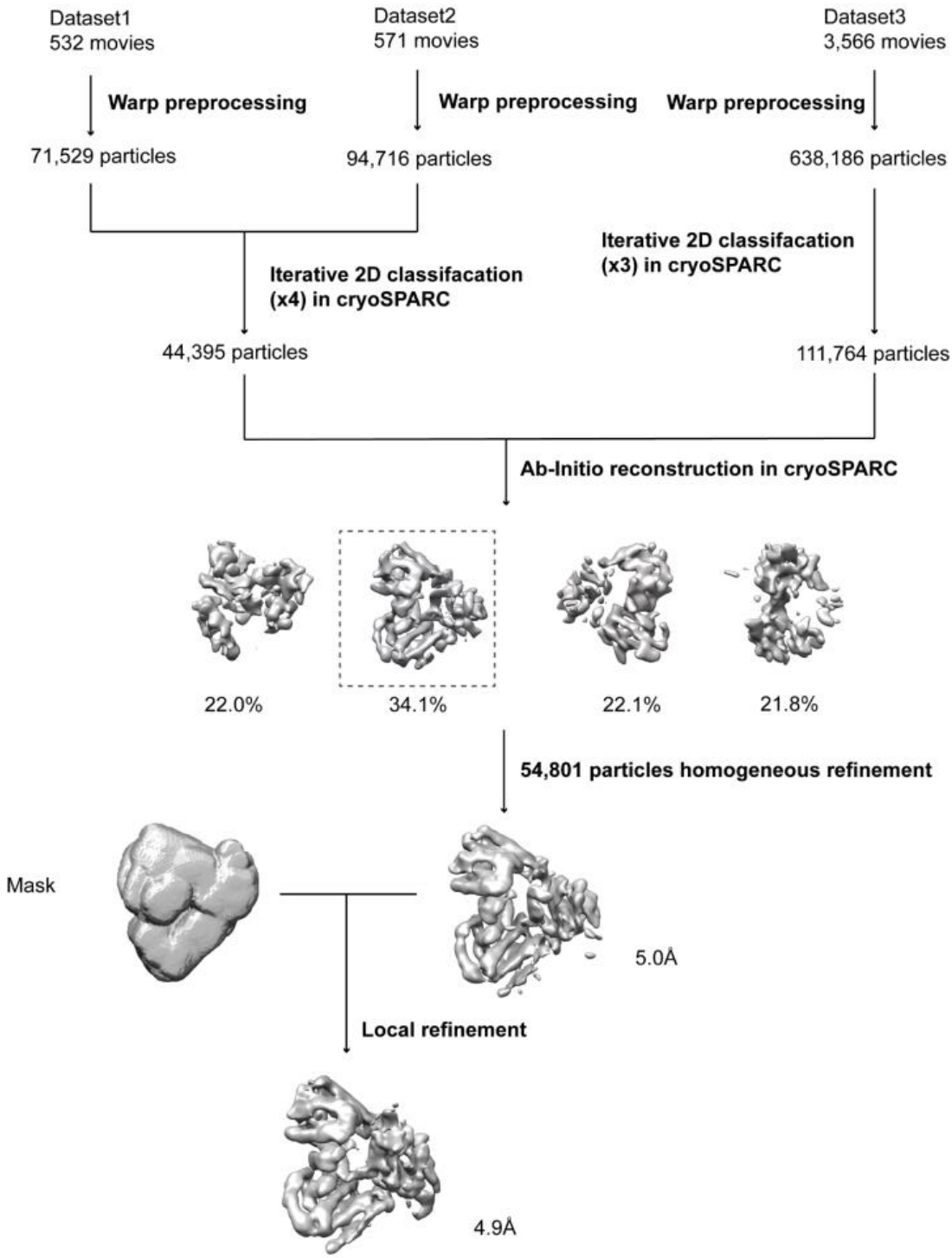

Fig. S4.11. Cryo-EM processing tree for KIFBP:KIF18A. Overview of analysis strategy for KIFBP:KIF18A.

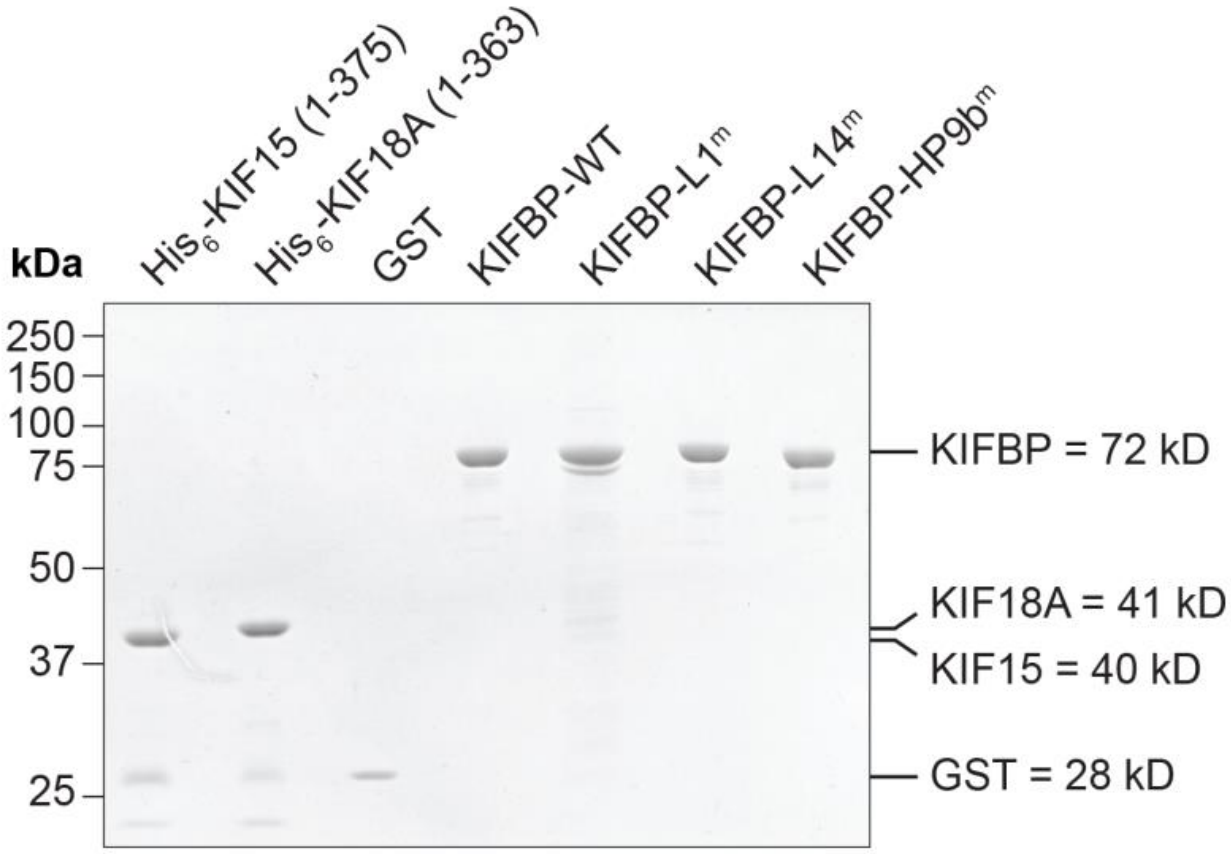

Fig. S4.12. Input of individual proteins used in the pull-down binding assay. Representative Coomassie gel of 1 µg of each protein used in the pull-down assays in Figure 6C & D.

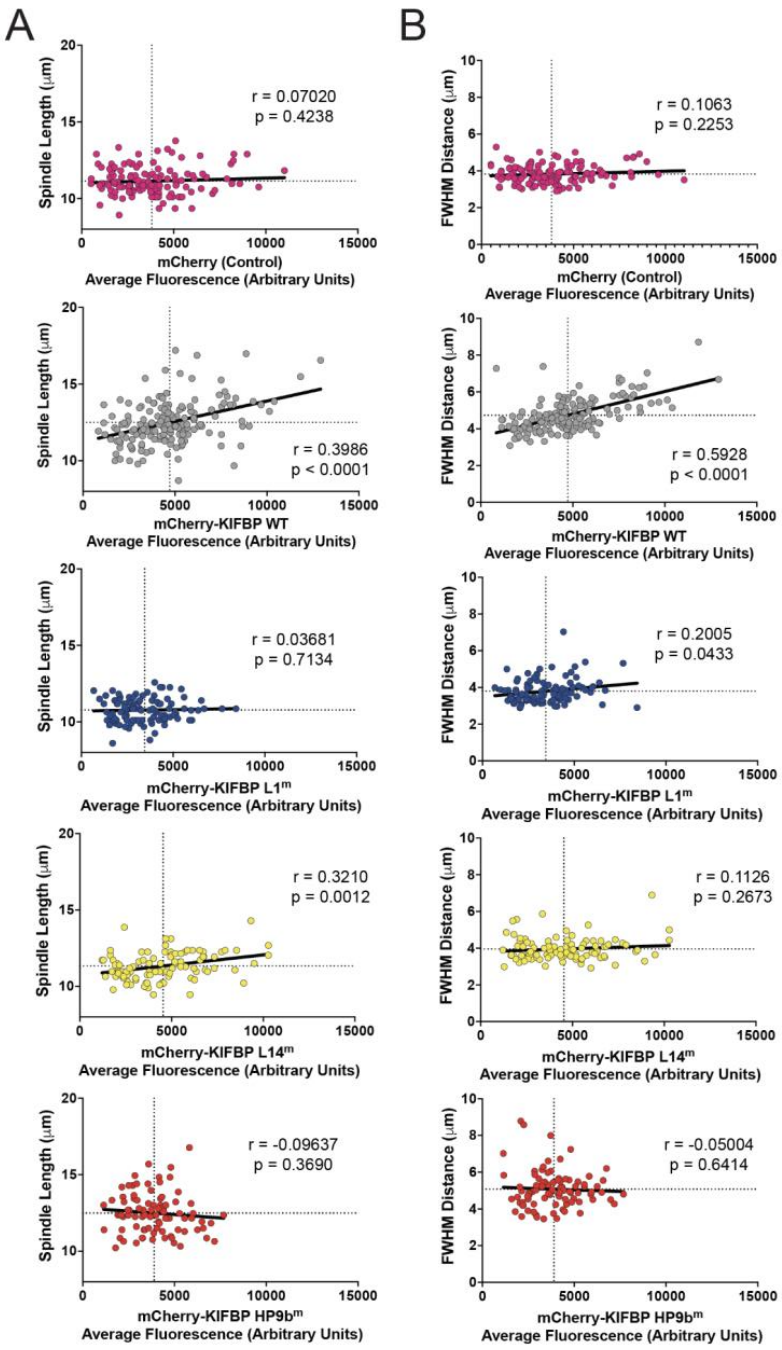

Fig. S4.13. Mitotic effects of mCherry-KIFBP-WT scale with expression level. (A) Plots of Spindle Length versus Average mCherry Fluorescence for HeLa Kyoto cells overexpressing mCherry or indicated mCherry-KIFBP construct. Each dot represents a single cell. Data presented from a minimum of three independent experiments. Dotted lines represent the mean value for Spindle Length or Average mCherry Fluorescence. Solid line is a linear regression showing the trend of the data. The Pearson's correlation coefficient (r) and two-tailed p-value with 95% confidence interval are shown for each plot. (B) Plots of Full-Width at Half Maximum (FWHM) Distance versus Average mCherry Fluorescence for HeLa Kyoto cells overexpressing mCherry or indicated mCherry-KIFBP construct. Each dot represents a single cell. Data presented from a minimum of three independent experiments. Dotted lines represent the mean value for FWHM distance or Average mCherry Fluorescence. Solid line is a linear regression showing the trend of the data. The Pearson's correlation coefficient (r) and two-tailed p-value with 95% confidence interval are shown for each plot.

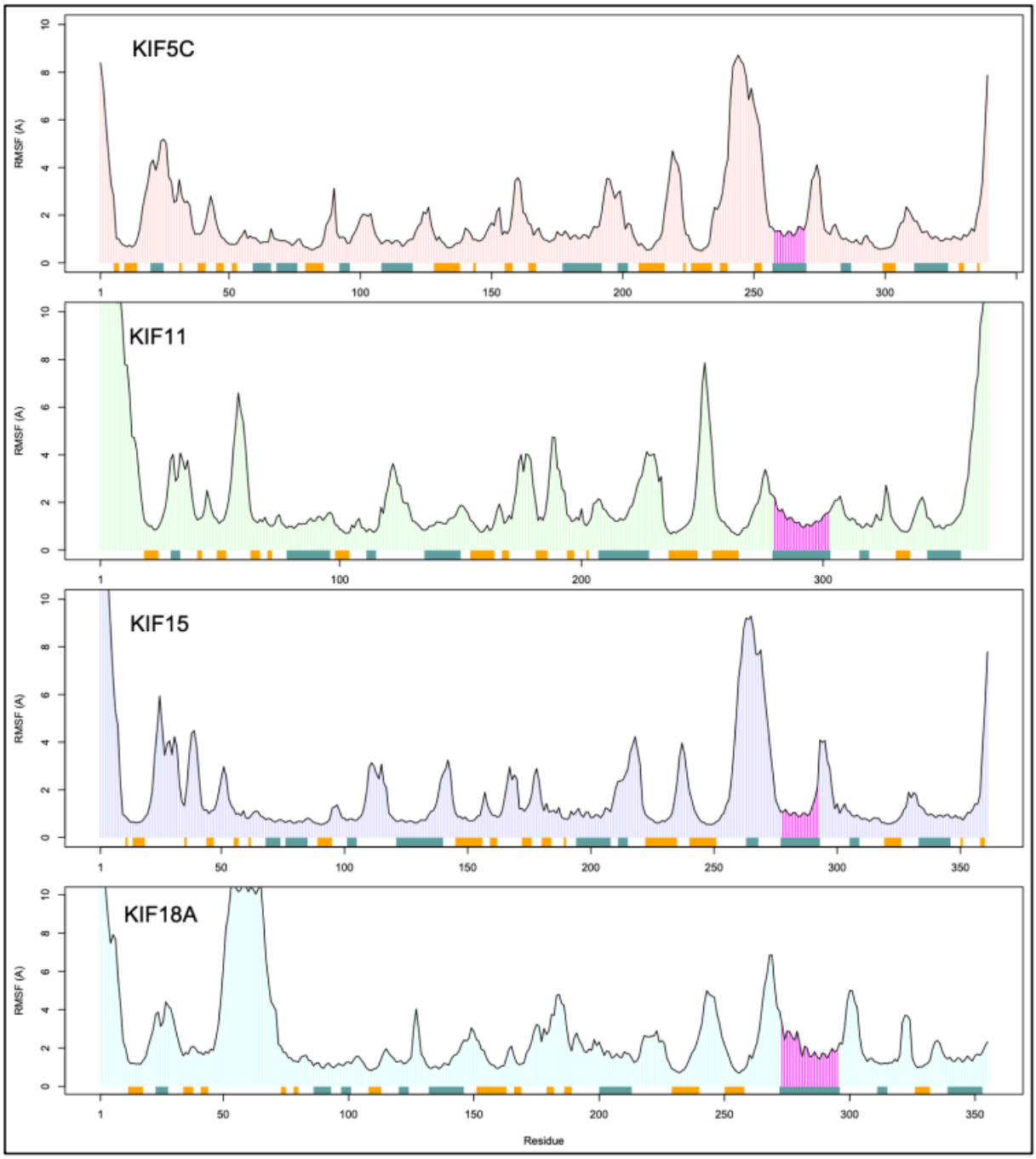

Fig. S4.14. Comparison of structural fluctuations for kinesin motors in solution as measured by MD. Shown are root mean squared fluctuations (RMSF) for kinesin motor domains in solution. The ribbon at the bottom of each plot shows the secondary structure - green indicates α-helices and orange represents β-strands. The position of α4 is marked by magenta for each protein.

Appendix A.2: Supplementary Tables

Table S4.1. Cryo-EM data collection, analysis, and validation statistics for KIFBP (full).

	Structure: KIFBP (full) (EMD-24745) (PDB 7RYQ)		
Data collection			
Grids	UltrAuFoil	UltrAuFoil	UltrAuFoil
Vitrification method	FEI Vitrobot	FEI Vitrobot	FEI Vitrobot
Microscope	Glacios	Glacios	Glacios
Session name	20jul13c	20jul07a	20jul11b
Magnification	45000X	45000X	45000x
Voltage (kV)	200	200	200
Stage tilt (°)	0	0	0
Detector	K2 Summit	K2 Summit	K2 Summit
Recording mode	Counting	Counting	Counting
Total electron exposure ($e^-/Å^2$)	58.5	68.4	65.0
Number of frames	45	40	35
Defocus range (μm)	0.8 – 2.0	0.8 – 2.0	0.8-2.0
Pixel size (Å)	0.98	0.98	0.98
Data processing			
Number of micrographs	5,349	1,596	4,144
Initial particle images (no.)	1,121,348	403,869	913,455
Final particle images (no.)	115,464	32,422	43,210
Final particles in refinement	154,176		
Symmetry	C1		
Map resolution (Å)	4.6		
Refinement			
Initial model used (PDB code)	N/A		
Cryo-efficiency (cryoEF)	0.7		
Model resolution (Å)	4.6		
FSC threshold	0.143		
Map sharpening *B* factor ($Å^2$)	-50		
Model composition			
Non-hydrogen atoms	4332		
Protein residues	527		
Ligands	0		
B factors ($Å^2$)	N/A		
Protein			
Ligand			
R.m.s. deviations	N/A		
Bond lengths (Å)			
Bond angles (°)			
Validation	N/A		
MolProbity score			
Clashscore			
Poor rotamers (%)			
Ramachandran plot	N/A		
Favored (%)			
Allowed (%)			
Disallowed (%)			

Table S4.2. Cryo-EM data collection, analysis, and validation statistics for KIFBP (core).

	Structure: KIFBP (core) (EMD-24677) (PDB 7RSQ)
Data collection	
Grids	UltrAuFoil
Vitrification method	FEI Vitrobot
Microscope	Glacios
Session name	20jul11b
Magnification	45000X
Voltage (kV)	200
Stage tilt (°)	0
Detector	K2 Summit
Recording mode	Counting
Total electron exposure (e^{-}/Å^2)	65
Number of frames	35
Defocus range (μm)	0.8 – 2.0
Pixel size (Å)	0.98
Data processing	
Number of micrographs	4,144
Initial particle images (no.)	913,455
Final particles in refinement	128,190
Symmetry	C1
Map resolution (Å)	3.8
Refinement	
Cryo-efficiency (cryoEF)	0.5
FSC model to map (0.143, 0.5)	3.5, 4.5
Initial model used (PDB code)	N/A
Model resolution (Å)	3.8
FSC threshold	0.143
Map sharpening *B* factor (Å^2)	-50
Model composition	
Non-hydrogen atoms	2015
Protein residues	246
Ligands	0
B factors (Å^2)	
Protein	57.76
Ligand	N/A
R.m.s. deviations	
Bond lengths (Å)	0.008
Bond angles (°)	0.942
Validation	
MolProbity score	1.65
Clashscore	3.25
Poor rotamers (%)	2.88
Ramachandran plot	
Favored (%)	96.90
Allowed (%)	3.10
Disallowed (%)	0

Table S4.3. Cryo-EM data collection, analysis, and validation statistics for KIFBP:KIF15.

	Structure: KIFBP:KIF15 (EMD-24744) (PDB 7RYP)			
Data collection				
Grids	UltrAuFoil	UltrAuFoil	UltrAuFoil	UltrAuFoil
Vitrification method	FEI Vitrobot	FEI Vitrobot	FEI Vitrobot	FEI Vitrobot
Microscope	Glacios	Glacios	Glacios	Glacios
Session name	20aug23f	20aug30b	20sep17h	20sep25f
Magnification	45000X	45000X	45000X	45000X
Voltage (kV)	200	200	200	200
Stage tilt (°)	0	0	0	0
Detector	K2 Summit	K2 Summit	K2 Summit	K2 Summit
Recording mode	Counting	Counting	Counting	Counting
Total electron exposure ($e^-/Å^2$)	83.6	60.1	61.25	60.76
Number of frames	40	30	35	35
Defocus range (μm)	0.8 – 2.0	0.8 – 2.0	0.8-2.0	0.8-2.0
Pixel size (Å)	0.98	0.98	0.98	0.98
Data processing				
Number of micrographs	1,007	972	1,247	2,958
Initial particle images (no.)	324,933	282,365	394,676	1,031,191
Final particle images (no.)	25,182	32,231	41,674	90,897
Final particles in refinement	101,698			
Symmetry	C1			
Map resolution (Å)	4.8			
Refinement				
Initial model used (PDB code)	4BN2			
Cryo-efficiency (cryoEF)	0.58			
Model resolution (Å)	4.8			
FSC threshold	0.143			
FSC model to map (0.143, 0.5)	4.8, 7.1			
Map sharpening *B* factor ($Å^2$)	-200			
Model composition				
Non-hydrogen atoms	5699			
Protein residues	725			
Ligands	0			
B factors ($Å^2$)				
Protein	199			
Ligand	0			
R.m.s. deviations				
Bond lengths (Å)	0.015			
Bond angles (°)	1.382			
Validation				
MolProbity score	1.68			
Clashscore	4.15			
Poor rotamers (%)	0			
Ramachandran plot				
Favored (%)	92.08			
Allowed (%)	6.22			
Disallowed (%)	1.70			

Table S4.4. Cryo-EM data collection, analysis, and validation statistics for KIFBP:KIF18A.

	Structure: KIFBP:KIF18A (EMD-24672) (PDB 7RSI)		
Data collection			
Grids	UltrAuFoil	UltrAuFoil	UltrAuFoil
Vitrification method	FEI Vitrobot	FEI Vitrobot	FEI Vitrobot
Microscope	Talos Arctica	Talos Arctica	Talos Arctica
Session name	20oct06g	20nov05c	21jan22b
Magnification	45000X	45000X	45000x
Voltage (kV)	200	200	200
Stage tilt (°)	0	0	0
Detector	K2 Summit	K2 Summit	K2 Summit
Recording mode	Counting	Counting	Counting
Total electron exposure (e^{-}/Å^2)	57.0	51.8	61.2
Number of frames	35	35	40
Defocus range (μm)	0.8 – 2.0	0.8 – 2.0	0.8-2.0
Pixel size (Å)	0.91	0.91	0.91
Data processing			
Number of micrographs	532	571	3,566
Initial particle images (no.)	71,529	94,716	638,186
Final particle images (no.)	44,395		111,764
Final particles in refinement	54,801		
Symmetry	C1		
Map resolution (Å)	4.9		
Refinement			
Initial model used (PDB code)	3LRE		
Cryo-efficiency (cryoEF)	0.67		
Model resolution (Å)	4.9		
FSC threshold	0.143		
Map sharpening *B* factor (Å^2)	-163.5		
Model composition	N/A		
Non-hydrogen atoms			
Protein residues			
Ligands			
B factors (Å^2)	N/A		
Protein			
Ligand			
R.m.s. deviations	N/A		
Bond lengths (Å)			
Bond angles (°)			
Validation	N/A		
MolProbity score			
Clashscore			
Poor rotamers (%)			
Ramachandran plot	N/A		
Favored (%)			
Allowed (%)			
Disallowed (%)			

Table S4.5. High-confidence crosslinks between KIFBP and KIF15. A summary of all high-confidence crosslinks identified between KIFBP and the KIF15 motor domain using mass spectrometry and the lysine-targeting crosslinker BS3. The position of KIFBP and KIF15 residues of each crosslink are shown.

KIFBP Residue	KIF15 Residue
26	273
	283
	319
	361
30	273
	283
	319
	361
	364
	366
36	273
	283
205	273
	283
307	283
	319
350	364
556	361
	366
564	283
	364
610	319
	361
	364
	366
617	361
	364